Iron-based Superconductors in High Magnetic Fields

—

Zur Erlangung des akademischen Grades eines
DOKTORS DER NATURWISSENSCHAFTEN (Dr. rer. nat.)

von der KIT-Fakultät für Physik des
Karlsruher Instituts für Technologie (KIT)
angenommene

DISSERTATION

von

Dipl.-Phys. Loïc Doussoulin

Referent: Pr. Thierry Klein (Université Grenoble Alpes)
Referent: Pr. Matthieu Le Tacon (KIT)
Korreferent: Dr. Christophe Marcenat (CEA Grenoble)
Korreferent: Dr. Frédéric Hardy (KIT)

Tag der mündlichen Prüfung: 10.12.2021

Acknowledgements

Lors de la rédaction d'une thèse, il est de coutume d'écrire certaines parties auxquelles il est impossible d'échapper. Il y a bien évidemment le corps du manuscrit, mais aussi une conclusion, ou bien une bibliographie... mais lors de ma thèse j'ai préféré garder la rédaction du meilleur pour la fin même, si c'est cela qui apparaîtra en premier lors de la lecture de ce manuscrit : les remerciements. Il est évidemment dur de faire une liste exhaustive des personnes qui m'ont aidé lors de ma thèse et de peser les mots justes pour chaque personne. Mes mots ne retransmettront qu'en partie à quel point je veux remercier ces personnes mais, pour finir la rédaction de ce manuscrit, je vais tenter de faire ça avec la rigueur la moins scientifique possible pour une fois.

Mes premières pensées vont évidemment à ma famille. Elle m'a toujours soutenu pendant ce long parcours de plus de 3 ans, et qui avait commencé même bien avant. Je voudrais tout d'abord remercier ma petite sœur, Ilona, pour toujours avoir pris soin de moi alors que parfois c'était elle qui était le plus dans le besoin ; ma mère, Agnès, pour son soutien infaillible, et mon père, Christophe, pour les discutions partagées, que ce soit sur la physique ou non. Mais aussi mes grands parents, Sébastien, Christiane, Roger et Marie, sans qui tout cela n'aurait pas été possible et qui même s'ils ne comprenaient pas forcement tout ce que je faisais, étaient toujours là. Je vous en serai éternellement reconnaissant. Concernant la famille, je voudrais aussi remercier mon beau-père, Olivier, pour m'avoir aussi servi de guide dans cette voie qu'est la recherche. Sans chacun d'entre eux, je n'en serai sûrement pas là aujourd'hui.
En parlant de recherche, il me faut aussi remercier les nombreuses personnes qui ont travaillé avec moi et sur lesquelles j'ai pu m'appuyer. En effet,

discussions.

: Sergui et Charlotte. Toutes les deux ont premièrement relu ma thèse, et sans forcement comprendre tous ce que je racontais, mais ont aussi été là pendant les moments les plus durs avec un soutien sans faille. Merci beaucoup! Et je voudrais quand même ajouter un petit mot de plus pour Sergui : j'ai bien avancé dans l'alphabet et me suis envolé!

Abstract

Iron-based superconductors are a recent discovery in the history of superconductivity. Discovered about ten years ago, their phase doping-temperature diagrams are close to some materials like cuprates. When cuprates show schematically a Mott insulator phase, a pseudogap phase and a superconducting phase, iron-based superconductors mainly show three transitions: a nematic transition, a magnetic transition and a superconducting transition. However, the simplest of the iron-based superconductors, FeSe, does not show a magnetic phase at ambient conditions. Its low Fermi energy suggests the presence of fluctuations that might lead to the observation of the vortex lattice melting over its entire phase diagram. This will be presented in the first chapter of this thesis.

Specific heat was chosen as the main measurement technique of our samples. Two set-ups were used: the Dual Slope Method and alternative Calorimetry. The alternative calorimetry device allows access to high magnetic fields up to 35T and thus gives the opportunity to study the complete phase diagram of our compounds. It is also a particularly sensitive probe to phase transitions, which is one of the core topics of this thesis. In the second chapter, I will present the thermodynamic properties of interest to obtain our phase diagram as well as the different set-ups used during our work.

The third chapter presents the measurements made during the PhD and their analysis. A first part focuses on the pure FeSe compound. Our data reveal an excess of specific heat before the superconducting transition attributed to the presence of a transition between a solid and a vortex liquid. Using a scaling approach we deduce the fictitious upper critical field line. The temperature dependence of this field shows an important effect of Cooper pair breaking by paramagnetic effects, mainly when the magnetic field is oriented along FeSe layers. The melting of the vortex lattice

also shows that beyond thermal fluctuations, possible quantum fluctuations could be present. Finally we study the possible appearance of a Fulde-Ferrell-Larkin-Ovchinnikov phase. The second part of this chapter focuses on the $FeSe_{0.88}S_{0.12}$ doped compound. A comparative study of its phase diagram with that of FeSe is conducted, revealing a great similarity between the two compounds. Moreover a new anomaly is detected in our specific heat data, which is still under investigation.

Abstract

Les supraconducteurs à base de fer sont une découverte récente dans l'histoire
de la supraconductivité. Découvert il y a une dizaine d'année, leurs dia-
grammes de phase se rapprochent de certains matériaux comme les cuprates.
Quand les cuprates montrent de manière schématique une phase isolant de
Mott, une phase pseudogap et une phase supraconductrice, les supraconduc-
teurs à base de fer montrent principalement trois transitions : une transition
nématique, une transition magnétique et une transition supraconductrice.
Cependant le composé le plus simple parmi les supraconducteurs à base
de Fer, FeSe, ne montre pas de phase magnétique à conditions ambiantes.
Son énergie de Fermi faible laissent entrevoir la presence de fluctuations qui
pourrait mener à l'observation de la fusion du réseau de vortex sur la total-
ité de son diagramme de phase et d'étudier les effets qui peuvent influencer
la ligne du champ critique supérieur. Ceci sera présenté durant le premier
chapitre de cette thèse.

La chaleur spécifique a été choisi comme technique de mesure principale des
échantillons. Deux techniques ont été utilisées : la Dual Slope Method et la
calorimétrie alternative. Le dispositif de calorimétrie alternative permettant
l'accès à des champs magnétiques intenses jusqu'à 35T, il donne l'occasion
d'étudier le diagramme de phase complet de nos composés. C'est aussi une
sonde particulièrement sensible aux transitions de phase, ce qui est l'objet
de cette thèse. Dans le deuxième chapitre, j'exposerai donc les propriétés
thermodynamiques intéressantes pour obtenir notre diagramme de phase
ainsi que les différents dispositifs utilisés au cours de nos travaux.

Le troisième chapitre expose les mesures faites au cours du doctorat ainsi que
leurs analyses. Une première partie se focalise sur le composé pur FeSe. Nos
données révèlent un excès de chaleur spécifique avant la transition supracon-
ductrice attribué à la présence d'un transition entre un solide et un liquide

de vortex. A l'aide d'une approche par loi d'échelle nous déduisons la ligne fictive du champ critique supérieur. La dépendance en température de ce champ trahit un effet important de brisure de paires de Cooper par effets paramagnétiques, principalement quand le champ magnétique est orienté le long de couches de FeSe. La fusion du réseau de vortex montre aussi qu'au delà de fluctuations thermiques, de possibles fluctuations quantiques pourraient être présentes. Enfin nous étudions la possible apparition d'une phase de Fulde-Ferrell-Larkin-Ovchinnikov. La deuxième partie de ce chapitre se concentre sur le composé dopé $FeSe_{0.88}S_{0.12}$. Une étude comparative de son diagramme de phase avec celui de FeSe y est menée, révélant une grande similarité entre les deux composés. De plus une nouvelle anomalie est détecté dans nos données de chaleur spécifique. Cette dernière est toujours en cours d'investigation.

Abstract

Supraleiter auf Eisenbasis sind eine neue Entdeckung in der Geschichte
der Supraleitung. Ihre Phasendotierungs-Temperatur-Diagramme, die vor
etwa zehn Jahren entdeckt wurden, ähneln denen einiger Materialien wie
z. B. Kuprate. Während Kuprate schematisch eine Mott-Isolator-Phase,
eine Pseudogap-Phase und eine supraleitende Phase aufweisen, zeigen eisen-
basierte Supraleiter hauptsächlich drei Übergänge: einen nematischen Über-
gang, einen magnetischen Übergang und einen supraleitenden Übergang.
Der einfachste der eisenbasierten Supraleiter, FeSe, zeigt jedoch bei Umge-
bungsbedingungen keine magnetische Phase. Seine niedrige Fermi-Energie
deutet auf das Vorhandensein von Fluktuationen hin, die zur Beobach-
tung des Schmelzens des Wirbelgitters über sein gesamtes Phasendiagramm
führen könnten. Dies wird im ersten Kapitel dieser Arbeit vorgestellt.

Die spezifische Wärme wurde als Hauptmessverfahren für unsere Proben
gewählt. Es wurden zwei Versuchsaufbauten verwendet: die Dual Slope-
Methode und die alternative Kalorimetrie. Das alternative Kalorimetriegerät
ermöglicht den Zugang zu hohen Magnetfeldern bis zu 35T und bietet somit
die Möglichkeit, das vollständige Phasendiagramm unserer Verbindungen zu
untersuchen. Sie ist auch eine besonders empfindliche Sonde für Phasenübergänge,
was eines der Kernthemen dieser Arbeit ist. Im zweiten Kapitel werde ich die
thermodynamischen Eigenschaften vorstellen, die für die Erstellung unseres
Phasendiagramms von Interesse sind, sowie die verschiedenen Versuchsauf-
bauten, die während unserer Arbeit verwendet wurden.

Im dritten Kapitel werden die im Rahmen der Doktorarbeit durchgeführten
Messungen und ihre Auswertung vorgestellt. Ein erster Teil konzentriert sich
auf die reine FeSe-Verbindung. Unsere Daten zeigen einen Überschuss an
spezifischer Wärme vor dem supraleitenden Übergang, der auf das Vorhan-
densein eines Übergangs zwischen einem Festkörper und einer Wirbelflüs-

sigkeit zurückzuführen ist. Mithilfe eines Skalierungsansatzes leiten wir die fiktive obere kritische Feldlinie ab. Die Temperaturabhängigkeit dieses Feldes zeigt eine wichtige Auswirkung der Cooper-Paar-Auflösung durch paramagnetische Effekte, vor allem wenn das Magnetfeld entlang der FeSe-Schichten ausgerichtet ist. Das Schmelzen des Wirbelgitters zeigt auch, dass neben thermischen Fluktuationen auch Quantenfluktuationen auftreten können. Schließlich untersuchen wir das mögliche Auftreten einer Fulde-Ferrell-Larkin-Ovchinnikov-Phase. Der zweite Teil dieses Kapitels konzentriert sich auf die mit $FeSe_{0.88}S_{0.12}$ dotierte Verbindung. Es wird eine vergleichende Studie ihres Phasendiagramms mit dem von FeSe durchgeführt, wobei eine große Ähnlichkeit zwischen den beiden Verbindungen festgestellt wird. Außerdem wurde eine neue Anomalie in unseren Daten zur spezifischen Wärme entdeckt, die noch untersucht wird.

Contents

CONTENTS

List of Figures

LIST OF FIGURES

List of Tables

1

Introduction

1.1 A bit of History

1.2 Thermodynamics in high-temperature superconductors

Superconductivity was discovered in 1911 by Heike Kammerlingh-Onnes in Leiden. After managing to liquefy helium, he measured the resistivity of mercury with temperature and observed a sudden drop to zero at 4.2 K [(3)]. A few years later, in 1933, Meissner and Ochsenfeld discovered the second major characteristic of superconductors: it is a perfect diamagnetic [(4)]. Since then thousands of articles have attempted to explain what happens inside a superconductor. An important step was taken by Ginzburg and Landau in 1950 [(5)], who explained the phenomenology of superconductors and characterized it by three aspects : infinite conductivity, an order parameter, and perfect diamagnetism. The next significant step occurred in 1957, when Bardeen, Cooper and Schrieffer, described how most of the superconductors worked at the time. They explained that an energy gap opens at low temperature due to electron-phonon coupling and giving birth to superconductivity [(6)]. Yet the rise of the so-called high temperature superconductors (HTSCs), discovered by Bednorz and Müller in 1986, overrides this theory. Nevertheless the phenomenological aspect of Ginzburg and Landau remains applicable [(7)]. Having a basic theory that fits to them, HTSCs are perfect to study the vortex matter which appears in type II superconductors and many studies were conducted for example on YBCO.

1.2.1   Ginzburg-Landau theory

While type I superconductors only exhibits two phases, a fully superconducting sample or non superconducting sample; type II superconductors have a higher amount of phases which will be discussed, mainly arising from a mixed state, where a sample can be superconducting in some areas (vortices) and non-superconducting in others. The phenomenology here can be explained by the Ginzburg-Landau theory which is based on the free energy of a charged superconductors in a magnetic field. Landau started to describe ferromagnetism and then Ginzburg extended it to superconductivity by assuming the existence of a macroscopic wave function ψ, being also the order parameter of superconductivity [[8]]. The free energy can therefore be written as :

$$f_s = f_n + \alpha|\psi|^2 + \frac{1}{2}\beta|\psi|^4 \tag{1.1}$$

Where f_s is the free energy in the superconducting state and f_n the one in the normal state. To take into account the spatial variations of the order parameter, a kinetic term, $\frac{\hbar}{2m}|\nabla\psi|^2$, must be added to Eq 1.1. Having added a magnetic field in this equation, two terms appears : the contribution of the magnetic field to the energy density, $\frac{1}{2\mu_0}B^2$; and the interaction of the electrons with the field in the kinetic energy, $\nabla \to \nabla - \frac{iq}{\hbar}A$. In the end the free energy can be written as :

$$f_s = f_n + \alpha|\psi|^2 + \frac{1}{2}\beta|\psi|^4 + \frac{\hbar^2}{2m}|\left[\nabla - \frac{iq}{\hbar}A\right]\psi|^2 + \frac{1}{2\mu_0}B^2 \tag{1.2}$$

Close to transition temperature, T_c, α can be written as $\alpha_0(T - T_c)$. That is one of the hypothesis made by Ginzburg and Landau: all the coefficients can be written as a regular function of the temperature. It is decided to take only the first order. By integrating f_s over the volume and minimizing it with respect to ψ and A, it is then possible to get the two Ginzburg-Landau equations :

$$\alpha\psi + \beta|\psi|^2\psi - \frac{\hbar^2}{2m}\left[\nabla - \frac{iq}{\hbar}A\right]^2\psi = 0 \tag{1.3}$$

$$\nabla \times H = -\frac{4\pi q}{m}\left(\frac{i\hbar}{2}[\psi^*\nabla\psi - \psi\nabla\psi^*] - q|\psi|^2A\right) \tag{1.4}$$

Solving these equations gives two characteristic lengths. Eq 1.3 gives an idea about how the order parameter varies with the distance, and allows to give an expression to the so
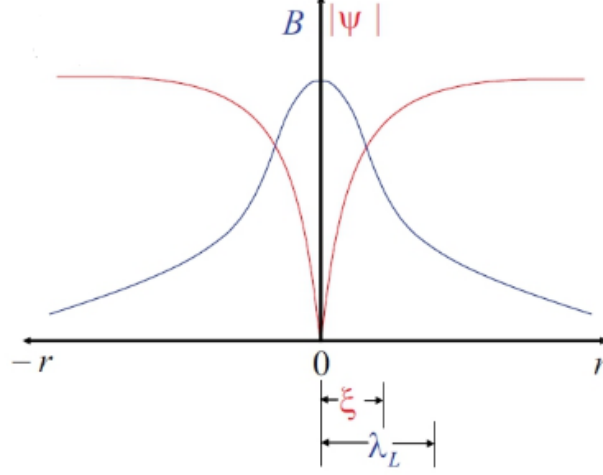
Figure 1.1: Penetration and coherence length around a vortex

called coherence length, ξ.

$$\psi = \left(\frac{|\alpha|}{\beta}\right)^{1/2} \tanh\left(\frac{x}{\sqrt{2}\xi}\right) \tag{1.5}$$

$$\xi(T) = \left(\frac{\hbar^2}{2m\alpha_0 T_c}\right)^{1/2} \left(1 - \frac{T}{T_c}\right)^{-1/2} \tag{1.6}$$

Eq 1.4 can be solved to obtain the penetration depth, λ, which gives the typical value of the variations of the field in the sample.

$$\lambda(T) = \left(\frac{m\beta}{4\pi q^2 \alpha_0 T_c}\right)^{1/2} \left(1 - \frac{T}{T_c}\right)^{-1/2} \tag{1.7}$$

Fig. 1.1 shows the typical lengths around a vortex in a type II superconductor.

Let us now try to understand a bit more Eq. 1.2 and focus on the kinetic energy term. ψ is a complex function and can therefore be written as, $|\psi|e^{i\phi}$. The kinetic energy can thus be written as :

$$\frac{\hbar^2}{2m}\left|\left[\nabla - \frac{iq}{\hbar}A\right]\psi\right|^2 = \frac{\hbar^2}{2m}\left[(\nabla|\psi|)^2 + (\nabla\phi - \frac{q}{\hbar}A)^2|\psi|^2\right] \tag{1.8}$$

By identification, one can find the superfluid velocity, $v_s = \frac{1}{m}(\nabla\phi - \frac{q}{\hbar c}A)$. That velocity is useful to understand how the flux quantization works. With the second Ginzburg-Landau equation, one knows that the supercurrent responsible for the Meissner effect,

i.e. the diamagnetism, only flows on a small layer of the cross section of a thickness λ, so that away from the center of a contour the current is zero and then $v_s = 0$. It follows

$$\oint v_s.dl = \oint \frac{1}{m}(\nabla\phi - \frac{q}{\hbar}A) = 2\pi n + \frac{q}{\hbar}\Phi \tag{1.9}$$

$$\Phi = \frac{nh}{q} = n\Phi_0 \tag{1.10}$$

Where n is an integer and Φ_0 is the flux quantum responsible for the flux quantization.

Let us now look at critical fields in the superconductor and examine when does superconductivity disappear. The overall energy of the system is conserved so that the system's condensation energy in zero field, $f_s - f_n$, must be equal to the one of the magnetic energy at the critical field where the Meissner effect no longer exists.

$$f_s - f_n = -\frac{H_c^2}{8\pi} \tag{1.11}$$

$$H_c = \sqrt{\frac{2\pi\alpha_0^2}{\beta}(T - T_c)} \tag{1.12}$$

One can also try to minimize f_s close to the transition. It means that $|\psi|^2 \approx 0$ so that one can neglect the 4-th order term in Eq 1.2. One can also only minimize the kinetic term in that expression because the second order term will only affect the normalization. After writing $\overrightarrow{A} = Hy\overrightarrow{x}$, and considering a solution with the form $\psi = \eta(y)e^{-ik_x x - ik_z z}$, one tries to find the eigen values :

$$\frac{\hbar}{2m}\left[(k_x + \frac{y}{l_m^2})^2 - \frac{\partial^2}{\partial y^2} - k_z^2\right]\eta(y) = E\eta(y) \tag{1.13}$$

where $l_m = \sqrt{1/\hbar qH}$. It recalls the expression of an harmonic oscillator and the problem is similar to the Landau levels and one finds the eigen energy to be :

$$E = \frac{qH\hbar}{2m} \tag{1.14}$$

Introducing it back in Eq. 1.2

$$f = \left(\alpha_0(T - T_c) + \frac{qH\hbar}{2m}\right)|\psi|^2 + \beta|\psi|^4 \tag{1.15}$$

A change in the sign of the quadratic coefficient gives rise to another form of the function, which can be interpreted as a phase transition. This is the criteria for a second critical field:

$$H_{c2} = \frac{2\alpha_0 m}{q\hbar}(T_c - T) \tag{1.16}$$

Following this, the next question is, which one of these fields is the limiting criteria to express when superconductivity disappears in the sample. In the first case, at H_c, the field is completely expelled of the sample, while in the second there might be some spatial variations of the order parameters, creating vortices in the sample at H_{c2}. Thus the differentiation criteria between type I and type II superconductors, is to check which one of these fields is more likely to appear first in the $H - T$ phase diagram. Since the Ginzburg-Landau formalism is only valid close to T_c, one only compares the two slopes.

$$\left.\frac{dH_{c2}}{dT}\right|_{T_c} = \left.\frac{dH_c}{dT}\right|_{T_c} \tag{1.17}$$

$$\frac{1}{2} = \frac{m^2 b}{\pi q^2} \tag{1.18}$$

Defining the Ginzburg-Landau parameter as $\kappa = \lambda/\xi$, one finally get the final criteria to differentiate between the two types of superconductors :

$$\kappa^2 = \frac{1}{2} \tag{1.19}$$

Therefore in a type I superconductors, κ is smaller than $1/2$ and greater in a type II.

1.2.2   Superconducting fluctuations

Since superconductivity is suppressed with field and temperature, some variations of the order parameter may exist before the superconductive transition actually happens, which are called fluctuations, and we want to check here in what part of the $H - T$ phase diagram they take place.

Let us first assume the Ginzburg Landau functional without any field and try to express the specific heat of the system.

$$f_s = f_n + \alpha|\psi|^2 + \frac{1}{2}\beta|\psi|^4 + \frac{\hbar^2}{2m}|\nabla\psi|^2 \tag{1.20}$$
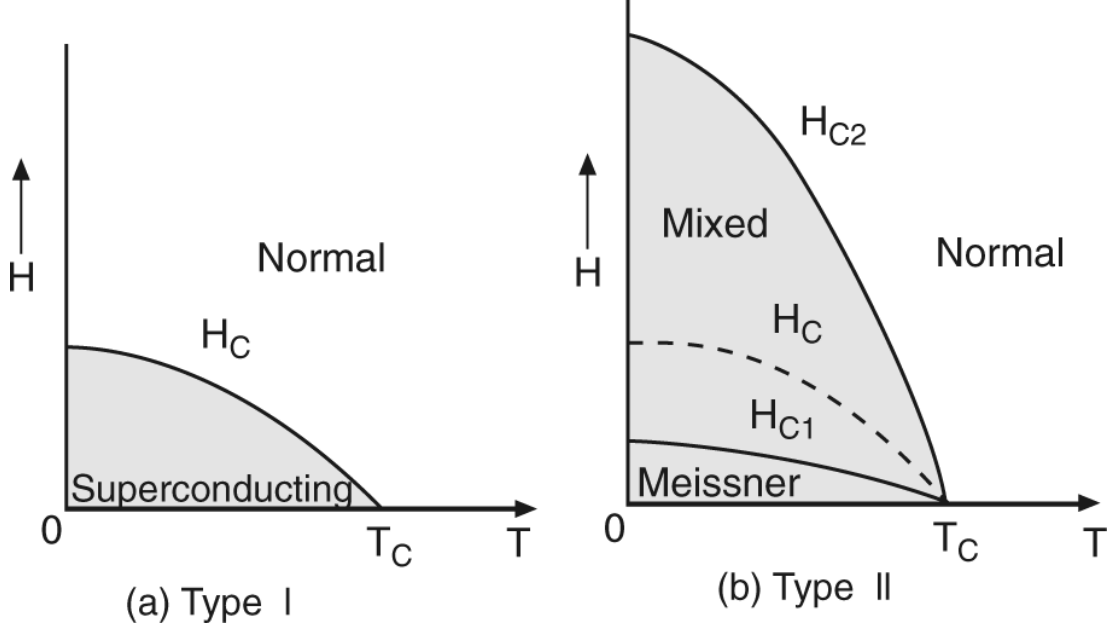
Figure 1.2: Magnetic phase diagram for type-I and type-II superconductors. From [[9]]

As a first approximation $|\psi|^4$ will be neglected (also called Gaussian approximation) and the order parameter is written as a Fourier transform :

$$\psi(\overrightarrow{r}) = \frac{1}{\sqrt{V}} \sum_k \psi_k e^{i\overrightarrow{k}\overrightarrow{r}} \tag{1.21}$$

By integrating the function, $F(\psi) = \int d^3 r(f_s - f_n)$, one finally obtains :

$$F(\psi) = \sum_k \left[\alpha + \frac{\hbar^2 k^2}{2m} \right] |\psi_k|^2 \tag{1.22}$$

The partition function, defined as $Z = \int d\psi e^{\frac{-F(\psi)}{k_b T}}$, is therefore equal to :

$$Z = \prod_k \sqrt{\frac{\pi k_b T}{\alpha + \frac{\hbar^2 k^2}{2m}}} \tag{1.23}$$

Using the definition of the specific heat being $C/T = \partial S/\partial T$, and $S = -\partial F/\partial T = \partial k_B T \ln(Z)/\partial T$, the specific heat can finally be written as :

$$C = \frac{k_B V}{4\pi^2 \xi_0^3} \left[\frac{1}{3} - \frac{5(1+\tau)}{2} + \frac{\arctan(\tau^{-1/2})}{2\tau^{1/2}}(1+\tau)(5\tau + 1) \right] \tag{1.24}$$

with $\tau = (T - T_c)/T_c$. Only considering the most diverging term close to T_c, the specific heat is then :

$$C = \frac{k_B V}{8\pi\xi_0^3} \left(\frac{T_c}{T - T_c} \right)^{1/2} \tag{1.25}$$

The former expression is entirely obtained by the Ginzburg Landau theory neglecting the $|\psi|^4$ term, this is called the Gaussian approximation. However this approximation can not be applied on the entire phase diagram, as indeed fluctuations are known to be strong close to the transition and one can not neglect the quartic term, this is the critical region. The remaining question is: where are the limits of applicability of the fluctuation corrections to the heat capacity obtained above ? The fluctuation corrections must match the value of the corresponding physical values. Concerning the specific heat it gives the Ginzburg criterion, by comparing the fluctuation corrections obtained above and the specific heat jump obtained by mean-field theory, $\Delta C_{mf} = H_c^2 V / 4\pi T_c$. Comparing these equations one gets:

$$\frac{T - T_c}{T_c} = \frac{1}{4} \left(\frac{k_B T_c}{H_c^2 \xi^3} \right)^2 \tag{1.26}$$

Giving a definition to the Ginzburg number, G_i.

$$G_i = \frac{1}{2} \left(\frac{k_B T_c}{H_c^2 \xi^3} \right)^2 \tag{1.27}$$

So that when $T - T_c < 0.5 G_i T_c$, it is not possible to only consider Gaussian fluctuations and the quartic term must be taken into account. The Ginzburg number here is a comparison between the thermal energy due to T_c and the condensation energy. If the superconductor is layered then the Ginzburg number is divided by $\epsilon = \sqrt{m/M}$, the square root of the ratio of the quasiparticle's effective mass parallel to the superconducting plan and perpendicular to the superconducting plane.

In field, these fluctuations are enhanced and the field dependant Ginzburg number $G_i(H)$ follows that law :

$$G_i(H) = G_i^{1/3} \left(\frac{H}{H_{c2}' T_c} \right)^{2/3} \tag{1.28}$$

Let us try to have a more detailed representation of what is happening in the Gaussian approximation and compare it in the critical region. In the Gaussian approximation, the order parameter and its fluctuations are supposed to be weak enough so that the

quadratic term in the Ginzburg Laudau functionnal is much higher than the quartic term. However going closer to the critical region, the quartic term becomes bigger and it is not possible to neglect it at some point. We can thus write that the crossover happens when :

$$\alpha < |\psi|^2 > = \frac{1}{2}\beta < |\psi|^4 > \tag{1.29}$$

Since we are looking at the limit value where it is possible to decouple fluctuations, let us write that they are independent ($< |\psi|^2 >^2 = < |\psi|^4 >$) and that will give us the criterion for the crossover. From that it is possible to deduce a typical length $\xi_G = (\beta m^2 k_B T_c/\hbar^4)^{-1}$ which describe the scope of the interactions in the system. If $\xi(T) < \xi_G$ then the correlated regions are smaller than the scope of the interactions between the fluctuations and it is possible to average the fluctuations in order to neglect the interactions. In that scenario the Gaussian approximation is valid. On the other side, if $\xi(T) > \xi_G$, the interactions within the fluctuations are quite high and one can not neglect them, this is the critical regime [(10)].

1.2.3 The vortex matter

1.2.3.1 General physics of the vortex matter

As we discussed above there are several types of superconductors. Abrikosov proposed in 1957 a phase diagram, based on the Ginzburg-Landau theory to have a better idea of the vortex matter in a superconductor [(11)]. In that phase diagram (cf Fig. 1.2), for a field $H < H_{c1}$, there is a complete expulsion of the magnetic field and the entire sample is superconducting: this is called the Meissner phase. For a higher field, a different phase arises, the mixed state, sometimes called Shubnikov phase. Here the magnetic field penetrates the sample in the shape of vortices. They form an Abrikosov lattice, that is triangular (at least in the framework of that theory). When increasing the field, more field penetrates the sample until the vortices proliferate and overlap each others and reach a second critical field H_{c2}, where there is no more superconductivity. Now applying current in the superconductor, the vortices will start to move under the action of the Lorentz force. It might also be countered by a viscous force, which would slow down the motion of the flux lines. However it will still produce an electrical field, giving birth to some dissipation power, resulting in the disappearance of one of the properties of a perfect superconductor : the resistance is no longer equal to zero.

That behaviour gives a good phenomenological result of the low temperature and conventional superconductors. Nevertheless, some type II superconductors still exhibits the zero resistance property for a field smaller than H_{c2}. In order to have that property, the vortices need to stop moving. This is achieved when they are pinned. In that case, a force F_{pin} is stronger than the Lorentz force and the vortices are motionless, allowing to have the zero resistivity property. That is true as long as there is some disorder in the system, which is luckily the case quite often. In that formalism, when putting a current in the superconductor and reducing it, the zero resistivity point will give a critical current, j_c, at which the Lorentz force is higher than the pinning force. The critical current is bound by a limit, j_0 at which the kinetic energy of the quasiparticles is higher than the gap value. The ratio of j_c/j_0 is a good measurement of the pinning strength.

This development is only due to a mean field picture. However we saw that fluctuations somewhat contribute to superconductivity. In the case of thermal fluctuations, the vortices will move around an equilibrium position, and if the fluctuation length becomes bigger than a certain amount of the lattice constant of the Abrikosov lattice (typically 20%), then a so-called melting transition occurs and creates a new phase, called vortex liquid. If there is some current is the material, the vortices can now move for a current smaller than the critical current. In fact, thermal fluctuations allow some thermally activated jump, and so to dissipate some power. This is called the creep phenomenon. There also might be a glassy phase. In that scenario the pinning force is very strong, and one of the characteristics of that phase is the destruction of the Abrikosov lattice. Moreover, if the disorder is not too strong, the elastic properties of the vortex lattice are preserved and its destruction is quite weak. This is called a Bragg glass. The lattice is here quasi ordered, with no dislocations and a power law decay of the crystalline order [[12]]. On the other hand if the disorder is too strong no order can be found and the resulting phase is the vortex glass. Fig 1.3 shows schematically how these phases appear in the phase diagram while Fig. 1.4 shows the phase diagram deduced by Bouqet et al for YBCO. [[13]].

The strength of the thermal fluctuations is well described by the Ginzburg number, G_i. Going to lower temperatures, the thermal fluctuations will be very weak and one could think that the vortex lattice properties would only be governed by the quenched
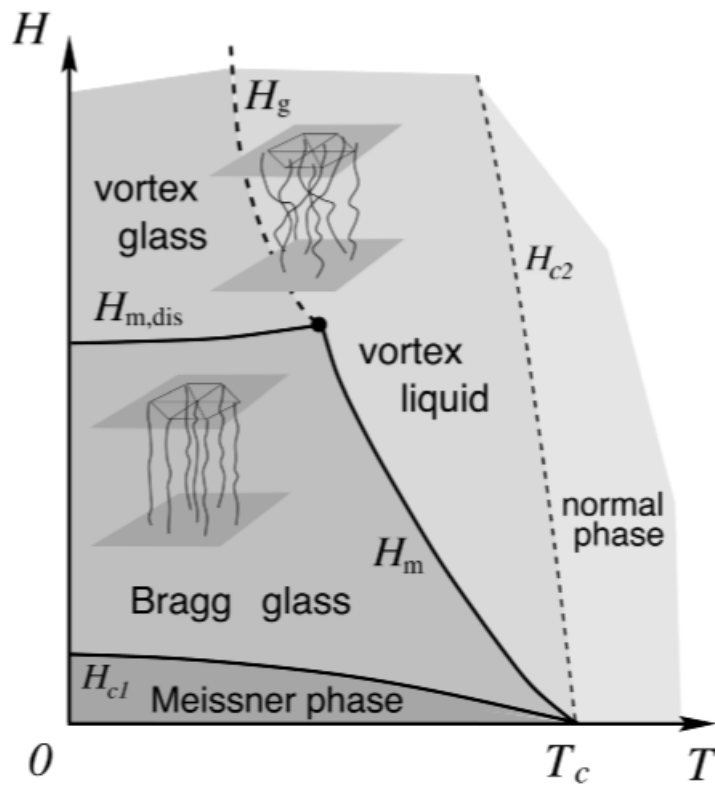
Figure 1.3: Schematic phase diagram of the vortex matter. In a scenario with no pinning then the $H_{m,dis}$ line does not exist and H_m extends to lower temperature. From [[14](#)]
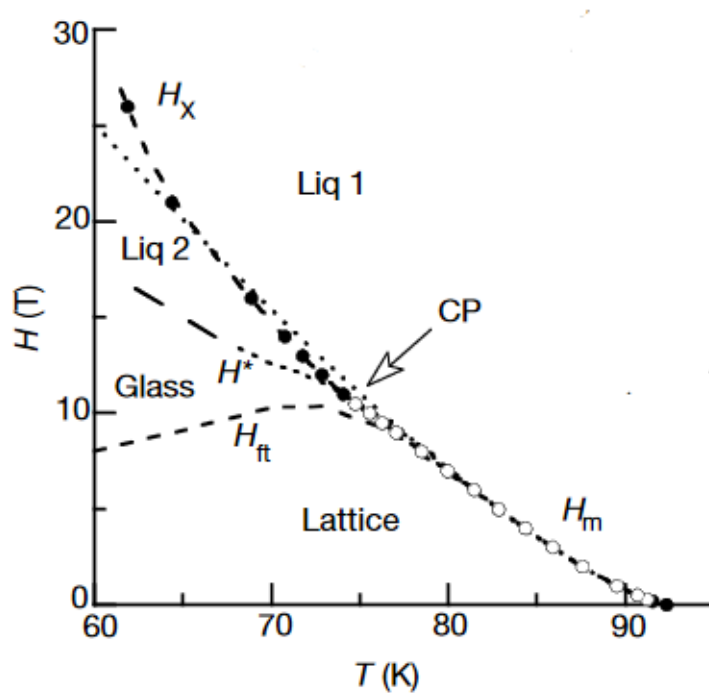
Figure 1.4: Phase diagram for the vortex state in YBCO. The dotted line represents the line of first-order melting for H < 5 T. H_X is the phase boundary between two observed liquid phases. H_{ft} represents the lattice-glass transition. CP indicates a critical point. From [13]

disorder of the system. However similar to thermal fluctuations at high temperatures, another type of fluctuations is very strong a low temperature even if present all over the temperature range : quantum fluctuations. They are mainly governed by the normal state resistivity, ρ^n. As an analog to G_i for thermal fluctuations and j_c/j_0 for the quenched disorder, we can give a dimensionless parameter that will quantify the strength of the quantum fluctuations :

$$Q = \frac{e^2}{\hbar} \frac{\rho^n}{\epsilon \xi},\tag{1.30}$$

The next table presents the numerical values of these three parameters for different superconductors.

	NbTi	KBaBiO	YBaCuO
$T_c(\text{K})$	10	30	100
$H_{c2}(\text{T})$	10	25-30	100
G_i	10^{-8}	10^{-5} - 10^{-4}	10^{-3}
Q	10^{-3}	0.1	0.1
J_c/J_0	0.1	10^{-2} - 10^{-1}	10^{-3} - 10^{-2}

Table 1.1: Comparison of the different parameters influencing the vortex lattice melting in different superconductors

Let us now try to look at a bit more in details at the properties of the vortex matter, focusing mainly on the vortex lattice melting which will be at the core of that thesis. In fact when the thermal energy of the system in not negligible in comparison to the elastic energy of the vortex lattice and the pinning energy, a mean field approach is no longer valid and one need a deeper theory.

1.2.3.2 Elasticity of the vortex lattice

Every vortex has an energy responsible for its properties. That energy is due to several effects : the condensation energy and the kinetic energy of the screening current flowing around the vortex. In the end, following the Ginzburg-Landau development, it will give a line energy :

$$\epsilon_l = \left(\frac{\phi_0}{2\pi\lambda}\right)^2 \left(\ln\left(\frac{\lambda}{\xi}\right) + 0.497\right)\tag{1.31}$$

In that sense, the magnetic field will only penetrate the sample when the line energy of a vortex is superior to the magnetic energy $\phi_0 H/4\pi$, providing the limit of the Meissner state :

$$H_{c1} = \frac{\phi_0}{2\pi\lambda}\left(\ln\left(\frac{\lambda}{\xi}\right) + 0.497\right) \tag{1.32}$$

When the vortices will start to overlap each other then the normal state is recovered. That happens when the density is of the order of ξ^{-2}. Each vortex having a line tension allows some collective properties to arise. Trying to describe these properties can only be achieved by comparing the different phenomenons happening in the vortex matter. However usually the displacement of a vortex is so small that one can apply the linear elastic theory to describe the vortex matter. The linear elastic force, F_{elas}, of the lattice is expressed most conveniently in the k-space. The displacement $\mathbf{u}_i(z) = \mathbf{r}_i(z) - \mathbf{R}_i$, of a vortex in the ideal position $\mathbf{R}_i = (X_i, Y_i, z)$ is described by its Fourier components :

$$\mathbf{u}_i(z) = \int_{BZ} \frac{d^3k}{8\pi^3}\mathbf{u}(\mathbf{k})e^{i\mathbf{k}\mathbf{R}_i} \tag{1.33}$$

$$\mathbf{u}(\mathbf{k}) = \frac{\phi_0}{B}\sum_i \int_{-\xi}^{\xi} dz\mathbf{u}_i(z)e^{i-\mathbf{k}\mathbf{R}_i} \tag{1.34}$$

with $\mathbf{u}(\mathbf{k})$ written down as $(u_x; u_y, 0)$, one finds the linear elastic force to be :

$$F_{elas} = \frac{1}{2}\int_{BZ} \frac{d^3k}{8\pi^3}u_\alpha(\mathbf{k})\phi_{\alpha\beta}(\mathbf{k})u_\beta^*(\mathbf{k}) \tag{1.35}$$

Here $(\alpha, \beta) = (x, y)$ and $\phi_{\alpha\beta}(\mathbf{k})$ is called the elastic matrix. It is real, symmetric and periodic in the k-space. That matrix is related to the different elastic modulus :c_{11} for compression, c_{44} for tilt, and c_{66} for shear. One can write the element of that matrix as :

$$\phi_{x,y}(\mathbf{k}) = (c_{11} - c_{66})k_x k_y + \delta_{xy}[(k_x^2 + k_y^2)c_{66} + k_z^2 c_{44} + \alpha_L(\mathbf{k})]. \tag{1.36}$$

$\alpha_L(\mathbf{k})$ is the Labusch parameter, which describes the elastic interaction of the pinning potential of impurities with the vortex lattice. If all vortices are pinned individually for example that parameter is k-independent. In the case of a uniform distortion, the different elastic moduli can be expressed via the following system :

$$c_{11} - c_{66} = B^2 \frac{\partial^2 F}{\partial B^2} \tag{1.37}$$

1. INTRODUCTION

$$c_{44} = B\frac{\partial F}{\partial B} \tag{1.38}$$

$$c_{66} \approx \frac{B\phi_0}{16\pi\lambda^2\mu_0}\left(1 - \frac{1}{2\kappa^2}\right)(1 - b^2)(1 - 0.58b + 0.29b^2). \tag{1.39}$$

Here $b = B/B_{c2}$. The last equation shows that at the limit between a type I and a type II superconductor (i.e. when $\kappa = 1/\sqrt{2}$), the c_{66} modulus vanishes, and all vortex arrangements have the same energy. It also vanishes when the vortex are overlapping each other (i.e. $\lambda \to \infty$ or $B \to B_{c2}$) or when the vortex lattice is melting.

Close to T_c, in the Ginzburg Landau approximation, Brandt [[15]] gives the free energy of an arrangement of curved vortices by the expression :

$$F(r_i(z)) = \frac{\phi_0^2}{8\pi\lambda\mu_0}\sum_i\sum_j\left(\int dr_i \int dr_j \frac{e^{r_{ij}/\lambda'}}{r_{ij}} - \int |dr_i| \int |dr_j| \frac{e^{r_{ij}/\xi'}}{r_{ij}}\right), \tag{1.40}$$

with

$$r_{ij} = |r_i - r_j| \tag{1.41}$$

$$\lambda' = \lambda/\langle|\psi|^2\rangle^{1/2} \sim \lambda/\sqrt{1-b} \tag{1.42}$$

$$\xi' = \xi/\sqrt{2(1-b)} \tag{1.43}$$

The first term in Eq. 1.40 is the vortex-vortex repulsive interaction with an effective penetration depth λ', the second term is the attractive vortex-vortex interaction due to the superconducting condensation energy of overlapping vortices with an effective coherence length ξ' and the vortex self-energy is included in the diagonal term.

The quadratic k-dependence of $\phi_{\alpha\beta}$ is only valid in a regime where $k < \lambda$, which is very central to the Brillouin zone. In fact the matrix has to be periodic with the lattice. λ and ξ being enhanced by the field as λ' and ξ', the interaction length is usually bigger than the vortex spacing and then c_{11} and c_{44} strongly depend on the k-vector of the disturbance. This is called the non-locality of the vortex lattice. The vortex lattice softens strongly for short range wavelengths of compressional and tilt distortions than it is for a uniform compression or tilt. The elastic matrix of the vortex lattice was calculated from the Ginzburg Landau theory by solving $\phi(r)$ and $B(r)$ up to terms linear

in arbitrarily chosen displacements. Remarkably, it turns out that the correct expansion parameter near B_{c2} for periodic $u_i(z)$ is not the spatial average $\langle|\psi|^2\rangle \sim (1-b)$ but the parameter $\langle|\psi|^2\rangle/(k^2\lambda^2)$. It gives then the tilt and compression moduli as :

$$c_{11}(k) \approx c_{44}(k) = \frac{B^2/\mu_0}{1 + k^2\lambda^2/\langle|\psi|^2\rangle} \tag{1.44}$$

1.2.3.3 Vortex lattice melting

Now knowing the elastic properties of the vortex matter, it is possible to calculate the mean square thermal displacement $\langle u \rangle$ of the vortex positions within the linear elastic theory by ascribing a thermal energy $1/2k_B T$ to each elastic mode of the vortex lattice,

$$\frac{1}{2}\langle u_\alpha(k)\phi_{\alpha\beta}(k)u_\beta(k)\rangle = \frac{k_B T}{2}. \tag{1.45}$$

In order to get the mean square thermal displacement, one need to sum for all k over the Brillouin zone and k_z. The Brillouin zone is assimilated as a circle with a radius $k_{BZ} = (4\pi B/\phi_0)^{1/2}$.

$$\langle u^2 \rangle = k_B T \int_{BZ} \frac{d^2 k_\perp}{4\pi^2} \int_{-\infty}^{+\infty} \frac{dk_z}{2\pi}(\phi_{xx}^{-1}(k) + \phi_{yy}^{-1}(k)), \tag{1.46}$$

$$\langle u^2 \rangle = \frac{k_B T}{2\pi^2} \int_0^{k_{BZ}} dk_\perp k_\perp \int_0^{+\infty} dk_z \left(\frac{1}{c_{66}k_\perp^2 + c_{44}(k)k_z^2} + \frac{1}{c_{11}(k)k_\perp^2 + c_{44}(k)k_z^2} \right). \tag{1.47}$$

It might now be useful to estimate that integral in order to have an idea of the influence of the thermal fluctuations on the vortex lattice. We will now give another form to the k-dependent elastic moduli given by Houghton [(16)] which take into account the different effective masses in the plan, M and along the z-axis, M_z. The elastic moduli are expressed via a normalized wave-vector $q = k/k_{BZ}$:

$$c_{44}(k) = \frac{B^2}{4\pi}m_\lambda^2 \frac{M}{M_z}\left(\frac{1}{q_\perp^2 + (M/M_z)(q_z^2 + m_\lambda^2)} + 1 \right) \tag{1.48}$$

$$c_{11} = \frac{B^2}{4\pi}m_\lambda^2 \left(\frac{q^2 + (M/M_z)m_\lambda^2}{(q^2 + m_\lambda^2)(q_\perp^2 + (M/M_z)q_z^2 + (M/M_z)m_\lambda^2)} - \frac{1}{q_\perp^2 + (M/M_z)q_z^2 + m_\xi^2} \right) \tag{1.49}$$

with $m_\lambda^2 = (1-b)/(2b\kappa^2)$ and $m_\xi^2 = (1-b)/b$ and c_{66} is still considered dispersionless. These expressions are reduced to known expressions in the local limit but a crossover to the non local behaviour is achieved when $q^2 \geq m_\lambda^2$.

Houghton said only a numerical evaluation of Eq. 1.47 could be achieved, but considering the smallness of the parameter m_λ, it is possible to neglect c_{11} in Eq. 1.47. Babich [(17)] gives then the expression :

$$\langle u^2 \rangle = a_0^2 \beta_A \frac{\sqrt{G_i}}{2\pi} \frac{t}{1-b} \sqrt{\frac{BB_{c2}(0)}{B_{c2}^2(T)}} \left(I_1 + I_2\right), \tag{1.50}$$

$$I_1 = \frac{2}{A(1+A)} \left(\sqrt{1 + (1+A)^2} - 1 \right), \tag{1.51}$$

$$I_2 = \frac{2}{3m_\xi} \left(2 + 3m_\xi - m_\xi^3 + (m_\xi^2 - m_\xi - 1)\sqrt{1 + (1+m_\xi)^2} \right), \tag{1.52}$$

where $A = \sqrt{(1-b)/4}$, a_0 is the spacing in between the vortices and β_A is the Abrikosov constant, equal to 1.16 in the case of a triangular lattice. One sees that the amplitude of the thermal fluctuations is related to the Ginzburg number, which we saw, determines the width of the fluctuation regime of a superconductor.

Following that result it is now important to find a way to know when the vortex lattice melts by introducing the Lindemann criterion. In the Lindemann theory, similarly to a crystal lattice, the vortex lattice is melting when the mean thermal displacement of the vortex reaches a certain fraction of the spacing between the vortices. It means that when $\langle u^2 \rangle^{1/2} = c_L a$, where c_L is the Lindemann constant of the order of $0.1 - 0.3$, the lattice undergoes a melting transition. Looking at Eq. 1.50, the complete expression of $B_{c2}(t)$ over the complete $H-T$ phase diagram is needed to have the precise dependence of the melting line. Nonetheless let us write that close to T_c, we can write $B_{c2}(T) = B_{c2}(0)(1-t)$. Since I_1 and I_2 have finite values close to T_c, one finds in the end that only considering thermal fluctuations, the melting line follows :

$$B_m(T) = B_0 \left(\frac{1-t}{t} \right)^2, \tag{1.53}$$

and

$$B_0 = \frac{\pi \epsilon \phi_0}{\lambda^2(0)} \left(\frac{c_L^2 \phi_0^2}{8\pi^2 \lambda(0) k_B T_c} \right)^2. \tag{1.54}$$
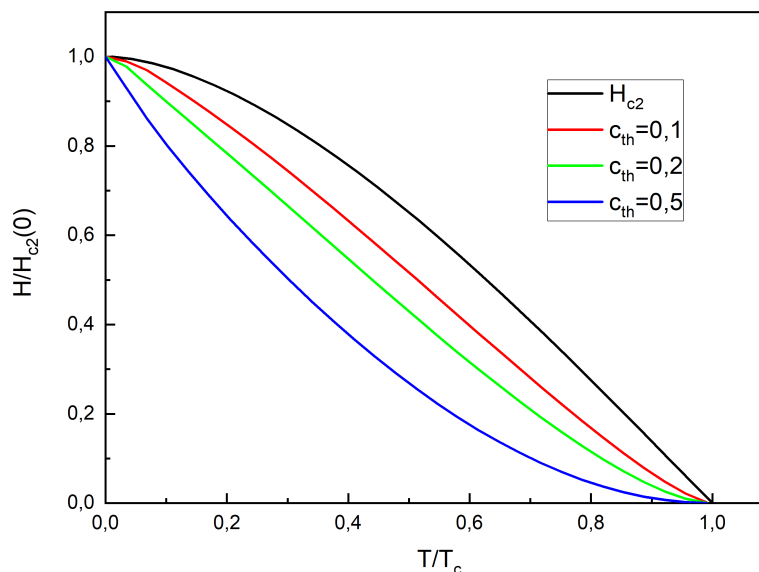
Figure 1.5: Melting line for different values of c_{th},the thermal coefficient measuring the strength of the thermal fluctuations part to the melting only considering thermal fluctuations

B_0 here only logically depends on $\lambda(0)$ and not on $\xi(0)$. On the other side, the melting line will coincide with B_{c2} at zero temperature because there are no thermal fluctuations in that condition. Fig 1.5 clearly shows that dependence and one can also see that the bigger G_i the farther from H_{c2} the melting line is. That is because the Ginzburg number quantifies the thermal fluctuations, and the bigger the fluctuations are the more visible the melting will be.

For now we only took thermal fluctuations into account, which strength is partially determined by G_i. Yet earlier we also talked about quantum fluctuations, which strength is correlated to Q. In order to take these fluctuations into account, one can start with the same method : by calculating the mean square displacement of the vortices. We will have a formulation with the same form as Eq. 1.47, but slightly modified by the fact that we need to sum over the different Matsubara frequencies, $\omega_n = 2\pi n k_B T/\hbar$ [[18]]. The term for $n = 0$ is equal to the thermal fluctuations part, and the rest is what we will call the quantum fluctuations part. This is why we can separate the mean square displacement into two parts : one due to thermal fluctuations and the other one due to

quantum fluctuations.

$$\frac{\langle u^2 \rangle}{a_0^2} = c_L^2 (c_{th} f_{th}(t,b) + c_{qu} f_{qu}(t,b)), \qquad (1.55)$$

where c_{th} will be related to G_i and c_{qu} to Q. Thanks to Blatter in ([18]) it is possible to have an expression for the quantum part of the mean square displacement. Firstly, he writes a fluctuation-dissipation theorem, which is equivalent to Eq. 1.47 :

$$\langle u^2 \rangle = \frac{\hbar}{i} \int_{-\infty}^{+\infty} \frac{d\omega}{2\pi} \coth\left(\frac{\hbar\omega}{2k_B T}\right) \int_0^{k_{BZ}} \frac{dk_\perp}{4\pi} \int_0^{+\infty} \frac{dk_z}{\pi}$$
$$\left(\frac{1}{c_{66}k_\perp^2 + c_{44}(k)k_z^2 - i\omega\eta} + \frac{1}{c_{11}(k)k_\perp^2 + c_{44}(k)k_z^2 - i\omega\eta}\right). \qquad (1.56)$$

Here $\eta = B_{c2}\phi_0\rho_n$ is the Bardeen-Stephen viscosity coefficient due to the motion of vortex. Secondly, Blatter divides that integral into two parts, and explains that the quantum part in Eq. 1.56 is equal to :

$$f_0(\alpha, \beta) = \frac{1}{2} \int_0^1 dx \int_0^1 dy \ln\left(1 + \beta^2\left((1 + \frac{\alpha^2 x}{y^2})^2\right)\right), \qquad (1.57)$$

where $\alpha = 2/\sqrt{\pi}\nu$, $\beta = 2/\pi b(1-b)$, and ν is a numerical constant of the order of unity which is used to limit the divergence of the integral by only integrating over few vortex neighbors. It is an important point to take into account since the value of c_{qu} could change at least of one order of magnitude depending on the value of ν. Blatter does not give any calculated form of that integral, but only analyses the behavior in specific regions of the phase diagram, depending on the parameters. However is it possible to find an analytical expression for it. Looking back at Eq. 1.55 one may then define :

$$f_{qu} = b^{3/2} \frac{f_{q1} + f_{q2} + f_{q3}}{2}, \qquad (1.58)$$

$$f_{q1} = \frac{1}{3\alpha^2}(2\alpha^3\sqrt{\beta}f_{q11} - f_{q12}), \qquad (1.59)$$

$$f_{q11} = \frac{2\beta - 3i}{(\beta - i)^{3/2}}\tan^{-1}\left(\frac{\sqrt{\beta - i}}{\alpha\sqrt{\beta}}\right) + \frac{2\beta + 3i}{(\beta + i)^{3/2}}\tan^{-1}\left(\frac{\sqrt{\beta + i}}{\alpha\sqrt{\beta}}\right), \qquad (1.60)$$

$$f_{q12} = \frac{2\alpha^2(\beta^2 + 3)}{\beta^2 + 1} + (3\alpha^2 + 1)\ln\left((\alpha^2\beta + \beta)^2 + 1\right) - 2, \qquad (1.61)$$

$$f_{q2} = \frac{2}{3}(\alpha\sqrt{\beta}f_{q21} + f_{q22}), \tag{1.62}$$

$$f_{q21} = \frac{i}{(\beta - i)^{3/2}}\tan^{-1}\left(\frac{\sqrt{\beta - i}}{\alpha\sqrt{\beta}}\right) - \frac{i}{(\beta + i)^{3/2}}\tan^{-1}\left(\frac{\sqrt{\beta + i}}{\alpha\sqrt{\beta}}\right), \tag{1.63}$$

$$f_{q22} = \frac{\tan^{-1}(\alpha^2\beta + \beta)}{\alpha^2\beta} + \frac{2}{\beta^2 + 1}, \tag{1.64}$$

$$f_{q3} = \frac{1}{3\alpha^2\beta}\left(\beta\left(\ln(\beta^2 + 1) - 2\right) + 2\tan^{-1}(\beta)\right), \tag{1.65}$$

Even if some complex numbers appear in the formula, the resulting function is always real. Let us now check the asymptotic behavior. For example, $\beta \to \infty$ gives the behaviour in the two regions where b is small or close to one. In both cases f_{qu} taking the different terms' limits of f_{qu}, some of them cancel each others out and in the end it varies like $\ln(\beta)$. Since close to T_c, β follows a law in $B_{c2}(1 - t)/B$, we find in the end a linear dependence of the melting line :

$$B_m(T) = B_1(1 - t) \tag{1.66}$$

It is also interesting to look at the value of the melting when $T = 0$. Here we can see a specific behavior due to quantum fluctuations, which states that the melting can happen at a field, $B_m(0)$, different from B_{c2} even at zero temperature. We find that :

$$B_m(0) = H_{c2}\left(1 - \frac{2}{\pi}\exp\left(\alpha\left(\frac{2\pi}{3} - \frac{\alpha}{2}\right)\right) \times \exp\left(-\frac{\pi^3 c_l^2}{2Q}\right)\right). \tag{1.67}$$

All these features are clearly visible in Fig 1.6 which shows the linear dependence close to T_c and the melting field different from $H_{c2}(0)$ at zero temperature.

In the end, looking at the thermal fluctuations we will only use the formula given by Sudbo which is verified close to the melting line usually, and simplified compare d to Eq. 1.50. From now on we will define f_{th} in Eq. 1.55 by the following ([19]) :

$$f_{th}(t, b) = \frac{t}{\sqrt{B_{c2}/B_{c2}(0)}}\frac{\sqrt{b}}{1 - b}\left(\frac{4(\sqrt{2} - 1)}{\sqrt{1 - b}} + 1\right). \tag{1.68}$$

In the same Eq. 1.55, we now have to define the thermal and quantum coefficient in front of each function. We find that :

$$c_{th} = \frac{\sqrt{G_i}}{2\pi c_L^2}, \tag{1.69}$$
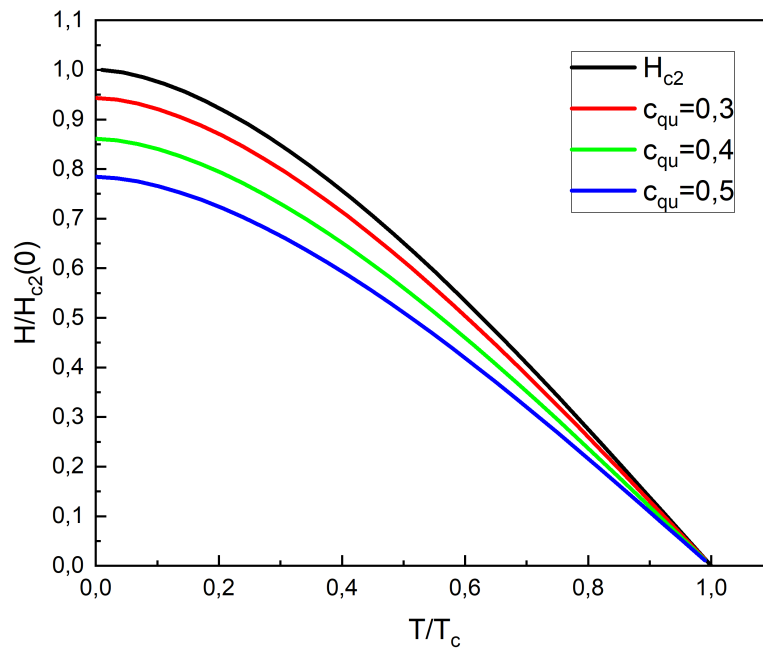
Figure 1.6: Melting line for different values of c_{qu}, the quantum coefficient measuring the strength of the quantum fluctuations part to the melting, only considering quantum fluctuations
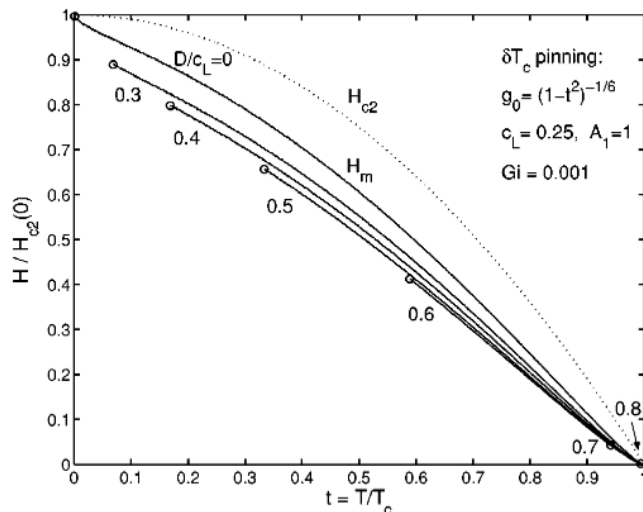
Figure 1.7: Melting line for the vortex lattice with quenched disorder. From [(20)]. D is the pinning strength. The bigger D is the shorter the melting line is and it is shifting from T_c. It should be noticed that when the pinning is strong, the melting line does not merge with the upper critical fiel line.

$$c_{qu} = \frac{\sqrt{2}Q\nu}{\sqrt{\pi^7}c_L^2}. \tag{1.70}$$

From this point we have an expression for the melting line, only ignoring any effect due to disorder. Fig. 1.7 shows the effect of pinning on the phase diagram. The origin of the pinning is assumed to be caused by point defects in this phase diagram. Basically what we have to remember about that is that the stronger the pinning is, the more the melting line shift from the upper critical field and from the melting line without pinning, i.e at fixed temperature the melting field decreases with pinning. One of the other effect is also that there is no merging between the upper critical field and the melting.

We now have to deal with other issues: we have to know the dependence of B_{c2} and to know several constants of the material to have the exact behaviour of the melting line. We will take a closer look to the dependence of the upper critical field in the next section.

1.2.4 Temperature dependence of H_{c2}

It that part we will try to go into more details concerning the temperature dependence of the upper critical field. Several mechanisms are involved here and will be introduced : namely orbital and Pauli pair breaking and the Fulde and Ferrell, Larkin and Ovchinnikov (FFLO) phase.

1.2.4.1 Orbital and Pauli pair breaking

Orbital pair breaking   First let us introduce the classical view of orbital pair breaking. In that image the quasiparticle pair breaks because of the Lorentz force. This gives the same result for the upper critical field as we calculated before with the Ginzburg Landau equation. By other way of explanation, if we see the pair from the point of view of the Lorentz force, each electron will describe a circle with a Larmor radius :

$$r_L = \frac{m v_F}{e \mu_0 H}.$$
(1.71)

If the radius becomes larger than the coherence length, then the pair will break and gives an orbital limiting field :

$$H_{c2}^{orb}(t) = \frac{\phi_0}{2 \pi \xi^2(T)}$$
(1.72)

$$\xi(T) = \frac{0.18 \hbar v_F}{k_B T_c \sqrt{1 - t}}$$
(1.73)

That gives a linear dependence of the orbital upper critical field close to T_c, which corresponds to what we used to see in the behavior of the melting in the same conditions.

Paramagnetic pair breaking   There is another scenario which we did not analyze until now. Since the Cooper pairs are made of the quasiparticles with opposite spins, if the magnetic field is strong enough to align them in the same direction the pair will also break. This is what we call the Pauli limit or the paramagnetic limit. Clogston [[21]] explains the limit by comparing the difference between the Zeeman energy in the normal and superconducting phase with the pairs' condensation energy.

$$\frac{1}{2}(\chi_n - \chi_s) H_p^2(T) = \frac{\mu_0 H_c^2(T)}{2},$$
(1.74)

(a) Orbital pair breaking   **(b)** Paramagnetic pair breaking
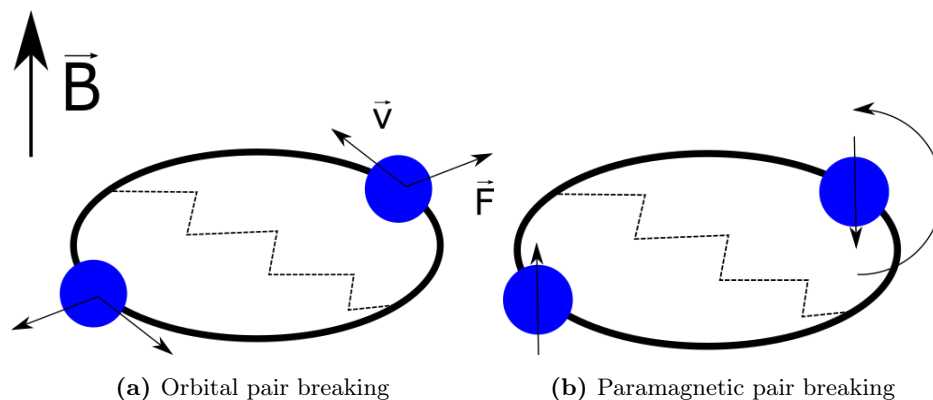
Figure 1.8: Two different mechanisms responsible for the pair breaking

where, χ_n and χ_s denote respectively the paramagnetic susceptibility in the normal and superconducting states and H_p is the Pauli limiting field, due to the Zeeman splitting. $\chi_n = (g\mu_b/2)^2 N(E_F)$, (g might be different from 2) and $\chi_s = 0$ because the electrons condense into pairs with a zero spin. We also know the expression for the critical field from the BCS theory : $H_c^2/2\mu_0 = N(E_F)\Delta(0)^2/2$. $N(E_F)$ is the density of states at the Fermi level and $\Delta(0)$ is the gap value at zero temperature. This is only true if there is only one gap responsible for superconductivity. It gives a value for the Pauli limiting field at zero temperature :

$$H_p(0) = \frac{\sqrt{2}\Delta(0)}{g\mu_b} \tag{1.75}$$

In order to compare paramagnetic effects with orbital effects we usually use the Maki parameter defined as :

$$\alpha_M = \sqrt{2}\frac{H_{orb}(0)}{H_p(0)}. \tag{1.76}$$

Until now, we have only considered two separate cases. However it is possible to obtain an expression considering the two mechanisms at the same time, which is provided in the Werthamer-Helfand-Hohenberg (WHH) theory [(22)].

Most of the superconductors that we will study during the thesis are supposed to be in the clean limit (only valid when the coherence length is much smaller compare to the mean free path). Brison et al. [(23)] give a expression of the upper critical field of a s-wave single band superconductor, considering orbital and Pauli pair breaking and being in the clean limit (Eq. 1.77). That expression is only valid if the transition remains
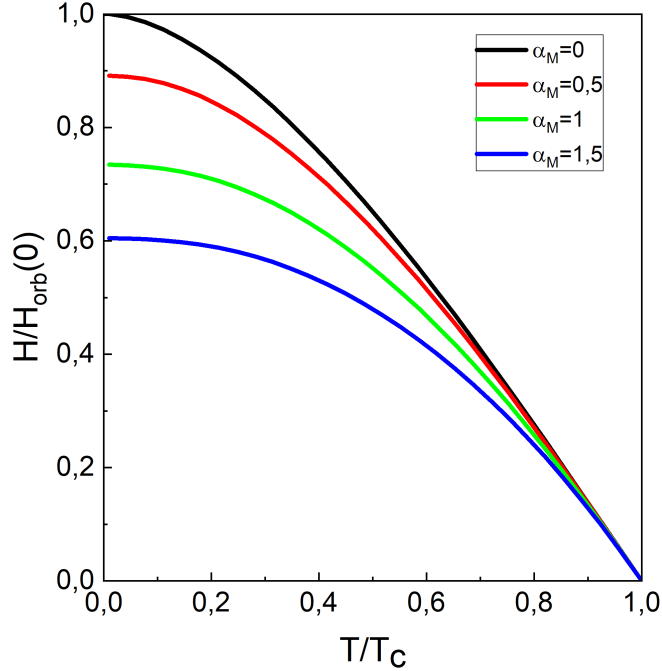
Figure 1.9: Upper critical field in the clean limit normalized by the purely orbital upper critical field at zero temperature as a function of reduced temperature for different Maki parameters, only taking orbital and paramagnetic effects into account

second order down to zero temperature, which is not true for large Maki number.

$$\ln(t) = \int_0^\infty \frac{dy}{sh(y)} \int_0^1 dx \left[\cos\left(0.28\frac{\alpha H}{H_{orb}(0)}\frac{y}{t}\right) \times \exp\left(-0.25\frac{y^2(1-x^2)}{t^2}\frac{H}{H_{orb}(0)}\right) - 1 \right].$$
(1.77)

In the limit where $T = 0$, when $\alpha \to 0$ we find that the upper critical field mimics the pure orbital behavior whereas in the limit $\alpha \to \infty$ it behaves in the pure Pauli limit behavior. However close to T_c, H_{c2} should be governed by the orbital limit. Fig.1.9 shows the dependence of the upper critical field following Eq. 1.77 for different Maki parameters.

Vortex lattice melting and upper critical field   Adashi and Ikeda [(24)] predicted that two different behaviors can be observed when comparing the melting line and the upper critical field, assuming only thermal fluctuations, no vortex pinning effect and paramagnetic depairing. The two possible phase diagram are visible in Fig. 1.10. In this article they argued that considering thermal fluctuations no H_{c2} line would be
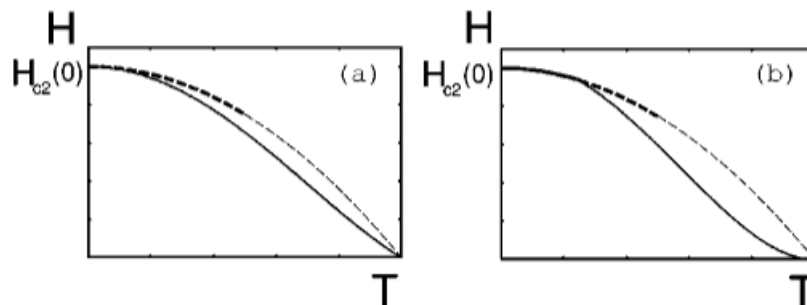
Figure 1.10: Two candidates of a schematic $H - T$ phase diagram of a bulk type II superconductor with paramagnetic depairing in the case of thermal fluctuations and with no vortex pinning effect. The dotted line corresponds to the upper critical field, and the continuous line the vortex lattice melting. In (b) the vortex lattice disappears before T=0K. From [(24)]

observed and instead the only genuine phase transition is the melting line. They also explained that in the case of a weak enough fluctuations, reducing upon cooling, the melting line might meet the hypothetical upper critical field before zero temperature and would therefore coincide over the low temperature part of the phase diagram, with a first order transition. The resulting phase diagram is then available in Fig. 1.10b.

It is interesting to compare the phase diagram of Adashi and Ikeda with the one obtained by Houzet and Mineev [(25)] in the case of strong paramagnetic depairing. The last ones argued that in the pure paramagnetic limit ($\alpha_M \to \infty$) it exists a temperature $T^* = 0.56 T_c$, where the second order transition happening at the upper critical field transforms into a first order transition. The smaller the Maki parameter is, the smaller T^* becomes. One can sump up their work by giving the comparison of two phase diagrams, one with a small Maki parameter and another with a high one, as illustrated in Fig. 1.11. They also considered the possible appearance of a superconducting modulated phase, which will be introduced in the next section.

1.2.4.2 FFLO

We should now investigate a bit more the paramagnetic behavior of the quasiparticles pairs just before the pair could be destroyed. Due to the Zeeman effect, each quasiparticle sees its energy being shifted in the opposite direction of its spin by $h = g\mu_b H$. In the pure paramagnetic limit if the magnetic field is not too strong then the pair might
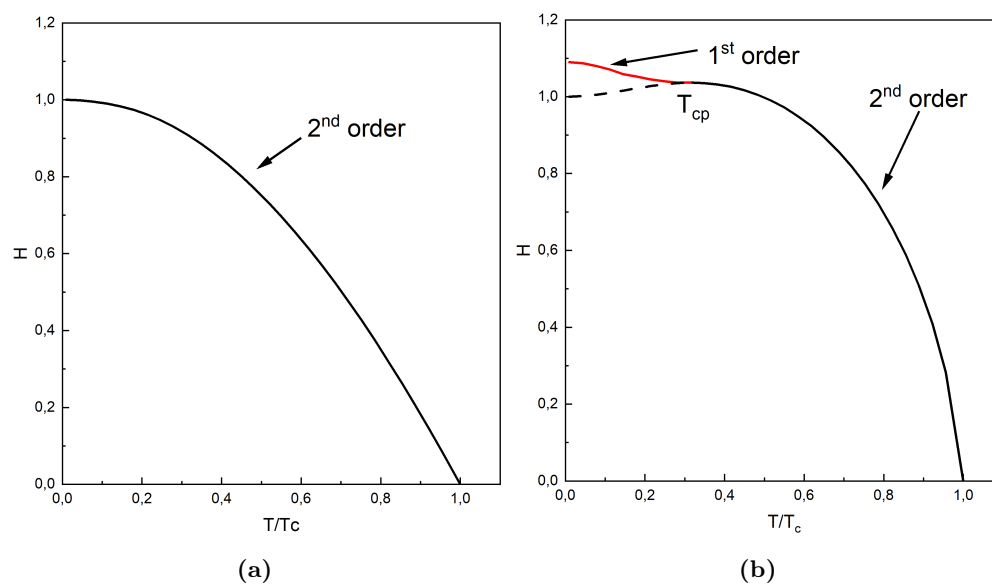
Figure 1.11: Schematic dependence of the upper critical field line in the clean limit following the consideration of Houzet and Mineev for a small (a) and a high value (b) of the Maki parameter. In the case of a small Maki parameter the transition at the upper critical field is always second order (black line), while in the case of a high value of the Maki parameter, the transition line becomes first order at low temperature (red line) and the dependence calculated by Eq. 1.77 (dashed line is no longer true. T_{cp} marks the critical point at which the behaviour changes.
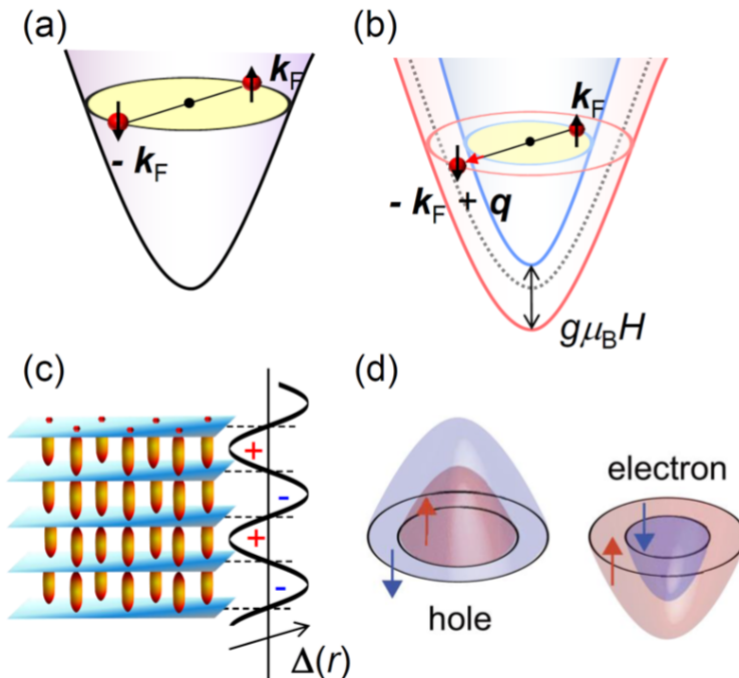
Figure 1.12: (a) Schematic illustration of Cooper pairing in the BCS state. (b) Pairing state in the FFLO state. (c) Schematic illustration of the superconducting order parameter Δ in real space and segmentation of the vortices by planar nodes. (d) Schematic electronic structures of hole and electron pockets close to the FFLO state. From [[28]]

subsist. Yet in order to accomplish that, the momentum of the quasiparticles shifts proportionally to the Zeeman splitting, and the pair gets a total momentum that is linear with h, as shown in Fig. 1.12(b). That moment in the reciprocal space is equivalent to an oscillation in the real space (see 1.12(c)), leading to a new superconducting state, with a modulation parameter, which is now called FFLO from Fulde, Ferrell, Larkin and Ovchinnikov who predicted that state [[26], [27]].

That state was calculated to be always favorable if the paramagnetic state is dominant compared to the orbital state. However this is not always true, for example we stated that close to T_c the orbital regime is dominant. From this point, the situation becomes more complex. The complete interactions between the orbital effects and the paramagnetic effects start to be more difficult to understand and it is harder to find a proper criterion to know when a FFLO phase might appear.

Observing the FFLO state might also be a difficult task. In fact in most superconduc-

tors, the paramagnetic effects are much smaller compared to the orbital ones. Yet some precise cases could help to enhance that ratio in favor of the Pauli limit. For example by having a higher effective mass, which is what happens in the heavy fermions systems, or maybe by having 2D compounds and orienting the field within the planes would limit the orbital effects. It was acknowledged that for a FFLO phase to appear, α_M must be superior to 1.8 [(29)] and it can only exist below a temperature $T^* = 0.56 T_c$ (that temperature is a bit lower in the case of a d-wave superconductor). It should also be noted that a very clean material is needed. In fact the impurities tend to reduce the chances for the appearance of a FFLO phase, by breaking the modulation responsible for that phase. If we take a closer look at the behavior of the quasiparticles in a FFLO phase, it is even possible to have a precise condition to define what is a clean material in the FFLO terminology. The quasiparticles have a momentum $q \sim 1/\xi_0$ and the incertitude due to diffusion by the impurities is $1/l$, l being the mean free path. The creation of the Cooper pairs with a momentum makes only sense if that incertitude is smaller compared to the momentum. It means that we have the same criterion as before : $l > \xi_0$. In the end, two mains features are expected to signify the appearance of the FFLO phase: first, a reinforcement of H_{c2} at low temperature, and second, a first order transition between the FFLO phase and the normal superconducting phase.

Buzdin [(30)] gives an implicit expression taking into account the orbital effects, the paramagnetic effects and the FFLO phase. The given formula for a Landau level m is :

$$
\frac{\ln t}{t} = Re \left[2\pi \sum_{\omega_n > 0} \left[\int \frac{\beta e^{-\beta y} dy (-1)^m L_m(2\beta y)}{\sqrt{\tilde{Q}^2 + y}} \times \tan^{-1} \left(\frac{T_c \sqrt{\tilde{Q}^2 + y}}{\omega_n + i\mu_B H} \right) - \frac{T_c}{\omega_n} \right] \right],
$$
(1.78)

where $\tilde{Q} = \frac{\hbar v_F Q}{2 T_c}$, $\beta = \frac{7\zeta(3)}{12\pi^2} \frac{T_c}{H} \left(\frac{dH}{dT} \right)_{T_c}$, L_m are the Laguerre polynomials, $\omega_n = \pi T(2n + 1)$ the Matsubara frequency and Q is the modulation vector of the FFLO phase. Since Q changes with the field, one needs to find the maximum of the curve $H(Q)$ at a specific temperature to get the value of H and Q at that temperature. Fig 1.13 gives a comparison of the upper critical field obtained while taking a FFLO phase or not for the same Maki parameter. We see that the main effect is to enhance the line at low temperature, where the superconducting phase appears.

In the same article it is specified that for a Maki parameter smaller than 9, only the lowest Landau level can be taken into account, which simplifies the expression. In
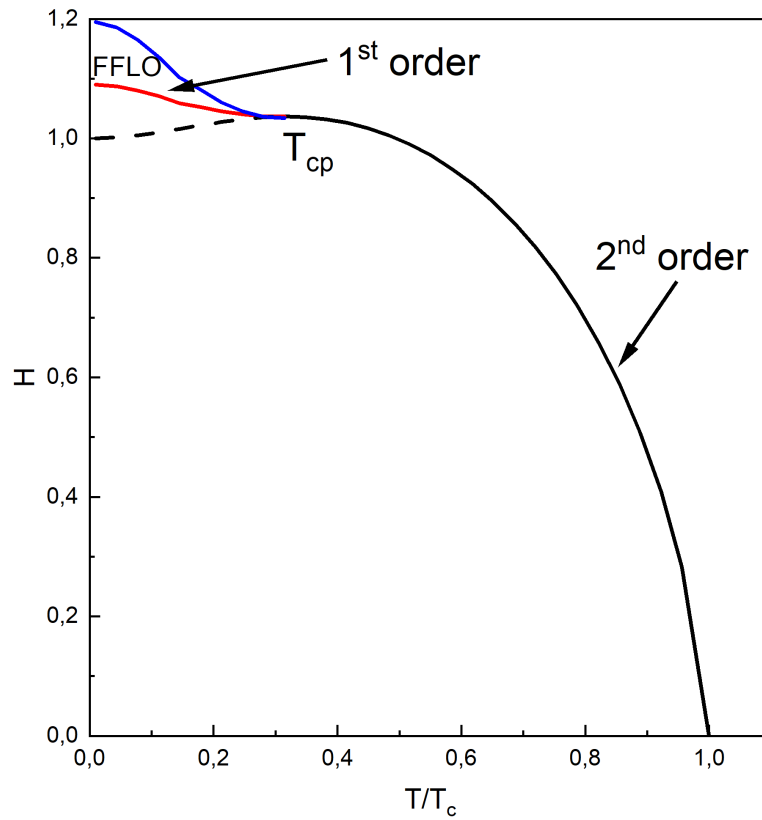
Figure 1.13: Schematic phase diagram considering the presence of a FFLO phase. In a scenario with a FFLO phase, one should observe a second order transition (black line) at high temperature before the FFLO phase appear. At low temperature, at a fixed temperature, and increasing the field, one first crosses the virtual line of Eq. 1.77 (dashed line) which does not exists anymore, and then a first order transition when entering the FFLO phase (red line). Recovering the normal state at higher field, the transition line is now second order (blue line). All these lines merge at a critical point T_{cp}
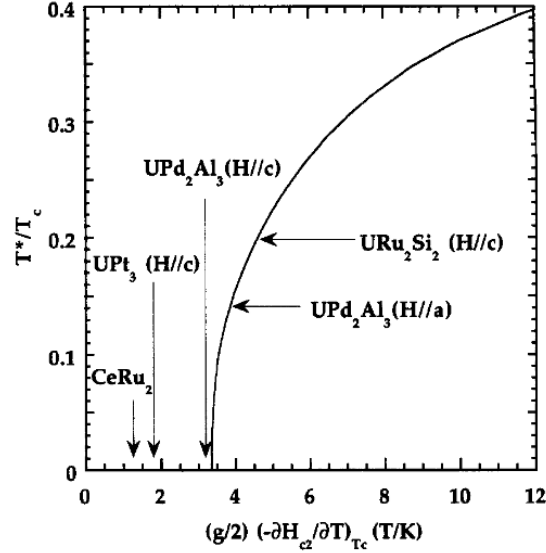
Figure 1.14: Theoritical prediction of the appearance of T^* as a function of the initial slope of H_{c2}. From [(23)].

that formalism the T^* temperature, at which the FFLO phase can appear, might be shifted to a lower temperature due to the orbital effect. Since the ratio of the orbital effect and the paramagnetic effect is given by the Maki parameter, one can plot the dependence of T^* as a function of α_m or equivalently as a function of the initial slope of the upper critical field ($\alpha_m = 0.27g \left(-\frac{dH_{c2}}{dT} \right)_{T_c}$). That was done by the same group in [(23)], where they give the following figure 1.14

1.3   Iron based superconductivity

We would like to focus presently on the material that will be used in this thesis : $FeSe_{1-x}S_x$. Firstly, we will start by introducing that material in a general overview about iron-based superconductivity. We will address general features that we think are relevant to iron-based superconductivity even if they are not observable in every compound. Afterwards, we will discuss some special features of our compound.

1.3.1   Crystal structure

In 2008, superconductivity was first discovered in a iron-based material : $LaO_{1-x}F_xFeAs$ [(31)]. It was found to have a T_c of 26K and opened an entirely new field of research

of superconductors, namely iron-based superconductivity. After that discovery, many different iron-based superconductors were discovered [(32)] and we now sort them between different families depending on their stochiometry (see Fig. 1.15). However they all share one common point: pnictogen (P,As) or chalcogen (Se,Te) mixed with iron in planes. One distinguishes mainly 4 families.

11 The 11-type materials are for now only iron chalcogenides, since FeAs does not crystallize into a layered structure [(33)]. On the other hand, FeSe does. The 11 materials are considered as the simplest materials in the iron-based superconductors, only consisting of layers of iron and a chalcogen. FeSe becomes superconducting at around 9K [(34)] and the T_c can be enhanced up to 37K with pressure[(35)]. FeTe crystals are also possible to synthesize and the combination of Se and Te gives $FeSe_xTe_{1-x}$ with a maximum T_c at $x = 0.5$ of 14K [(36)]. $FeSe_{1-x}S_x$ have also been synthesized giving a maximum T_c of 10.5 K around $x = 0.12$ [(37)]. In these compound, the substitute element takes the free positions of chalcogen atoms.

111 It is possible to intercalate atoms in between the Fe-chalcogen or Fe-pnictogen layers. By adding 5 atoms per unit cells one gets the 111 family. The most famous compound among these is certainly LiFeAs with a T_c of 18K [(38)]. The main problem of most of the compounds of this family is that they are highly reactive with air and therefore harder to study [(32)]. NaFeAs shows less reaction to the environment than LiFeAs but air exposure strongly affects T_c which seems to be around 23K in the optimal conditions [(39)].

122 The 122 family is widely studied in terms of holes and electron doping, forming a complex phase diagram, which we will talk about later on. $Ba_{1-x}K_xFe_2As_2$ is certainly one of the most studied compound of this family. That hole doped material shows a maximum T_c of 38K [(40)]. On the other hand the electron doped compound $Ba(Fe_{1-x}Co_x)_2As_2$ shows a maximum T_c of 22K [(41)]. Both have the same parent compound $BaFe_2As_2$ and its phase diagram shows similarities with a major part of the materials of the same family. The huge variety of crystals and the good crystal quality makes this family the favorite one to study and many articles were published to have a better understanding of iron-based superconductivity through the 122 family [(32)].
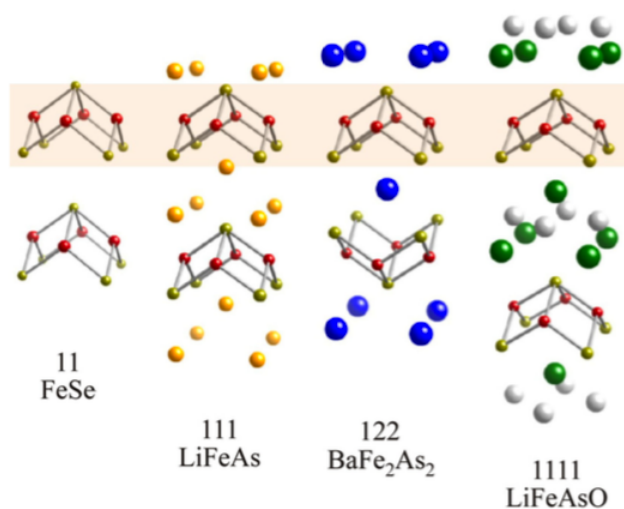
Figure 1.15: Crystal structures of some iron-based superconductors. From [(44)]

1111 The 1111 family was the first one to be discovered and shows the highest T_c among Fe-based superconductors. Only one month after the discovery of $LaO_{1-x}F_xFeAs$, substitution of La by some rare earth element, and among these Sm led to a T_c of 55K [(42)]. Logically they also show huge upper critical fields, which seems to be anisotropic in most cases. The resistive transition seems to be reminiscent of those observed in cuprates also [(43)].

Some other iron-based superconductors also exists with a more complex stochiometry, but we will not discuss those, since the highest amount of publications seems to focus on these 4 families.

1.3.2   Phase diagram

For several years after the discovery of superconductors, it was admitted that superconductivity would only appear for a temperature close to 30K. Bernt Matthias even gave 5 rules, called the Matthias rules, to find new superconductors in 1963 [(45)] :

-To have the highest possible symmetry in the system

-To have the highest possible density of states

-No oxygen

-No magnetism (for example iron)

-No insulator

However the discoveries of heavy fermions, cuprates and organic superconductors tend to prove that these rules are not always true, and these families were called "exotic" superconductors. Iron-based superconductors being part of the so-called "exotic" superconductors, they share the common characteristic with cuprates or heavy fermions systems to have a very rich phase diagram, full of different phases that tend to compete or sometimes cooperate with each other. One of the main focus of the research work on Fe-based superconductors nowadays is to characterize these phases and try to understand how they can compete or sometimes cooperate. In the iron-based superconductors mainly three phases are observable: a magnetic phase, a nematic phase and a superconducting phase.

Let us consider $BaFe_2As_2$ as a good representation of the phase diagram of iron-based superconductors. At room temperature and with no pressure or doping it as a tetragonal structure. Going at lower temperature it undergoes a structural transition (sometimes called nematic, we shall discuss later on) to an orthorombic symmetry and at the same time a magnetic transition from a paramagnetic state to a antiferromagnetic state [(46)]. When doping, the structural transition and the magnetic transition split but remain very close. Most of the compounds are not superconducting without any doping. Superconductivity forms into a dome at low temperature and close to the zero temperature point of the magnetic and nematic transitions [(46)]. Therefore one of the main questions of iron-based superconductors is the role of these transitions concerning superconductivity with a possible quantum critical point.

1.3.2.1 Superconducting phase

The Barden Cooper Schrirffer theory, which states that superconductivity is mediated by phonons, does not seem to work for Fe-based superconductors. First-principles studies have shown that if superconductivity in these systems was mediated by phonons, T_c should be around 1K, which seems to strongly disagree with what is observed [(48)]. Therefore two candidates are under focus in these systems to justify the creation of Cooper pairs: spin or charge fluctuations. Electronic fluctuations tend to evolve on a same time scale as the motion of the electrons which makes Cooper pairing hard. However Chubukov and Hirschfeld [(49)] argued that the crucial feature that allows an unconventional (i.e. not phonon mediated) pair state to minimize the repulsive Coulomb interaction is the fact that its gap function changes sign. In that sense the electrons
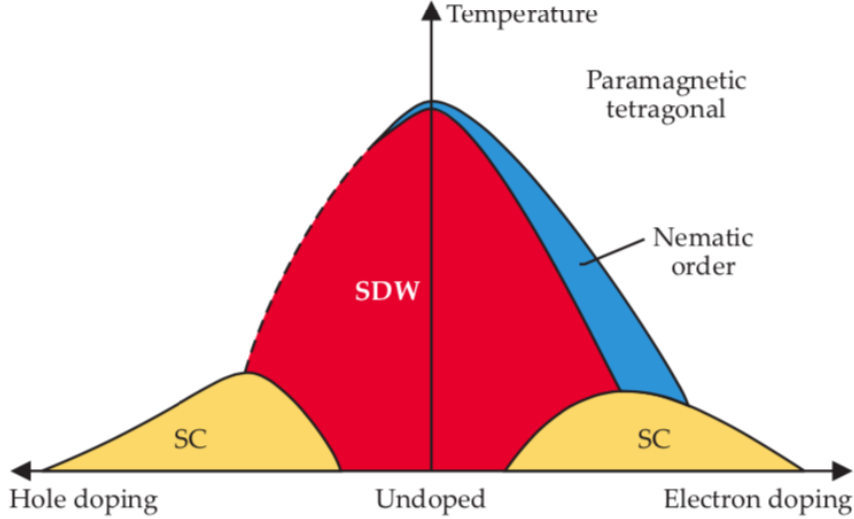
Figure 1.16: Typical phase diagram of iron-based superconductors in the parameter space of temperature and doping. From [(47)]

escape the Coulomb repulsion by avoiding each other in space rather than time. That could be the reason why most gap functions are anisotropic in momentum and often possess gap nodes. Even if the symmetry of the order parameter is currently discussed, in most iron-based materials it is believed that the right gap symmetry might be s^{+-} (see Fig 1.17). In such a state the gap in invariant under symmetry operations of the crystal, and thus might not exhibit symmetry imposed nodes, but the gap changes sign between the electron and holes pockets [(50)]. One can note that the s^{+-} and s^{++} states are both isotropic and only differ because of a phase shift of π between the hole and electron pockets. In the nodal s the gap vanishes at certain points on the electron pockets. Sometimes these nodes are called accidental nodes because they are not due to the symmetry but rather to the details of the pair interaction. The presence of nodes usually changes the low temperature behavior of the system. d-wave pairing is also under investigation, mainly in electron-doped systems.

In order to get s^{+-} superconductivity one needs the repulsion to be stronger between pockets than within them. Yet, usually it not the case, and the most popular scenario is that the strong interpocket interaction is due to spin fluctuations because the magnetic ordering vector Q of the magnetic phase is the same as the momentum
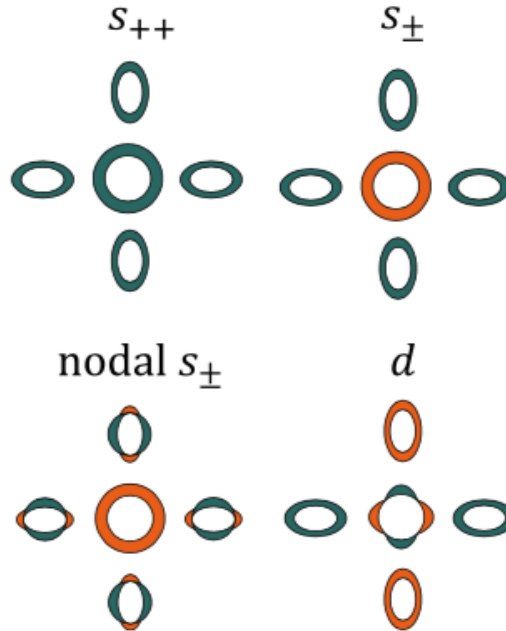
Figure 1.17: Different order parameters under discussion in iron-based superconductors in the 1-Fe Brillouin zone. From [([50])]

connecting hole and electron pockets.

1.3.2.2 Magnetic phase

Among all families of iron-based superconductors, the 122 and the 1111 are certainly the most commonly studied materials. The parent compound usually shows an antiferromagnetic order. It has a wave vector $(\pi, 0)$ in the one Fe Brillouin Zone. It connects electron to hole pockets, which have approximately the same size. That being said, we have good conditions for "nesting" of the Fermi surface, typically leading to a Spin Density Wave (SDW). The magnetic phase of iron-based superconductors is often referred to as SDW in order to stress out that magnetism is possible through itinerant electrons rather than through localized electron spins. This is a significant difference with cuprates here.

The magnetic phase in most iron-based superconductors is described as a stripe order, with spin aligning ferromagnetically in one direction and antiferromagnetically in the other. That order breaks the spin rotational symmetry but also a two fold symmetry

[[47]]. Since the magnetic order distinguishes two perpendicular in-plane direction, one could logically think that the magnetic order is intimately coupled to the orthorhombic distortion whereas the non-magnetic phase is coupled to the tetragonal structure. In some samples like $(Ba_{1-x}K_x)Fe_2As_2$ the structural transition and magnetic transition take place at the same time [[51]].

1.3.2.3 Nematic phase

Many measurements have found that when lowering the temperature, the magnetic phase is often preceded by a phase with broken tetragonal symmetry but unbroken spin rotational symmetry, this is the nematic phase [[52]]. The term nematicity comes from the liquid crystal field. Usually at room temperature crystal liquids will have no arrangement. However going at lower temperature they start to arrange themselves so that they will have a preferred direction. The nematic phase manifests itself through different experimental phenomenons :

-Structural distortion, where the lattice parameters a along the x-axis and b along the y-axis become different [[53]].

-Charge/orbital order where the occupation n_{xz} and n_{yz} associated to the d_{xz} and d_{yz} Fe-orbitals become also different [[54]].

-Spin order where the static spin susceptibility becomes different along the q_x and q_y directions of the Brillouin zone [[55]].

Since all properties have an in-plane anisotropy in the orthorhombic phase due to symmetry, it is quite hard to gather more information about the origin of the nematicity in Fe-based superconductors [[56]]. It is believed that the nematic and magnetic transition might have some coupling, since, if not together, they are very close by. It was for example observed that magnetic fluctuations increase below the structural transition [[57]] as well as spin-spin correlation length [[58]]. It was also shown that the structural distortion increases below the magnetic transition [[53]]. That close interaction between magnetism and nematicity support the idea that nematicity might be a consequence of magnetic interaction, in the spin nematic scenario. Since stipe-like correlations distinguish into two directions, they break tetragonal symmetry and help the structural transition to happen.

1.4 FeSe : a special case

1.4.1 A new phase diagram

Temperature doping phase diagram   Even if it is the simplest iron-based super-conductors, FeSe is a very special case among these, and is therefore very interesting when looking at the different phases. It is possible to exchange selenium with sulfur in order to get $FeSe_{1-x}S_x$. Sulfur being in the same column as Selenium in the periodic table, the number of charge carrier will stay the same. However the main effect of substituting selenium by sulfur is chemical pressure. This is because the sulfur atom is smaller than the selenium atom. Owing to that the crystal cell is smaller, almost the same as with hydrostatic pressure. At a temperature of 90K with no sulfur, the material undergoes the nematic/structural transition. The first surprising feature happens here because no magnetic order is observed when lowering the temperature, and only super-conductivity is found at a temperature of approximately 9K [(59)]. Even when adding some sulfur, no magnetic order seems to rise and the nematic transition decreases until it reaches a putative quantum critical point around $x \approx 0.16$ [(60)]. When the doping is superior to 0.16 the system always stays in the tetragonal structure. Considering the superconductivity there is also an interesting behavior. T_c is already present in the parent compound and slowly goes a bit higher to reach a maximum close to $x = 0.12$ with $T_c = 10.5$K. When the structural transition disappears, T_c likely goes through a step to lower temperature and stays flat around a value of 6K to finally reach 0K close to $x = 0.40$ [(61)]. The FeS compound is however superconducting at 6K.

Temperature pressure phase diagram   Fig. 1.19 shows the temperature-pressure phase diagram of bulk FeSe. At ambient pressure it undergoes the nematic transition at $T_s \approx$90K [(63)] but no magnetic transition. Only under the application of pressure can the magnetic order be restored at a pressure of 1GPa [(64)] while T_s decreases and T_c increases to a maximum of 37K at 6GPa [(65)]. This is an unusual feature for iron-based materials [(66)]. X-ray diffraction under pressure combined with Mössbauer spectroscopy showed that the structural and magnetic transition collapse at 1.6 GPa [(67)] as it can be seen in Fig. 1.19. Specific heat studies also agree on that feature [(68)]. Interestingly, the dependence of T_c is closely linked to the appearance of the other phases. For instance, it goes through a local maximum around 1 GPa exactly where the
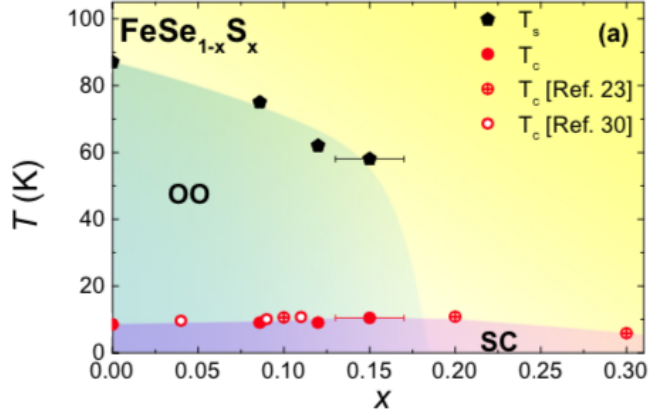
Figure 1.18: Temperature-doping phase diagram of bulk FeSe. From [(62)]

magnetic order starts to rise end reaches another maximum when the magnetic order is suppressed [(69)]. One of the main question here is about the nature of the magnetic order: is it stripe-like as in other iron-based superconductors ? For the moment no neutron diffraction experiments did manage to observe any magnetic signal. However some studies revealed some common features between the 122 family, where stripe-like order is observed and FeSe [(53),(67),(70)], suggesting that all Fe-based materials might have the same type of magnetic order.

1.4.2 Electronic properties

Compensated semimetal behaviour FeSe is a compensated semimetal, meaning that the electrons and holes densities are the same and are quite low compared to that of a metal [(71)]. One of the interesting features in FeSe is the magnetoresistance observed in the orthorhombic phase, being the signature of the large mean free path in compensated semimetal [(72)]. At the same time spin fluctuations start to appear, which might play a role in the modification of the electronic structure in that phase [(73)]. The upper critical field anisotropy and its dependence in doped samples [(74)] goes also in favor of a multiband behavior of FeSe.

Another interesting feature in FeSe is its Fermi energy. Kasahara et al. [(28)] estimate it around 3-7 meV for the electrons and 8-10 meV for the holes. These energies are of the same order of magnitude as the one of superconducting gap [(75)]. In such conditions one can say that we are close to a BCS-BEC crossover (BCS for Bardeen
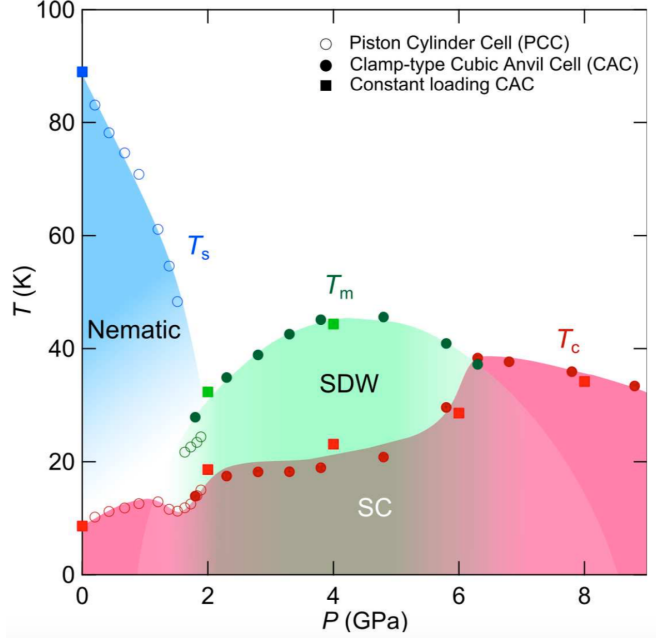
Figure 1.19: Temperature-pressure phase diagram of bulk FeSe. From [(69)]

Cooper Schrieffer and BEC for Bose-Einstein Condensate), where some properties could be at the midpoint between superconductivity and a Bose-Einstein condensate.

ARPES measurements In the nematic phase, ARPES measurements show a quasi 2D hole pocket around the Γ point. It is strongly distorted, having an elliptical shape, compare to the one observed in the tetragonal phase. When that pocket seems to be observable in every ARPES measurements, the precise shape of the electron pockets is still under debate and several scenario have been proposed. Some measurements show a bow-tie shaped electron pocket at the M_x point [(76)]. In addition other measurements performed on twinned crystals propose petal shaped electron pockets at the M_x and M_y points [(62)], when other experiments using nano-ARPES [(77)] also on twinned crystals go in favor on a single electron pocket at the M_x point. The absence or presence of another tiny electron pocket at the M_y point has also not reached consensus. Based on these observations, Shibauchi and al. [(78)] propose 4 possible Fermi surface structure in FeSe as illustrated in Fig. 1.21b.

1. INTRODUCTION

Quantum oscillations   Quantum oscillations have been performed by several groups using different techniques in order to have a better understanding of the electronic properties of FeSe in the nematic phase [(79), (80), (2)]. The fast Fourier transform spectra usually shows 6 peaks (see Fig. 1.20) corresponding to the frequencies observed in the quantum oscillations signal with relatively small frequencies compare to other Fe based superconductors($<$700T). The β and δ frequencies are associated with the extremal areas of the hole band, both having a similar effective mass of 4 m_e. The γ frequency is associated with the maximum area of the outer electron pocket with an effective mass of 7 m_e [(80)]. Then there are several possible explanations for the other frequencies. One of these suggests that the minimum area of the pocket gives the α_1 frequency, suggesting only one electron pocket. α_2 would be an harmonic of α_1 and ϵ would be an harmonic of β. That is the scenario proposed by Terashima et al. [(80)]. On the other hand a second scenario proposed by Coldea et al. [(81)] suggests that the minimum of the outer electron pocket is associated with ϵ, and that there would be an additional small electron pockets giving birth to the α_1 and α_2 frequencies. Other measurements [(78)] also agree on the fact that the electron pocket might by disconnected and separated in two, but also explained that the precise nature of the shape of the electron pocket is very sensitive to the Fermi energy. As shown in Fig. 1.21a, the electron pocket as a fork-tailed shape near the Fermi level and very subtle changes, like in the number of carriers, could change the Fermi level to shift and therefore reconnect the electron pocket.

In the end one can sum up all possible scenarii in the next figure.

Superconducting gap   There is a consensus about the anisotropic nature of the superconducting gap of FeSe. It was shown with Bogoliubov quasiparticle interference that $\Delta_{max}/\Delta_{min}$=15 [(83)]. In the same article Sprau et al. argued that the gap structure of FeSe consists of one electron gap and one hole gap with comparable average gap amplitudes, the one of the holes being of 1.5 meV and the one of the electrons being of -1.2 meV. Specific heat data [(84)] also agree on a two band scenario with line nodes (this feature remains controversial), being consistent with the ARPES and quantum oscillations studies from above. In the case where an electron pocket would appear at the M_x point, it is said that that pocket carries a very small spectral weight and a
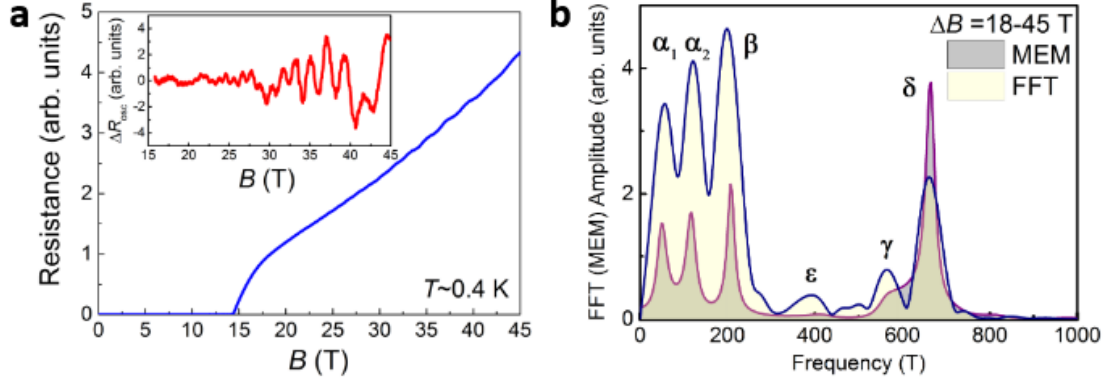
Figure 1.20: (a) Magnetotransport in a single crystal of Fese at 0.4K. The inset shows the oscillatory part of the signal, reminiscent of quantum oscillations. (b) Fast Fourier transform spectra of the same signal. From [[82]]

(a)   (b)
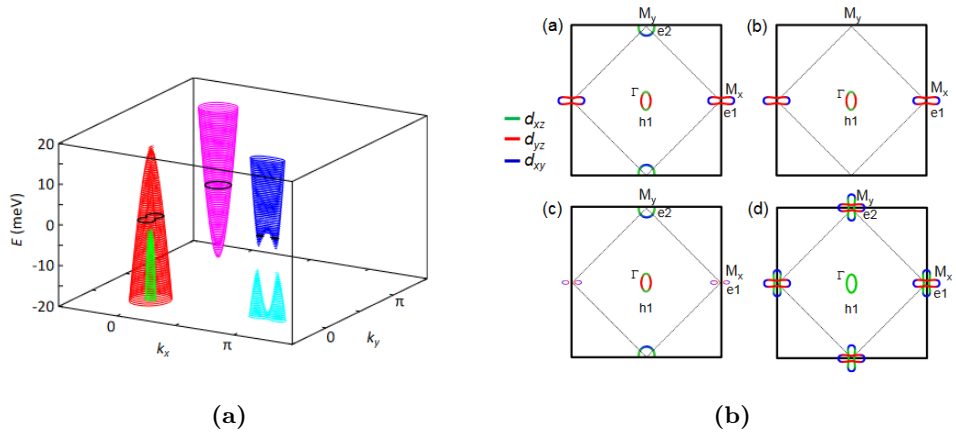
Figure 1.21: (a) Schematic energy dispersion of the hole and electron pockets in the nematic phase of FeSe. (b)Four possible Fermi surface structure of FeSe based on ARPES and quantum oscillations. In all the possibilities, a hole band is found the the point. The electron pocket around the M_x point has a bow-tie shape for (a) and (b), and another electron pocket is present at the M_y point in (a). In (c), the electron pocket is disconnected. In (d) petal shaped pockets are found both at M_x and M_y. From [[78]]

zero superconducting gap [(85)]. Both specific heat studies cited above agree on a weak coupling scenario in the BCS framework, with a value of $\Delta C_e/\gamma_n T_c \approx 1.7$.

1.4.3   FeSe in high magnetic fields

A-B phase   FeSe shows some very special and sometimes controversial features in high magnetic fields. The first one that we can find in the literature is the presence of a high field superconducting phase, separated from the low field superconducting phase, only visible when the magnetic field is applied parallel to the c-axis [(28)]. Surprisingly the separation between these two phases is field independent. Thermal conductivity shows a cusp-like feature at a field H^* (see Fig. 1.22a). On the other hand going at higher field, one can still see superconductivity and the irreversibility line measured by magnetic torque. Resistivity seems to appear at a higher field also, where the irreversibility field H_{irr} (see Fig. 1.22b) and the zero resistance measured point coincides very well. The peak measured in the torque data is related to the melting of the vortex lattice. At the same time the resistivity shows a interesting behaviour (see Fig. 1.22c). The magnetoresistance increases at low temperature being typical of the behaviour of compensated semimetal but at high field in the normal phase it finally decreases after showing a broad maximum around 15K. That decrease in the resistivity is ascribed to strong superconducting fluctuations in the normal phase. Fig. 1.23 shows the obtained phase diagram from these measurements.

FFLO phase   Looking in the other direction (with the magnetic field along the FeSe layers, parallel to the a or b-axis), it seems very likely that another phase appears at high fields also. Magnetocaloric effect measurements showed an anomaly in the superconducting state at high fields [(86)] and a clear discontinuous downward jump was found in thermal conductivity data at 24T [(28)] (see Fig. 1.24a). These measurements being in the irreversible part of the phase diagram one should be careful about any thermodynamical measurements. Surprisingly superconductivity seems to be still present above these features as indicated by resisitivity measurements (see Fig. 1.24b). The resistivity shows also a surprising behaviour : the broad transition at high temperature becomes abruptly sharp at low temperature. The new found phase is believed to be a
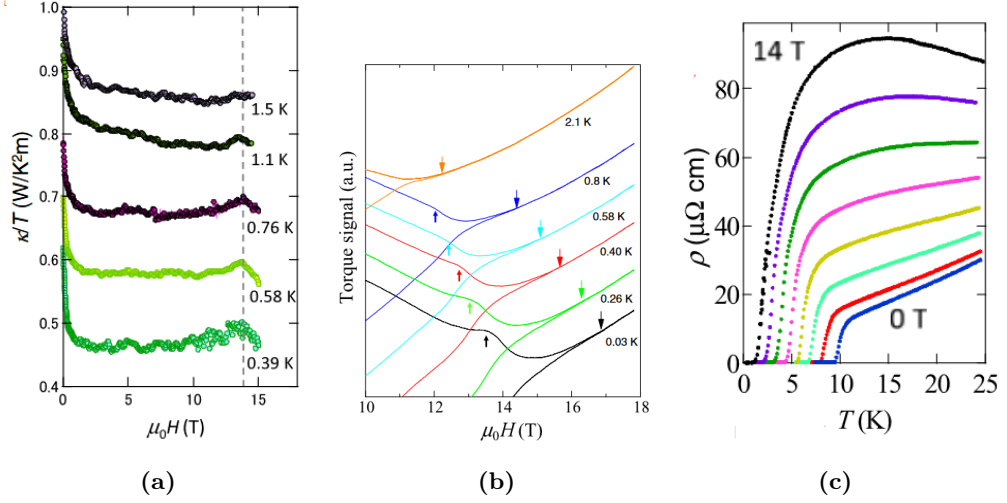
Figure 1.22: (a) Magnetic-field dependence of the thermal conductivity at low temperatures when the field is perpendicular to the FeSe layers. At H^*, it shows a cusp-like peak, suggestive of a nearly temperature-independent transition. (b) Field dependence of the magnetic torque at low temperatures. Downward (upward) arrows mark the positions of the irreversibility (peak) field. (c) Temperature dependence of the resistivity. From [[28]]
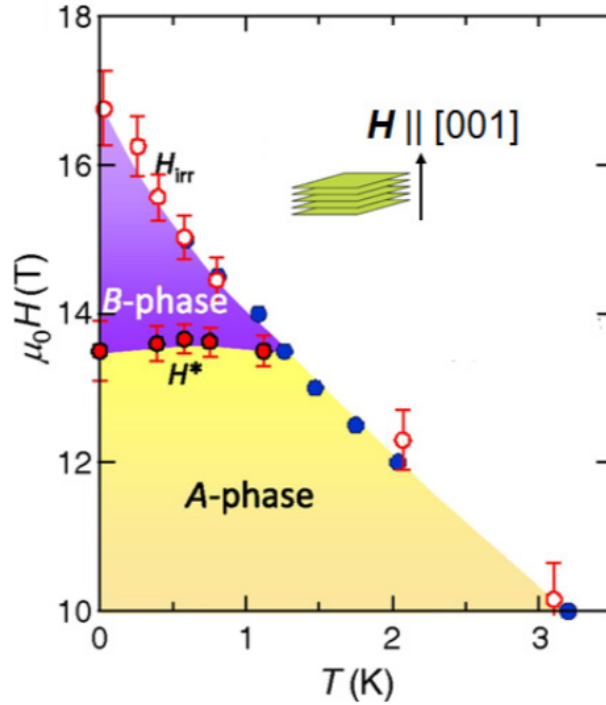
Figure 1.23: High field phase diagram of FeSe with field oriented perpendicular to the FeSe layers. From [[28]]

FFLO phase. The obtained phase diagram in Fig. 1.25 shows the two different super-conducting phases, a classical BCS phase at low field and a FFLO phase at higher field. A firm experimental proof of a FFLO state is still missing, and a great deal of studies focused on that point in different materials. Some signatures have been reported in heavy fermions materials like $CeCoIn_5$ [(87)] and organic superconductors like $\kappa-(ET)_2Cu(NCS)_2$ ([(88)], [(1)]). In these materials, a phase transition seems to occur below the upper critical field at low temperature. However due to possible vortices phase transitions or magnetic transitions, the presence of a classic FFLO state is still very controversial. Some other systems like $CeCu_2Si_2$ [(89)] and KFe_2As_2 [(90)] might also show a possible FFLO state. There are only a few candidates that might satisfy the conditions to observe a FFLO state, however FeSe might be in the list of these candidates. First, the calculated Maki parameter is found to be quite high [(79),(91)] which could indicates that the orbital effects might be low compare to paramagnetic effects, and that might favor a FFLO formation. Also high quality crystal are now available which is also a prerequisite to get a FFLO state. Ok and al. [(86)] showed that a possible FFLO state could be stabilized with nesting, and that nesting is possible around 24T via a wave-vector $(0, \pi)$.

1.4.4 Melting of the vortex lattice

The symmetry of the vortex lattice is shaped by the material properties. We saw that in Abrikosov work, in a simple scenario, without any pinning and in a isotropic superconductor, the vortex lattice is hexagonal. However, this symmetry is not the only one that was observed and some materials seems to exhibit a squared symmetry [(93)]. It was found that in fact the hexagonal and square lattice are very close in energy with only 2% difference [(94)]. Only a weak anisotropy can change the balance and lead to a change in the vortex symmetry. A rhombic symmetry was also found to be able to stabilize in the case of a d-wave gap with magnetic field [(95)]. Surprisingly FeSe was found recently to exhibit such a transition [(96)]. The field at which the transition takes place was observed by spectroscopy but also in specific heat where a kink is observed and a change in the slope of C_p as a function of the magnetic field. Such a feature is visible in Fig. 1.26. Such a dependence of the specific heat was also observed by Ok et al. [(86)] and was assigned to a closing of a small superconducting gap. Interestingly, the clos-
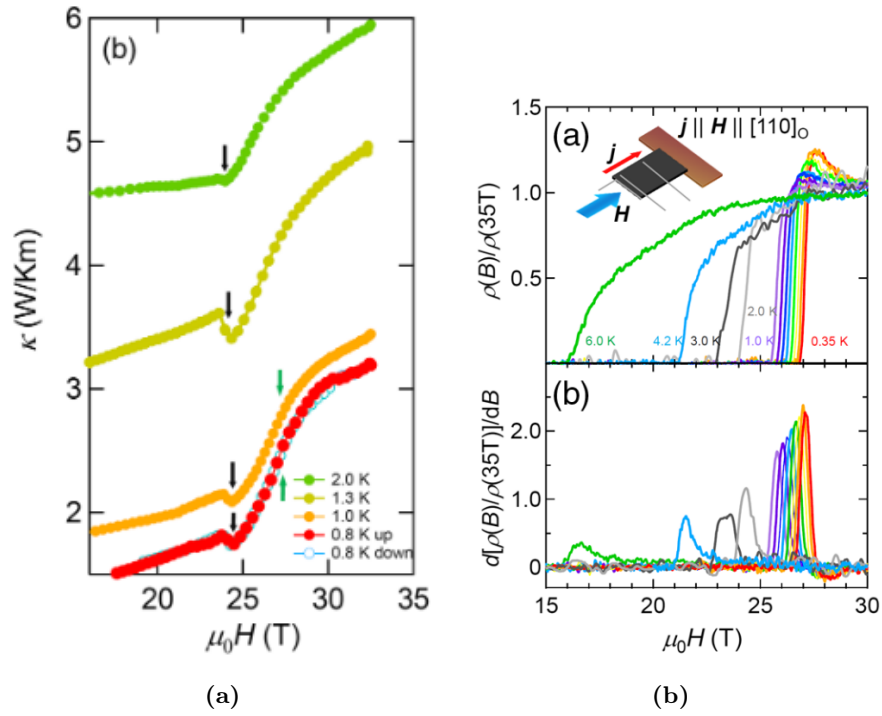
Figure 1.24: (a) Magnetic field dependence of the thermal conductivity in FeSe when the field is parallel to the FeSe layers at low temperature. A discontinuous downward jump at $\mu_0 H$=24 T appears inside the superconducting state as indicated by the black arrows. The black arrows indicates the field H_p measured with resistivity (b) Magnetic field dependence of the normalized resistivity and its derivative. The broad transition at high temperature becomes very sharp abruptly at low temperature. From [[92]]
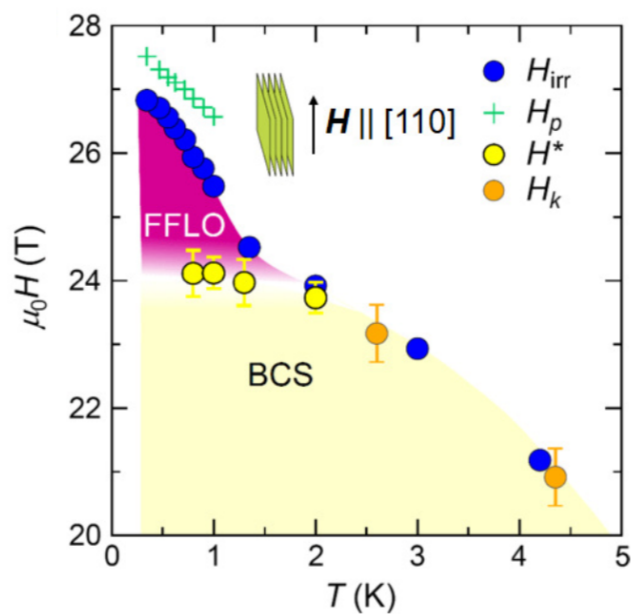
Figure 1.25: High field phase diagram of FeSe with field oriented along to the FeSe layers. Blue circles and green crosses show H_{irr} and H_p determined by resistivity measurements. Orange and yellow circles show H_k and H^* determined by thermal-conductivity measurements. From [[92]]
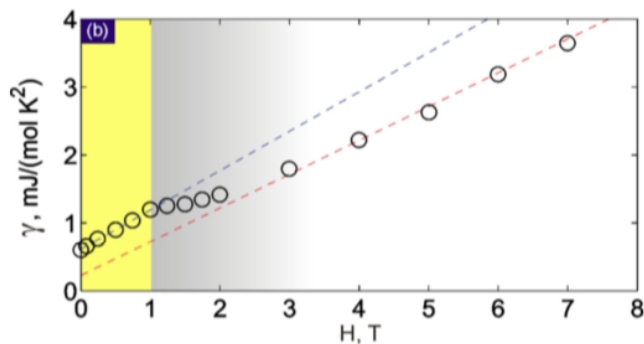
Figure 1.26: Dependence of the specific heat of FeSe on the magnetic field. From [(96)]. It is argued that the feature around 1T might be related to a change in the vortex lattice symmetry, itself related to a the closing a superconducting gap. Such a dependence is reminiscent of data obtained by Ok et al. [(86)].

ing of a small superconducting gap could lead to a change in the lattice symmetry [(96)].

On the other hand, FeSe seems to be a perfect material in order to study the vortex lattice melting. As we argued before, one of the key feature in order to observe the vortex lattice melting is the Ginzburg number, G_i. The first example of first order melting was found in cuprates (that will be discussed later in the case of specific heat, see Fig. 2.7) which have a high Ginzburg number due to their high T_c, short coherence length and large anisotropy (see Tab 1.2). In some good quality samples, the reversible magnetization shows a discontinuity [(97)], and thermal expansion [(98)] and specific heat [(99)] have a peak superimposed on a step. We now have other material that exhibits vortex lattice melting such as Nb_3Sn [(98)], $SnMo_6S_8$ [(100)] and some iron-based superconductors ([(101)],[(102)]).

One of the main question about the melting is its behaviour at low temperature. The main problem regarding that in cuprates is the high values of H_{c2}, that is usually inaccessible, or if accessible the residual disorder makes it impossible to observe the melting line.

We believe that FeSe is the perfect candidate to study in details the vortex lattice melting. We have now good crystal quality and the upper critical field at zero tempera-

ture is accessible in both direction in high magnetic field facilities. When looking at the typical characteristics of it, it seems very likely that we might at least observe melting in a part of the phase diagram (see Table. 1.2). In fact the vortex lattice melting was observed in $YBa_2Cu_3O_7$, $RbEuFe_4As_4$ and FeSe seems to have a Ginzburg number very close to the values in these materials. It is also several orders of magnitude higher than the one of classical materials like niobium. Therefore we think that the vortex liquid will occupy a large enough portion of the phase diagram and will be possible to detect.

	$YBa_2Cu_3O_7$	Nb	$RbEuFe_4As_4$	FeSe
T_c (K)	93.7	9.25	36.5	9.1
$H'_{c2,c}$ (T/K)	1.8	0.044	4.2	3
Γ	7.8	1	1.7	2-4
$\xi_{ab}(0)$ (nm)	1.4	28.6	1.46	5.2
$\lambda_{ab}(0)$ (nm)	75	21.3	98	445
G_i	2×10^{-3}	6.9×10^{-12}	5.3×10^{-5}	10^{-4}

Table 1.2: Superconducting parameters and Ginzburg numbers of different materials. Γ is the anisotropy of the upper critical field. ([[103]],[[104]],[[105]],[[106]],[[107]],[[99]],[[91]]

1.5 FeSe$_{1-x}$S$_x$: motivations

English version Despite being the simplest materials among iron-based superconductors, FeSe is still under a lot of investigations and far from being totally understood. We just saw that it shows some special behavior, such as the absence of a magnetic phase at ambient pressure and might be in a so-called BCS-BEC crossover. FeSe$_{1-x}$S$_x$, the isovalent doped system, shows similar T_c to the parent compound and its physics seems to be very close. The sulfur atoms are supposed to act like pressure on the system which might help to get closer to the magnetic phase also. FeSe$_{0.88}$S$_{0.12}$ exhibits a value of T_c close to the maximum of the system and should therefore be interesting to know more about superconductivity.

FeSe$_{1-x}$S$_x$ has a T_c close to 10K which makes it quite easy to access. H_{c2} at zero temperature is also accessible in high magnetic fields facilities such as the LNCMI Grenoble,

having fields up to 36T. The properties of the material seems also to be perfectly appropriate in order to study vortex melting over the entire $H - T$ phase diagram and have a better understanding of it. Looking at the value of $G_i \approx 10^{-4}$ one can hope to observe a vortex liquid phase over a significant part of the $H - T$ phase diagram, and also to be able to see it in thermodynamical measurements.

When looking at Tab. 1.2, one can estimate from the values of H'_{c2} and Γ that $H_{orb,c} \approx$ 20T and $H_{orb,ab}(0) \approx 80$T. From the same data one can also estimate that the Maki parameters in both direction would be approximately about $\alpha_{M,c} \approx 1$ and $\alpha_{M,ab} \approx 5$ (cf Sec. 1.2.4.2). This indicates that FeSe might be a candidate for strong paramagnetic effects affecting the pair breaking and should therefore deserve some investigations to confirm that or not.

The high field part of the phase diagram seems also to be very interesting when looking at the literature. The presence of a Fulde, Ferrell, Larkin and Ovchinnikov phase as been suggested by several groups and the value of $\alpha_{M,ab} \approx 5$ goes also in favor of that. Therefore we think that the FeSe$_{1-x}$S$_x$ system deserves an in-depth analysis of its $H - T$ phase diagram and this is what shall be done in the following sections of this thesis. However we shall first focus on the measurements used to obtain the phase diagrams and this is what will be done in the next chapter.

Version française Bien qu'il soit le matériau le plus simple parmi les supraconducteurs à base de fer, FeSe fait encore l'objet de nombreuses recherches et est loin d'être totalement compris. Nous venons de voir qu'il présente un comportement particulier, comme l'absence d'une phase magnétique à pression ambiante, et qu'il pourrait se trouver dans ce que l'on appelle un BCS-BEC "crossover". FeSe$_{1-x}$S$_x$, le système dopé de manière isovalente, présente une T_c similaire à celui du composé parent et sa physique semble être très proche. Les atomes de soufre sont censés agir comme une pression hydrostatique sur le système, ce qui pourrait aider à se rapprocher de la phase magnétique également. FeSe$_{0,88}$S$_{0,12}$ présente une valeur de T_c proche du maximum du système et devrait donc être intéressant pour en savoir plus sur la supraconductivité. FeSe$_{1-x}$S$_x$ a une T_c proche de 10K ce qui le rend assez facile d'accès. H_{c2} à température nulle est également accessible dans des installations à haut champ magnétique comme le LNCMI Grenoble, dont les champs peuvent atteindre 36T. Les propriétés du matériau semblent

également parfaitement appropriées pour étudier la fusion des vortex sur l'ensemble du diagramme de phase $H - T$ et en avoir une meilleure compréhension. En regardant la valeur de $G_i \approx 10^{-4}$ on peut espérer observer une phase liquide de vortex sur une partie significative du diagramme de phase $H - T$, et aussi d'être capable de la voir dans les mesures thermodynamiques.

En regardant le Tab. 1.2, on peut estimer à partir des valeurs de H'_{c2} et Γ que $H_{orb,c} \approx$ 20T et $H_{orb,ab}(0) \approx 80$T. A partir des mêmes données, on peut également estimer que les paramètres de Maki dans les deux directions seraient approximativement de $\alpha_{M,c} \approx$ 1 et $\alpha_{M,ab} \approx 5$ (cf Sec. 1.2.4.2). Cela indique que FeSe pourrait être un candidat pour de forts effets paramagnétiques affectant la brisure de paires de Cooper et devrait donc mériter des recherches pour le confirmer ceci ou non.

La partie à haut champ du diagramme de phase semble également être très intéressante lorsqu'on examine l'état de l'art. La présence d'une phase de Fulde, Ferrell, Larkin et Ovchinnikov a été suggérée par plusieurs groupes et la valeur de $\alpha_{M,ab} \approx 5$ va également dans ce sens.

Nous pensons donc que le système $FeSe_{1-x}S_x$ mérite une analyse approfondie de son diagramme de phase $H - T$ et c'est ce qui sera fait dans les sections suivantes de cette thèse. Cependant, nous allons d'abord nous concentrer sur les mesures utilisées pour obtenir les diagrammes de phase et c'est ce qui sera fait dans le chapitre suivant.

2

Experimental techniques

2.1 Specific heat

2.1.1 About thermodynamics

Thermodynamics deals with heat exchanges between a system, what is outside of that system and how that system is evolving with time. It relies on two widely known principles, helping one to understand how this evolution works through different but narrow parameters.

One first needs to describe and determine the system and its exchanges with the outside. Two variables are introduced: the temperature T and entropy S. Both of them enable defining the heat exchange during a reversible transformation: $\delta Q = T dS$. One also usually needs to define the work exchange with the system δW. From then on, it is possible to describe the differential form of thermodynamic functions like the inner energy U, the enthalpy H, or the free energy F and free enthalpy G. Equilibrium is usually found at the extremum of one of these functions. For example, at fixed pressure and temperature, the free enthalpy is minimal at equilibrium.

Once the system is well described by these variables, one can link them to other thermodynamics variables like the thermal dilatation or the specific heat. This is our main goal in the section. Every system has some specifics and we want to understand what will contribute to the specific heat and in what manner.

2. EXPERIMENTAL TECHNIQUES

2.1.2   General definition of the specific heat

As explained above, the heat capacity is a thermodynamic variable that can be described by other variables like the inner energy or the entropy. It connects the amount of heat one needs to put in a system δQ to the infinitesimal rise of temperature dT. As a consequence, from the second principle of thermodynamics, one can express the heat capacity as a function of the entropy.

$$\delta Q = CdT = TdS, \tag{2.1}$$

$$C = T\frac{\partial S}{\partial T}, \tag{2.2}$$

where we considered that dS is only due to changes in the temperature and not in the field or pressure for example. If one wants to consider that, one should write $dS = C/TdT + \partial S/\partial H dH + \partial S/\partial P dP + ...$. To be precise, the specific heat is usually expressed at constant volume, C_v, or at constant pressure, C_p and is related to thermodynamic variables by :

$$C_v = T\left.\frac{\partial S}{\partial T}\right|_v = -T\left.\frac{\partial^2 F}{\partial T^2}\right|_v = \left.\frac{\partial U}{\partial T}\right|_v, \tag{2.3}$$

$$C_v = T\left.\frac{\partial S}{\partial T}\right|_p = -T\left.\frac{\partial^2 G}{\partial T^2}\right|_p = \left.\frac{\partial H}{\partial T}\right|_p. \tag{2.4}$$

Looking at the definitions of C_v, one can easily see that this is a very good probe to understand the thermodynamics of a system. It is related to the free energy and the entropy and can therefore be sensible to phase transitions. The Mayer's relation connects both C_v and C_p with the isobaric thermal dilatation coefficient α_p, the isothermal compressibility coefficient, χ_T, the volume V and the temperature, T :

$$C_p - C_v = \frac{\alpha_p^2 VT}{\chi_T}. \tag{2.5}$$

A first interesting approximation is to say that $C_p = C_v$, meaning that the thermal dilatation is very low. This is true at very low temperature, well below the melting temperature. This approximation is very useful as all the contributions to the specific heat that we will see are at constant volume. However in our experiments only the pressure is constant.

Another problem in the specific heat is that we were only considering a heat input in the system, but other variables can contribute to the variation of the system's temperature. Indeed for instance, a magnetic field in a magnetic material can cause a change in the temperature, this is called the magnetocaloric effect.

At the beginning of Sec. 2.1.2, we were talking about specific heat and we suddenly jumped to heat capacity. An alert reader may fail to understand for what reason for this change. The heat capacity, C, in an extensive variable, measured in $J.K^{-1}$, therefore it depends on the material but also on the number of moles in it. On the other hand, the specific heat, c, in an intensive variable, measured in $J.K^{-1}.g^{-1}$, $J.K^{-1}.m^{-3}$ or $J.K^{-1}.mol^{-1}$ and only depends on the material.

In the kind of system that we will measure, different contributions to the specific heat will add to each other. In a solid, the particles can be excited by the temperature and contribute in different ways to the specific heat. We shall explore this in the following sections.

2.1.3 Phonons

A solid is often made out of periodic arrangement of atoms. These atoms of moving around a equilibirum positions due to the temperature. They are moving in a collective pattern and are called phonons. The amplitude of that movement rises with temperature and thus contributes to the specific heat.
During the XIX century, the first expression of the specific heat was given by Dulong and Petit, noticing that many solids have the same specific heat at room temperature :

$$c_v = 3R = 23.93 J.K^{-1}.mol-1. \tag{2.6}$$

This law is almost the same for an ideal gas. In fact, one can imagine the phonons as an ideal gas, with 3 spatial degrees of freedom and 3 rotational degrees of freedom. Thus the inner energy of a gas is $U = \frac{6}{2}Nk_bT$ and one finds again the Dulong and Petit law. That law works very well at room temperature, although some noticeable changes can be observed while going the lower temperature. Taking the example of diamond, the specific heat does not match the Dulong and Petit law at ambiant temperature but going

to higher temperature, one recovers it. Boltzmann soon tried to explain the behavior of atoms in a solid by modeling it in a harmonic well formed by the interactions with other atoms in the system and finding the same results as before. This is due to the classical treatment of these atoms' behavior. The problem here is that at low temperature, phonons are considered as bosons with a quantum point of view.

At the beginning of the XXth century, Einstein had with the same idea as Boltzmann, and said that all the atoms are in the same harmonic well with the same "Einstein's" frequency. The results is an exponential rise of the specific heat at low temperature, saturating at high temperature to the Dulong and Petit law. This was a first attempt to fit the specific heat data and it worked quite well. However it was observed that most of the solid had a T^3 behavior at low temperature and this was not the case with Einstein's model.

A few years afterwards, Debye assumed that there was a dispersion relation for the frequency of the phonons. We now know that the energy of a phonon depends on its wave vector, and also that phonons have severals branches : acoustics and optics. Debye only considered the acoustic phonons and described the oscillations as a wave with a frequency $\omega(k) = vk$, with v being the sound velocity, and for each k there are 3 oscillations mode, one for each direction of motion. In order to take into account the saturation at high temperature, one need to fix the upper limit of the integral over the k, until all modes are excited. The specific heat can then be written as :

$$c_V = 3 \frac{\partial}{\partial T} \int \int_0^{k_D} \hbar\omega(k)(n_B(k) + \frac{1}{2})k^2 \frac{dk}{(2\pi)^3} d\Omega \qquad (2.7)$$

with $k_D^3 = \frac{V}{6\pi^2 N}$, N being the number of particles, and n_B the occupation probability, following the Bose-Einstein statistic [[108]]. Rearranging the different terms, one gets:

$$c_V = \frac{9Nk_b}{V} \left(\frac{T}{\Theta_D}\right)^3 \int_0^{\frac{\Theta_D}{T}} \frac{x^4 e^x dx}{(e^x - 1)^2}, \qquad (2.8)$$

with $\Theta_D = \frac{\hbar v k_D}{k_B}$ being the Debye temperature, where all the modes start to be excited. When the temperature is sufficiently small compared to the Debye temperature, the specific heat can be simplified as:

$$c_V = \frac{12\pi^4}{5} R \left(\frac{T}{\Theta_D}\right)^2 = \beta T^3 \qquad (2.9)$$

where β is the phonon coefficient. However, when observing the phonon contribution, one should always check the assumption of being far away from the Debye temperature is true, otherwise the asumption of $\omega = vk$ and that $\Theta_D/T = \infty$ are not true anymore. When this is not the case some other coefficients can add themselves and one obtains:

$$c_V = \beta_3 T^3 + \beta_5 T^5 + \beta_7 T^7 + ... \tag{2.10}$$

For more details about that see Sec.2.1.7. The Debye law works very well for some solids, however, at low temperature another term is found for metals due to electrons.

2.1.4 Electrons

For metals, the conduction electrons have to be taken into account. Given a system of electrons, with chemical potential μ, the probability of an eigenstate with an energy ϵ to be occupied is given by the Fermi statistics [(108)]:

$$f_F(\epsilon, \mu) = \frac{1}{e^{\beta(\epsilon-\mu)} - 1} \tag{2.11}$$

Most of metals can be very well described by the Fermi formalism, with a new effective mass, m^*, describing the effect of the interaction on the electrons. Thus the energy of an electron with a wave vector k can be written as $\epsilon(k) = \frac{\hbar^2 k^2}{2m^*}$. Integrating the probability of occupation over all k gives us the number of electrons of the system, and multiplying it by the corresponding energy will give the total energy of the system.

$$N = \int_0^\infty g(\epsilon) f_F(\epsilon, \mu) d\epsilon, \tag{2.12}$$

$$E = \int_0^\infty \epsilon g(\epsilon) f_F(\epsilon, \mu) d\epsilon, \tag{2.13}$$

where $g(\epsilon)$ is the density of state at a given energy. Considering only a low temperature regime compare to the Fermi temperature, we can assume that the Fermi distribution is almost like a step function. If $g(\epsilon)$ does not fluctuate too much in a region of $k_b T$ close to μ, one can apply the Sommerfeld development :

$$N = \int_0^\mu g(\epsilon) d\epsilon + \frac{\pi^2}{6}(k_B T)^2 g'(\mu), \tag{2.14}$$

$$E = \int_0^\mu \epsilon g(\epsilon) d\epsilon + \frac{\pi^2}{6}(k_B T)^2 (\mu g'(\mu) + g(\mu)). \tag{2.15}$$

It implies that the energy variation from the ground state is given by :

$$\Delta E = \frac{\pi^2}{6}(k_B T)^2 g(\epsilon_F).$$

(2.16)

Therefore the specific heat is :

$$C_V = \frac{\pi^2}{3}k_B^2 T g(\epsilon_F) = \gamma T$$

(2.17)

with $\gamma = \frac{\pi^2}{3}k_B^2 g(\epsilon_F)$ being the Sommerfeld coefficient for the specific heat. To understand this result we can interpret it as this: the energy rises close to $T = 0$ is mainly due to the part of electrons in a range of $k_B T$ below ϵ_F getting excited and rising in a range of $k_B T$ above ϵ_F. The number of excited electrons per unit of volume is then $k_B T$ multiplied by the density of states per unit of volume $g(\epsilon_F)$. The excitation energy being close to $k_B T$, the thermal energy density shall be of the order of $g(\epsilon_F)(k_B T)^2$. In the case of several bands, one needs to sum up over all the effective mass of each band to obtain the coefficient γ.

After this calculation, we now can give a model of the specific heat in metal :

$$\frac{C_v}{T} = \gamma + \beta T^2.$$

(2.18)

One should also notify that in the case where the Fermi energy is close to the thermal energy, then the Sommerfeld development is not applicable and it is not possible to define any Sommerfeld coefficient being independent of the temperature.

2.1.5 Superconductivity

We just saw that the most important part in the electron contribution to the specific heat comes from the Fermi level and the density of states. When superconductivity appears, electrons couple and a gap, $\Delta(k)$, opens up at the Fermi level. This gives another contribution to the specific heat. In fact while going at lower temperature, a jump is observed at T_c and gives a very different behavior compared to a normal metal. By adding a sufficient magnetic field, the normal behavior is restored. In 1957, Bardeen, Cooper and Schrieffer (BCS) managed to give a first explanation for the microscopic behavior of electrons to explain superconductivity. In the paper [[6]], the energy of an electron if given by:

$$\epsilon(k) = \sqrt{\epsilon_0(k)^2 + |\Delta(k)|^2},$$

(2.19)

where ϵ_0 is defined as ϵ from the section above (without superconductivity). For the s-wave superconductor, the isotropic case, $(\Delta(k) = \Delta)$, which was studied in the BCS theory, the density of state is fully gaped within the gap with singularities at the two energy gaps $\pm\Delta$. One contribution will come from the variation of the excited states due to the Fermi statistics and the other will come from the variation of the superconducting gap with the temperature. In the low temperature regime, one can simplify calculation, giving the following expression :

$$C_{s-wave} = -\frac{2}{T}\sum_k \frac{\partial f_F(\epsilon, T)}{\partial \epsilon}) \left(\epsilon(k)^2 + \frac{\beta}{2}\frac{\partial \Delta^2}{\partial \beta}\right) = \frac{2k_B}{(k_B T)^{3/2}}g(E_F)\Delta_0^{5/2}e^{-\frac{\Delta_0}{k_B T}}, \quad (2.20)$$

with Δ_0 being the gap at zero temperature. That law gives a zero contribution at zero temperature, rising with temperature, following a thermal activation law. However this behavior does not seem to work for every superconductors. Some of them, like cuprates, have a quadratic dependence of the specific heat in the low temperature regime. This is due to the gap being not isotropic, as with the cuprates for example, where there is d-wave gap. In the case of a d-wave superconductor, there are some nodes in the (π, π) direction, where the gap value is zero, while in the $(0, \pm\pi)$ and $(\pm\pi, 0)$ directions, the gap reaches its maximum value. The gap is described by $\Delta(k) = \Delta_0 \cos(2\theta)$. It also means that all excitations are not gaped as show in Fig 2.1, and some quasiparticules can be excited at very low temperature, leading to a different behavior of the specific heat. For a d-wave superconductor, at low temperature we have [(109)] :

$$C_{d-wave} = \alpha T^2, \quad (2.21)$$

where α is a constant depending on the properties of the material. It is then possible to determine what type of superconductor we have by plotting the temperature dependence of the specific heat.

2.1.6   The α model for superconductivity

As we have just presented, in the BCS model, the superconductor is assumed to have only a single-band isotropic Fermi surface. It is not the case for many superconductors. We explained the possible deviation from the BCS-model in the case of nodes in the gap, but a lot of superconductors do not match exactly the BCS value of $\Delta/k_B T_c = 1.764$.
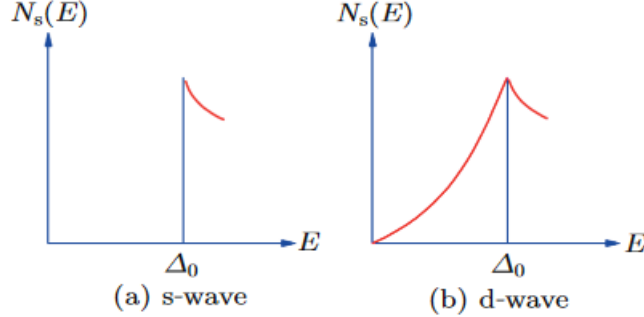
Figure 2.1: Density of states for two different kind of gaps. From Ref ([110])

.

Owing to Padamsee, Neighbor, and Shiffman [([111])] we now have a phenomenological model to fit some specific heat data, called the α-model. In that model the specific heat is described as:

$$
\frac{C_s}{\gamma_n T_c} = \frac{6\alpha^3}{\pi^2 t} \int_0^{\frac{k_b \theta_D}{\Delta_0}} f(1-f) \left(\frac{\tilde{E}^2 + \tilde{\Delta}^2}{t} - \frac{1}{2} \frac{d\tilde{\Delta}^2}{dt} \right) d\tilde{\epsilon}, \qquad (2.22)
$$

Where $t = T/T_c$, Δ_0 is the gap as zero Kelvin, $\tilde{\epsilon} = \epsilon/\Delta_0$, $\tilde{\Delta} = \Delta/\Delta_0$, $\tilde{E} = \sqrt{\tilde{\epsilon}^2 + \tilde{\Delta}^2}$, $f = (\exp^{\frac{\alpha E}{T}} + 1)^{-1}$ is the Fermi distribution considering α, and $\alpha = \Delta_0/k_b T_c$.

In the BCS case, $\alpha = 1.764$ is fixed. Yet, in the present model α can vary. It still supposes a BCS-like superconducting gap, with a phonon-electron coupling. However the value of α gives some information about the diverse mechanisms at work in the material. While an α value higher than the BCS one is explained by a strong phonon-electron coupling, a lower value could mean that the gap is not isotropic in the weak coupling limit [([112])]. In the case of multiband superconductivity, a phenomenological model was developed to explain the specific heat behavior of MgB_2 by Bouquet and al [([113])]. It only supposes two different contributions from two different bands in the α-model without any interband coupling in order to fit the specific heat data. Fig. 2.2 shows a figure extracted from the article of Bouquet et al. modeling the specific heat of MgB_2 considering two gaps. The existence of different superconducting gaps is also under debate in the case of FeSe, and different models have been applied in order to fit its specific heat [([114]), ([84]), ([115])]. Fig. 2.3 shows the different models proposed by Muratov et al [([114])].
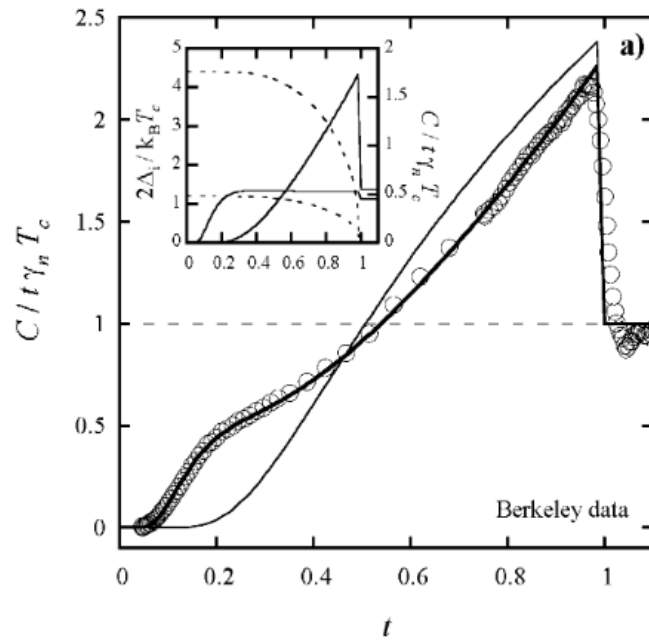
Figure 2.2: BCS-normalized specific heat (thin line), experimental data (circle), and two-gap fits (thick lines), vs. the reduced temperature of MgB_2. The inset shows the two different fitted gaps. From [(113)]
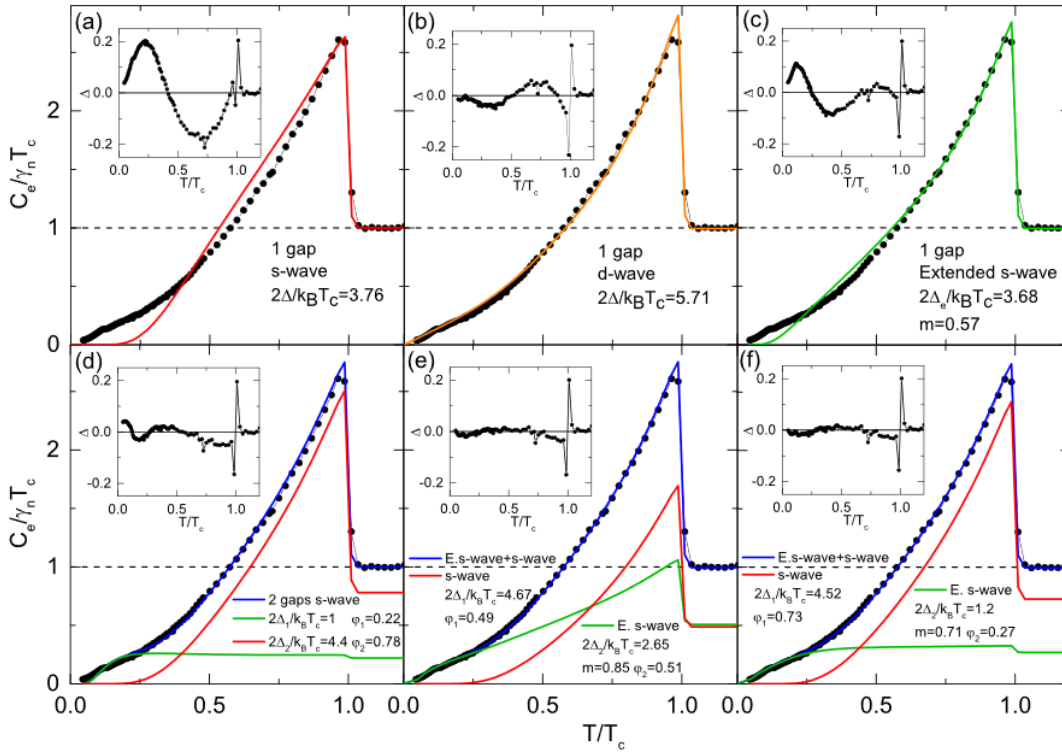
Figure 2.3: Normalized electronic specific heat fitted for the following cases: (a) s-wave, (b) d-wave, (c) extended s-wave, (d) two gaps with both isotropic s-wave, (e,f) two gaps with coexisting of s-wave and extended s-wave. Insets show the deviation between experimental data and the corresponding models. From [(114)]

2.1.7   Effect of a magnetic field

In a type II superconductors, for a higher field value than H_{c1} and smaller than H_{c2}, the magnetic flux will enter the superconductor and form vortices in it. One vortex, of a typical size of ξ^2, adds a quantum of flux, Φ_0, giving a total vortex density of $\frac{B}{\Phi_0}$. Since within the vortex cores there is still a finite density of states, this will add a contribution γ_n to the specific heat. The density of vortices being proportional to the magnetic field, the specific heat will follow a linear relation with the field :

$$C = \gamma_n \frac{B\xi^2}{T\Phi_0} = \gamma_n \frac{H}{H_{c2}} T \qquad (2.23)$$

However the vortex cores are not the only things contributing to the specific heat. In the case of nodal superconductors, only a small part of the density of states comes from the localized electrons in the vortex cores. There is a supercurrent around the vortex cores. That supercurrent leads to a shift in the energy due to its velocity, which particularly affects the nodal region at low energy. This gives another dependence of the specific heat with the field which was calculated by Volovik in [(116)],

$$C = \gamma_n \sqrt{\frac{H}{H_{c2}}} T. \qquad (2.24)$$

This expression is due to some simplifications and is only valid for a regime where $\sqrt{\frac{H}{H_{c2}}} \ll \frac{T}{T_c} \ll 1$. Thus, by looking at the field dependence of the specific heat it is possible to see if a superconductor is nodal or not. Another useful property that can be extracted from such a curve is the magnetic field, H_{c2}. This one is observed but the specific heat saturates and then recover its normal state, which has no field dependence. In the case of multigap superconductors the main effect one may observe in the field dependant specific heat is a change in the slope, since when a gap closes the density of states due to that gap will not participate in the superconducting behaviour of the specific heat and only gives a constant part. This lead for example to multigap analysis in FeSe in [(117)].

Recap on how to observe superconductivity   Let us have now a recap on how to observe superconductivity in a superconductor. The phonon contribution to the specific heat is usually quite important compared to the electron contribution at T_c. The goal here is to subtract the phonon contribution to observe only the specific heat due to the

electrons. Here we usually have two options. Since the phonons are not influenced by the superconductivity, one can make a fit of the Debye model above T_c to get the phonon contribution and then subtract it from the total specific heat. As explained before, we should always check that the assumption of being at a very small temperature compare to the Debye temperature is true.

Let us check the example of FeSe with a Debye temperature, T_D, estimated around 240K which was inferred from our data. We shall numerically calculate the exact integral in Eq. 2.8 and try to fit it with a different orders polynomials over the range of temperature that is of interest (0K-20K). Fig. 2.4 shows the distance of the fit to the theoretical curve. In Fig. 2.4a we perform a simple least squares method and we see for instance that there are some errors for all polynomial forms at low temperature when fitting from 0K to 20K. In Fig. 2.4b the fit is now weighted where we force the have a better fit at low temperature and it seems that the error is reduced the higher order the polynomial has. Still we estimate the error to be of 1 ‰for a 7th order polynomial. In the case of FeSe let us see was will induce such an error of 3 ‰which seems to be the average looking at our calculations. We estimate C/T to be around 40 mJ.mol^{-1}K^{-2} at T_c, which gives an error of 0.12 mJ.mol^{-1}K^{-2}. Considering a value of $\gamma_n = 6.5$mJ.mol^{-1}K^{-2} that induces a error of approximately 2 %.

Another way to obtain this phonon contribution is to observe the material in the normal state. This can be achieved by destroying superconductivity with high magnetic field. The resulting specific heat is a linear term due to the Sommerfeld coefficient and a T^3 term due to the phonons as well as higher orders terms. This is a way to avoid the difficulty of high order terms. Since the superconducting gap is closed due to the magnetic field, there are no more paired quasiparticles. To observe the superconducting anomaly, one can therefore subtract the specific heat in the normal state at high field from other curves where superconductivity still exists.

2.1.8 Effect of the magnetic field : Quantum Oscillations

We now have to be a bit more precise about the normal state of a superconductor. We have just presented that when the magnetic field is higher than H_{c2}, the specific heat becomes constant. This is only true when we do not take into account the Landau Levels (LL).

(a) Simple fit   **(b)** Weighted fit
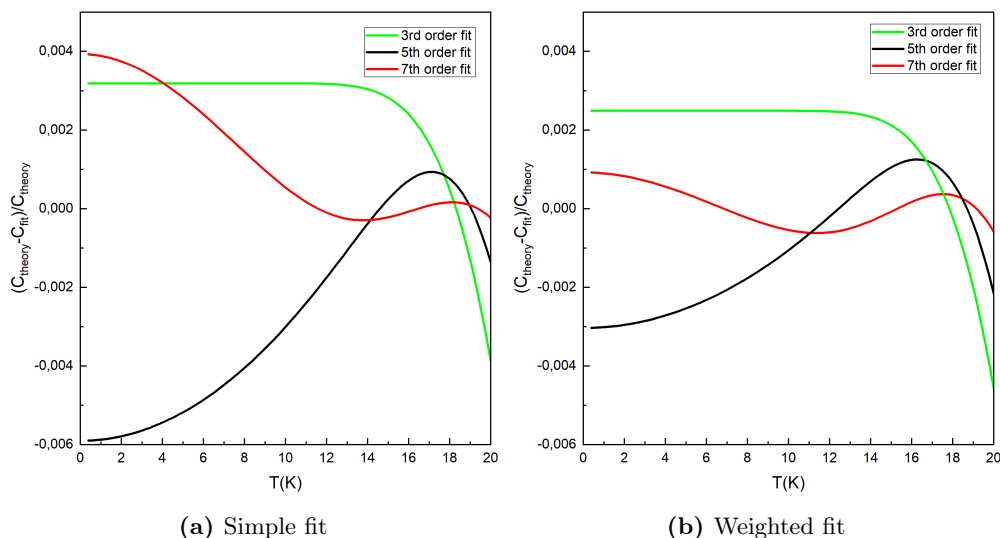
Figure 2.4: Normalized difference of the exact calculation of Eq. 2.8 and a fit of the order specified in the caption (no even terms are included in the fits). We used here a Debye temperature T_D=240K, close to the one in FeSe.

In quantum physics, submitting a charged particle to a constant magnetic field will cause the quantization of the orbit of that particle. That particle can then only occupy specific orbits with a specific energy, $E = \hbar\omega_c(n + \frac{1}{2})$, they are called Landau Levels. Each levels degeneracy is proportional to the strength of the magnetic field. This results in a saw tooth-like density of states (see Fig.2.5), due to delta functions like Landau levels crossing the Fermi Surface. Thus all thermodynamic properties increase as step function when a LL comes closer to the Fermi level. However, disorder and temperature have the tendency to smear the LL and instead of a step like functions, an oscillatory behavior emerges. For example, if the thermal energy, k_bT, becomes bigger than the spacing between levels, $\hbar\omega_c$, it might be hard to observe these oscillations. That is the reason why all measurements of quantum oscillations are made at very low temperature, close to the order of magnitude of $1K$. As we said, applying a magnetic field causes the Landau tubes to cross the Fermi surface perpendicular to the field:

$$A_F = \frac{2\pi e B}{\hbar}.$$

(2.25)

As B changes, the thermodynamic properties will oscillate with a frequency :

$$\Delta\frac{1}{B} = \frac{2\pi e}{\hbar}\frac{1}{A_F}.$$

(2.26)
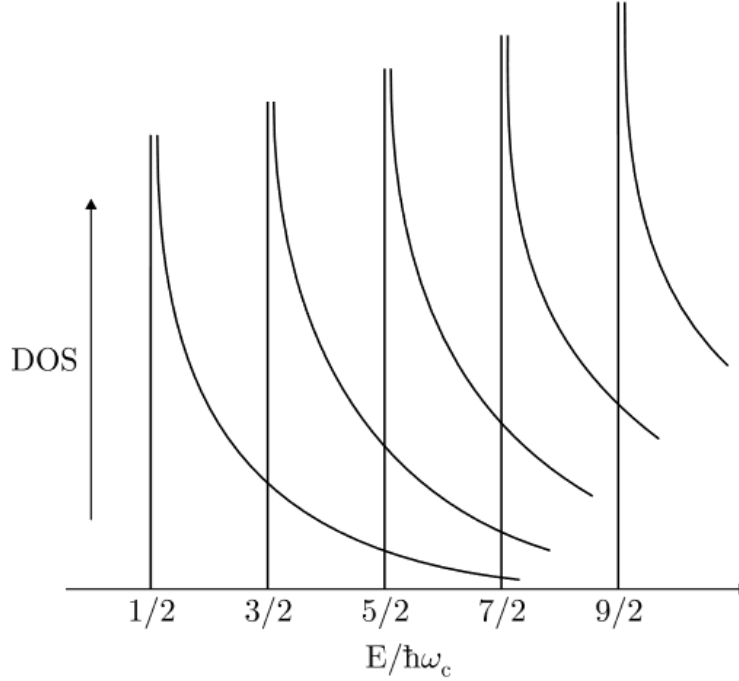
Figure 2.5: Density of states in a magnetic field.

Multiples frequencies can be observed in the case of a non-trivial Fermi surface. Some more calculations can give a more detailed theory for the oscillating part of the specific heat. The Lifshitz-Kosevitch theory, taking into account the effect of temperature, the scattering of the quasiparticles and the splitting due to the spin gives [(118)] :

$$\Delta C(T, H) = -AT \sum_{p=1}^{\infty} R_D J_0 \left(4\pi p \frac{t_w}{\hbar\omega_c} \right) \cos \left(2\pi p \left(\frac{\mu}{\hbar\omega_c} - \frac{1}{2} \right) \right) f''(x) \qquad (2.27)$$

where :

-A is a constant,

-$R_D = \exp((-2\pi^2 p k_B T_D)/(\hbar\omega_c))$ is the Dingle term,

-T_D is the Dingle temperature,

-$x = -2\pi^2 p k_B T/\hbar\omega_c$,

-$f''(x) = x((1 + \cosh^2(x))/\sinh^3(x) - 2\cosh(x)/\sinh^2(x))$,

-J_0 is a Bessel function of the first kind and

-t_w is the c-axis hopping term resulting in some small warping of the 2D Fermi surface. Here we can identify an easy way to have access to the effective mass with the quantum
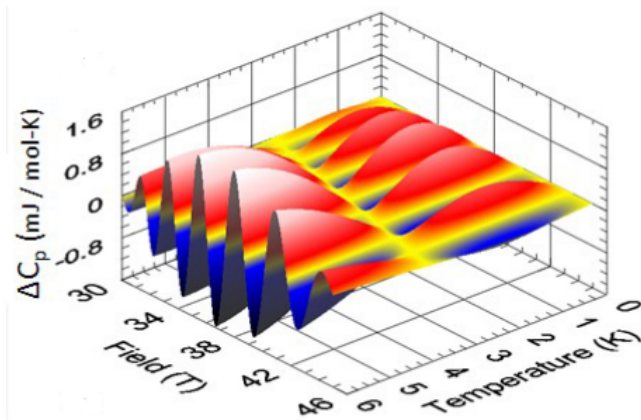
Figure 2.6: Quantum oscillations in specific heat using the Lifshitz-Kosevitch formula as a function of field and temperature. From [(118)]. The nodes in the curves allow to have a direct access to the cyclotron mass

oscillation in the specific heat. In fact when $f''(x) = 0$, close to $x = 1.6$, some nodes will be observed. This is clearly visible in Fig. 2.6 and is one of the main advantages of the quantum oscillations' specific heat measurement. Having the position of different nodes for different temperature allows to have a very good estimation of the effective mass.

2.1.9 Vortex lattice melting

The mean field theory of type II superconductors explains the formation of a vortex lattice as a result of a continuous phase transition from the normal state at H_{c2}. That was well described by Abrikosov in (11). The presence of thermal fluctuations were not taken into account in that scenario, and they can qualitatively modify the phenomenology of the vortex lattice formation. In such a scenario, H_{c2} is not clearly defined and is closer to a crossover between the normal state and a vortex liquid state. Going lower in field the vortex matter undergoes the only genuine transition : the vortex lattice melting. That first order transition corresponds to the transition between a liquid and a solid vortex state [(119)]. Therefore a sharp peak should be observable in the specific heat as illustrated in the case of YBCO in Fig. 2.7. Fig. 2.8 shows a peak in the thermal expansivity data of YBCO and a jump in the magnetization data typical of a
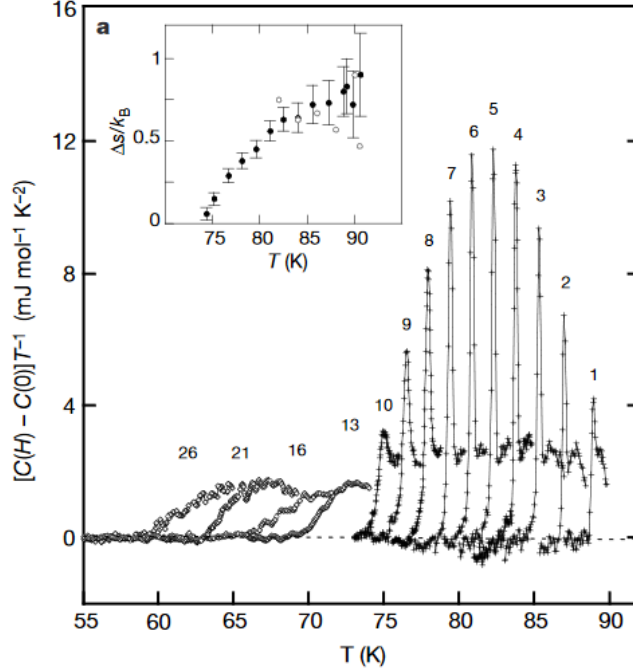
Figure 2.7: Specific heat data of YBCO showing a first order peak at the vortex lattice melting transition. From [(13)]

first order melting transition.

The extent of the vortex liquid region is mostly defined by G_i and c_L. The bigger the thermal fluctuations are, the bigger G_i is and then the wider the vortex liquid region is. In the LLL approximation (which will be introduced in the next section), at a temperature $T - T_c \approx G_i T_c$, the fluctuations contribution to the specific heat is approximately equal to the specific heat jump at the superconducting transition (cf Sec. 1.2.2).

It is possible to estimate the excess specific heat due to melting. In (122), Moler et al. explained that in a 3D vortex lattice the maximum heat capacity due to the vortex lattice melting would be of $2k_b$ per vortex. However this is only considering vortices being rigid rodes. Considering flexible vortices, one may have some degrees of freedom that would lead to an enhancement of the specific heat jump. This is for example possible in layered superconductors where it was considered in the same article, that the jump is multiplied here by the numbers of layers adding the same number of degrees
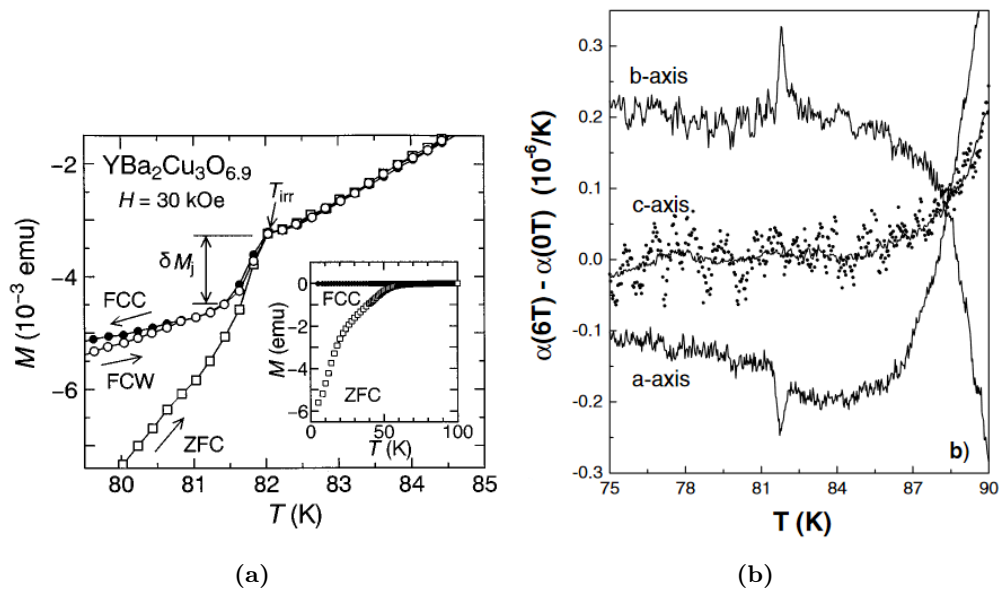
Figure 2.8: (a) Temperature dependence of the magnetization of YBCO in ZFC, FCC, and FCW processes at H=30 kOe parallel to the c axis, showing a jump just before the irreversibility line. From [(120)]. (b) Thermal expansivity of the a, b and c axes of YBCO in H=6 T applied parallel to the c-axis, showing a peak attributed to melting. From [(121)].

of freedom to the vortices. Nevertheless, it often leads to an overestimation of the value of the observed jump [(123)]. Such a behavior was observed for example in cuprates where it was found that the entropy jump associated with the vortex lattice melting was around 0.5 k_B per vortex per layer [(124),(99),(13)].

2.1.10 Scaling law

It is interesting to look at the scaling behavior of thermodynamic quantities to analyze a bit more in details the nature of the thermal fluctuations. Near the upper critical field and within the mean field theory the superconducting order parameter is given by the lowest-Landau level (LLL) wave function. In the next lines we will thus be focusing on the LLL model of fluctuations. If the field is high enough, meaning $H > G_i H'_{c2} T_c$ then the fluctuating order parameter can be approximated as a linear combination of the LLL wave functions, and the contributions of the higher levels would be treated in the Gaussian approximation. If that condition is fulfilled the broadening of the superconducting transition is well described by the dependant Ginzburg number

$G_i(H) = G_i^{1/3} \left(\frac{H}{H'_{c2}Tc} \right)^{2/3}$. In that framework, , Thouless shows in ([125]) that there is a universal scaling function of a single scaling parameter for the superconducting part $\delta C_e(H,T)$ of the specific heat divided by the mean-field superconducting heat $\delta C_m f(H,T)$:

$$a_T = r_T \frac{T - T_c(H)}{(HT)^{2/3}}, \tag{2.28}$$

where the normalized parameter r_T is defined by

$$r_T = \left(\frac{2H_{c2}'^2 T_c}{G_i} \right)^{1/3} \tag{2.29}$$

The parameter a_T measures here the shift of the temperature with respect to the mean field transition normalized by the fluctuation broadening. This approach using the Ginzburg-Laundau theory is only valid close to T_c. Li and Rosenstein gave an analytical expression in the case of the 3D scaling in [([126])] (see Eq. 119 and Eq. 127). The expression is supposed to be valid when -25<a_T<8 and includes the contribution of the vortex lattice melting.

That scaling function is valid for temperature curves, however it is also possible to have a similar approach for field dependent curves. In that case we have

$$a_H = r_H \frac{H - H_{c2}(T)}{(HT)^{2/3}}, \tag{2.30}$$

and the renormalization constant is written as

$$r_H = \left(\frac{2T_c}{G_i H'_{c2}} \right)^{1/3}. \tag{2.31}$$

Fig [2.9] shows the dependence of the scaling function found in ([126]) and the scaled data of RbEuFe$_4$As$_4$ showing very good agreement. The jump observed at $a_T = -9.5$ corresponds to the melting criterion in the LLL regime. This gives a universal scaling function for the melting that was described in ([102]). This equation does not use any perturbation theory and should therefore be exact. The only part of it using perturbation theory is the value of the constant $a_T = -9.5$. This gives therefore another way of analyzing it compare to the Lindemann criterion. Following the melting criterion of Li and Rosenstein and the mean field dependence of the superconducting parameters, Koshelev et al. [([102])] found that :

$$\frac{(1 - 0.46b_m)(1 - b_m)^{3/2}}{8\sqrt{2b_m}} = \frac{\sqrt{G_i}t}{\sqrt{1-t}}. \tag{2.32}$$
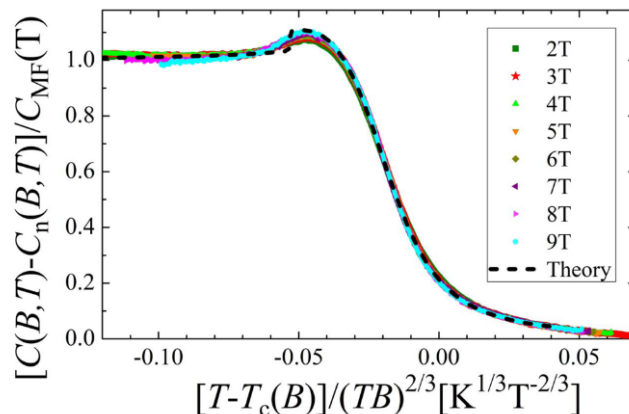
Figure 2.9: Scaling plot of the specific heat in the lowest-Landau-level regime for high magnetic fields in RbEuFe$_4$As$_4$. The black dashed line is the theoretical curve given by Li and Rosenstein in [(126)]. From [(102)]

However that expression is not valid at very low field, where the distance between the vortices is comparable to the penetration length and in the region of strong fluctuations where $1 - t < G_i$. Fig 2.10 shows a plot from the same article where four different materials are superimposed on the theoretical curve and showing good agreement with it. However one should keep in mind that in that article only orbital pair breaking is taken into account.

2.2 Techniques

2.2.1 Calorimetry

Now that we understand the specific heat is an interesting characteristic to study, we have to find a way to measure it. This is what shall be discussed in this section. Based on the heat equation, calorimetry is the measurement of temperature of a system as it undergoes a change from a well-defined initial thermondynamical state to another well-defined final thermodynamical state. The common way to change these states is through a heat generation of a well-known power. However there are several ways to do so, depending on how the sample is heated and how it is going to a final state. We will here focus on two techniques, which have been used during that PhD : the Dual Slope Method and AC calorimetry. Nevertheless, we will start by describing the most basic method as a introduction to the measurement of the specific heat: the relaxation
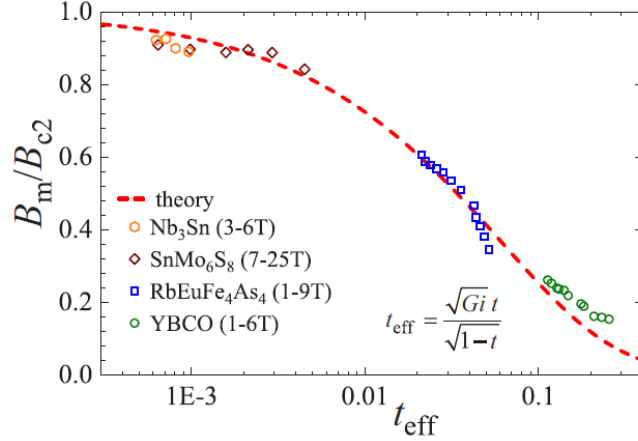
Figure 2.10: Universal plot for the vortex lattice melting transition. From [(102)]

method. In that method, the sample is heated with a power P. Power cutting causes the temperature to decay back to an initial state, through a thermal leak. The complete model can be found in Fig. 2.11. The measurement of the evolution of the temperature with time can give the specific heat of that system. This gives us a way to design a calorimeter. As one needs something to hold the sample, to heat it and to record the temperature, we will use in our experiments a sample holder, an electrical heater and a thermometer, grouped together in what we call addenda. The reason it is called as such is because it is added to the specific heat of the sample, which is not the only thing to absorb the heat generated. We will then measure a total specific heat, C_T, which is the sum of the specific heat, C_{sample} of the sample and the one of the addenda, $C_{addenda}$. Depending on the size of the sample, $C_{addenda}$ can be smaller, comparable or even bigger than C_{sample}. This is the reasons why we have to measure the specific heat without the sample first. We thus can have a good idea of the real specific heat of the sample after.

Let us supposed the easy case where we can write:

$$P = A\kappa\frac{\partial T}{\partial x} + C(T)\frac{\partial T}{\partial t}, \tag{2.33}$$

where P is the power that we put into the sample, A is the cross sectional area of the wires connected to the sample and the bath as a thermal leak and κ is the thermal conductivity, giving a thermal conductance $k = \kappa A/l$, with l the length of the wires. It
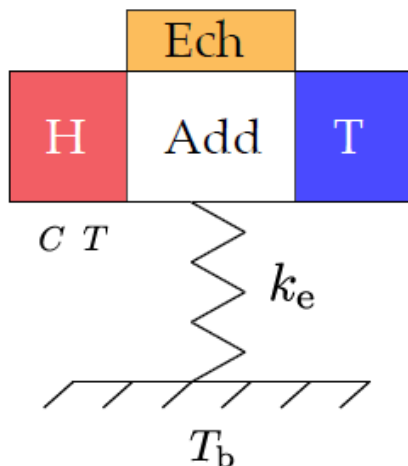
Figure 2.11: Thermal model of the simple chip allowing to determine the specific heat of a sample and the addenda. From [(109)]

gives:

$$C(T) = \frac{dT}{dt}^{-1}(P - k\Delta T), \tag{2.34}$$

and $\Delta = T - T_0$ being the rise of temperature between the initial state and the final state. Considering that the specific heat and the thermal conductivity do not vary over the temperature gap, one get an exponential decay law of the temperature to return to its initial state when the power is turned off,

$$\Delta(T)(t) = (T_1 - T_0)\exp^{\frac{-tk}{C}}. \tag{2.35}$$

Following the evolution of the temperature over time allows thus to find a time constant $\tau = C/k$, proportional to the specific heat. However we made the assumption that $C(T)$ is constant over the temperature variation, this is not always true, even more in the case of phase transition as we saw before. The phase transition will be observable but not well characterized. One should then heat the sample only of a few percent of the thermal bath. The problem is also that we need to acquire data point by point, which can be quite slow. Another problem to get the specific heat of a material here is that we need to know the thermal conductance of the wires very well, since we would only be able to have the time constant.

2.2.2 Dual Slope Method

The Dual slope method is an extension of the relaxation method. However it uses not only the heating or the cooling curve of the sample but both of them. Through the correlation of both of the curves, one of the biggest disadvantages of the relaxation method is avoid : one does not need to know the thermal conductance of the thermal leak. One can also measure in a continuous way over a wide range of temperature. Let us see how it works [(127)]. First the sample is heated by application of a power $\dot{Q}_h$ in order to reach a temperature T_1, and then the power is cut off to go back to the thermal bath temperature, exactly like in the relaxation method. It gives two equations, one for the heating and one for the cooling curve :

$$C(T)\frac{dT_h}{dt} = \dot{Q}_h(T) - \dot{Q}_0(T) + \dot{Q}_p(T) \tag{2.36}$$

$$C(T)\frac{dT_c}{dt} = -\dot{Q}_0(T) + \dot{Q}_p(T), \tag{2.37}$$

where h and c are for respectively heating and cooling, $\dot{Q}_0(T)$ is the power loss due to the thermal leak, and $\dot{Q}_p$ the parasitic stray heat of other forms like radiations. Let us now assume that the parasitic stray heat and the power loss due to the thermal leak do not vary in time over one measuring cycle, one can combine the two equations above in order to get the specific heat of the sample:

$$C(T) = \dot{Q}_h \left(\frac{dT_h}{dt} - \frac{dT_c}{dt} \right)^{-1} \tag{2.38}$$

Here there will be no problem due to variations of the specific heat during the measurement. One only need to take a small enough interval of temperature to get the slopes and then the specific heat. One need to take the same interval of temperature ΔT for both the heating and cooling curve, giving to different time interval Δt and $\Delta t'$ as illustrated in Fig. 2.12. In the limit where the interval is small enough, one get:

$$\frac{dT_h}{dt} - \frac{dT_c}{dt} = \frac{\Delta T}{\Delta t} \left(1 + \frac{\Delta t}{\Delta t'} \right) \tag{2.39}$$

The best way to be sure to observe correctly a phase transition is to adjust the rate of change of temperature so that the sample is always at thermal equilibrium.

It should also be pointed out that we supposed here no thermal link between the sample
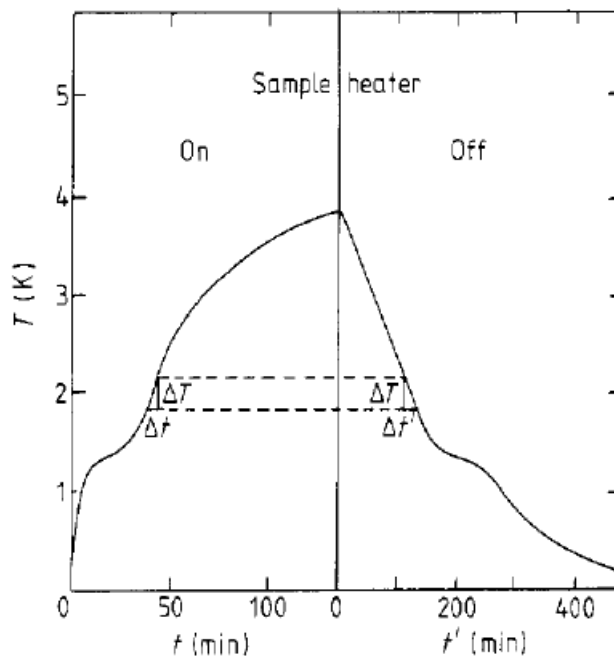
Figure 2.12: Typical measurement cycle for the dual slope method. From [[127]]

itself and the thermal bath and a perfect contact between the sample and the calorimeter. In order to achieve that the calorimeter is suspended in vacuum via wires that are used as the thermal leak we mentioned before.

Other problems can be encountered. One among these is a difference in temperature between the sample and the calorimeter. It can happen when the heat flow from the calorimeter does not only go in the sample but also in a similiar way goes to the leaks. It happens when the sample is a poor thermal conductor. To avoid that we use the same wires for the thermal leak and to provide electricity to the calorimeter. On the other side when the sample is a good thermal conductor, one of the problem might be the contact between the sample and the calorimeter. The contact might be bad if the effective surface area is too small or if the material used to contact the sample to the calorimeter is a bad conductor. To overcome that we use Apiezon grease, we heat it before putting the sample on the puck to ensure a good enough effective surface area. These effects lead to other time constant in the system and could cause some errors in the estimation of the specific heat. This is why one should always take these effects into account when dimensioning the calorimeter. However, all the calorimeters I used

during that thesis where dimensioned before I used it in order to be good enough to measure the specific heat.

2.2.3 AC Calorimetry

Ideal case In AC calorimetry the sample is not heated by a constant power but an alternative one, $P(t)$. In our experiments we use a resistive heater, to which we impose an electrical current of the form $I = I_{AC} \cos(\omega t)$, that will give an alternative power. Let us now examine first the perfect model which is also the easiest one. We will after try to see were problems could happen and their effect.

In the ideal case, the calorimeter is only made of a thermometer, a heater and a sample holder, at the same temperature, and the sample is perfectly coupled to the sample holder. All of these elements are connected to a thermal bath via a wires, which only have a thermal conductance, k_e. It is exactly the same model as we used to describe the relaxation method and dual slope method. As we said the heater is supplied by an electrical current $I = I_{AC} \cos(\omega t)$. This will give a power:

$$P_H(t) = R_H(I_{AC} \cos(\omega t))^2 = P_{AC}(1 + \cos(2\omega t)) \tag{2.40}$$

On the other side we also need to read the temperature with the thermometer. This one need to be also supplied by an electrical current and it does not need to be alternative. It will give a power, P_{DC}, to the calorimeter. So now we can write the same equation as in the relaxation method case but in AC:

$$C\frac{dT}{dt} = P_H(t) + P_T + k_e(T_b - T). \tag{2.41}$$

It is now possible to solve the equation 2.41 to get the continuous and alternative part of the temperature.

$$T_{AC} = \frac{P_{AC}}{k_e + 2i\omega C} \tag{2.42}$$

$$T_{DC} = T_b + \frac{P_{AC} + P_{DC}}{k_e} \tag{2.43}$$

Using the AC part of the temperature it is now possible to get the specific heat, even without knowing k_e. In fact the amplitude and the phase of the AC part is described by:

$$|T_{AC}| = \frac{P_{AC}}{\sqrt{k_e^2 + 4\omega^2 C^2}} \tag{2.44}$$
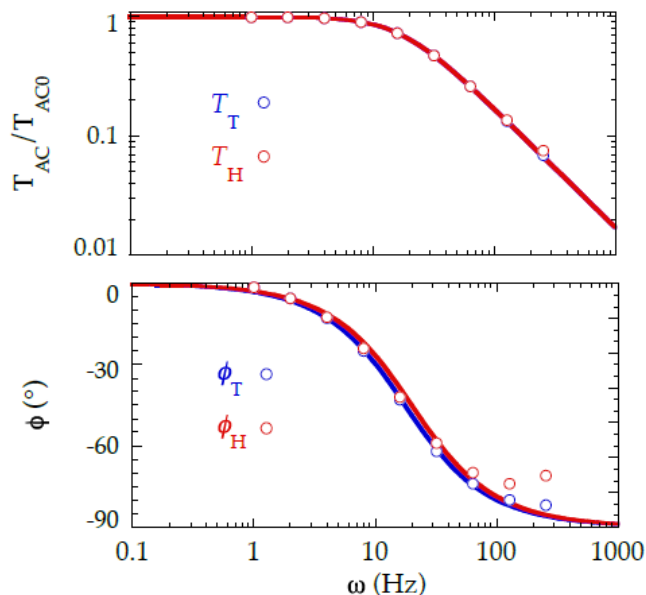
Figure 2.13: Normalized amplitude and phase of the temperature oscillations as a function of the frequency. The blue curve represents the thermometer and the red one the heater. The dots are data obtained at 2K and the lines are the fitted model we used before. This shows a good agreement with the ideal model at this temperature, where we observe no difference in the behaviour of the thermometer and the heater. In the next section, the question of the resolution will addressed and will give an indication about the best frequency to use. It will be seen that the phase shall be around 45° in order to have the best resolution, giving a frequency of the order of 10 Hz. From [(109)]

$$\phi = -\arctan \frac{2\omega C}{k_e} \tag{2.45}$$

If we can now measure the temperature oscillations and the alternative part of the power, it possible to get the heat capacity of the sample and the thermal conductance of the wires at the same time.

$$C = \frac{P_{AC}}{|T_{AC}|} \frac{|sin(\phi)|}{2\omega} \tag{2.46}$$

$$k_e = \frac{P_{AC}}{|T_{AC}|} \cos(\phi) \tag{2.47}$$

The main advantage of the AC calorimetry is a much higher signal to noise ratio compare to the other techniques. We need indeed a lock in amplifier to observe to

variation of temperature. This one allows to reduce the noise. The AC technique is also very good in terms of resolution, with typically in our setup a resolution of 10^{-4}

Here unlike the case of the dual slope method, we supposed that the specific heat does not vary when we change the temperature. To achieve that we will only use oscillations of the temperature that are of the order of few percent of the bath temperature. However it is possible to change the temperature of the bath in order to perform a continuous measurement over a wider range compare to the dual slope method. We might also encounter the same problems that we talked about in the section concerning the dual slope method. We will now investigate a bit more on that topic.

Thermal decoupling of the sample   We will first consider the case where the sample, with a heat capacity C_S, is not perfectly coupled to the sample holder, with a thermal conductance k_s. The sample holder with a heat capacity C_0 is still connected to the thermal bath via a thermal conductance k_e as illustrated in Fig. 2.14. In order to conserve the energy of the system one gets a system of two equations :

$$C_0 \frac{dT_0}{dt} = P_H(t) + P_T + k_e(T_b - T) + k_s(T_s - T_0), \tag{2.48}$$

$$C_s \frac{dT_s}{dt} = -k_s(T_s - T_0). \tag{2.49}$$

One can define here two time constants : $\tau_e = C/k_e$, C being the sum of the heat capacity of the addenda and the sample, and $\tau_s = C_s/k_s$. The first time constant is characteristic of the thermal relaxation of the entire system with the thermal bath. The second one gives to time needed for the sample to be at the same temperature as the platform. In the end it gives temperature oscillations on the sample holder (i.e. where we measure the temperature) with the same form as in the case where the sample and the platform are perfectly coupled.

$$|T_{AC,0}| = \frac{P_{AC}}{\sqrt{k_{eff}^2 + 4\omega^2 C_{eff}^2}} \tag{2.50}$$

$$\phi = -\arctan \frac{2\omega C_{eff}}{k_{eff}} \tag{2.51}$$

with $C_{eff} = C_0 + (1-g)C_s$ and $k_{eff} = k_e + gk_s$, where $g = \frac{(\omega\tau_s)^2}{1+(\omega\tau_s)^2}$. The effective heat capacity will be only the one of the addenda at high frequency as illustrated in Fig. 2.14b. The oscillations do not have the time to go in the sample, their amplitude will decrease sharply and it causes the resolution the be lower. However at low frequency it is possible to measure the total heat capacity. The main think we should care about here in the end is that $\omega\tau_i < 1$. On the other hand going at very low frequency will give $T_{AC,0} = P_{AC}/k_e$ and $\phi = -\arctan\omega\tau_e$, which gives no information about the heat capacity of the system. In fact, in these conditions, the sample holder will directly relax to the thermal bath. In the end we will measure the total heat capacity such that :

$$C = \frac{P_{AC}}{2\omega T_{AC,0}} \frac{\tau_e}{\tau_e + \tau_s} (\sin(\phi) + \omega\tau_s \cos(\phi)) \tag{2.52}$$

If the conditions are considered to be good then τ_i can be neglect, and one finds again the same as for the perfect case. Let us consider that simple case to learn a bit more on the resolution of the AC calorimetry. If we consider the phase resolution to be $\Delta\phi = \Delta T_{AC,0}/T_{AC,0}$, the specific heat resolution can be written as :

$$\frac{\Delta C}{C} = \frac{\Delta T_{AC,0}}{T_{AC,0}} \left(1 + \frac{1}{\tan(\phi)}\right) \tag{2.53}$$

That resolution is minimized for $\phi = 45°$. It means that the imaginary part and the real part of the signal have to be equal. Experimentally we are always trying to use a frequency to supply the heater such that the phase shift is always close to $45°$.

Thermal decoupling of the heater and thermometer It is also possible that the thermometer and the heater might be decoupled of the calorimeter itself. In order to illustrate that let us assume that the thermometer and the heater are connected to the calorimeter via a thermal conductance k_i as shown in Fig. 2.15a. One gets for such a system, three equations, one for the calorimeter itself, one for the thermometer and one for the heater :

$$C\frac{dT}{dt} = k_e(T_b - T) + k_i(T_H - T) + k_i(T_T - T), \tag{2.54}$$

$$P_H(t) = k_i(T_H - T), \tag{2.55}$$

(a)

(b)
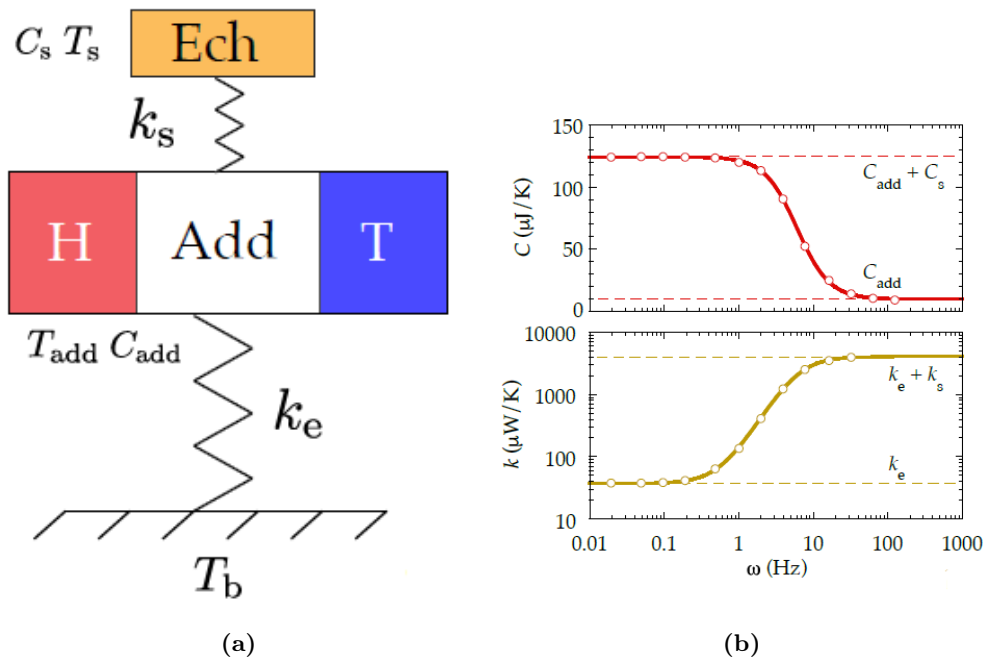
Figure 2.14: (a)Thermal model with a thermal decoupling of the sample. (b) Measured heat capacity and thermal leak as a function of the frequency when the sample is badly coupled to the calorimeter and fitted curves using the model above. From [(109)]

$$P_T = k_i(T_T - T). \tag{2.56}$$

Solving these equations gives the temperature on the side of the thermometer :

$$T_{AC}^T = \frac{P_{AC}}{k_e + 2i\omega C}, \tag{2.57}$$

$$T_{DC}^T = T_b + \frac{P_{AC} + P_{DC}}{k_e} + \frac{P_{DC}}{k_i}. \tag{2.58}$$

Basically what we found here is almost the same result as Eq. 2.42 and Eq. 2.43 except that the average temperature is shifted by a term P_{DC}/k_i. That means that it is still possible to get the right value of the heat capacity but the temperature we measure is not the one of the sample. The more P_{DC} is high and the less k_i is small, the bigger that error will be. And one finds the same result as in the perfect case when k_i is infinite. In order to have an idea of the value of k_i, one can record the temperature on the heater side. That gives :

$$T_{AC}^H = \frac{P_{AC}}{k_e + 2i\omega C} + \frac{P_{AC}}{k_i}, \tag{2.59}$$

$$T_{DC}^H = T_b + \frac{P_{AC} + P_{DC}}{k_e} + \frac{P_{AC}}{k_i}. \tag{2.60}$$

This time, one can not determine the right value of the heat capacity from the data recorded on the heater side. In fact the temperature oscillations have an additional term P_{AC}/k_i which makes oscillations bigger and therefore overestimates the value of the heat capacity. Looking at the continuous term, the temperature is also shifted by the same term, and we have the same problem as on the thermometer side. However taking a closer look at Eq. 2.58 and Eq. 2.60 and combining them, one can have a better idea of the value of k_i and compare it to k_e in order to check if the thermalisation is bad or good. Most of the time such a phenomenon occurs at low temperature as illustrated in Fig. 2.15b.
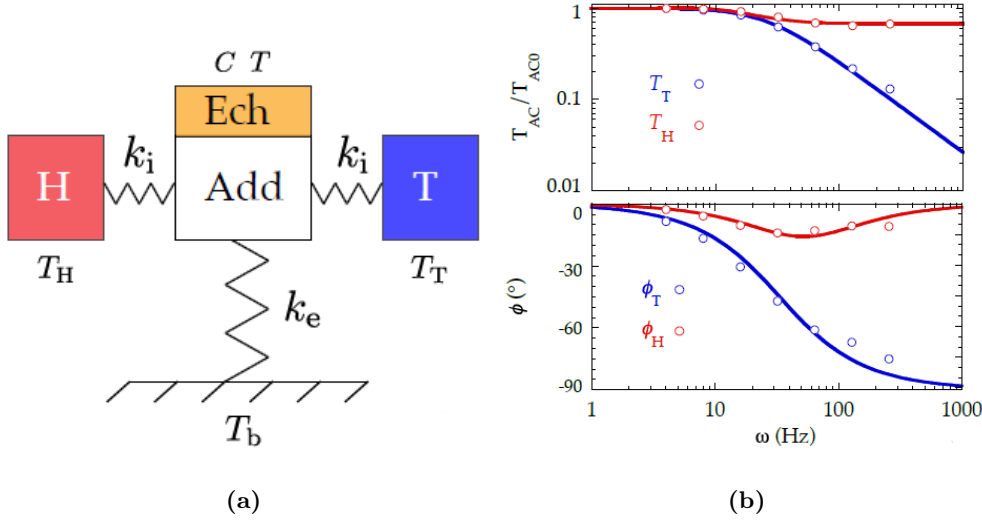
Figure 2.15: (a)Thermal model with a thermal decoupling of the thermometer and the heater. (b)Normalized amplitude and phase of the temperature oscillations as a function of the frequency. The blue curve represents the thermometer and the red one the heater. The dots are data obtained at 0.35K and the lines the fitted model we used before. Here the behaviour of the thermometer and heater are very different showing clearly that they are badly coupled. From [[109]]

2.2.4 A closer look at the experiments

We have now a better understanding of the different ways to measure heat capacity and some troubles we could encounter, let us take a closer look at the experiments. We will only focus on the Dual Slope Method used with the PPMS and the AC Calorimetry set up we used in Grenoble.

2.2.4.1 AC Calorimetry

How does it look like? The central part of the calorimeter is a small resistive chip, normally used as a thermometer, that we split into two parts, in order to have a thermometer and a heater. Since the resistance varies with temperature, we can use it as a thermometer. The chip is originally a Cernox, made of a sapphire substrate which has a layer of zirconium oxynitride on top, which is itself covered with an insulating layer. The resistive part is connected to gold contacts. They will be used later to connect the chip to the rest of the system.

The total resistance of the Cernox is of approximately 500 Ω, when splitted in two, we

Figure 2.16: Sketch of the different part of the calorimeter and their correspondence with the different thermal models. The sample in black is mounted on the Cernox in light gray, with some grease in blue. The thermometer in dark blue and the heater in red are connected to the Cernox via a thermal leak k_i. The chip is connected to the copper ring through wire with a thermal leak k_e. From [(109)]

usually have a resistance of approximately 230 Ω and another one of 270Ω. The later is usually used as a thermometer so as to have a better signal to get the heat capacity. In order to assure electrical but also thermal contact with the rest of the system, four metal wires are connected to the chip. The other side of the wires is connected to a copper ring in order to suspend to chip in its middle and avoid any unwanted contact, that might lead to shortcuts or thermal leaks. From there we have a four-contact measurement of the Resistance of the thermometer and the heater that will later be connected to the electronic part of the system. The sample is then mounted on the other side of the chip, and sticks to it thanks to a small amount of grease. Fig. 2.16 illustrate the description we made of the calorimeter and the correspondence with the different part of the thermal models we used before.

In order to avoid a thermal decoupling between the sample and the calorimeter, we have to pay attention on the amount of grease we use. When there is too few or when the contact surface between the sample, the grease and the chip is too small, one can have some problems like we described it before in Sec. 2.2.3. In order to avoid that one can use a heater gun to flatten to surface area of the grease and assure better contact, and therefore have a higher value of k_s. Looking at the internal thermal leak k_i it is way harder to adjust this value. It is an intrinsic property of the chip and one can only check its value at different temperature in order to correct the shift of temperature we

talked about in Sec. 2.2.3.

How to get the heat capacity ? Since we described the thermal models and the calorimeter, we now have to focus on how to get the heat capacity of our samples. From our different thermal models we know that we need to know the power input in the system and to record the time dependence of the temperature on the thermometer side in order to get the average temperature and the temperature oscillations. Recording the temperature on the heater side is also a good idea, so that we can have a better idea if we are in the case of an ideal model or not. Here we can already see a major problem, that is really time consuming: we need to know how to relate the resistance to the temperature precisely. In order to reduce the error we make on reading the temperature we need very precise calibration, and even if we can read very precisely temperature variation it is always hard to get the absolute temperature. Another problem on that side is the magnetoresistance of the chip. Therefore the calibration also needs to be done in high fields to limit the error. We will not focus on that part of the set-up here, since most of the calibrations we used during this thesis were done before it started. If the reader wants more information, he can refer to the thesis of Clément Girod [(109)] and Bastien Michon [(128)].

The calibration being done, we can now focus on how to read the resistance in order to get the information we need. When the system is heated with a power P_{AC}, the temperature will oscillate with an amplitude T_{AC} around the average temperature T_{DC}. If the oscillations are small enough (of the order of few percents of the average temperature), one can use a linear response approximation and write :

$$R(T) = R(T_{DC}) + \frac{dR}{dT}\bigg|_{T_{DC}} T_{AC} e^{2i\omega t}. \tag{2.61}$$

From that equation one sees that measuring the average resistance gives the average temperature, and measuring the oscillations of the resistance gives the temperature oscillations.

Determination of the average temperature T_{DC} In order to get the average temperature on the heater and thermometer side, we use two small amplitudes alternative currents i_T and i_H with different frequencies, ω_T and ω_H, compare to ω (typically over 100 Hz), such that their amplitudes will be very small compare to the one of I_{AC} and

will not influence the diagrams (Fig. 2.13, Fig. 2.14b and Fig. 2.15b) obtained earlier. In the end we have

$$I_T = I_{DC} + i_T e^{i\omega_T t}, \tag{2.62}$$

$$I_H = I_{AC} e^{i\omega t} + i_H e^{i\omega_H t}. \tag{2.63}$$

One has then to measure the voltage at ω_T and ω_H

$$V_{\omega_{H,T}} = R_{H,T}(T_{DC_{H,T}}) i_{H,T} \cos{(i\omega_{H,T} t)}. \tag{2.64}$$

From that one can get the resistance and therefore the average temperature.

Determination of the temperature oscillations T_{AC}   Since we now have the average temperature and also the calibrations of the chip, we can get the derivative $\frac{dR}{dT}\big|_{T_{DC}}$ on both sides of the chip and therefore, based on Eq. 2.61, also get the temperature oscillations. The voltage V_T due to I_{DC} in the thermometer is :

$$V_T = \left[R_T(T_{DC}) + \frac{dR_T}{dT}\bigg|_{T_{DC}} |T_{AC}| \cos{(2\omega t + \phi_T)} \right] I_{DC}, \tag{2.65}$$

$$V_T = R_T(T_{DC})I_{DC} + \frac{dR_T}{dT}\bigg|_{T_{DC}} |T_{AC}| \cos{(2\omega t + \phi_T)} I_{DC}, \tag{2.66}$$

$$V_T = V_{DC} + V_{2\omega} \cos{(2\omega t + \phi_T)}. \tag{2.67}$$

V_{DC} is filtered and only contains information about the average temperature, but the $V_{2\omega}$ signal gives us information about the phase and the amplitudes of the oscillations which is exactly what we need to determine the heat capacity of the sample.

On the heater side we have almost the same but with an alternative current:

$$V_H = \left[R_H(T_{DC}) + \frac{dR_H}{dT}\bigg|_{T_{DC}} |T_{AC}| \cos{(2\omega t + \phi_H)} \right] I_{AC} \cos{\omega t}, \tag{2.68}$$

$$V_H = R_H(T_{DC})I_{AC} \cos{(\omega t)} + \frac{dR_H}{dT}\bigg|_{T_{DC}} |T_{AC}| \frac{I_{AC}}{2} (\cos{(3\omega t + \phi_H)} + \cos{(\omega t + \phi_H)}), \tag{2.69}$$

$$V_H = V_\omega \cos{(\omega t + \phi_H)} + V_{3\omega} \cos{(3\omega t + \phi_H)}. \tag{2.70}$$

The only important part of the voltage here is the $V_{3\omega}$ signal which is giving the temperature oscillations of the heater.

Determination of the power P_{AC} The power due to the resistance of the heater with a current I_{AC} is:

$$P_H = \left[R_H(T_{DC}) + \frac{dR_H}{dT}\bigg|_{T_{DC}} |T_{AC}| \cos\left(2\omega t + \phi_H\right) \right] \left(I_{AC} \cos\left(\omega t\right)\right)^2. \qquad (2.71)$$

Ignoring the derivative therm in the resistance gives then the power :

$$P_H = \frac{I_{AC}^2}{2} R_H(T_{DC})(1 + \cos\left(2\omega t\right)) = P_{AC}(1 + \cos\left(2\omega t\right)). \qquad (2.72)$$

The derivative in the resistance gives another non-linear term due to the temperature oscillations. In order to reduce this term, we need to have small oscillations compared to the average temperature. Usually that ratio is around 5%. The worst case scenario happens at low temperature where such a term can be about several percents of the total power. Since we do not take this effect into account the heat capacity can be overestimated.

We now have an idea about how to get the different parameters that will help us to know the heat capacity. We should now check on the electronics that will measure the temperature on the heater and thermometer side and also generate the excitation power.

Measurements protocol   In the end you will find the protocol we use for our experiments. The goal of the protocol is mainly to check if we have good conditions for the measurement, i.e good thermal coupling.

1-Set up the bath temperature for the measurements and put to maximal value of i_H and i_T so that they are not heating the thermometer or heater, in order to have the best signal to noise ratio. We can also set up gains in our program so that the thermometer, heater and main thermometer have the same temperature.

2-Set up the value of I_{AC} and I_{DC} so that the temperature oscillations are less then 10% of the average temperature and that the voltages of $V_{2\omega}$ and $V_{3\omega}$ are in between one and ten millivolts.

3-Change the frequency of the measurements at the same temperature while checking on the behavior of the temperature oscillations, the value of the heat capacity and the values of k_e and k_i, in order to check if we can apply a simple thermal model. In such a case, one chooses the frequency such that the phase is 45°. If C is changing while

the frequency changes, then the sample is badly coupled to the calorimeter and one has two solutions : either to remount the sample or to lower the frequency so that the heat capacity remains constant. If the oscillations of the heater and the one of the thermometer are different, it means that the thermometer and the heater are badly coupled to the calorimeter and then one should lower I_{DC} so that the temperature of the thermometer reamains close to the one of the sample.

4-Check on step 3 for different temperatures over the measurements and if the parameters are not good enough for all of them then program a law as a function of temperature so that the parameters will be good for the entire run. After that one can start the measurement.

Measurements with a rotator   During this thesis, one of the main problems we wanted to focus on is a possible FFLO phase. Since such a phase is very sensitive to the angular position of the sample compared to the field, we decided to mount a rotator on our measurement cane. We had several options but given our opportunities we decided to go for an electrical rotator. Some minor modifications were made in order the calorimeter to fit in the cane. The rotator we used as a resistive angle reader. However, that part of the rotator broke and we decided to go for another technique of measurement of the angle. Also, since we wanted to measure the angle between the sample and the magnetic field such a method was not precise enough for us. Instead, we decided to measure the angle with a Hall probe. Hall probes have different sensitivity to the angle and the Hall voltage can be written as $V_{Hall} = V_0 \cos\theta + V_{offset}$, where θ is the angle between the field and the vector perpendicular to the probe. The Hall probe was positioned in order to have to best sensitivity such that we will look at angles close to $\theta = 90^o$. In our case we found out that we can measure an angle difference of approximately 0.1^o. However we still have a problem in our measurement. Since the sample if fixed on the sample holder with grease (giving already difference of angle between the sample and the sample holder) and the Hall probe is not fixed directly on the sample holder, the angle we measure between the magnetic field and the Hall probe is not exactly the same as the one between the magnetic field and the sample. In order to correct that we decided to use the superconducting properties of our samples to find out the angle difference between the Hall probe and the sample. In the following we

give a protocol for the best alignment we can achieve with our system.

1-First apply the same protocol as in the normal case.

2-Apply a small field and set up a temperature sweep close to T_c for different angles and measure the heat capacity of the sample.

3-Compare the superconducting anomaly of the sample for different angles. T_c should shift with the angle and being at its maximum when the field is along the c-axis or at its minimum when the field is along the ab-axis. 4-Note the angle measured when T_c is at its maximum or minimum, this one is when the sample is aligned. The value we noted is the angle difference between the sample and the Hall probe.

In our experiments, the angle between the sample and the Hall probe was typically of the order of 1%.

2.2.4.2 PPMS

The PPMS Dual slope technique uses basically the same element for the calorimeter as the AC technique. One can see in the following a quote from the PPMS specific heat manual:

As with other techniques for measuring heat capacity, the Quantum Design Heat Capacity option controls the heat added to and removed from a sample while monitoring the resulting change in temperature. During a measurement, a known amount of heat is applied at constant power for a fixed time, and then this heating period is followed by a cooling period of the same duration. A platform heater and platform thermometer are attached to the bottom side of the sample platform. Small wires provide the electrical connection to the platform heater and platform thermometer and also provide the thermal connection and structural support for the platform. The sample is mounted to the platform by using a thin layer of grease, which provides the required thermal contact to the platform. The integrated vacuum system in the cryostat provides a sufficient vacuum so that the thermal conductance between the sample platform and the thermal bath (puck) is totally dominated by the conductance of the wires. This gives a reproducible heat link to the bath with a corresponding time constant large enough to allow both the platform and sample to achieve sufficient thermal equilibrium during the measurement. The description of the puck is very close to the one we use for the AC technique. The main difference is the method used to extract the heat capacity of the sample.

2.2.5   Comparison of PPMS and AC Calorimeter

In the end we want to give here a comparison of the two different technique we used in this thesis. First, one should specify that the PPMS is much faster to measure a sample. The cooling of the sample can be achieved in a time scale of an hour. When we compare it to the cooling time of the AC calorimeter, this last one needs more than 12 hours. The PPMS also takes less time to measure over a temperature range in average but looses some resolution. The main advantage of the AC calorimeter lies in its resolution and the small sample size. Also it is possible to use our system at the LNCMI Grenoble to achieve field of 36T.

	PPMS	AC Calorimeter
Sample mass (mg)	1-200	0.1-1
Temperature range (K)	0.3-400	0.6-15
Magnetic field range (T)	0-14	0-36
Resolution (%)	1	0.1
Accuracy (%)	1-5	5

Table 2.1: Comparison of the PPMS and the AC Calorimeter

2.3   Specific heat : motivations

English version   The heat capacity gives lots of information about the lattice, electronic and magnetic properties of a material. Since at low temperature, it is a direct probe of energy levels, one can easily compare theories and data in order to have a better understanding of a material. Specific heat is also very sensitive to phase transitions. Another interesting property of the specific heat is the fact that it is a bulk probe, and will be sensitive to everything that is happening in the material and not just to some surface effects.

Since we want to focus on the phase diagram of FeSe, having such a probe would be very useful, particulary looking at the phase transitions. FeSe might be the host of some complex phenomena like a FFLO phase and different states of the vortex matter. Specific heat is sensible to all of these phenomena. At the vortex lattice melting transition, it should be marked at least by an excess of specific heat compare to a standard behaviour without any melting. A scaling theory was developed by Li and Rosenstein

allowing to extract the value of $H_{c2}(T)$ directly from specific heat measurements, also taking into account the vortex lattice melting. Since we want to focus on the properties of the $H - T$ phase diagram, particularly at the dependence of the upper critical field and the melting line, specific heat turns out to be a strong asset.

Two different set-ups are already present in Grenoble and Karlsruhe in order to measure specific heat. The PPMS in Karlsruhe uses the the Dual Slope Method and gives access to field up to 14T. In Grenoble an alternative calorimeter was developed with high resolution. It is also possible to use it in high magnetic field facilities and is therefore very useful to have the full $H - T$ phase diagram of $FeSe_{1-x}S_x$ in both directions. A rotator was also mounted on that set-up during my thesis which might an added value to look for a FFLO phase. All of these reasons make us believe that specific heat is a perfect tool to accomplish our work.

Version française La capacité thermique est une sonde très utile dans le sens où elle peut donner beaucoup d'informations sur les propriétés électroniques et magnétiques et celle du réseau cristallin d'un matériau. A basse température, elle est une sonde directe des niveaux d'énergie et peut donc être facilement comparée aux théories, alors que d'autres techniques comme la résistivité ont plus de mal à être directement liées à une théorie. La chaleur spécifique est également très sensible aux transitions de phase. Une autre propriété intéressante de la chaleur spécifique est le fait qu'il s'agit d'une sonde globale, qui sera sensible à tout ce qui se passe dans le matériau et pas seulement à certains effets de surface.

Comme nous voulons nous concentrer sur le diagramme de phase de FeSe, disposer d'une telle sonde serait très utile, en particulier pour étudier les transitions de phase. FeSe pourrait être l'hôte de certains phénomènes complexes comme une phase FFLO et différents états de la matière vortex. La chaleur spécifique est sensible à tous ces phénomènes. La transition de fusion du réseau de vortex devrait être marquée au moins par un excès de chaleur spécifique par rapport à un comportement standard sans aucune fusion. Une théorie de loi d'échelle a été développée par Li et Rosenstein permettant d'extraire la valeur de $H_{c2}(T)$ directement à partir des mesures de chaleur spécifique, en prenant également en compte la fusion du réseau de vortex. Comme nous voulons nous concentrer sur les propriétés du diagramme de phase $H - T$, en particulier sur la dépendance du champ critique supérieur et de la ligne de fusion, la chaleur spécifique

s'avère être un atout important.

Deux installations différentes sont déjà présentes à Grenoble et à Karlsruhe afin de mesurer la chaleur spécifique. Le PPMS de Karlsruhe utilise la méthode de la double pente et donne accès à des champs allant jusqu'à 14T. A Grenoble, un calorimètre alternatif à haute résolution a été développé. Il est également possible de l'utiliser dans des installations à haut champ magnétique et il est donc très utile pour tracer le diagramme de phase $H - T$ complet de $FeSe_{1-x}S_x$ dans les deux directions. Un rotateur a également été monté sur ce calorimètre pendant ma thèse, ce qui pourrait constituer une valeur ajoutée pour la recherche d'une phase FFLO. Toutes ces raisons nous font croire que la chaleur spécifique est une arme de choix pour accomplir notre travail.

3

Vortex lattice melting and upper critical field in FeSe$_{1-x}$S$_x$

3.1 Samples

Sample growth The samples used during this thesis were grown both at the Karlsruhe Institute of Technology and Néel Institut in Grenoble. I had the chance to assist some crystal growth. The techniques used in both places are mainly the same. We will discuss that in the following section.

FeSe consists of conducting layers of corner-sharing FeSe$_4$ tetrahedra stacked along the c-axis. We can distinguish two main phases of FeSe: the α-phase, which has an hexagonal NiAs type crystal structure; and the β-phase with a tetragonal PbO-type crystal structure. The stoichiometric α-FeSe is non-superconducting, but a small excess of Fe stabilizes the phase of β-Fe$_{1+\delta}$Se($\delta = 0.01 - 0.03$) which becomes superconducting. It is possible to substitute the selenium by some tellurium or sulfur. The second option was done in the time of the thesis. The method stays the same. It is quite hard to grow the superconducting phase of FeSe because of the narrow range of iron content where it can grow. Fig 3.1 shows a part of the binary phase diagram used to make the samples.

For an easier reading the complete binary phase diagram is not shown but it should be notified that the solidus is way above the β-phase, which makes it even harder to synthesize. Most of the time, the crystal growth from the melt results then in the hexagonal phase. Usually some iron is added to avoid the stoichiometric phase, but it
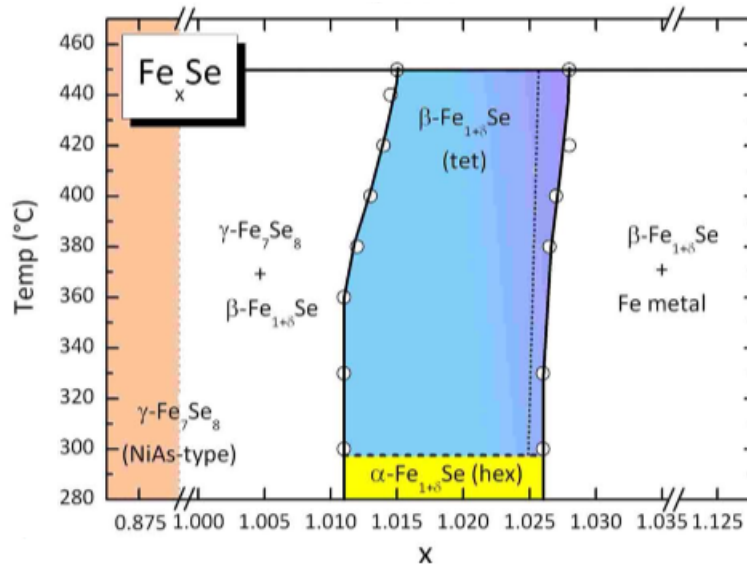
Figure 3.1: Binary phase diagram for Fe-Se. From ([63])

usually results in platelet of hexagonal symmetry which contains the β-phase but also a magnetic Fe$_7$Se$_8$ phase. A new technic was developed [([129])] were the sample results in a vapor-grown β-phase single-crystalline. Fe and Se powders are now mixed with a bit higher ratio of Fe (typically 1.1:1) together with a eutectic mixture of KCl and AlCl$_3$ (ratio 1:2) in a silica ampoule. Then that ampoule is placed in a oven and slowly warmed up. A temperature gradient is applied on the ampoule so that samples can directly form on the cold hand. Several temperature profile have been used, the first one used in Karlsruhe for example in 2013 was a cold end at 240°C, while the hot end is at 390°C. Some experiments also used a tilted oven or pellets of the mixture, positioned in diverse places of the ampoule.

Characterization on the samples The rest of the manuscript will be separated in two main parts, the study of pure FeSe and the study on the doped samples of FeSe$_{1-x}$S$_x$. We want here to give some characteristics of the different samples in zero field. In the rest of the manuscript, we will take as convention that $\mu_0 H = H$ and therefore H will be measured in Teslas. The specific heat of all measured samples is displayed in Fig. 3.2a, and the resistivity of some of them in Fig. 3.2b.

Looking at the temperature dependence of the specific heat one sees a clear discontinuity

in all samples, which is due to the fact that the sample undergoes a superconducting transition.Taking the value of T_c at 50% of the specific heat jump, FeSe shows clearly a smaller T_c of 8.9K compared to the doped samples. All other samples come from the same batch, named AAH55. This batch seems to be quite homogeneous by looking at the superconducting transition, showing approximately the same T_c around 10.4K. The dependence of the specific heat is also quite identical for all samples, only the AAH55m1 samples shows a strange feature of unknown origin at 7.5K which is not observable in other samples. Since that feature was only found in that sample, we decided to focus on other samples for the rest of the analysis. The transition is not abrupt as it should be in a perfect scenario and shows a width of approximately 0.8K for all samples, except the AAH55n6 sample that has a wider transition, extending over 1K. It should be notified that the curve presented here for that sample was obtained by averaging two data sets of two different measurements. Since the reproducibility of the measurements is not perfect it must lead to that slightly wider transition. The width of the transition was assigned to the presence of nematic domains within the sample [(84)]. Such a width will lead to some uncertainties during the next analysis. Since we will for example focus on the upper critical field, an error of $\Delta T/T_c \approx 10\%$, will lead to an error in $\Delta H_{c2}/H_{c2}$ of approximately 20% at zero temperature since H_{c2} varies like T_c^2.

The resistivity of AAH55n2 has been measured with a lock-in amplifier at 10 Hz and using a current of 0.05mA. AAH55n4 has been measured with a PPMS setup with a frequency of 6Hz and a current of 1mA. The resistivity plot (Fig. 3.2 shows two features. First at low temperature the superconducting transition at T_c and at higher temperature the nematic transition at T_s. Taking the zero resistivity as the criterion for T_c, it leads to a superconducting transition at approximately 10.4K in the dopes samples, which matches very well the temperature measured with specific heat. T_s is taken as the intersection of the two slopes before and after the transition. It gives for the AAH55n2 sample T_s =87K and for the AAH55n6 sample T_s =62K. Such a difference can be well understood by looking at the phase diagram of FeSe$_{1-x}$S$_x$ (see Fig. 1.18), where a small change in the doping x can lead to a big difference in the nematic transition temperature. If the batch is not perfectly homogeneous one can see such a difference. One should also note that the nematic transition for the AAH55n2 sample is wider compared to the AAH55n6 sample, similar to T_c showing a width of 2K for AAH55n2 while being only of 1K for AAH55n6. This must be related to some

disorder in the samples.

In the end we give a comparison of the characteristics of the samples with the literature in the next table, giving similar results.

	FeSe	AAH55n2	AAH55n4	AAH55n6	AAH55m1	FeSeS15
Doping	0	12	12	12	12	12
T_c	8.9	10.4	10.3	10.4	10.3	10.4
T_s	90	54	-	62	-	-
T_c (from ([2]))	9	10	10	10	10	10
T_s (from ([2]))	87	54	54	54	54	54
T_c (from ([130]))	9	10	10	10	10	10
T_s (from ([130]))	90	60	60	60	60	60

Table 3.1: Comparison of T_c and T_c in our samples with the literature. The width of the transition in the specific heat is about 10% of T_c, and T_c was taken as the mid-point of the transition height. The resistivity measurements are in a good with the specific heat measurements with a discrepancy of the order of 0.1K, one order of magnitude smaller than the width of the transition.

3.1.1 Quantum Oscillations

When a superconductor recovers its normal state by destroying superconductivity with a high magnetic field, electronic orbits are quantized in a Fermi liquid metal. It results in oscillations in $1/H$ visible in many quantity such as resistivity but also specific heat. One of the problems is that most of the time, the resolution needed to observe those oscillations in the specific heat is too high compared to the available resolution. But we believe that AC specific heat technique, allowing us to have a very good resolution of the order of 1 ‰, might be a solution to observe quantum oscillations in our samples. In Sec 2.1.8 we introduced the oscillatory component of the specific heat due to the Landau level quantization of the orbits, given by the Lifshitz-Kosevich formula 2.27.

Fig 3.3 shows the oscillatory part of the specific heat measured at LNCMI Grenoble, with fields up to 35T. The sample was mounted with the magnetic field parallel to the c-axis of FeSe, and we show here only the part of the specific heat were $H > H_{c2}(T)$. Here the data were smoothed by taking the data points plus the average and dividing it
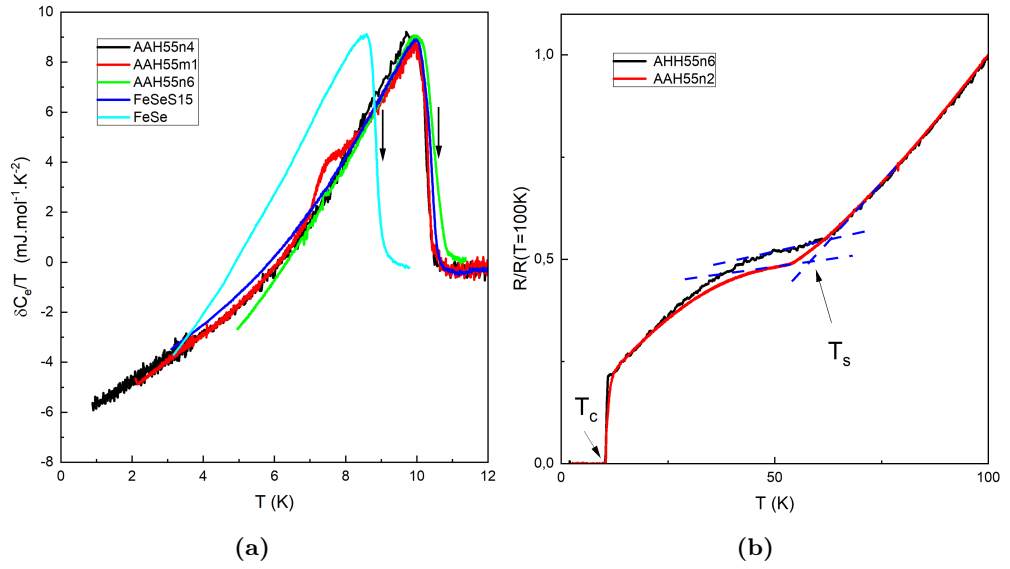
Figure 3.2: (a) Temperature dependence of the specific heat of the different samples measured during the thesis. AAH55 and FeSeS15 samples are doped with 12% sulfur. Arrows show the temperature where the superconducting transition happens, at the mid-point of the transition height. (b) Temperature dependence of the normalized resistance (R/R(T=100K)) of the doped samples. T_c is measured as the zero resistance point, while T_s is the intersection of two dashed slopes.
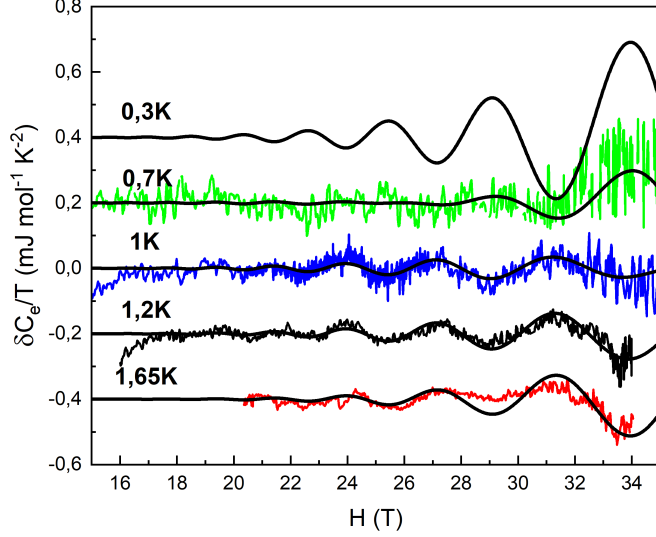
Figure 3.3: Quantum oscillations in $\delta C_e/T$ as a function of the magnetic field in FeSe. Colored line are the obtained data, while the black line is a rough fit performed down to 0.7K. The black line at 0.3K is only here to have an idea of how oscillations could look like at that temperature, since we could not reach such a low temperature with our setup.

by a 2. We then fit our data only to the first harmonic in the Lifshitz-Kosevich formula ($p=1$) and with no warping ($t_w=0$). In fact, the noise in our data does not allow for a very precise fit, and we prefer here to neglect any warping. We are only using one band to fit the oscillations again due to the noise in the data.

It is interesting to notice the curve at 0.7K seems to show very reduced oscillations and we attribute this to the fact that the function $f''(x)$ (see Eq. 2.27) changes sign for a value of x close to 1.6, showing a π-phase shift going through the value. This is visible in Fig 3.4 where that phase shift is clearly visible for temperature between 0.5K and 1K on the available magnetic field. Those nodes in $f''(x)$ are an added value of the specific heat quantum oscillations measurements and enable to have a direct access to the cyclotron mass. The inferred mass m^* is of the order of $4m_e$. We then fit the data with that cyclotron mass and a value of the frequency of the oscillations of $F_1 \approx 200T$ due to published articles ([(2)],[(80)]), and the fit gives a Dingle temperature of $T_D \approx 2.5K$. T_D quantifying the disorder in the sample and being quite low, it must be a reason why the oscillations are here visible.

Resistivity measurements made by Waston et al. in Ref. (2) (see Fig. 3.5) shows
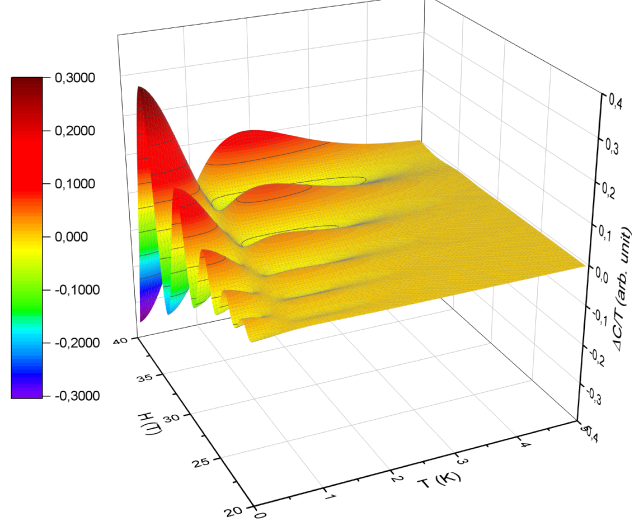
Figure 3.4: Quantum oscillations in $\delta C_e/T$ as a function of the temperature and the magnetic field, with an effective mass $m^* = 4m_e$

4 different frequencies and one of them seems to match our data. They found a band with a frequency, F_2, close to 200T and an effective mass around $4m_e$. Interestingly that band is the one with the highest amplitude (see Fig. 3.5) and this is the only one we observe. Another frequency of F_4=660T was also found with the same effective mass meaning that they could be related to same band. F_4 being the highest measured frequency, and ARPES measurements only seeing one hole band but possibly more electron bands, that means that in order to preserve charge balance in the system, F_4 as to be related to the hole band and therefore F_2 also is. In the case of FeSe is it possible to show that

$$\gamma = \frac{\pi a^2 k_B^2 N_a}{6\hbar^2} \sum_{bands} m^* = 0.7 \sum_{bands} m^*. \tag{3.1}$$

From the specific heat measurement we have estimated that γ=6.5 mJ.mol^{-1}K^{-2}. This shows that this band should be responsible of approximately 40% of the γ value. Watson et al. found in a three band model a very high value of γ=9.4 mJ.mol^{-1}K^{-2}, which would give in a two band model a value of 6.2 mJ.mol^{-1}K^{-2}, in a much better agreement with our value. Interestingly Terashima et al. [(80)] found also frequencies very close to the one observed by Watson et al. and gave a value of γ=6.2 mJ.mol^{-1}K^{-2} in a two band model. In such a scenario the hole band would be responsible of approximately

3. VORTEX LATTICE MELTING AND UPPER CRITICAL FIELD IN FESE$_{1-X}$S$_X$
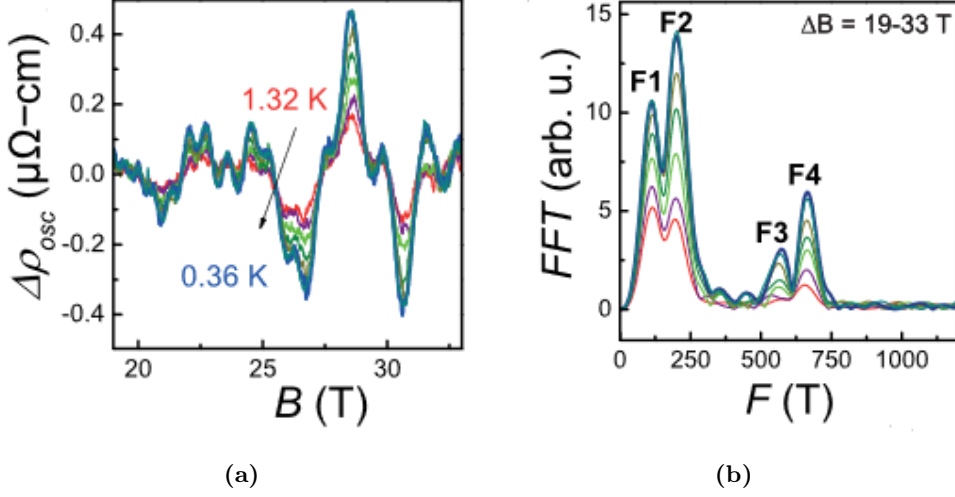
Figure 3.5: (a) Oscillatory part of the resistivity of FeSe (b) Fourier transform of the data in (a) identifying four different frequencies, corresponding to extremal areas on the Fermi surface. From [(2)]

50% of the γ value. All measurements are summarized in Tab. 3.2.

	F	Frequency (T)	m^*/m_e	Our measurements	γ (mJ.mol^{-1}K^{-2}) 3 bands	2 bands
Electrons	F_1	110	3	×	2.1	2.8
	F_3	550	6	×	4.2	
Holes	F_2	200	4	✓	2.8	
	F_4	660	4	×		

Table 3.2: Comparison of the quantum oscillations data our data and from Ref. (2)

In the next sections we will try to investigate more in details the full $H - T$ phase diagram of FeSe. It is a promising candidate to study the vortex matter, since its upper critical field seems to be attainable in both directions and its Ginzburg number should be of the order of 10^{-3}, indicating strong thermal fluctuations in the system. We will also try to study the behaviour of the upper critical field using orbital and paramagnetic models and its interplay with the melting.

3.2 Study on pure FeSe

3.2.1 Specific heat data

Subtraction of the phonon contribution and the Sommerfeld coefficient In order to study the superconductivity of the samples we have to focus on the electronic specific heat. When measuring the heat capacity of a sample, all contributions are measured. The first thing we need to do it so subtract the heat capacity of the addenda. In order to do that, we usually measure the addenda before putting any sample on the calorimeter. Then the sample is added and measured again. With that method we then only need to subtract the first curve obtained to the second one to get the heat capacity of the sample. Fig? 3.6a shows the measurements of the total specific heat and the addenda contribution. But here we are still left with another problem, we still have contribution to the specific heat of the phonon, or in a worst case scenario some Schotkky anomalies could also be present. So we have to find a way to get rid of these contributions to only be left with the electronic specific heat. We do not see in Schotkky anomalies in our data but we still have to subtract the phonon contribution. The method employed in Karlsruhe consists in doing a fit above T_c, where we suppose that the specific heat of the material in the normal state take the same form as for a metal, meaning : $C_n/T = \gamma_n + \beta T^2$. To take into account the deviations from that law at higher temperature we can add even terms to have a better fit : $C_n/T = \gamma_n + \beta_3 T^2 + \beta_5 T^4 + \beta_7 T^6 + ...$ as we discussed before. The coefficients here should be independent of the applied magnetic field, this is why we perform the fits at 0 T and the maximum available field, where superconductivity is supposed to be almost fully suppressed. We then plot $\delta C_e(T,H) = C_s(T,H) - C_n(T,H)$, where C_s is the specific heat in the superconducting state and C_n is the one in the normal state. The fit giving C_n is always performed in a way that the superconducting transition will be entropy conservative. It means that in the normal state the entropy should always be the same for every field. If so, one can fit the specific heat above the superconducting transition in order to enforce entropy conservation with that law : $C_n/T = \beta_3(T^2 - T_1^2/3) + \beta_5(T^4 - T_1^4/5) + ... + S(T_1)/T_1$; where T_1 is the temperature where the entropy was measured.

Another way of getting δC_e is to have access to a field that is high enough so that it will fully suppress superconductivity and then we only need to subtract the curve at the given field to the others at lower field assuming addenda are field independent. This is

3. VORTEX LATTICE MELTING AND UPPER CRITICAL FIELD IN FESE$_{1-X}$S$_X$

what we usually do in Grenoble. All of that was possible because we had access to the LNCMI Grenoble, a high magnetic field facility. Fields up to 36T have been reached during this thesis. Without such a facility, the phase diagrams of my thesis would not be complete.

Fig. 3.7 displays the temperature dependence of the difference between the specific heat of the superconducting state $C_s(T, H)$ and the normal state $C_n(T, H)$ for $H_{\|ab}$ and $H_{\perp ab}$. The normal state was determined by fitting the data at 18T with $H_{\perp ab}$ where we think that superconductivity was fully suppressed over the temperature range. We still used $C_n(T, H) = \gamma_n T + \beta_3 T^3$ and enforced entropy conservation above T_c in order to get the specific heat due to superconductivity. We also compared that method by directly suppressing the total heat capacity of the sample and addenda at 18T to the others curves and the result is the same. We find here a Sommerfeld coefficient $\gamma_n =$6.5 mJ mol^{-1} K^{-2} and a phonon term β_3=0.4 mJ mol^{-1} K^{-4}. Fig. 3.6b shows the specific heat of the sample (where the addenda contribution was substracted) and the fitted contribution of the Sommerfeld coefficient and the phonons. Comparing these values with former data obtained on others samples in the Karlsruhe group [(84)], a good agreement is obtained.

We can now compare the superconducting transition in that sample with the BCS-theory. In the BCS formalism we recall that $\Delta C/\gamma_n T_c$=1.43. We find here that ratio to be close to 1.4 which indicates that the mean field theory in the weak coupling limit could apply to our sample. However, that low value could be due to the multigap nature of FeSe or maybe also to the anisotropy of the gap as reported by Sato and al [(130)]. Fig 3.8 shows the field dependence of the specific heat of the same sample. The field dependence of the specific heat allows to have a direct access to the effect of the field on superconductivity. In fact, the Sommerfeld coefficient and the phonon terms being independent of the magnetic field value they will only give a constant term in the specific heat. In order to subtract that term, one needs to have the specific heat δC_e equal to zero in the normal state. This is what is done in Fig. 3.8. Data were fitted with a parabola at low field in order to deduce the mean field transition (dotted line). Before the superconducting transition, an excess of specific heat is found when comparing the data with a mean field transition (shaded area). This is typical of vortex lattice melting, since more degrees of freedom are allowed. However, it should be interesting to
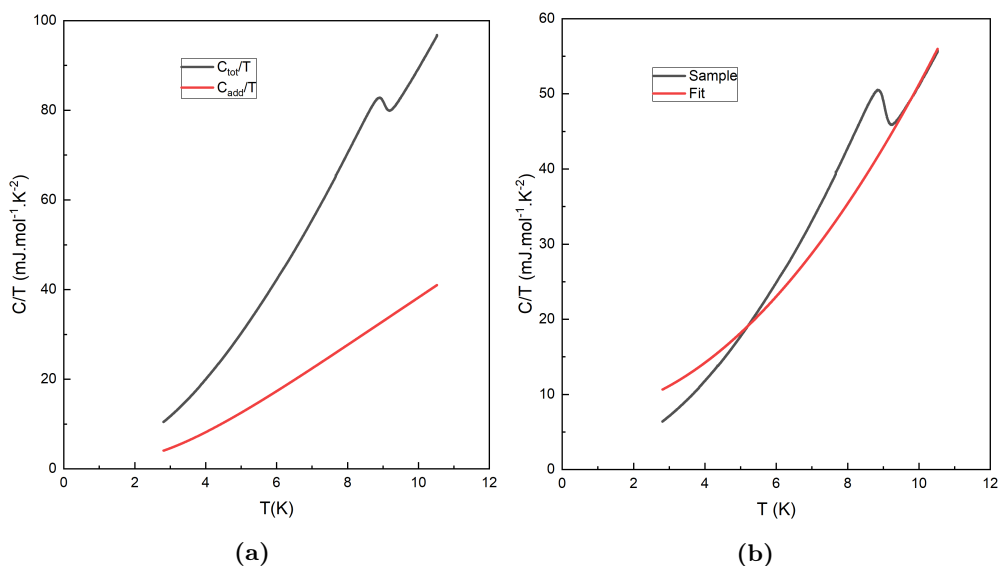
Figure 3.6: Specific heat of the FeSe sample and addenda. (a) Temperature dependence of C/T of the FeSe sample with the addenda in zero field (in gray) and only the addenda (in red). (b) Temperature dependence of the specific heat of the FeSe sample (in gray) in zero field and the entropy conserving fit performed corresponding to the phonon contribution and the Sommerfeld coefficient (in red).

check the range of superconducting fluctuations in the sample before going in a deeper analysis of the vortex melting. This is what we will do in the following.

Evidence for superconducting fluctuations   Thermal fluctuations tend to broaden the superconducting transition when applying a magnetic field. Looking at the temperature dependence of the specific heat in Fig 3.7 it is clearly visible that both directions tend to have a broader transition exceeding the intrinsic width of 1K. That broadening seems to be visible for fields higher than 2T when the field is applied along the c-axis and 9T for the other direction. Looking at the field dependence in Fig 3.8 that thermal fluctuations broadening is also visible. In a scenario without any fluctuations the specific heat would follow the dotted lines dependence with an abrupt transition at H_{c2}, however due to the fluctuations the transition extends over several Teslas.

Let us first take a look at the thermal fluctuations quantified by the Ginzburg number
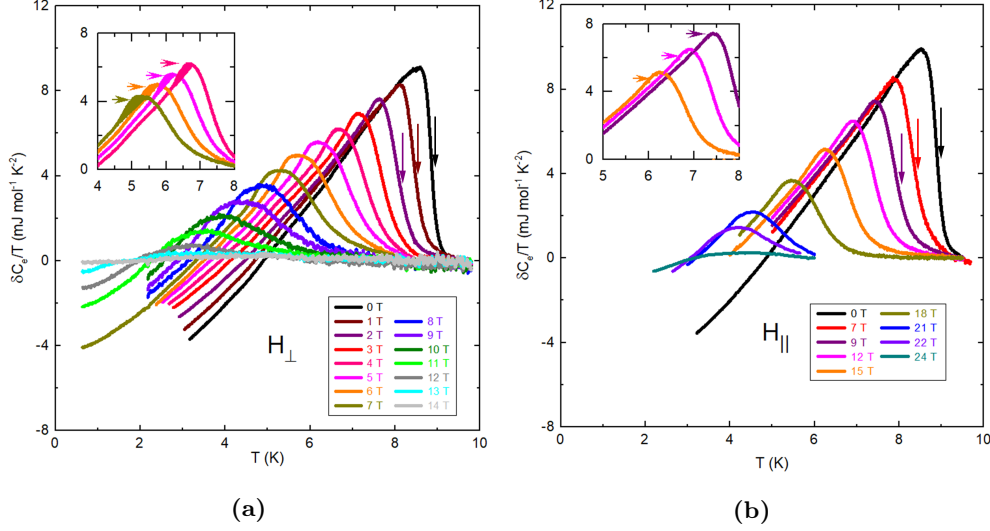
Figure 3.7: (a) Temperature dependence of $\delta C_e/T$ of FeSe when $H_{\perp ab}$. Arrows show the position of critical temperature for the first three fields. Inset : Excess of specific heat before the superconducting transition. The filled area correspond to that excess, and is related to vortex lattice melting. (b) Same but when the field is oriented H_{IIab}

[(131)]:

$$G_i = \frac{1}{2}\left(\frac{k_B T_c \Gamma \mu_0}{4\pi H_c^2(0)\xi_\perp^3(0)}\right)^2 \tag{3.2}$$

where $\xi_\perp$, $H_c(0)$ and $\Gamma = \xi_\perp(0)/\xi_{||}(0)$ are respectively the Ginzburg Landau in-plane coherence length, thermodynamic critical field (measured in Teslas) and anisotropy. It is possible to get some of these values from the data we already have. In fact [(132)]:

$$H_c(0) = \sqrt{\mu_0 \Delta C T_c} = 0.12T. \tag{3.3}$$

We can also get $\xi_\perp$ from the initial slope of $H_{c2}^\perp$:

$$\xi_\perp(0) = \sqrt{\frac{\phi_0}{2\pi H_{c2}' T_c}} = 3.5nm \tag{3.4}$$

Such a value of ξ can be compared with the mean free path. In (85), Cercellier et al. found the mean free path of FeSe to be around 55 μm, much larger than the coherence length we found here. One can therefore certainly assume that we are in the clean limit and that the broadening of the transition is due to the fluctuations, as we will see later using the LLL scaling theory. The anisotropy can be found by looking at the
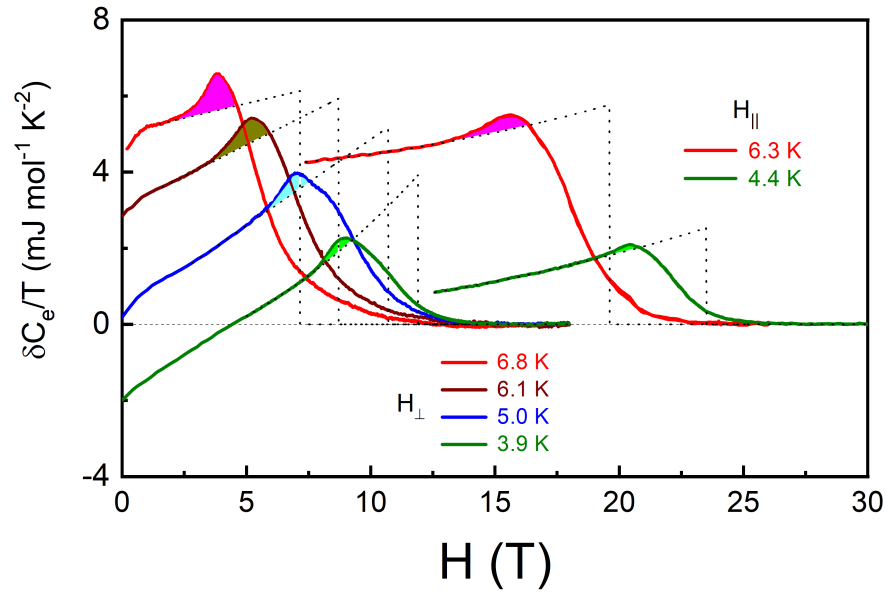
Figure 3.8: Field dependence of $\delta C_e/T$ of FeSe ($\delta C_e = C(H) - C(H > H_{c2})$). For both field orientations the dotted line represents an ideal single band mean field transition with a fit performed before the melting transition. The transition is chosen to take place at 20% of the jump height. The shaded area shows that an excess of specific heat is found before the superconducting transition when comparing the data with a mean field transition. This excess of specific heat is related to the vortex lattice melting.

3. VORTEX LATTICE MELTING AND UPPER CRITICAL FIELD IN FESE$_{1-X}$S$_X$

inset of Fig 3.9 where we found the 1T-2T curves with $H_{\perp ab}$ matches the 7T curve with field parallel to the layers. The inset also shows an approximate value of Γ as a function of temperature, where we find it to be around 4.5 for T>5. Such a value of the anisotropy is situated in between classical superconductors such a Nb that has $\Gamma = 1$ and highly anisotropic superconductors such as YBCO with a value of 7.8 (cf Tab. 1.2). It should also by noticed that the anisotropy decreases with decreasing temperature. Such a behavior was also observed in multiband systems such as MgB$_2$. Since FeSe is also a multiband system the anisotropy decrease with temperature might be the sign of a higher contribution of the band with lower band anisotropy at low temperature. However one can also explain it by looking at the pair breaking effects of the system. We will see that further in the discussion, but paramagnetic pair breaking is much stronger compare to orbital pair breaking at low temperature when $H_{\|ab}$. This is not the case when $H_{\perp ab}$. This kind of a behavior, being temperature dependent, must decrease the anisotropy at low temperature.

From now on it is possible to have as estimation of the Ginzburg number G_i. With the different values obtained before, we infer it to be G_i=1×10^{-3}. In most conventional type II superconductor the Ginzburg number is much lower. For example in Niobium $G_i \approx 7.10^{-12}$ [(103)], therefore the vortex liquid only occupies a tiny part of the phase diagram and is much harder to detect. The high value of the Ginzburg number in FeSe (similar to the one observed in YBCO where vortex lattice melting is observed, cf Tab. 1.2) gives us another proof of the possible observation of the vortex lattice melting in our samples. In fact the liquid state will certainly occupy a large portion of the phase diagram as indicated by Fig. 3.10. On that figure one can also see that the fraction occupied by the liquid state in FeSe is very close to the one observed in YBa$_2$Cu$_3$O$_7$ where the vortex lattice melting was clearly observed with specific heat.

Vortex lattice melting Lets us now come back on the feature we assumed to be related to vortex melting. To have a better view of that feature, Fig 3.11a shows $\Delta C_e/T(T,H) = \delta C_e(T,H) - \delta C_e(T,H_0)$, where H_0 =0T for field smaller than 9T and H_0 =7T for higher than that. A full proof of the melting transition would be a first order transition associated with a peak in C_e (see Fig. 2.7). However, we only observe
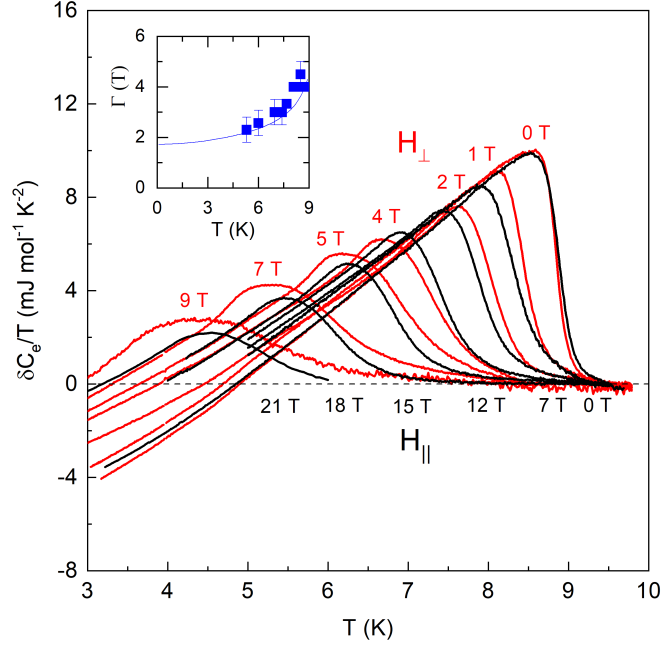
Figure 3.9: Comparison of the heat capacity of FeSe for the field in both direction. Inset : estimation of the temperature dependence of the H_{c2} anisotropy. Such a dependence of the anistropy might be inferred to the multigap nature of FeSe and to strong paramagnetic depairing.
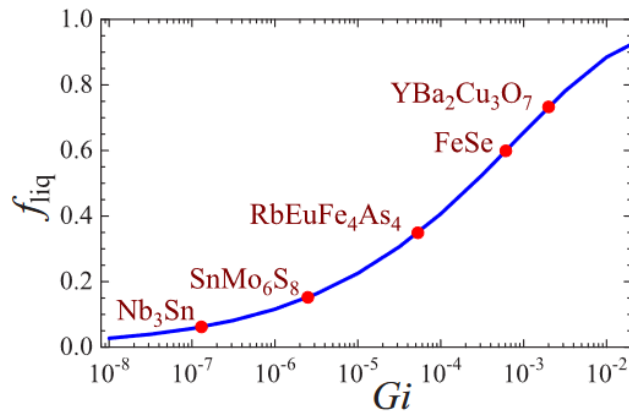
Figure 3.10: Dependence of the area fraction occupied by the liquid state, f_liq within the region where $[0.75T_c < T < T_c, B < B_{c2}(T)]$ on the Ginzburg number. From [[102]]

3. VORTEX LATTICE MELTING AND UPPER CRITICAL FIELD IN FESE$_{1-X}$S$_X$

a small step-like anomaly, not a peak like in the theory. But the distinctive feature observed is reminiscent here of what was observed for example by Roulin et al. [(133)] in YBa$_2$Cu$_3$0$_{6.94}$ as shown in Fig. 3.11. Roulin (see Fig. 3.11c) identified this feature to be caused by vortex lattice melting by comparing it with other data from resistance, magnetization and neutron diffraction. The fact that this transition is not first order but most likely second order might be due to the fact that this is not a solid to liquid transition but most certainly a glass to liquid transition as discussed in Ref. (133). The observation of the melting transition requires high quality sample, and even though we think that the quality of the sample is high here, a small disorder can shift a first order transition into a second order glass transition. However, the literature shows that the amount of defects is very small, being of one defect for 5000 Fe atoms. Watashige and al. observe with STM that twin boundaries are created at the nematic transition, due to the two possible orientations of the crystal structure in the nematic phase. They also observed that vortices tend to get trapped at the twin boundaries [(134)]. This might be the reason why we do not observe any first order transition. It should also be remembered that the vortex lattice melting is the only true phase transition in a strong type II superconductor with strong fluctuations.

In order to confirm that the anomaly we observe is even more similar to the one observed by Roulin [(124)], we now want to quantify the entropy jump in order to compare it. Comparing with the value of $\Delta S = 0.6k_b$ per vortex per superconducting layer (see Sec. 2.1.9), we find in our data a value closer to $\Delta C \approx 0.1k_b$ per vortex per superconducting layer by integrating the excess specific heat observed in Fig. 3.11 when $H_{\perp ab}$. This shows a good agreement in between the two sets of data by being in the same order of magnitude.

As we discussed before, the vortex melting is also visible in the H sweep measurements, with an excess of specific heat just before the superconducting transition starts to happen as observed in Fig. 3.8. Even if that excess is visible in both directions of the field orientation, it is less pronounced when $H_{||ab}$. It is here only visible in the mid-range of the phase diagram where $7 < H_{||} < 21T$ (see Fig. 3.11b). An interesting point to notice here is that no melting could be observed for $T < 3K$, where we recover a broadened mean field transition (see Fig. 3.12). We will investigate that interesting

(a) $H_{\perp ab}$

(b) $H_{||ab}$

(c)
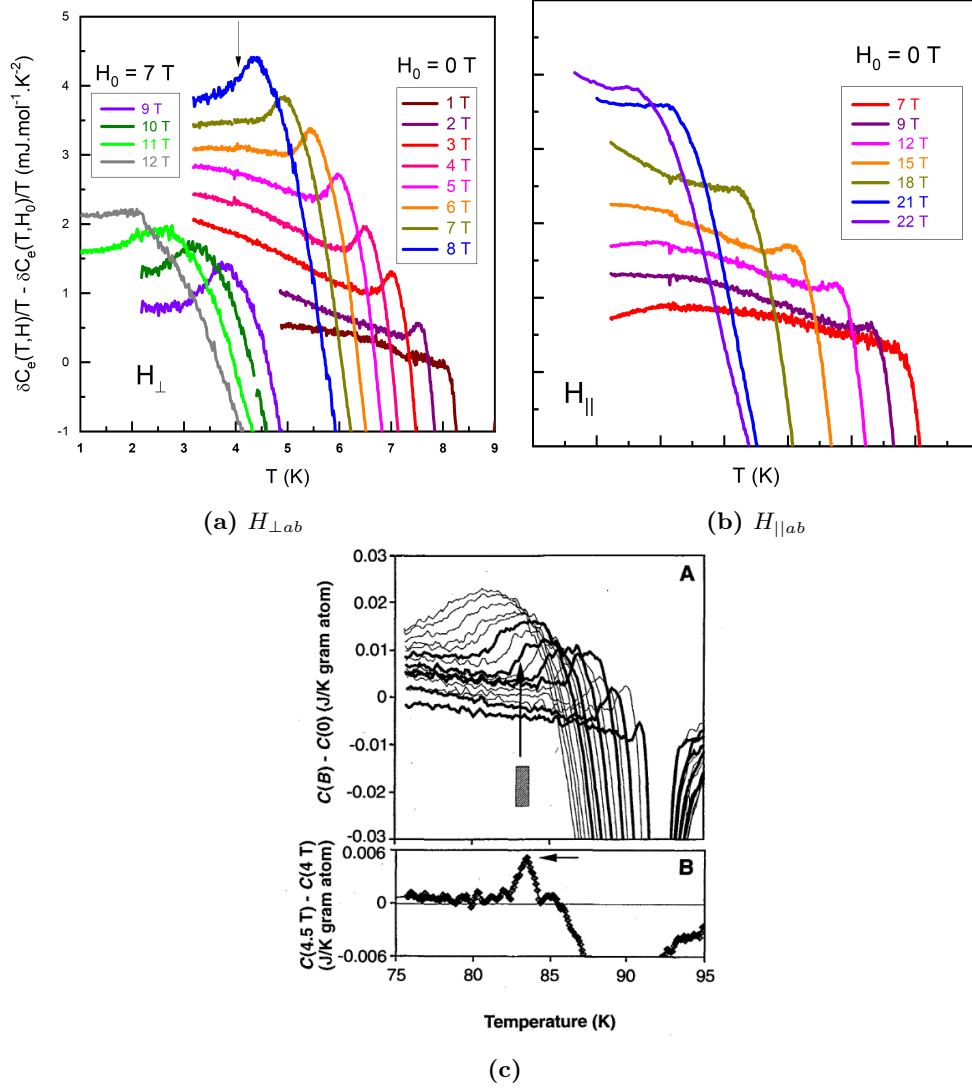
Figure 3.11: (a) Temperature dependence of $\Delta C_e/T$ of FeSe with $H_{\perp ab}$. For fields higher than 8T, the 7T curve was substracted. (b) Temperature dependence of $\Delta C_e/T$ of FeSe with $H_{||ab}$. In both directions, the criterion for melting is taken as the mid-point of the increase of the excess of specific heat as indicated by the arrow in (a). (c) Same in $YBa_2Cu_3O_{6.94}$. From [[124]]. The two features observed in both compounds are very similar. It was attributed to melting in $YBa_2Cu_3O_{6.94}$.
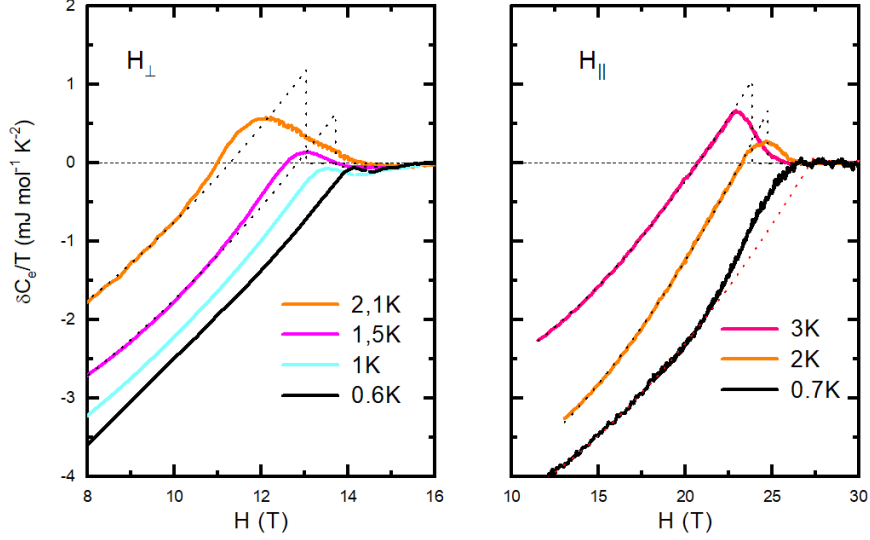
Figure 3.12: Field dependence of $\delta C_e/T$ of FeSe at low temperature for both field directions. Dashed lines represent our supposition for the behaviour of the mean field specific heat C_{mf}. The transition takes place at $\delta C/C_{mf}$=0.2 . When $H_{||ab}$, no melting is observable and an excess of specific heat from 22T to 27T is visible at 0.7K. When $H_{\perp ab}$ the curves were normalized at 18T, whereas in the other direction it was normalized at 28T. The broadening of the transition can be understood in terms of fluctuations since the LLL scaling applies very well to our data as we will see it in Sec. 3.2.1.1

feature a bit more in Sec 3.2.3.

It is then possible to build a $H - T$ phase diagram where we put the melting line observed both in field and temperature sweep, and both field orientation. Fig 3.13 shows that phase diagram, where the melting criterion was taken as the mid-point in the increasing part of the excess of specific heat, as indicated by the arrow in Fig. 3.11a. For $H_{\perp ab}$ (blue symbols) it seems like the dependence of the melting is very much linear, on the other side when $H_{||ab}$ it seems like we deviate from a linear law when the field is around 8T. That phase diagram also indicates that no melting was observable at low temperature when $H_{||ab}$.

3.2.1.1 Quantitative analysis of the field-induced transition broadening

Mean field fit We now have the phase diagram with the melting, but most of the analysis of the vortex melting requires the temperature dependence of the upper critical
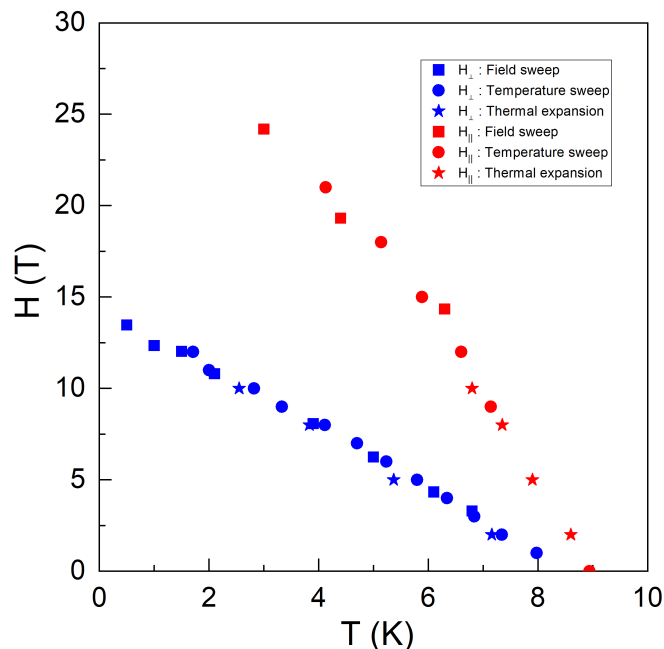
Figure 3.13: $H - T$ phase diagram of the melting in FeSe. Thermal expansion data are from [(131)].

field. In Sec. 2.1.10 we introduced the LLL scaling of the specific heat that allows to estimate $H_{c2}(T)$.

First, in order to check if such a scaling theory is applicable we have to be sure to attempt fields higher than $H_{LLL} = G_i H'_{c2} T_c \approx 10mT$ for $H_{\perp ab}$ and $60mT$ in the other direction. In such a case the Cooper pairs are in their lowest Landau level, and thus the approximation is good. Another scaling theory could also be used: the 3D XY scaling, in the region where critical fluctuations appear. In the region of the phase diagram where these fluctuations appear the correlation length $\xi_{XY} = \xi_0 (1 - T/T_c)^\nu$, with $\nu \approx 2/3$ needs to be smaller compare the magnetic scale $l_H = \sqrt{\phi_0 / \pi H}$. This allows to find a criterion in field where the 3D XY regime breaks. It is found that for a field $H > H_{XY} = 2H_{c2}(0)G_i^{2\nu}$ the 3D XY model can not be justified anymore. This gives in our case less than a mT for both directions. This is why we will focus on the LLL scaling in the following.

In order to proceed to the LLL scaling, the first thing we need to do is to have the behaviour of δC_{mf}. In the Ginzburg Landau theory, the jump in specific heat observed

3. VORTEX LATTICE MELTING AND UPPER CRITICAL FIELD IN FESE$_{1-X}$S$_X$
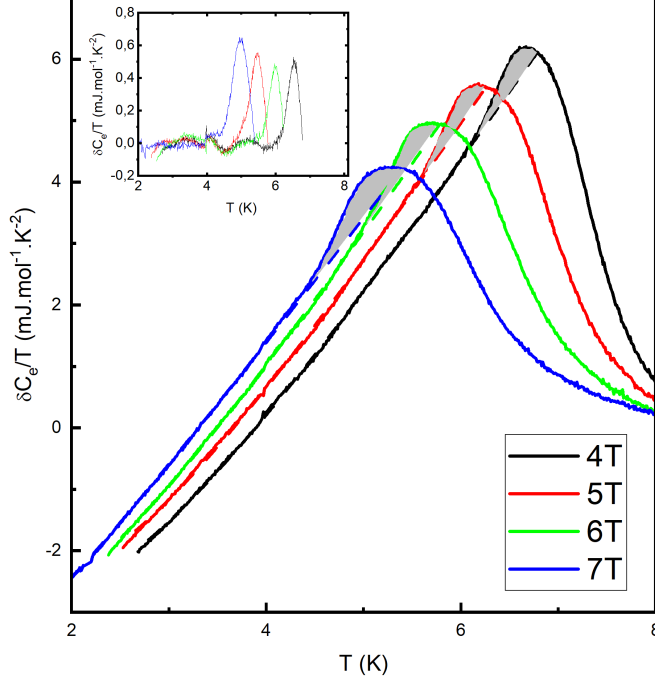
Figure 3.14: Example of a mean field fit used on $\delta C_e/T$ in order to perform a scaling analysis. In that example the magnetic field is along the FeSe layers ($H_{||ab}$). The dashed lines correspond to the mean field fit and the shaded area to the excess of specific heat compare to the mean field line. Inset : Difference between the data and the mean field fit.

at T_c is independent of the temperature. But looking at Fig. 3.7 we can see a strong variation in that quantity depending on the temperature. The interesting part of the scaling being in the region of the fluctuations, we decided to normalize our data with δC_{mf} being a fit of a second order polynomial for a temperature lower than the melting and extrapolating it to higher temperature in the transition region, similar to what was done by Koshelev et al. in RbEuFe$_4$As$_4$ [[102]]. Such fits are shown on Fig 3.14 where we can see a good match between the inferred δC_{mf} and our data. The same procedure was used in the field sweep curves as illustrated in Fig 3.8.

Scaling analysis Now having the dependence of $\delta C_{mf}(T)$ it is possible to try to scale our data to the LLL scaling function calculated by Li and Rosenstein [[126]]. For the temperature sweeps, two free fitting parameters are used for each field: r_T and $T_c(H)$ (see Eq. 2.29). An average value of r_T can be found and used after that for each field, to have a better value of $T_c(H)$. The same routine is used for the field
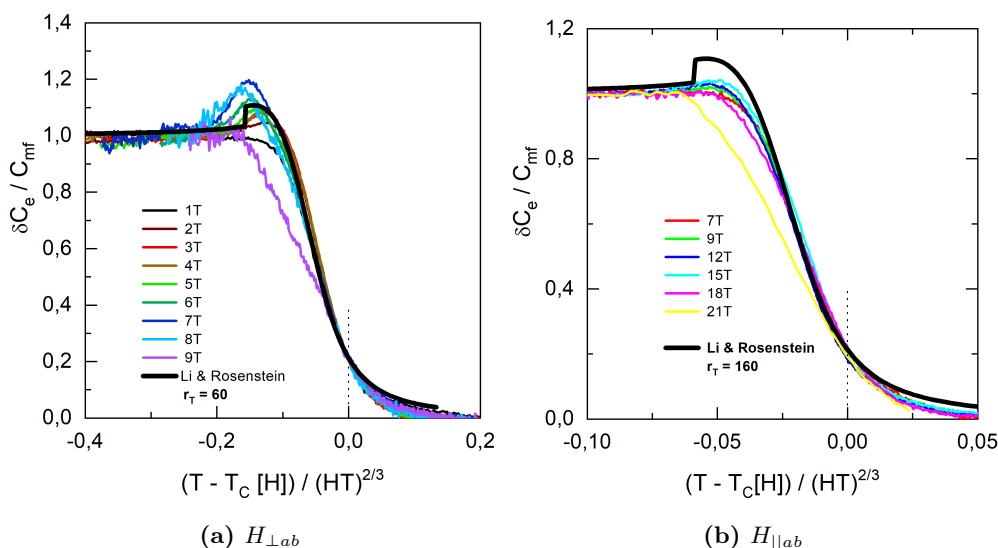
Figure 3.15: 3D-LLL scaling of the temperature dependent specific heat of FeSe. The bold line represents the theoretical line by Li and Rosenstein [[126]], and the colored lines are deduced from our data for different fields. In (a) the position of the expected specific heat discontinuity matches very well the maximum of our experimental data.

sweep but with r_H and $H_{c2}(T)$ (see Eq. 2.31). Such an analysis was also done with RbEuFe$_4$As$_4$ [[102]] and was quite successful. Fig 3.15 shows our scaling analysis for the temperature sweep curves and seems to have quite a good agreement with the theory. It is also worth noting that the position of the expected specific heat discontinuity matches the experimental data very well. From the fit, it is deduced that $r_{T\perp} = 60\text{K}^{-1/3}\text{T}^{2/3}$ and $r_{T\parallel} = 160\text{K}^{-1/3}\text{T}^{2/3}$. From that it is possible to have the anisotropy ratio $\Gamma = (r_{T\parallel}/r_{T\perp})^{3/2} = 4.3$ showing also a good agreement with the values previously found. The predicted values of r_T also matches very well the one we found experimentally since they were supposed to be respectively of 55 and 152 using Eq. 2.29. However, it seems more difficult to fit our data for large field values (see Fig. 3.15, the 7T curve when $H_{\perp ab}$ and 21T when $H_{\parallel ab}$). As shown in Eq. 2.29 the reason is that r_T is related to H'_{c2}, itself being independent of the temperature. This is only true when high order gradient terms are neglected in the Ginzburg Landau equation, which is only true at low fields.

The same scaling analysis is performed in Fig. 3.16 using the field sweep curves in both directions. Here, in that case, when $H_{\perp ab}$, again we find a good match be-

3. VORTEX LATTICE MELTING AND UPPER CRITICAL FIELD IN FESE$_{1-X}$S$_X$

(a) $H_{\perp ab}$ **(b)** $H_{||ab}$
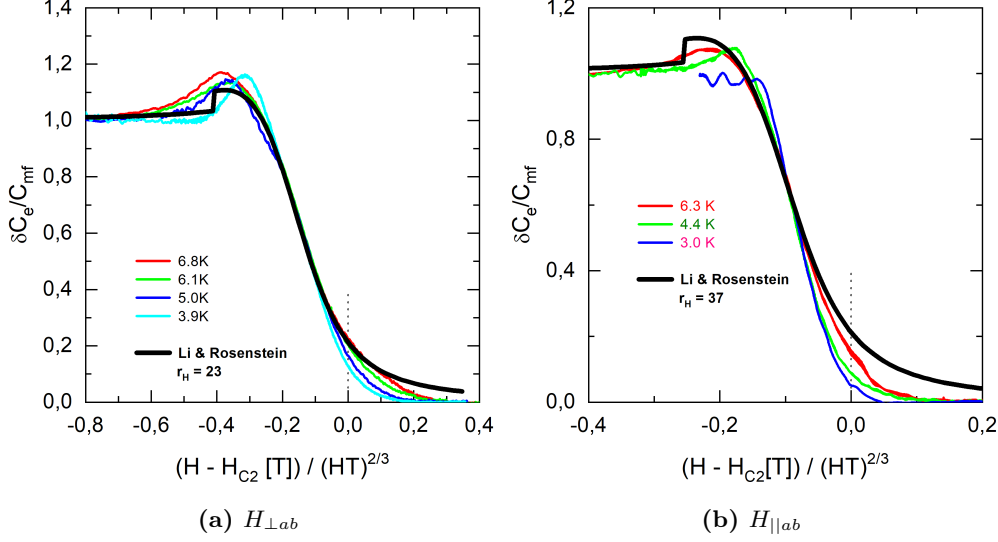
Figure 3.16: 3D-LLL scaling of the H-dependent specific heat of FeSe. The bold line represents the theoretical line by Li and Rosenstein [(126)], and the colored lines are deduced from our data for different fields. Once again the maximum of our data matches well the discontinuity in the theoretical line when $H_{\perp ab}$.

tween our scaling analysis and the theoretical curve of Li and Rosenstein [(126)] with $r_{H\perp}$=23K$^{-1/3}$T$^{2/3}$, when the expected value from a theoretical point a view (from Eq. 2.31) would be 18K$^{-1/3}$T$^{2/3}$. But in the other direction it seems to be difficult to have a match for low temperature curves when $T<$6K. In the lower two third of the phase diagram it seems like the LLL scaling analysis breaks down when $H_{||ab}$. One of the reasons is that the LLL scaling used in our analysis only accounts for orbital effects, but when $H_{||ab}$, some strong paramagnetic effects can rise and would then cause the LLL scaling to break down.

When the scaling approach was not possible (i.e. at high fields and low temperatures) we used a similar criterion as the one of Li and Rosenstein to extract the value of H_{c2}. In their theoretical curve, Li and Rosenstein found that the temperature or field at which the upper critical field is crossed gives a value of $\delta C/C_{mf}$=0.2. Therefore we used that criterion in order to have the upper critical field dependence in our phase diagram in the low temperature region.

Upper critical field and complete phase diagram   Our scaling approach allows to complete the phase diagram with the H_{c2} line deduced from the scaling analysis.

	Experiments	Theory
$r_{T\perp}$ (K$^{-1/3}$T$^{2/3}$)	60	55
$r_{H\perp}$ (K$^{-1/3}$T$^{2/3}$)	23	18
$r_{T\parallel}$ (K$^{-1/3}$T$^{2/3}$)	160	152

Table 3.3: Comparison of the experimentally deduced scaling parameters r_T and r_H with the theory

The LLL scaling is a powerful way to get H_{c2} in the $H - T$ phase diagram. We report on Fig. 3.17 the melting line (filled symbols) and the upper critical field deduced from the LLL scaling analysis (empty symbols other than hexagons). However, the LLL scaling is also limited in some regions of it and at high fields a mean-field criterion was used (hexagons empty symbols). The upper critical field line was supposed to happen at 20% of the anomaly based on the scaling analysis of Li and Rosenstein (when $T = T_c(H)$, $\delta C_e/C_{mf} = 0.2$). Li and Rosenstein [(126)] explained that the LLL scaling first only applies in region where $H \gg H_{c1}$. Second their model is valid when κ is high (in our sample we find $\kappa_\perp \approx 100$ and $\kappa_\parallel \approx 400$) and near T_c. Going at higher field and lower temperature some other problems arise: only orbital effects are taken into account, with no paramagnetic effects and the LLL scaling focuses only on thermal fluctuations and no possible quantum fluctuations are taken into account.

In Fig. 3.17 one sees for example that we supposed a maximum upper critical field of approximately 14T close to zero temperature when $H_{\perp ab}$. In fact we started first with measurements until 18T (see Fig.3.12) and supposed that the normal state was recovered of such a value of field. However, we performed later measurements until 32T and looking at Fig. 3.18 one can observe a surprising behaviour. That figure displays the field dependence of the heat capacity of our sample at low temperature. Usually the normal state is recovered when the heat capacity is constant. We explained that the upper critical field is a crossover and not a phase transition. This is one of the reason why it might be quite hard to have a precise value of $H_{c2}(0.7K)$ only by looking at the data. Looking at Fig. 3.18 the specific heat varies about approximately 6% between the melting anomaly and the part where it gets constant. That region where it varies is quite large, going from 14T to 20T. Taking into account a possible influence of the noise for the variation of the signal still lives a large fluctuating part. In fact, the

(a) $H_{\perp ab}$ **(b)** $H_{||ab}$
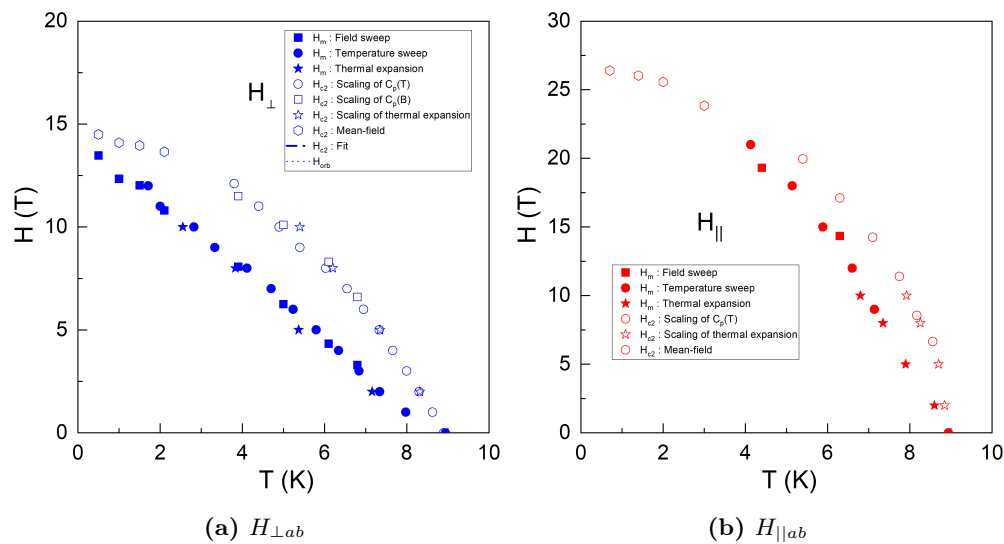
Figure 3.17: $H - T$ phase diagram of FeSe for the field in both directions. Open symbols corresponds to the upper critical field and filled symbols to the melting anomaly. The upper critical field for both directions of field in the high field region (H>13T for $H_{\perp ab}$ and H>22T for $H_{||ab}$) was determined by supposing a mean field like transition (see Fig. 3.12) whereas the other data concerning the upper critical field were obtained using a scaling analysis. Thermal expansion data are from ([131]).
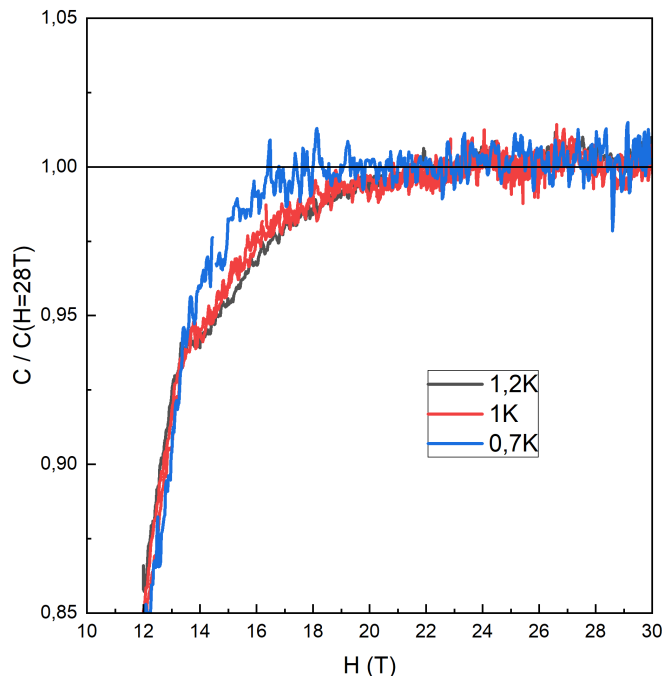
Figure 3.18: High field dependence of the specific heat of FeSe at low temperature. A large region between where the specific heat is not constant is observed after the melting.

maximum noise at these fields being around 1%, the fluctuating part would reduces in the worst case scenario to values going from 15T to 19T. In Ref. (86), the specific heat data obtained by Ok et al. also show an increase of the specific heat after what was designated as the upper critical field around 14T at low temperature. Their value of the upper critical field is likely to correspond to what we think is the melting anomaly. Interestingly Kasahara et al. noticed the presence of a possible new superconducting high field phase in the same direction, starting around 14T until 17T (cf. Sec. 1.4.3). It is still not clear if the variations of $\gamma(H)$ are related to that phase. However we are still left with a question : where is $H_{c2}(0)$? We shall address the effects of different possible values of $H_{c2}(0)$ in the next sections.

3.2.2 Quantitative analysis of the phase diagram

In order to learn a bit more on the properties of FeSe it would be now interesting to examine the behaviour of the upper critical field, but also of the melting line.In the following, we shall do a more detailed analysis of these phenomenons. The analysis will

be done using a one band scheme though FeSe is a two band superconductor. In fact the average amplitude of the hole and the electron gaps are very close [(83)], which justify the one band approximation (cf. Sec. 3.1.1). Thereafter, the pinning will also be neglected.

3.2.2.1 H_{c2} : Orbital and paramagnetic limit

H $\perp$ FeSe layers We will first here take a close look at the phase diagram when $H_{\perp ab}$. In an easy scenario, which would be the first one to come to mind, the upper critical field could be examined only in terms of orbital effects. In such a scenario the orbital field at zero temperature, $H_{orb}(0)$, only depends on the initial slope of upper critical field and T_c, following $H_{orb}(0) = -0.727H'_{c2}T_c$ in the BCS theory. The measured initial slope (deduced from data in the linear region close to T_c, i.e T>7K) in our phase diagram is $H'_{c2\perp} = -3 \pm 0.25$TK^{-1}, thus giving $H_{orb}(0) = 20 \pm 1.5$ T (dotted line in Fig. 3.19). From the discussion above, we saw that even if $H_{c2}(0)$ is quite hard to get, its value should be in the interval of 14T to 20T at low temperature.In a scenario where we only take orbital effects into account, we find $H_{c2}(0) = H_{orb}(0) = 20$T. That might work looking at Fig. 3.18, where the specific heat is constant for a field superior to 20T. The fact of having $H_{c2}(0)$ different from $H_m(0)$ is not a real problem we considering quantum fluctuations, but we shall address that point later on in Sec. 3.2.2.3. However, we must then address the problem in Fig. 3.19 of having data from scaling and mean-field (empty symbols) that would not work with such a scenario (dotted line). If these data are correct, then a way to have a better match between the theoretical curve and our data is to think about paramagnetic effects, that have the effect to lower the upper critical field close to zero temperature. In order to do so, we try a fit from Eq. 1.77, where the only free parameter is the Pauli limiting field at zero temperature, $H_p(0)$. It leads to the dashed curve in Fig. 3.19 which agrees quite well with our data, and we find $H_p(0) = 26.5$. To compare the strength of the Pauli depairing compare to orbital effects, we calculate the Maki parameter, $\alpha_{M\perp} = 1.1$, which shows a relevant effect of the paramagnetic depairing. However such a scenario can not really explain why the specific heat varies about 6% in between 14T and 20T.

H || FeSe layers We will now take a closer look on the curves in the other direction, when $H_{||ab}$. Looking at the phase diagram (see Fig. 3.20), we can already see that
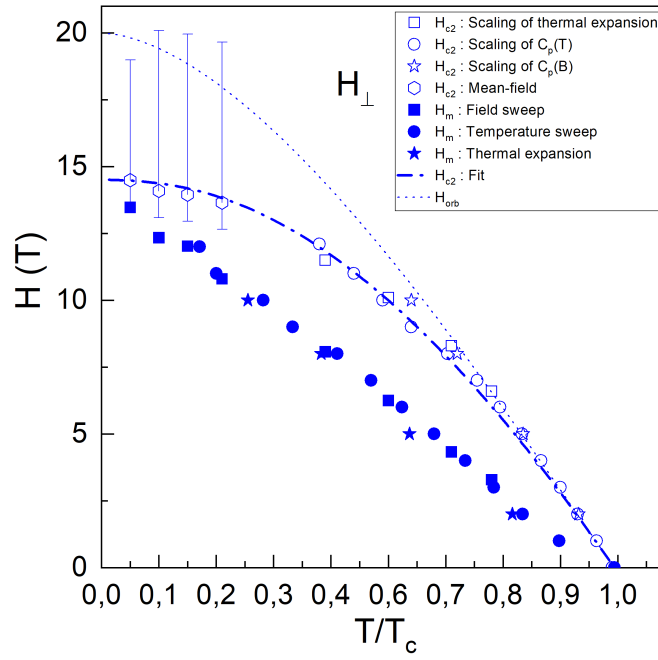
Figure 3.19: $H - T$ phase diagram of FeSe with $H_{\perp ab}$ with fit of H_{c2} taking into account orbital and paramagnetic effects. Thermal expansion data are from [[131]]. Open symbols represent the upper critical field, and filled symbols the melting line. The dotted line represents a purely orbital model where the Maki parameter is equal to zero while for the dashed line the Maki parameter is taken as a free parameter (cf. Eq. [1.77])
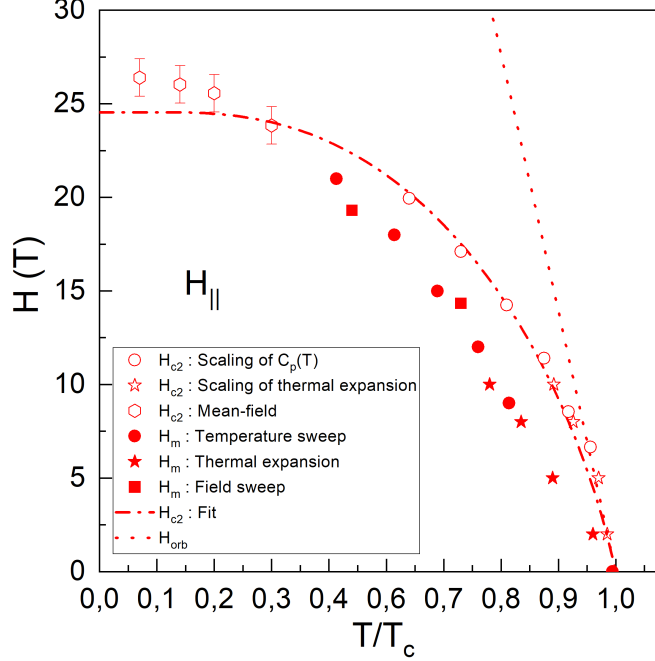
Figure 3.20: $H - T$ phase diagram of FeSe with $H_{||ab}$ with fit of H_{c2} taking into account orbital and paramagnetic effects. Thermal expansion data were measured on the same sample in Karlsruhe in [[131]]. Open symbols represent the upper critical field, and filled symbols the melting line. The dotted line represents a purely orbital model where the Maki parameter is equal to zero while for the dashed line the Maki parameter is chosen using an anisotropy of 4.5 (cf. Eq. 1.77).

the situation is not the same and that the curvatures of H_{c2} seems to be already very pronounced even at low field. The Pauli depairing thus plays a very important role all over the phase diagram. To verify that, we can check on the Maki parameter in this direction, which can be calculated from the anisotropy ratio and the Maki parameter in the other direction: $\alpha_{M||} = \Gamma\alpha_{M\perp} \approx 4.5$. Such a value clearly indicates the predominant role of the paramagnetic effects compared to the the orbital ones in that direction.

In Fig. 3.20 we plot $H_{orb,||}(T) = \Gamma H_{orb,\perp}(T)$ (dotted curve). This shows clearly an overestimation of the upper critical field from the data. Taking into account strong paramagnetic effect through the inferred value of $\alpha_{M||} = 4.5$ and $H_{orb||} = \Gamma H_{orb\perp} = -13.8 \text{TK}^{-1}$, we thus have no fitting parameter and deduce the dashed curve taking into account paramagnetic depairing. This shows a good match with our data. In a scenario where we would only use orbital effects, $H_{orb}(0)$ would be around 90T, which

is way above what we have found. The inferred curve reproduces our data very well but it seems that at a temperature $T^* = 3K$ the fit underestimates the upper critical field. Interestingly at the same temperature T^*, the melting curve and the H_{c2} tend to merge. We will talk about that later on in Sec. 3.2.3

3.2.2.2 Melting : Thermal fluctuations

Now that we know the upper critical field dependence we can calculate the temperature dependence of the vortex melting line. Let us start with the easiest case when the melting line is observed over the all phase diagram, i.e for $H_{\perp ab}$. First we will assume only thermal fluctuations and try to apply a Lindemann criterion. From Eq. 1.50 and using the value of G_i and $H_{c2}(T)$ we can plot the melting line using the Lindemann coefficient c_L. Fig. 3.21 shows the result of the calculation for $c_L = 0.15$. That value of the Lindemann parameter seems to agree with the empirical data that states that c_L should be in between 0.1 and 0.3. The line matches the melting line data we obtained very well until the lowest temperature, where the melting line exhibits an upward curvature. That means that the only genuine visible phase transition over the all phase diagram is the melting line in our material when the field in oriented perpendicular to the FeSe layer. This shows also that even by neglecting the pinning force we still have a very good agreement in between the theory and our data.

When H is parallel to the Fes layers, the scenario seems to be more complicated. First the melting line is no longer observed before reaching the highest critical field at approximately $T^* = 3K$. One explanation for this could be the influence of disorder. In (20), Mikitik and Brandt tried to quantify the influence of disorder on the $H - T$ phase diagram (see Fig. 1.7). It turns out that the quantity determining the strength of the pinning compared to thermal and quantum fluctuations is D/c_L with $D^2 \approx j_c/j_0$ (j_c being the zero field critical current density and j_0 the depairing current density). From [(135)] it was found that $j_c \approx 3 \times 10^4$ A.cm^{-2}, and $j_0 \approx 10^7$ A.cm^{-2}. We thus obtain $D/c_L = 0.3$. Fig. 1.7 shows the influence of pinning on the melting line. Here we see that in such a case the melting line does not go to the lowest temperature even in the case of $D/c_L = 0.3$. However, the melting line should lie very close to the one without any pinning and also lower than $T/T_c = 0.1$ and this is not the case in our data. The pinning certainly comes from domain walls appearing at the nematic transition since
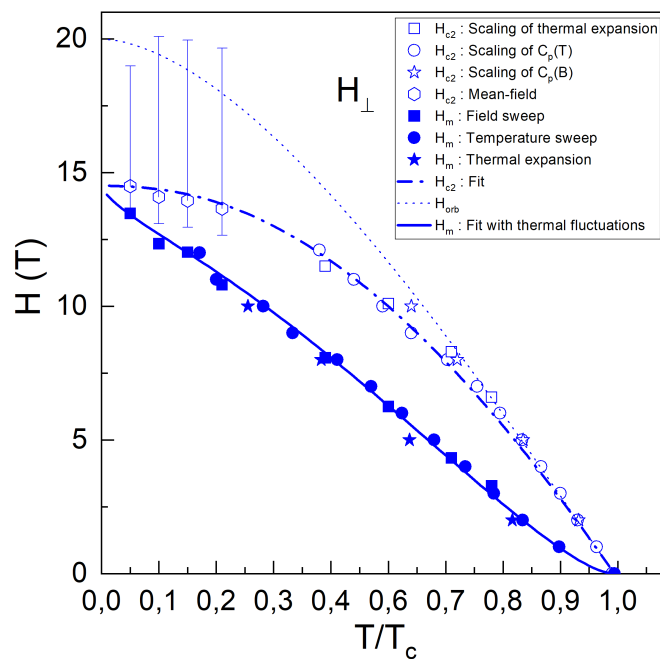
Figure 3.21: $H - T$ phase diagram of FeSe with $H_{||ab}$ with fit of the melting line taking only into account thermal fluctuations. Open symbols represent the upper critical field, and filled symbols the melting line. The dotted line represents a purely orbital model where the Maki parameter is equal to zero while for the dashed line the Maki parameter was fitted (cf. Eq. 1.77). The continuous line is fitted using Eq. 1.50.

the typical concentration of Fe vacancies is less than one impurity per 5000 Fe atoms [(134)]. In such a scenario the pinning by the twin boundaries is less efficient when $H_{\parallel ab}$. Since we managed to have a good agreement between the theory and our data without any pinning when $H_{\perp ab}$, it means that the influence of pinning in the other direction must also be negligeable.

As we said before it is here interesting to notice that the melting line and the upper critical field line seems to merge at a temperature $T^* = 3K$ (see Fig. 3.20), which is not related to the pinning in our data. Such a scenario was predicted theoretically by Adashi and Ikeda, which we talked about in Sec. 1.2.4.1 (see Fig. 1.10). Below T^* the vortex lattice has no chance to melt and directly undergoes a transition from a solid state to a normal state where the Pauli effects are strong. This means that the real phase transition is now the upper critical field, and below T^* that would be the vortex lattice melting. One of the explication here might be the strong paramagnetic effects which tend to strongly reduce $H_{c2}(T)$ and cause the melting and upper critical field to join as argued by Adashi and Ikeda. The vortex lattice melting is still going up in the phase diagram until it crosses the reduced upper critical field. In such a scenario it is not possible to use our Lindemann equation which states that the melting line is always under the upper critical field.

We can also try to fit our melting line on the universal plot from (102) (cf Eq. 2.32). Such a plot is performed in Fig. 3.22. Here we can see that our data when $H_{\perp ab}$ match quite well the universal curves. However it is not the case when $H_{\parallel ab}$, this is again certainly due to the fact that strong paramagnetic effects are observed in that direction which would tend to change the dependence of the $H_m/H_{c2}(T)$ ratio and that were not taken into account on the universal curve. Consequently, the fact that the data when $H_{\perp ab}$ matches quite well the universal curve, is a sign that the paramagnetic effects are very weak in this direction. However it does not really help us to have a firm opinion on the debate in Sec. 3.2.1.1.

3.2.2.3 Melting : Quantum fluctuations

Low field: linear or quadratic dependence of the melting A closer inspection at Fig. 3.18 shows that the transition to the normal state extends over approximately 6T while $\Delta B_{c2} \approx 3T$ this might be understood in terms of quantum fluctuations, this
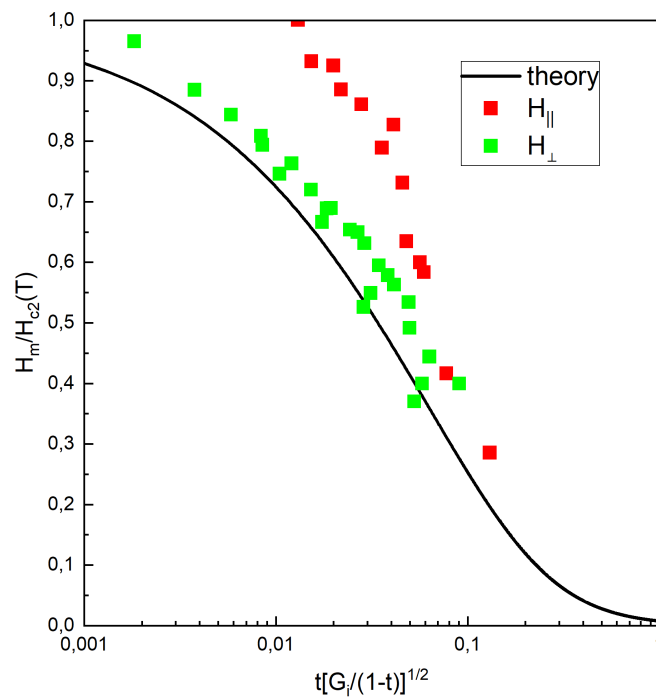
Figure 3.22: Universal plot for the vortex lattice melting transition (following Eq. 2.32, black line) with our data on FeSe superimposed. The y-axis is the melting field divided by the temperature dependent upper critical field. Green data correspond to $H_{\perp ab}$ and red data to $H_{||ab}$. Data for $H_{\perp ab}$ fit quite well the theoretical line, whereas the data for $H_{||ab}$ show a discrepancy, certainly due to paramagnetic pair breaking.
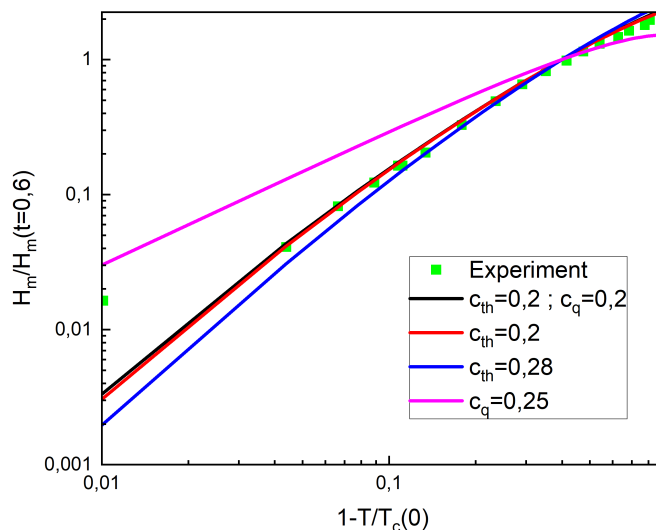
Figure 3.23: Normalized melting line as a function of $1 - t$ on a logarithmic scale for different quantum and thermal coefficients. c_q and c_{th} are taken from Eq. 1.70 and Eq. 1.69. The value of c_{th} determined from the last analysis is 0.2.

is why we propose an analysis about that here. A way to check for possible quantum fluctuations is to look at the temperature dependence of the melting line close to T_c. We argued about the fact that quantum fluctuations have a linear dependence close to T_c when thermal fluctuations have a quadratic temperature dependence close to T_c as well. Looking at that region of the phase diagram might help us to look for further information. We plot the normalized melting line on a logarithmic scale in Fig. 3.23 to have a better look at the dependence close to T_c.

Logically it is not possible to take only quantum fluctuations into account. One sees also that a small change in the thermal coefficient can induce a noticeable distance from the experimental points. Thus the value of $c_{th} = \sqrt{G_i}/2\pi c_L^2 = 0.2$ found from the previous analysis must be robust. It seems however very complicated to differentiate between a scenario where we only have thermal fluctuations (red line) and a scenario having thermal and quantum fluctuations (black line). Different values of the quantum coefficients were tried and all the lines were very close to each other, indicating how versatile can $c_q = \sqrt{2}\rho_n\nu e^2/\epsilon\sqrt{\pi^7}\xi_0\hbar$ be. It should however be notified that this value of c_q seems to be of the right order of magnitude, and we will talk about that more in details in the next section. It is quite hard to have a firm affirmation close to T_c but

in the next paragraph we take a closer look at the low temperature part of the phase diagram to try to get out of that problem.

High field: $H_{c2}(0)$ **and** $H_m(0)$ In Sec. 3.2.2.1 we suggested to $H_{c2}(0)$ might be higher than the inferred value from the scaling analysis due to the remaining visible fluctuating part of $\gamma(H)$ in the field sweep measurements at very low temperature when $H_{\perp ab}$. However, the melting line is still below 15T at the lowest temperature available. In Sec. 1.2.3.3 we saw that one of the influence of the quantum fluctuations is to split the melting line from the upper critical field at zero temperature. This is why we think that some quantum fluctuations are possibly observable in our phase diagram. In Fig 3.18 $\gamma(H)$ at 0.7K varies at least until 16T. If the melting line lies around 15T at $T = 0$K that would mean that quantum fluctuations are clearly visible. However, we are not sure where is exactly $H_{c2}(0)$. This is why we propose a figure (Fig. 3.24) where we plot the thermal and quantum coefficients, c_{th} and c_q (from Sec. 1.2.3.3) as a function of a possible $H_{c2}(0)$ based on a fit of the melting line we found. It is however still tricky to have a precise value of the thermal and quantum coefficient due to the uncertainties of the fit : at 14.2T for example the uncertainty of c_q is of 0.02, indicating that there might be still quantum fluctuations in this region. However that uncertainty reduces when the possible value of H_{c2} get higher and is less than 5% at 15.5T.

 In Fig. 3.24, we see that the thermal coefficient remains mainly the same even by changing drastically the value of $H_{c2}(0)$. On the other hand, the quantum coefficient seems to have a wide range of variations and could even exceed the thermal coefficient at a value of $H_{c2}(0) = 15.5$T which is clearly possible based on the field sweep measurements. Considering the value of $\rho_0 \approx 5\mu\Omega$.cm from Bristow et al. (136) and the values of ξ_0, ϵ and c_L obtained before one gets that $c_q \approx 0.2\nu$. In Sec. 1.2.3.3 we explained that ν should be of the order of unity, which seems to work perfectly here. By doing the same with the thermal coefficient one finds a value of G_i close to 10^{-3} which is in a very good agreement with the inferred value from before.

The main point in this analysis is not to affirm that quantum fluctuations must be present in FeSe, but from our data we can not totally rule out this type of fluctuations.
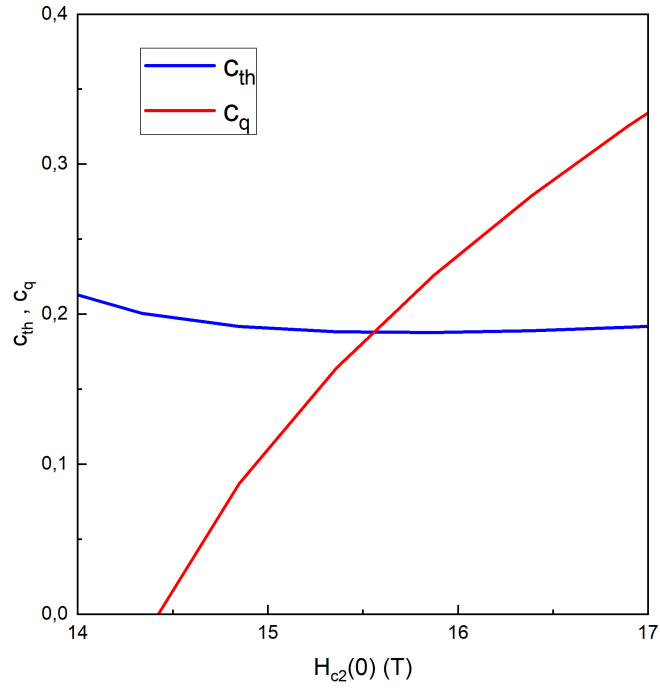
Figure 3.24: Thermal and quantum coefficients as a function of $H_{c2}(0)$. c_q and c_{th} refer respectively to Eq. 1.70 and Eq. 1.69. Here we performed a fit of the data extracted from melting (cf. Fig. 3.21) and the value of the upper critical field at $T = 0K$ was used as a variables. c_{th} and c_q were used as fitting parameters and we plot here the values of c_{th} and c_q for extracted from fits for different values of $H_{c2}(0)$.
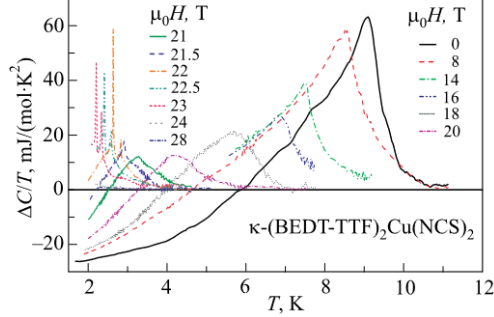
Figure 3.25: Temperature dependence of the specific-heat difference between the superconducting and normal state of κ-(BEDT-TTF)$_2$Cu(NCS)$_2$ in magnetic fields applied parallel to the superconducting layers. From ([1])

3.2.3 FFLO phase

In the next section, we shall focus on the high field region of the phase diagram and the possibility of a FFLO phase is discussed.

3.2.3.1 Absence of thermodynamic proof

In the standard case, two transitions should be observed when a FFLO phase appears. First of all, a first order transition between the BCS state and the FFLO state, and then a second order transition between the FFLO state and the normal state. A true thermodynamic proof of the observation of a FFLO phase would be to see such transitions in our data. For example, Fig. 3.25 shows the work done be Lortz et al. in [(137)], where they attribute the two different transitions in κ-(BEDT-TTF)$_2$Cu(NCS)$_2$ to the presence of a FFLO phase in that compound. The second order phase transition is observed all over the temperature range, from 0K to T_c and at low temperature a first order peak appears which is the sign of the transition between the uniform and modulated superconducting phases.

From our data, and the available magnetic fields, it was quite hard to have a strong evidence of a FFLO phase since no first order transition was observed. This is why we dedice to investigate on the existence of a FFLO phase by looking at two phase diagrams. First, a $H - T$ phase diagram that should be marked by the appearance of a high field phase and a deviation from the standard behaviour of H_{c2}. And second an angle-field phase diagram. Since the FFLO phase is very sensitive to the sample

orientation with field, if a FFLO phase is visible when $H_{||ab}$, the anomalies due to that phase will disappear when the sample rotates. Also it is possible that the sample was not perfectly aligned with the field in our first experiments and that might be the reason why we did not observe any first order transition.

3.2.3.2 $H - T$ phase diagram

The $H - T$ phase diagram of FeSe reveals a feature when looking at direction where $H_{||ab}$. The upper critical field, measured in Fig. 3.20, seems to show some kind of discontinuity at high field at a temperature T^*, where the melting joins the upper critical field. Below T^* no melting is observable and the upper critical field shows a kink at the same temperature. This could be an indication of a FFLO phase. In fact, when fitting the upper critical field, with the optimal Maki parameter, the WHH fitting line (see Eq. 1.77) does not coincide with our data at low temperature, below T^* but shows a good agreement before that temperature (see Fig. 3.20). Brison et al. [(23)] showed that a Maki parameter larger than 3.4 might induce a FFLO phase (see Fig. 1.14). This is the case for our sample when $H_{||ab}$ and adding FFLO phase in our fitting routine might help to get a better agreement at high fields. Based on Eq. 1.78, for a given temperature, the curve $H(Q)$ is calculated numerically. Among all possible values of Q, the only one which will be realised in the system is the one found at the minimum of $H(Q)$. Thus, it is possible to have access to both H and Q. Using the value $\alpha_{M,||} = 4.5$ and $H'_{c2} = -13.8 T.K^{-1}$ found before, we plot Fig. 3.26 with help of Eq. 1.78. This time a very good agreement between our data and the fit over the entire phase diagram was found. The magenta line in this figure shows a purely Pauli limited upper critical field, and the dotted line the difference between a uniform BCS state and a modulated FFLO state. In a 3D system with strong Pauli limitation, the FFLO phase should only occupy a small portion of the phase diagram and this is what is found in our analysis since the FFLO phase field range is only about 2T at zero temperature. However, it should be notified that the incertitude on H_{c2} at low temperature, based on the transition width in zero field, is also about 2T. This makes it quite difficult to have a clear conclusion on the existence or not of a FFLO phase.

(a)

(b)
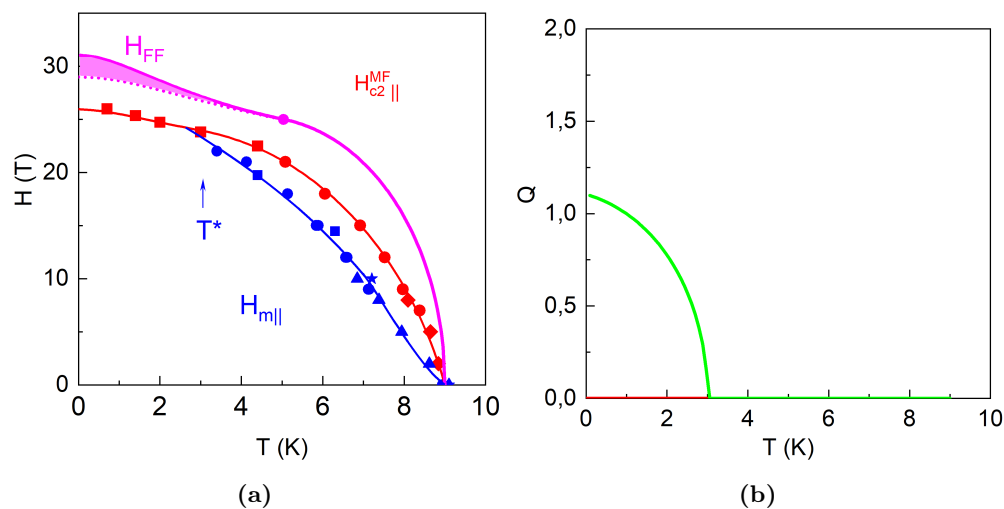
Figure 3.26: A possible FFLO phase with $H_{||ab}$. (a) is a $H - T$ phase diagram of FeSe for $H_{||ab}$, taking into account a possible FFLO phase. Blue (red) symbols represent the melting data (upper critical field data). The blue line is only a guide for the eyes of where the melting line could be. The continuous red line is a fit performed using Eq. 1.78 for the upper critical field, assuming a FFLO phase with a modulation vector $Q(T)$ represented in (b). For comparison, the solid and dotted magenta line are second- and first-order transitions calculated for the pure Pauli-limited case. The shaded area denotes the extent of the FFLO region in the $H - T$ plane. T^* is the temperature where the melting and the upper critical field lines meet.

Kasahara et al. [[92]] found that thermal conductivity is a very good probe to check on the presence of a FFLO phase. A comparison of their data within our phase diagram is given Fig. 3.27. They also measured resistivity and interestingly the progressive disappearance of the vortex melting anomaly until T^* in our data is in good agreement with the reduction of the resistive transition width in their data attributed to the emergence of the FFLO phase. They found an anomaly close to 24T from 0K to 2K, in thermal conductivity, which is assigned to the entrance into the FFLO phase, where the melting transition and the upper critical field would meet in our phase diagram. However, we do not observe any transition at such a field and our data correlates much better with a kink-like minimum observed in the thermal conductivity, which would correspond to our upper critical field deduced from our mean-field analysis for $H >$24T. The zero resistivity point matches quite well the melting line in the low field region. In the end, our phase diagram is found to be roughly in good agreement with the one of Kasahara et al. A comparison is also made with data from Ok et al. [[86]] deduced from resistivity measurements. The conclusion is the same : the points deduced from resistivity measurements matches very well the melting until it disappears in our phase diagram. Then it follows the dependence of the upper critical field for $H >$24T, which was also assigned to the emergence of a FFLO phase by Ok et al. However as we explained before the FFLO phase should be marked by a first order transition in the specific heat which we do not observe here. This is why further investigations are needed to affirm the presence of a FFLO phase.

3.2.3.3   Rotation of FeSe

In this section we will talk about a possible observation of a thermodynamic proof of a FFLO phase in FeSe. The sample was mounted on a rotator and we applied the protocol as described in Sec. 2.2.4.1 in order to align as much as we could the sample with the magnetic field. The angle resolution was found to be approximately 0.05^o, estimated from the resolution of the Hall probe mounted on the set-up. The sample was then rotated in both directions starting from $\theta = 0^o$ when the field is aligned with the FeSe layers at a temperature of 1.85K, the maximum reachable temperature with this setup (slightly higher than temperatures of Fig. 3.18, where the maximum temperature was 1.2K and the sample was aligned in the field). The same dependence of the specific heat was observed from both sides (anti clockwise and clockwise). The FFLO phase is
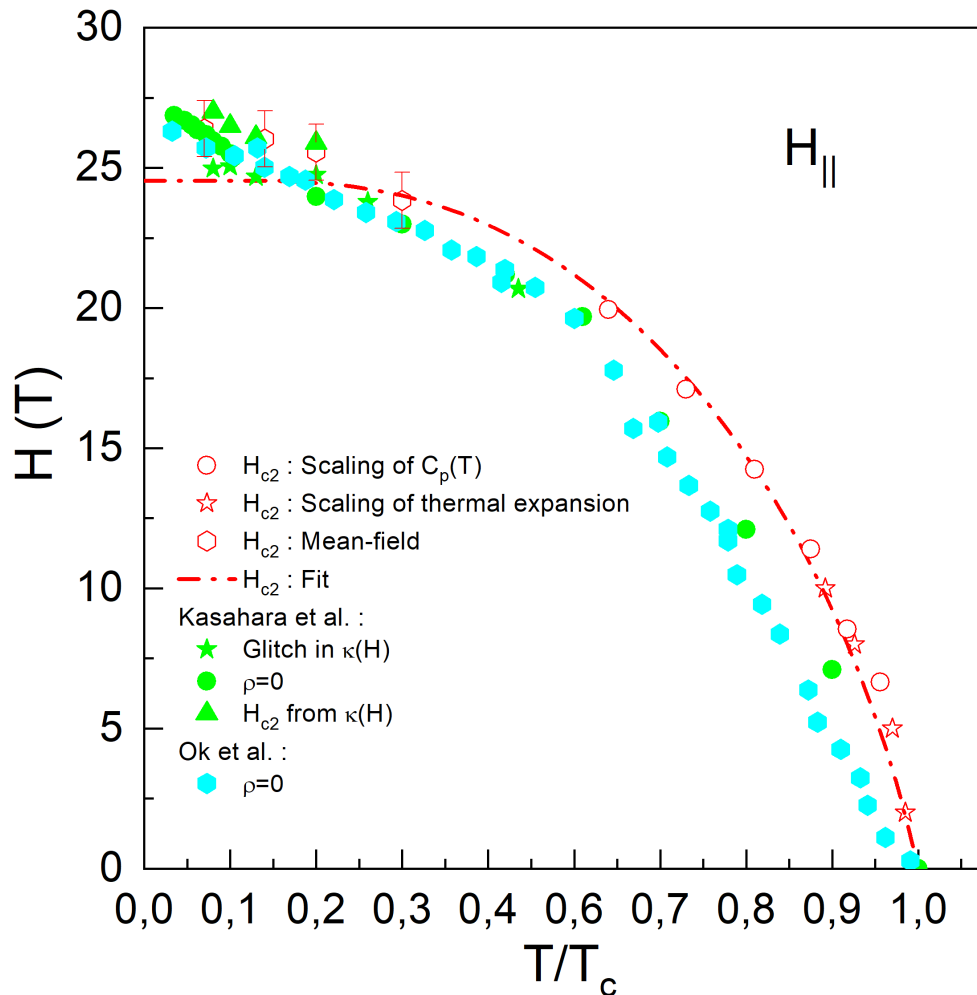
Figure 3.27: Comparison of our phase diagram (in red) with data from Kasahara et al. (in green) [[92]] and Ok et al. [[86]] (in blue). The dashed line corresponds to a fit of the upper critical field without any FFLO phase. Kasahara et al. obtained their data measuring the resistivity and thermal conduction and Ok et al. with resistivity. Our data show rather a good agreement with their data at high field. At low field a small discrepancy is observed, certainly due to the fact the our data are deduced from specific heat measurements, while other groups measure the resistivity and therefore certainly the melting anomaly.

known to be very sensitive to the orientation of the sample with field. Typically for β''-$(ET)_2SF_5CH_2CF_2SO_3$ it was found that the FFLO phase only appears for $\theta < 0.4^o$. In the end the measurements revealed an intriguing feature at high fields. Close to 0° several steps of 0.1^o were made in order to look for a first order transition, but none was found for an angle range of 0-25° The most representative data are show in Fig. 3.28.

Looking at Fig. 3.28 we observe a broad feature with a maximum at 24.7T for low angles. The maximum of the specific heat is noted as H_{max}, and the higher the angle is, the more H_{max} shifts to low fields. Three other features are observed. First, a kink close to 24T, noted as H_{kink}. Second, a change in the slope of the field dependence of the specific heat at low field, noted as H_{b1} and a second one at higher field, noted as H_{b2} before the specific heat is constant. We plot a phase diagram as a function a field and angle in Fig. 3.29 where all these features are displayed.

Ok et al. [(86)], did similar measurements of FeSe for various angles and also found some noticeable features. They measured TDO frequencies, and torque magnetometry and the their data is displayed also in Fig. 3.29 for comparison. They found two high field phases at low temperatures that they believe to be related to nesting effects as shown in Fig. 3.30 (c) and (d). The first transition H_1 has been attributed to a Spin Density Wave only stable in the superconducting phase while the second one could be a FFLO phase. It is argued that the FFLO phase due to the intraband superconducting coupling can be a candidate, dominantly in the α Fermi sheet, which has the largest superconducting gap. Their angle dependant phase diagram shows that the FFLO phase could appear in between 22T and 25T for angles smaller than 15° and temperatures smaller than 2K. However, such a large range of angle where a FFLO phase is observable is quite surprising, when looking at other materials we cited before.

Our results match on some points the article of Ok et al. as shown in Fig. 3.29. First, H_{max} matches very well the TDO data of Ok et al. H_{b1}, which seems to be the extension of H_{max} at higher angles, is also in quite a good agreement with the TDO data. Second, a feature, H_{kink}, is observed at high fields for angles smaller than $\approx 10^o$ in our case, but the Korean group observed it for a wider angle range but at a smaller temperature with torque magnetometry. They found a nesting condition at $H \approx 24T$ which is the same as H_{kink}. However, the feature we denoted as H_{b2} is also at the same field for high angle
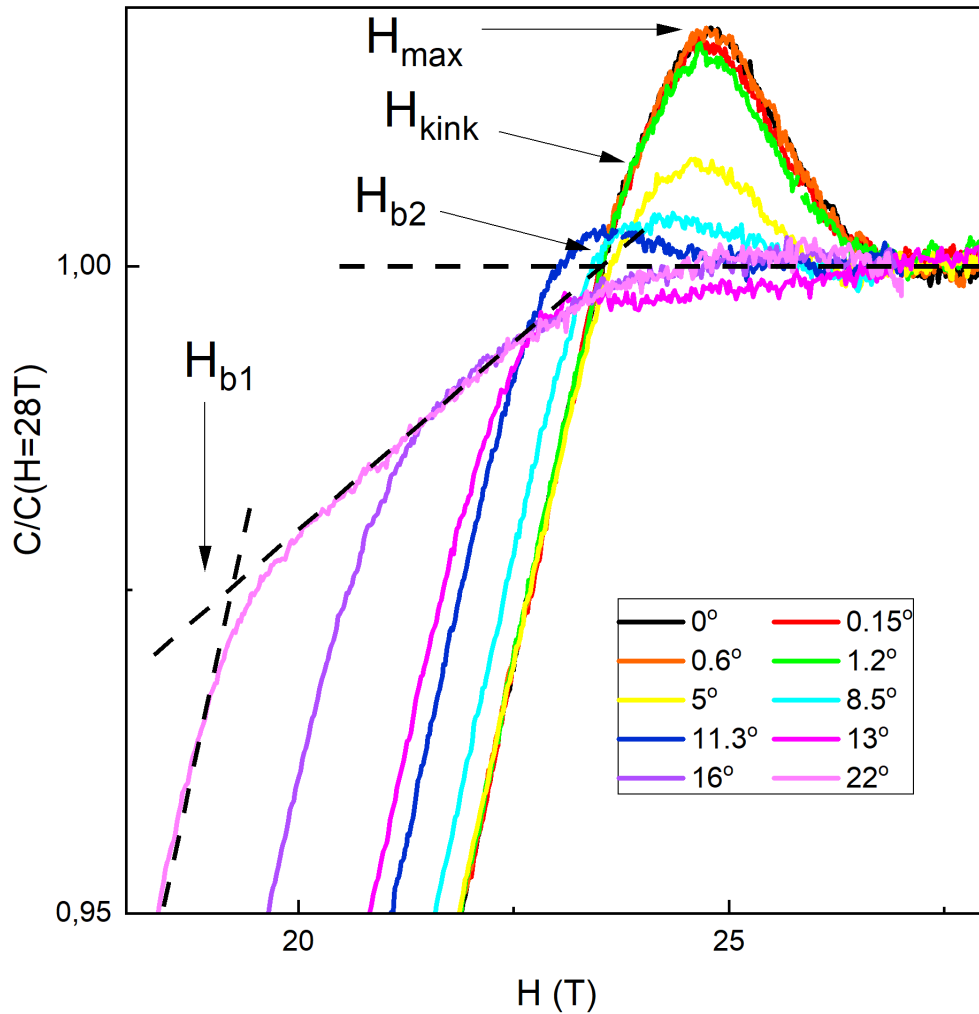
Figure 3.28: Normalized specific heat of FeSe as a function of the magnetic field for various angle. θ is the angle between the FeSe layers and the magnetic field. We measured at a temperature of 1.85K. H_{max} is the maximum of the specific heat. H_{kink} is a small break in the slope when the normalized specific heat is over 1. H_{b1} is a change in the slope of the dependence of the specific heat at low field and H_{b2} is the field before the specific heat is constant.
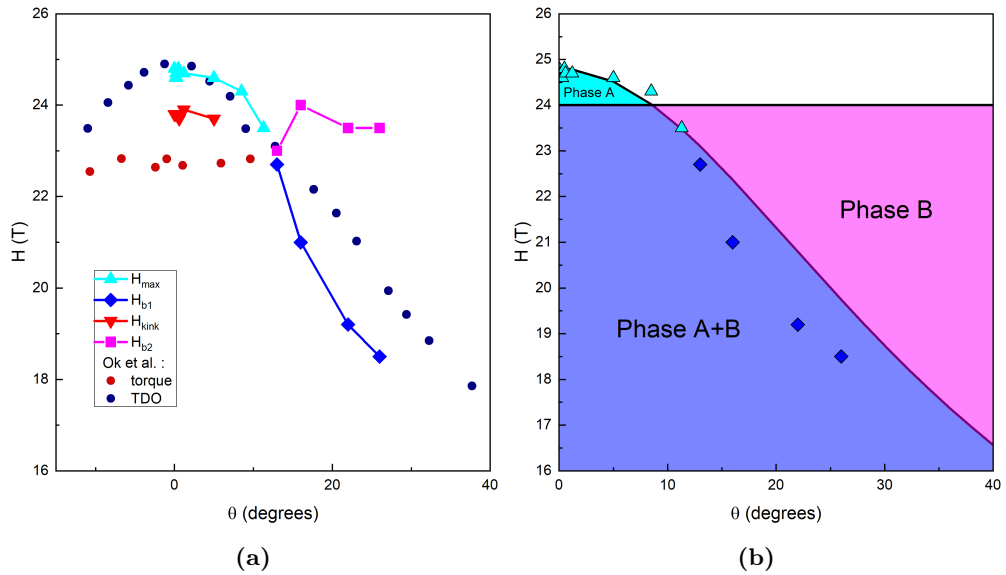
Figure 3.29: (a) Phase diagram of FeSe as a function of the magnetic field and angle at 1.85K. All measured fields are inferred from Fig. 3.28. Measurements from Ok et al. [86] are displayed for comparison. (b) Schematic interpretation of the phase diagram in (a). The phase A as the same dependence in angle as the upper critical field, and should therefore be related to superconductivity. The phase B is constant for every angle at 24T. Data points correspond to the ones in (a)
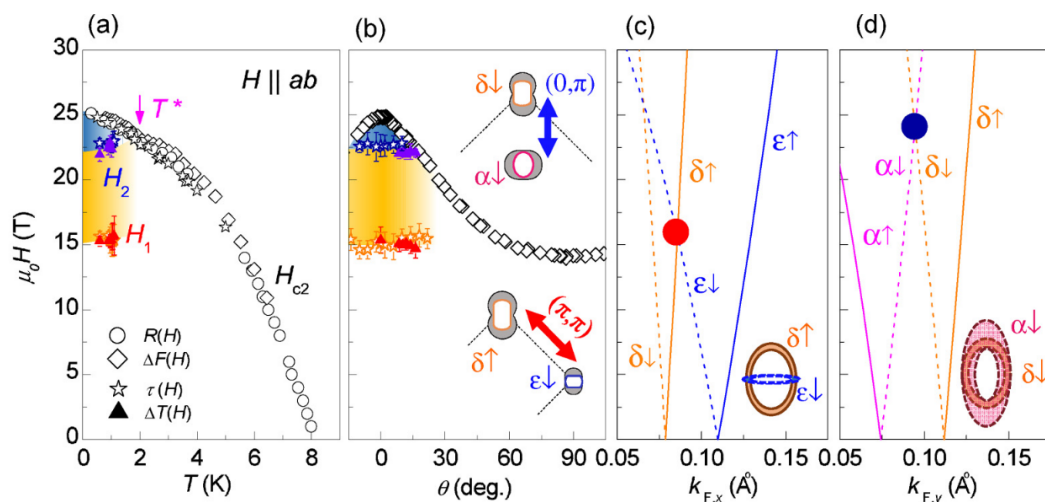
Figure 3.30: Magnetic phase diagrams of FeSe as a function of temperature (a) and orientation (b). Magnetic field dependent Fermi vectors along two orthogonal directions of k_x (c) and k_y (d) for $\uparrow$ (solid line) and $\downarrow$ (dashed line) spins in the plane of $k_z = 0$. The good matches between the Fermi vectors of $\epsilon \downarrow$ and $\delta \uparrow$ Fermi surfaces along the k_x direction near H_1 and also between those of $\delta \downarrow$ and $\alpha \downarrow$ Fermi surfaces along k_y direction near H_2 are indicated by red and blue circles, respectively. The corresponding nesting conditions between different pairs of the spin-split Fermi surfaces at H_1 and H_2 are schematically shown in the insets. From (86)

values and could be the extension of H_{kink}. This is our interpretation given by Fig. 3.29b. In such a scenario H_{max} and H_{b1} have the classical angular dependence of characteristic field of anisotropic superconductors, $H_c(\theta) = H_{c,\perp} \sqrt{(\cos{(\theta)})^2 + \Gamma^{-2} \sin{(\theta)}^2}$ and are therefore attributed to a superconducting phase, named phase A in Fig. 3.29b. The anomaly detected by Ok et al. around 23T with torque magnetometry and magnetocaloric effect and attributed to the emergence of the FFLO phase seems to hold after the destruction of phase A at high angle values in our data when looking at H_{kink} and H_{b2}. They are both very close to 24T and could therefore be related to the appearance of another phase, named phase B in Fig. 3.29b. Such an interpretation of our data should therefore contradicts a scenario where a FFLO phase appears at high field since we still observe the anomaly related to that phase in the normal state. However, it is still ambiguous to call the magenta region of our interpretation of the phase diagram the normal phase since the specific heat is not constant in that region as seen in Fig. 3.28. This is an intriguing feature which deserves more investigations.

3.2.4 Conclusion on the study of FeSe

We have determined the full $H - T$ phase diagram of FeSe for both field directions. Our specific heat data reveal the presence of a vortex lattice melting transition down to zero temperature when $H_{\perp ab}$ and down to T^*=3K when $H_{||ab}$. A scaling analysis was performed, proving the existence of Gaussian fluctuations in our system. A good agreement between the experimental and theoretical values of r_T and r_H used for scaling was obtained. That scaling analysis allows to find the temperature dependence of the mean-field upper critical field. We then studied the effects of orbital and Pauli depairing on that curve. Our analysis of the temperature dependence of the upper critical field relies only on one fitting parameter, which is the Maki parameter found when $H_{\perp ab}$. All other quantities where found using our measurements. It was found that a possible effect of the Pauli depairing was already present in that direction, whereas it is absolutely impossible to neglect it when $H_{||ab}$, leading to $\alpha_{M,||} \approx 4.5$. We argue that the predominance of the paramagnetic effects at low temperature, causing the reduction of the upper critical field, causes the disappearance of the vortex lattice melting below T^* when $H_{||ab}$.

3. VORTEX LATTICE MELTING AND UPPER CRITICAL FIELD IN FESE$_{1-X}$S$_X$

The melting line was also analyzed using a Lindemann criterion, which leads to a Lindemann constant of $c_L = 0.15$. It is however still complicated to know the real nature of the fluctuations causing the melting. In fact at low temperature field dependence of the specific heat shows a broad transition to the normal state that could be due to quantum fluctuations. While the thermal coefficient, c_{th} used to fit our data is quite robust, it is also possible that quantum fluctuations were observed.

When the field is along the Fese planes a slight deviation from the WHH curve was found at low temperature, right after the vortex lattice melting transition joins the upper critical field line. We argue that it might be related to a FFLO phase. Our $H - T$ phase diagram was found to be roughly in a good agreement with measurements from Kasahara et al. and Ok et al. which assigned the upturn in the temperature dependence of the upper critical field to the appearance of a FFLO phase. However no first order transition was observed in our data, which would be the sign of the entrance into a FFLO phase. Therefore a angular study was conducted. It reveals the presence of 4 anomalies visible at different angle values. We assigned these features to two different phases : one related to superconductivity and another one at a fixed field value for every angle, even outside the superconducting phase. If such a phase exists it would contradicts the existence of a FFLO phase in our sample.

3.3   Study on FeSe$_{0.88}$S$_{0.12}$

In Sec. 1.3.2 we introduced the phase diagram of sulfur substituted FeSe. In this thesis we focused on other batches with 12% substitution, giving FeSe$_{0.88}$S$_{0.12}$ samples. We will focus on two batches: AAH15 and AAH55, both having a concentration in sulfur of 12%. These samples are still under the nematic dome in the substitution-temperature phase diagram, and are also close to the maximum T_c observed in that system. In the following sections we will introduce our resistivity and specific heat measurements in order to look once again at the melting properties in our samples. The idea behind that is to measure the complete $H - T$ phase diagram and compare it with Fese but when T_s is reduced, and with changes in the electronic structure.

3.3.1   Resistivity data

Resistivity seems to be a good probe to look at the vortex lattice melting. In fact the resistivity of the material undergoes a regime close to T_c where it is going from a normal behaviour to a superconducting behaviour where it reaches zero resistivity. However the zero resistivity point is not a probe for the upper critical field line but rather for the melting of the vortex lattice since when the flux lines can move freely some dissipation effects will take place in the material. Kwok et al. studied for example the melting line in YBCO with resistivity [(138)]

3.3.1.1   Raw data

We show here the temperature dependence of the normalized resistance of two representative samples of our batches. AAH55n2 has been measured with a lock-in amplifier at 10 Hz and using a current of 0.05mA. AAH15n4 has been measured with a PPMS setup with a frequency of 6Hz and a current of 1mA. Both of our batches show a residual resistivity ratio, $RRR = \rho(300K)/\rho_n(0K)$ of approximately 40, similar to the one observed by Kasahara et al. in FeSe in [(28)], where we extrapolated the resistivity to zero temperature to obtain $\rho_n(0K)$.

One of the distinctive features in the system is the magnetoresistance observed in the nematic state similar to what is observed in Fig. 3.31. Fig. 3.32 shows that the
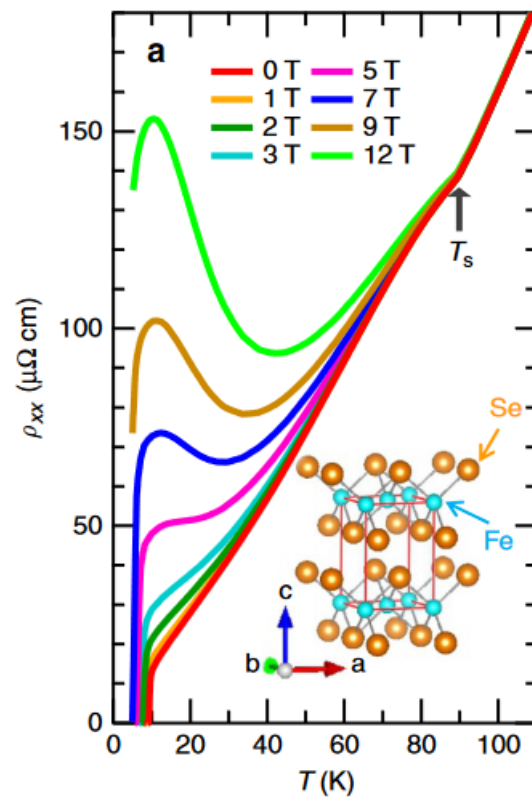
Figure 3.31: Temperature dependence of ρ_{xx} in magnetic fields of FeSe when $H_{\perp ab}$. From [[139]]

superconducting transition shift with the magnetic field and also becomes broader due to fluctuations. A surprising feature also arises with stronger magnetic field ($H > 12T$) at low temperature. The resistivity is going down until a temperature of 8K and then starts to go up and will eventually go down to become superconductive. The upturn is associated to high magnetoresistance. The magnetoresistance being mainly influenced by the product of the scatering time of the hole and electron bands, this is an indication of high quality crystal [(139)]. The down turn, observed also for field higher than the upper critical field, was assigned to large superconducting fluctuations in FeSe by Kasahara et al. in Ref. (139), which tend to reduce the resistivity. However, it seems that contrary to FeSe no downturn is observed at very high fields. It was found by Bristow et al. in [(136)] that such a behaviour is observed for sample for a concentration higher the 10% and within the nematic phase (see Fig. 3.31 for comparison). It is argued that since T_c and the upper critical field are comparable with FeSe, that change in the resistivity slope must be driven by field induced effects influencing the scattering or electronic properties. It is believed from ARPES measurement that close to $x \approx 11\%$, the β hole pocket centered at the Z point crosses the Fermi level [(62)]. Interestingly in Fig. 3.33 the curve at 1K displays some quantum oscillations which matches very well the one observed by Coldea et al. in [(82)]. In the same article, it is explained that for a sulfur substitution of 12% the quantum oscillations are dominated by the appearance of the inner β hole band and one of the frequency observed for that band it close to 100T which is qualitatively what we observe. It means that the upturn at high field and low temperature must be related to the appearance of the β hole band.

Fig. 3.33 displays the resistance dependence with field. The magnetoresistance usually follows a H^2 dependence in systems with a single dominant scattering time [(136)]. This is however not the case in our data. Fig. 3.33 shows a very good agreement with a $H^{1.3}$ law at 1K, 5K and 12K. This indicates that the magnetoresistance behaviour is not related to only one scattering time. Bristow et al. [(136)] found that outside of the nematic phase one recover the H^2 behaviour, suggesting that inside the nematic phase the Fermi surface of FeSe$_{1-x}$S$_x$ distorts anisotropically and unusual types of scattering could appear, giving rise to diverse scattering time.

(a) AAH55n4

(b) AAH55n2
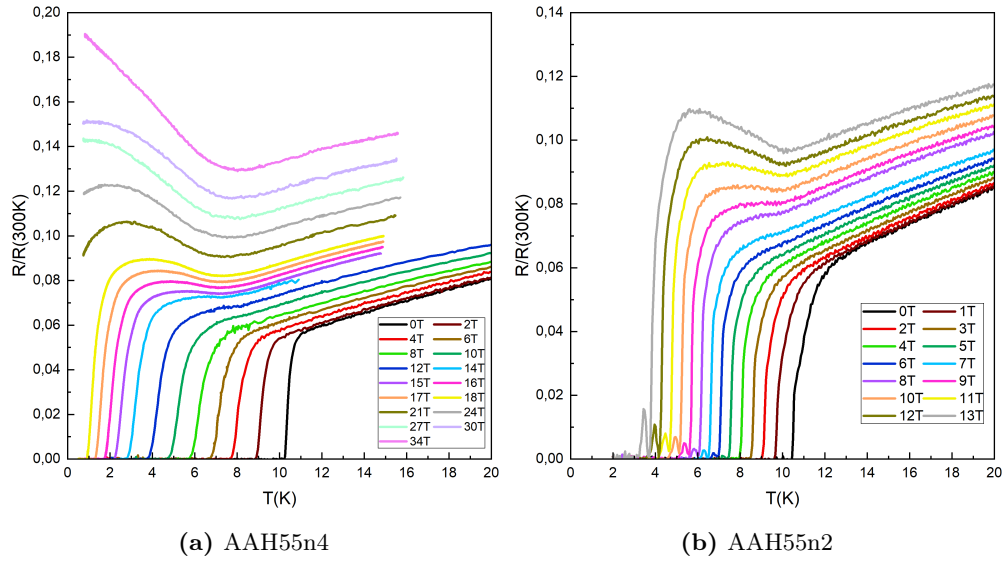
Figure 3.32: Temperature dependence of $R/R(300K)$ of FeSe$_{0.88}$S$_{0.12}$ samples with $H_{\perp ab}$
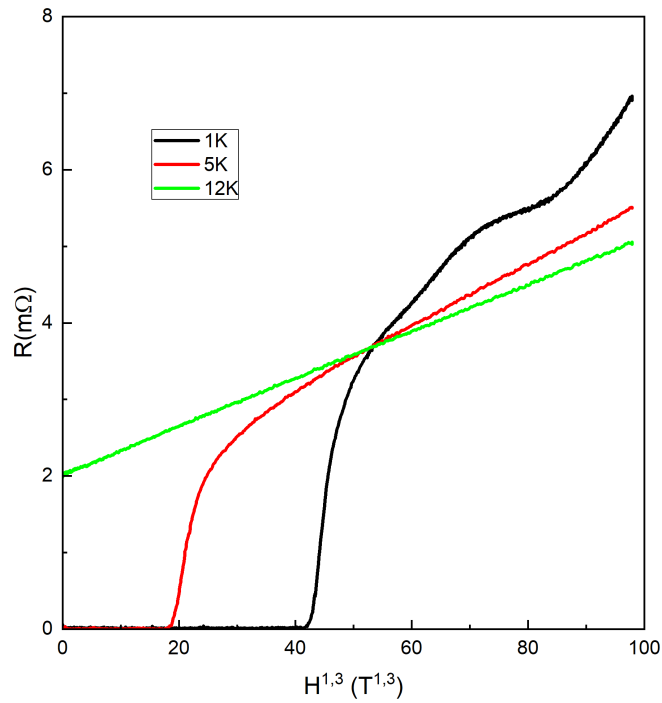
Figure 3.33: Resistance of AAH15n4 as a function of $H^{1.3}$
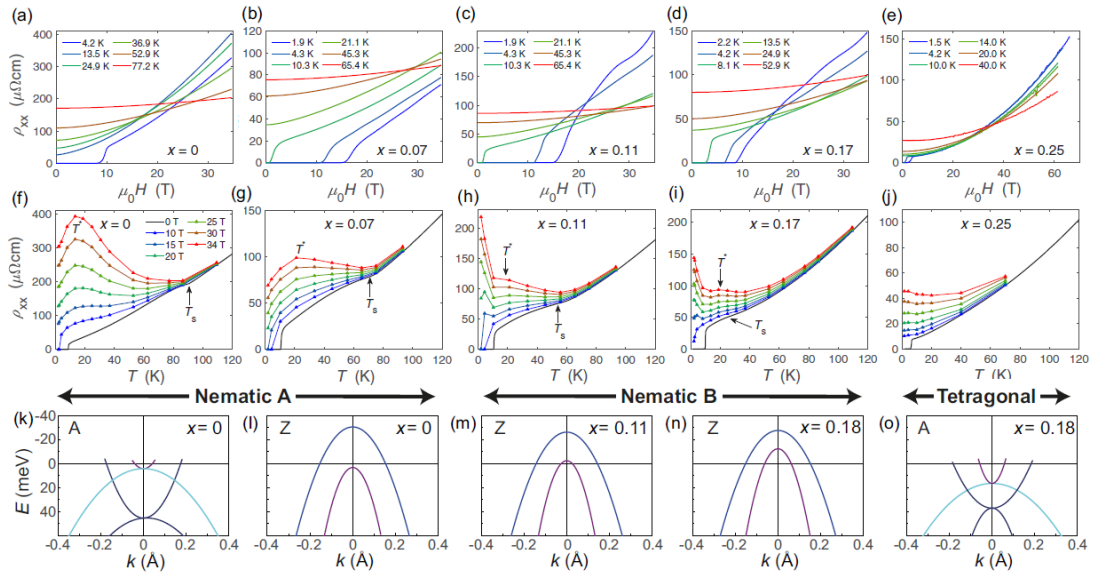
Figure 3.34: (a)–(e) Field-dependent in-plane resistivity at different temperatures for different compositions, inside and outside the nematic phase. (f)–(j) Resistivity against temperature in zero field (solid line) and at fixed magnetic fields (symbols), as extracted from the top panel for different compositions. (k)–(o) Schematic band dispersion at low temperatures at two high symmetry points at the top of the Brillouin zone, Z and A, for different compositions. From [[136]]. The behaviour of the 11% sample is reminiscent of what is observed in our samples, indicating that features we observe might me related to the emergence of the hole band.
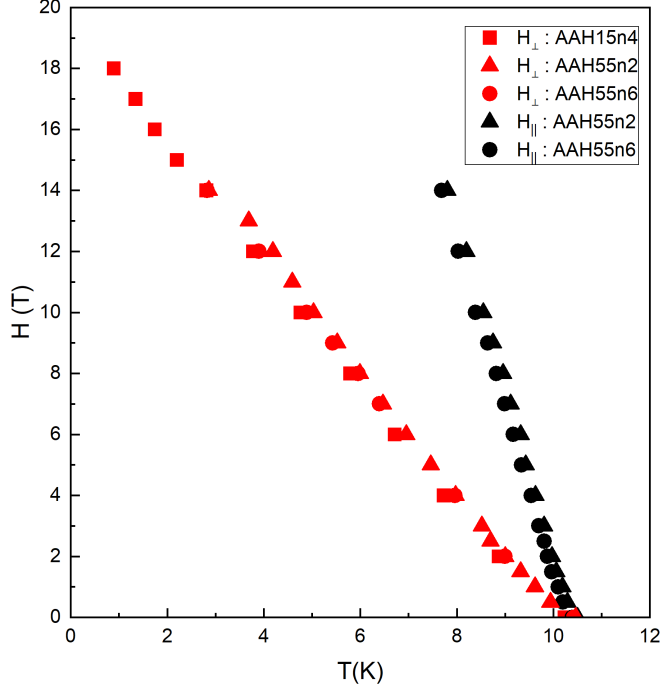
Figure 3.35: $H - T$ phase diagram showing the $R = 0\Omega$ point for diverse samples of
FeSe$_{0.88}$S$_{0.12}$. Since the transition is very abrupt, we estimate that the incertitude for the
$R = 0\Omega$ point is smaller that the symbols width.

3.3.1.2 Phase diagram

Now that we have a better understanding of the behaviour of the resistance in our
sample we will focus on the vortex lattice melting. First, our samples show a higher
T_c (the criterion here is the zero resistance point) compare to FeSe, with T_c=10.3K for
AAH15n4 and T_c=10.4K for AAH55n2. A comparison with another sample of the same
batch (AAH55n6) gives a maximum shift in T_c of 0.1K. We can also extract the point
where $R = 0\Omega$ for different magnetic field and plot a $H - T$ phase diagram showing the
melting line. This is what is done in Fig. 3.35. We will give a more detailed analysis of
the phase diagram when we also have the points from the specific heat data.

3.3.2 Specific heat data

Raw data   Once again we measured the specific heat of our samples in order to prop-
erly identify the vortex lattice melting and try to have the dependence of the upper
critical field. For the characterization of the sample with zero field measurement we

(a) Field perpendicular to the layers **(b)** Field parallel to the layers
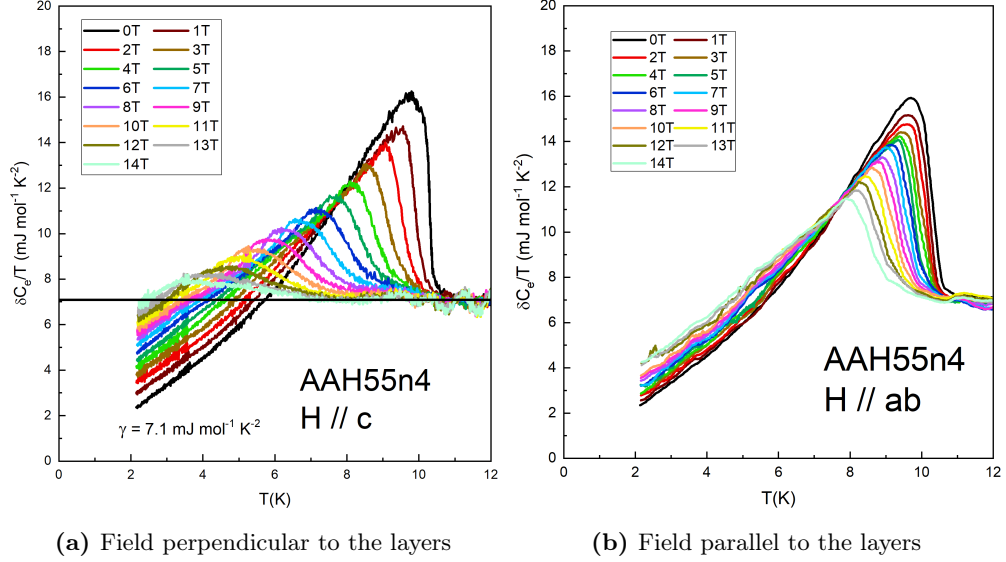
Figure 3.36: Temperature dependence of $\delta C_e/T$ of the AAH55n4 sample

refer to Sec. 3.1. Fig. 3.36 shows $\delta C_e/T$ as a function of temperature for different magnetic fields for the sample AAH55n4. Here a fit was performed above T_c at 0T and 14T to subtract the phonon contribution, in the same condition we used for FeSe. We identify here β_3=0.44 mJ mol^{-1} K^{-4} and $\gamma = 7.1$ mJ mol^{-1} K^{-2} giving a 10% rise in the values compared to FeSe. These values give us a ratio $\Delta C/\gamma_n T_c$=1.3, once again close to the one observed in FeSe which was 1.3. This value smaller than the BCS one is ascribed either to the anisotropy of the superconducting gaps or the presence of multiple gaps. Once again our data revealed a broadening of the transition with increasing magnetic field, which indicates that we can try once again to scale our data to the Li and Rosenstein scaling function; that will be discussed in Sec. 3.3.3.2.

3.3.3 Analysis of the data

In the following section we will basically go through the same analysis as we did in the case of FeSe. We will not give the same amount of details but only notify the main steps of the analysis.

143
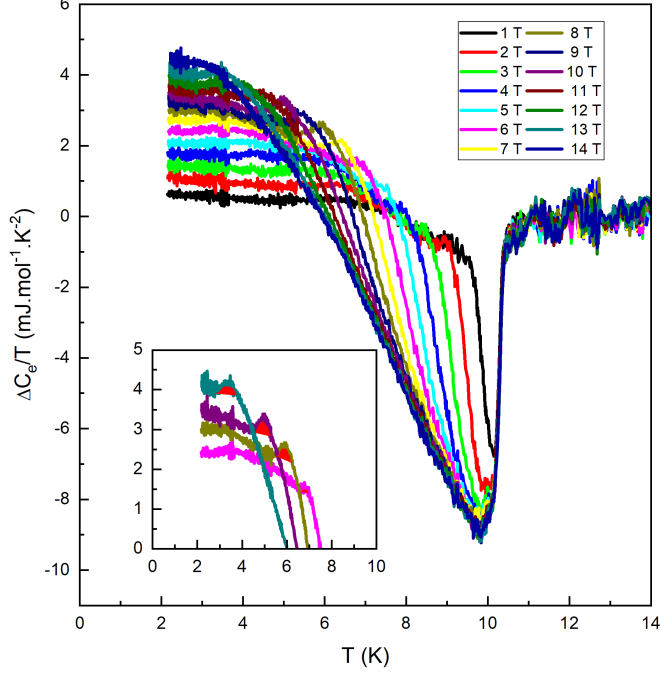
Figure 3.37: Temperature dependence of $\Delta C_e/T$ of the AAH55n4 sample with field perpendicular to the layers. Inset: Zoom in order to have a better view on the excess of specific heat before the transition. The red shaded area correspond to that excess.

3.3.3.1 Melting

We find a value of the Ginzburg number G_i close to the one of FeSe, which gives $G_i = 1 \times 10^{-3}$, using the same reasoning as we used for FeSe in Sec. 3.2.1. Being of the same order of magnitude it would be logical to also observe melting in the 12% dopped samples. We displays the substraction of the 0 T curve to the in-field curves in Fig. 3.37 for the AAH55n4 sample, where we clearly observe once again an excess in the specific heat just before the superconducting transition starts to happen but still no first order peak (see inset of Fig. 3.37), certainly meaning that we have once again a solid to liquid transition. That excess of specific heat shows the same properties in position or amount as in FeSe. From such a plot we extract the melting anomaly to put it in the $H - T$ phase diagram that we display later on.

3.3.3.2 Scaling analysis

Since our scaling analysis seemed to work quite well on FeSe we decide to go for the same analysis again in order to get the upper critical field line in the $H - T$ phase diagram. However, we still need to check what field is needed to reach to LLL, we find here $H_{LLL} = G_i H'_{c2} T_c = 45$mT for $H_{\perp ab}$, and 205mT in the other direction, and we will perform the scaling analysis only at fields higher than these values. We once again use second order polynomial fits to obtain the dependence of δC_{mf}. FeSe and FeSe$_{0.88}$S$_{0.12}$ having similar T_c, G_i and melting line, we first tried to use the values of r_T that we found for FeSe. It turns out that the scaling works very well as it can be seen in Fig. 3.38, where we show the scaling analysis from the temperature sweeps of the AAH55n4 sample. When comparing this figure with the one obtained in the case of FeSe (cf Fig. 3.15a), it is clearly visible that our data are noisier for the doped samples. It is certainly due to two factors, first the doped samples are smaller than the FeSe samples, and secondly the data were obtained using the Dual Slope technique for the doped samples and the AC technique for the FeSe samples. We used here $r_{T\perp} = 60$K$^{-1/3}$T$^{2/3}$ and $r_{T||} = 160$K$^{-1/3}$T$^{2/3}$, when the theoretical values where supposed to be $r_{T\perp} = 66$K$^{-1/3}$T$^{2/3}$ and $r_{T||} = 184$K$^{-1/3}$T$^{2/3}$. This still shows a good agreement between the inferred values and the theory. Although, we still have the same problem at high fields where it becomes harder to get a good agreement between the theoretical curves and our data. In FeSe when $H_{\perp ab}$ we could only get a correct scaling for a maximum field value of 9T. However, for FeSe$_{0.88}$S$_{0.12}$, due to a slightly higher upper critical field, it seems that we can still perform a correct scaling for a field of 11T. This is once again due to the paramagnetic effects being more important at high fields.

3.3.4 Comparison with FeSe

Now we can plot the complete $H - T$ phase diagram of FeSe$_{0.88}$S$_{0.12}$. Fig. 3.39 shows the melting line extracted from temperature and field sweep measurements and the upper critical field deduced from the scaling analysis for the AAH55 batch. We consider now a difference in the derivative of H_{c2} close to T_c. Considering an initial slope $dH_{c2\perp}/dT = -4$T K^{-1} and $dH_{c2||}/dT = -18.5$T K^{-1} and a Maki parameter $\alpha_{M\perp} = 1.3$ and $\alpha_{M\perp} = 5.2$ we find the black and red lines in Fig. 3.39. These values

(a) $H_{\perp ab}$ **(b)** $H_{||ab}$
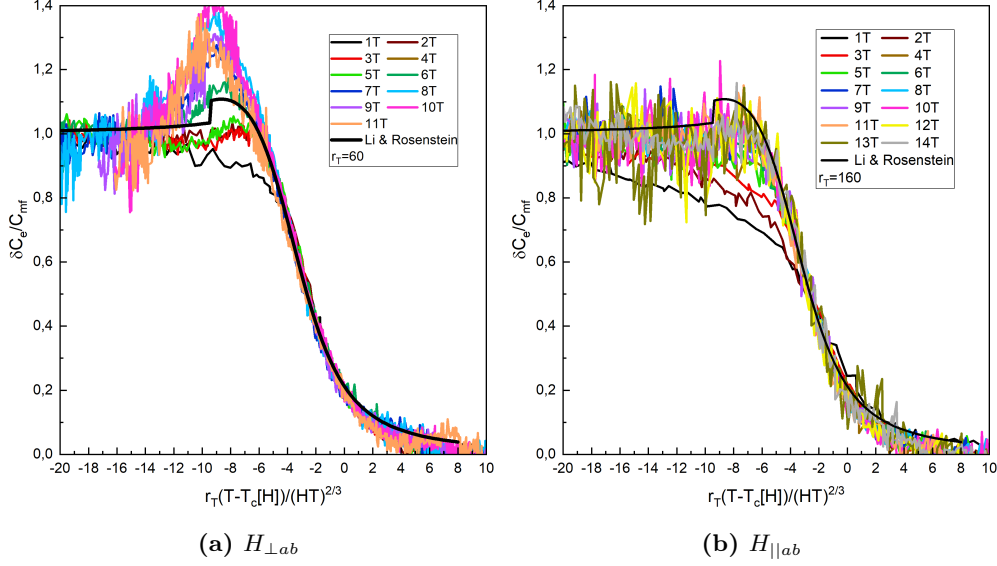
Figure 3.38: 3D-LLL scaling of the temperature dependent specific heat of the AAH55n4 sample. The black curve is the theoretical scaling line following the publication of Li and Rosenstein [(126)] while the colored curves are the one fitted from our data for each field.

show again the predominant role of paramagnetic effects in that compound in a similar way to FeSe. Tab. 3.4 shows a comparison of the different values obtained from the scaling analysis and the phase diagram in both compounds.

Even if we were not able to have the upper critical field dependence at low temperature when the field is oriented along the FeSe planes it is interesting to notice that the melting line and the upper critical field line seems to cross once again but at a temperature $T^* = 2.5K$. Let us imagine a scenario close to the case of FeSe, where we argued that the melting line merges with the upper critical field at T^* and a FFLO phase starts to appear at the same temperature. In such a scenario, and having $\alpha_{M_\perp} = 5.2$, one can deduce the temperature T^* by looking at the figure of Brison and al. [(23)] (see Fig. 1.14). It is found that for $\alpha_{M_\perp} = 5.2$, T^*/T_c should be around 0.35. That gives in theory a value of T^* of 3.5K. This time the agreement is not as good as it was before in the case of FeSe. However, one should keep in mind that T^* in the framework of Brison et al. denotes the appearance of the FFLO phase and not the temperature where the vortex melting and the upper critical field merge.
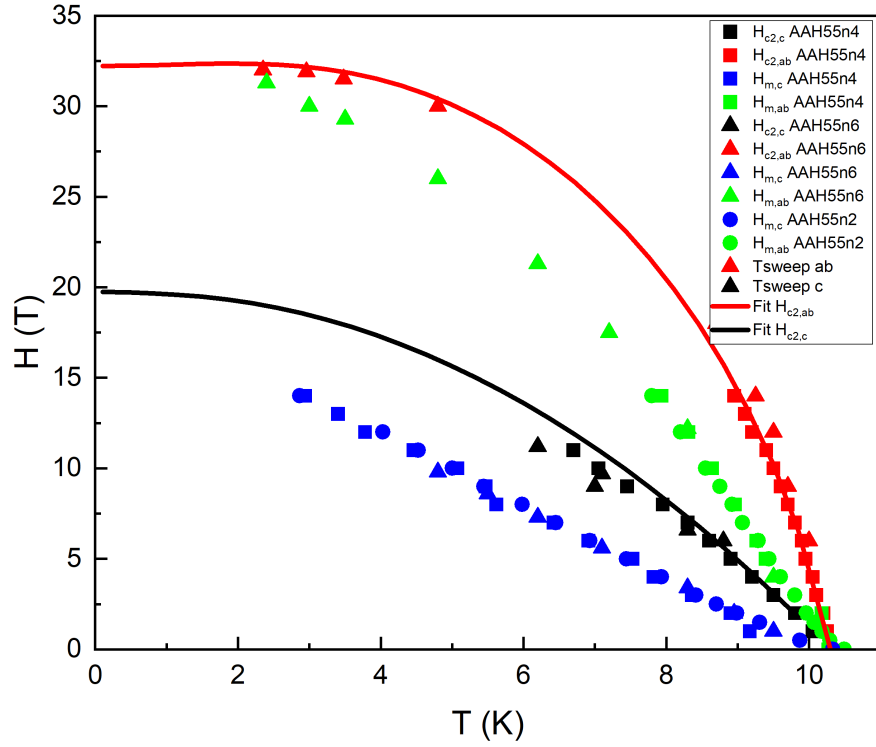
Figure 3.39: $H-T$ phase diagram of the AAH55 batch for both directions of the magnetic field with fit of H_{c2} taking into account orbital and paramagnetic effects. Blue and green symbols represent respectively the melting data when $H_{\perp ab}$ and $H_{||ab}$. The black and red symbols do respectively the same but for the upper critical field. Both the black and red lines are fits performed using the Maki parameter as a free variable following Eq. 1.77.

	G_i	r_T	r_H	$H_p(0)(T)$	$H_{orb}(0)(T)$	α_M
FeSe, $H_\perp$	1×10^{-3}	60	23	26.5	20	1.1
FeSe, $H_{||}$	1×10^{-3}	160	-	29	90	4.5
FeSe$_{0.88}$S$_{0.12}$, $H_\perp$	1.1×10^{-3}	60	23	33	30	1.3
FeSe$_{0.88}$S$_{0.12}$, $H_{||}$	1.1×10^{-3}	160	-	38	138	5.2

Table 3.4: Comparison of the superconducting parameters in FeSe and FeSe$_{0.88}$S$_{0.12}$. We did not perform any analysis of the quantum fluctuations for FeSe$_{0.88}$S$_{0.12}$ since both materials are very similar properties.

3.3.4.1 Phase diagram

Scaled phase diagram Since the properties of FeSe and FeSe$_{0.88}$S$_{0.12}$ seems to be the same when looking at the H_{c2} dependence, we tried to compare the two materials. We believe that our materials could be in the clean limit. In such a case, the initial slope of the upper critical field and the Maki parameter scale with T_c [(140), (141)]. The upper critical field should therefore scales with T_c^2, whereas in the dirty limit due to the scattering by impurities, it only scales with T_c. From Fig. 3.40 one can see that all the melting points seem to collapse on one same line, when one scales the temperature with T_c and the magnetic field with T_c^2. Given the T_c of each materials, and the values of the initial slope and the deduced Maki parameter, one finds that the scaled upper critical field of FeSe and FeSe$_{0.88}$S$_{0.12}$ when $H_{||ab}$ only differs with a maximum value of 3%, which is within our error bars. In the other direction this values goes even lower than 1%. The difference here is mainly due to the difference in the paramagnetic effects in both compounds. In fact, when the sample contains sulfur one observe slightly stronger paramagnetic effects. This however correlates very well with the evolution of T_c, since the ratio between the Maki parameter and T_c looks the same in both materials, with a value close to 0.5.

Surprisingly Xiang et al. [(142)] noticed that the anomaly of the specific heat at T_c in iron-based superconductors violates the BCS rules of $\Delta C/\gamma T_c = 1.43$ and rather follows a rule like $\Delta C|_{T_c} \propto T_c^3$. This law was found to be true for lots of Fe-based materials but it was suggested that such a scaling behaviour is rather true for one system of superconductors, mainly the 122-family since most of the studies were made on that family. They found for example that a FeSe$_{0.5}$Te$_{0.5}$ is close to the scaling law but not exactly the same. Kogan [(143)] gives a theory to explain such a scaling behaviour,
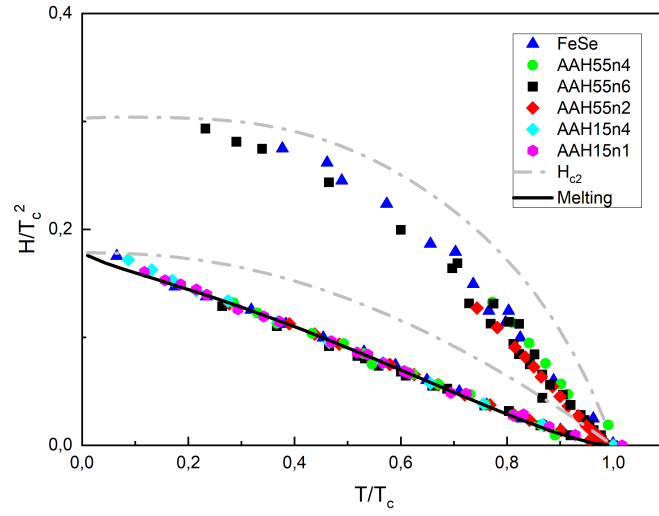
Figure 3.40: Scaled phase diagram of the FeSe$_{1-x}$S$_x$ system. All melting data for all samples (FeSe and FeSe$_{0.88}$S$_{0.12}$) are summarized here. Each color represents one sample for both directions. The dashed grey line is the scaled upper critical field and the solid black line the fit we performed earlier for the melting line. The higher part of the phase diagram corresponds to the direction where $H_{||ab}$ while the lower part corresponds to the direction where $H_{\perp ab}$. The scaling of the magnetic field with T_c^2 means that the sample is in the clean limit. In the clean limit $H'_{c2} \propto 1/(\xi_0^2 T_c) \propto T_c$ whereas in the dirty limit $H'_{c2} \propto 1/(\xi_0 T_c)$ which is T_c independent.

suggesting that one may observe it in anisotropic superconductors with strong pair breaking (this theory is however only using one band). In our materials we found also something close to that law, even if iron based superconductors clearly do not have only have one Fermi sheet, but suggesting strong pair breaking. In fact, one find when comparing our data from FeSe and from FeSe$_{0.88}$S$_{0.12}$ that $\Delta C_{12\%} = 1.75\Delta C_{0\%}$ which would give in a scenario where $\Delta C|_{T_c} \propto T_c^3$, $\Delta C_{12\%} = 1.55\Delta C_{0\%}$. Such a difference might be due to the length width of the transition that might induce a reduction of the height of the anomaly.

Considering such a scaling behaviour of the specific heat jump at T_c and the scaling of other superconducting constants given by Kogan, we can deduce from a theoretical point a view that the values of the scaling parameters r_T and r_H, used in Sec. 3.3.3.2, of the two compounds are related with the following equations :

$$\Delta C_{12\%} = \left(\frac{T_{c_{12\%}}}{T_{c_{0\%}}}\right)^3 \Delta C_{0\%} \tag{3.5}$$

$$H_{c,12\%} = \left(\frac{T_{c_{12\%}}}{T_{c_{0\%}}}\right)^2 H_{c,0\%} \tag{3.6}$$

$$\xi_{\perp,12\%} = \frac{T_{c_{0\%}}}{T_{c_{12\%}}}\xi_{\perp,0\%} \tag{3.7}$$

$$G_{i,12\%} = G_{i,0\%} \tag{3.8}$$

$$r_{T_{12\%}} = \frac{T_{c_{12\%}}}{T_{c_{0\%}}}r_{T_{0\%}} = 1.15r_{T_{0\%}} \tag{3.9}$$

$$r_{H_{12\%}} = r_{H_{0\%}} \tag{3.10}$$

In the end, we find that the scaling of r_T and r_H from a theoretical point of view agrees quite well with the experimental value inferred from the scaling analysis (see Tab. 3.4). r_T and r_H being respectively the same in both compounds then gives a further indication of a possible scaling of the specific heat jump at T_c with T_c^3, which would not be the case in a classic BCS scenario where the specific heat jumps at T_c scales

with T_c. Furthermore, Kogan gives a simple universal relation between superconducting quantities :

$$\frac{\Delta C(\beta T_c^2)^2}{\mu_0 H'_{c2}} \approx 10^{-17} Tm^2, \tag{3.11}$$

where $\beta = d\lambda/dT^2$ at low temperature. From Ref. (144) one can deduce $\beta \approx 4.10^{-9}m.K^{-2}$. This gives a value of $\Delta C(\beta T_c^2)^2/(\mu_0 H'_{c2,c}) \approx 10.10^{-17}$ in a relative good agreement with the theory.

3.3.5 A new anomaly

Introduction of the new anomaly   We introduced earlier another possible phase transition visible in the specific heat in FeSe$_{0.88}$S$_{0.12}$. In fact, we observe a kink in the magnetic field dependence of the specific heat, visible both in the Dual Slope technique and in the AC technique. That anomaly (noted as the local maximum of the field dependent specific heat) is clearly visible in all measured samples, but seems to be however less visible in the temperature dependence of the specific heat. Fig. 3.41 and Fig. 3.42 show the field dependence of the specific heat of one of the measured sample, and one observes a kink before the melting transition indicated by the arrow on the figures. It is clearly visible in a mid-range temperature and field and is clearly harder to see at high temperature since the superconducting anomaly and the new anomaly superimpose. For $H_{\perp ab}$, the anomaly is visible from 7.1K (dark blue curve) to 4.8K (black curve), while in the other direction it is visible from 7.15K (magenta curve) to 2.3K (black curve). At lower temperature the anomaly is still visible but the height of the kink strongly reduces.

Phase diagram: comparison with melting   Since the beginning we are interested in the $H-T$ phase diagram of our sample, let us try to place that anomaly in that phase diagram with the coordinates (H^*, T^*). Fig. 3.43 shows such a phase diagram. The anomaly is within the superconducting phase as shown by the light blue and magenta hexagons. As explained before, no points are plotted at high temperature since it is quite challenging to separate the superconducting anomaly and that new transition. It is quite intriguing to notify that the behavior of that new anomaly scales very well with the melting anomaly. In fact, the melting line $H_m(T)$ and the anomaly at $H^*(T)$ have
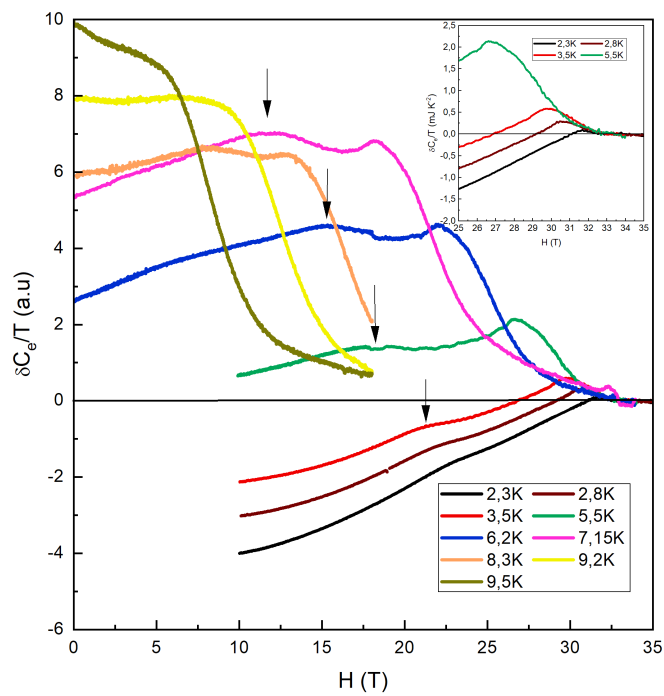
Figure 3.41: $\delta C_e/T$ of the AAH55n6 sample measured with AC calorimetry as a function of the magnetic field with $H_{||ab}$. A kink, indicated by the arrows (taken as the local maximum of $\delta C_e/T$), is observable before the melting transition, that might be related to possible vortex lattice structural transition. Inset: zoom on the high field part of the curves.
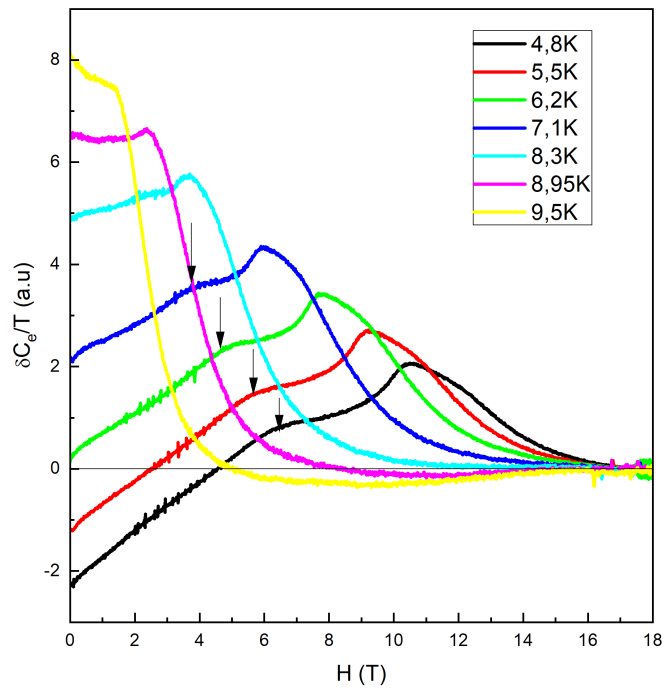
Figure 3.42: $\delta C_e/T$ of the AAH55n6 sample measured with AC calorimetry as a function of the magnetic field with $H_{\perp ab}$. Another kink, indicated by the arrows (taken as the local maximum of $\delta C_e/T$), is observable before the melting transition, that might be related to possible vortex lattice structural transition.

3. VORTEX LATTICE MELTING AND UPPER CRITICAL FIELD IN FESE$_{1-X}$S$_X$
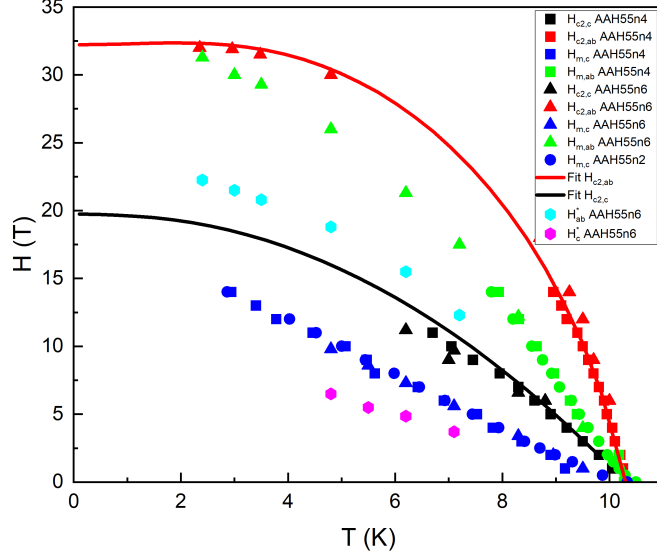
Figure 3.43: Complete $H - T$ phase diagram of FeSe$_{0.88}$S$_{0.12}$ with the new observed anomaly. The symbols and lines are the same as in Fig. 3.39 except that the new anomaly (indicated by arrows in Fig. 3.42 and Fig. 3.41) is represented by the light blue and magenta hexagons.

the same ratio over the all measured phase diagram but is different for both directions. One has $H_{m,ab}(T)/H_{ab}^*(T) = 1.4$ and $H_{m,c}(T)/H_c^*(T) = 1.6$.

Entropy conservation As explained before the new anomaly in the specific heat data might be related to the vortex lattice melting. If related to superconductivity, the specific heat data should be entropy conserving. In Fig. 3.36, the subtraction of the phonon background was made in order to conserve entropy. However we measured the FeSeS15 sample (still FeSe$_{0.88}$S$_{0.12}$) in high magnetic fields with the AC technique and this allows to recover the normal state and subtract the phonon background without any fit. When doing something like that, Fig. 3.44 is obtained. This figure shows an unusual behavior. For a field $H >7$T and a temperature $T/T_c<0.6$ all curve superimpose and have the same temperature dependence. This superposition suggests that the entropy might not conserve for every field, which would be unexpected.

We will therefore look at the entropy of the sample measured with the AC technique. In order to do so, the curve is integrated from 0K to T_c where it should then stay constant. The low temperature data are not available and a linear extrapolation is
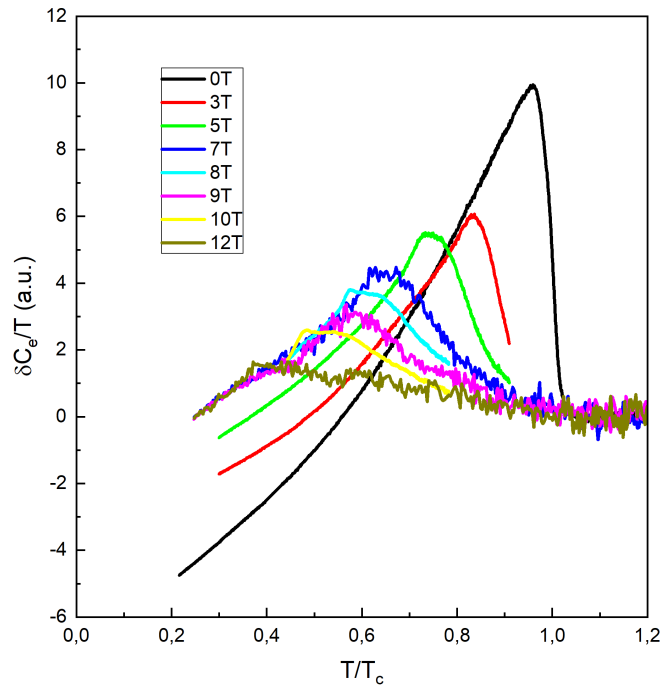
Figure 3.44: $\delta C_e/T$ of FeSe$_{0.88}$S$_{0.12}$ (FeSeS15 sample) as a function of temperature measured with the AC technique. The curves superimpose for $H > 7T$ and $T/T_c < 0.6$.
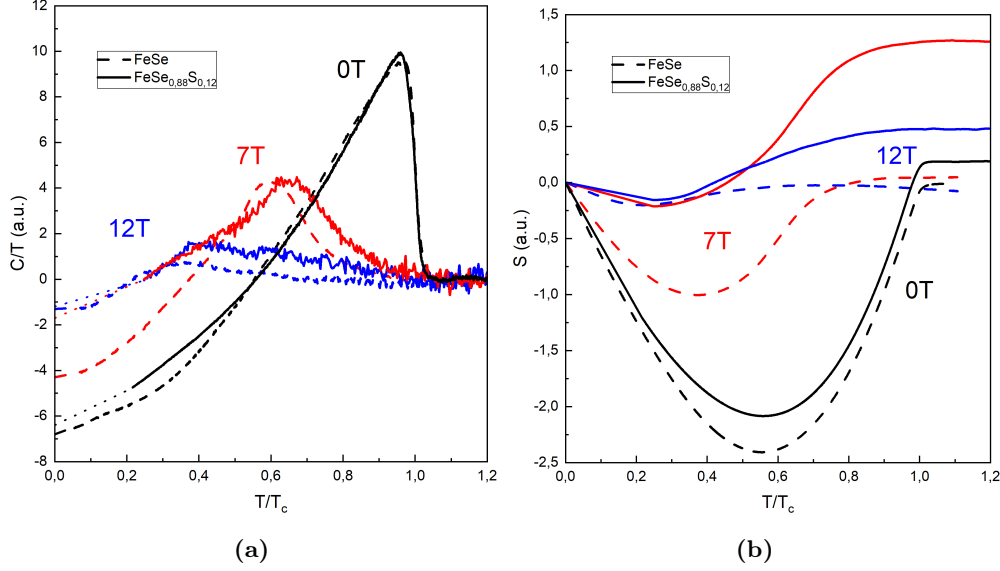
Figure 3.45: (a) Comparison of the specific heat in FeSe and FeSe$_{0.88}$S$_{0.12}$ as a function of temperature. (b) Comparison of the entropy in FeSe and FeSe$_{0.88}$S$_{0.12}$ as a function of temperature. In both figures $H_{\perp ab}$. The dotted line (respectively the solid line) represents the data obtained for FeSe (respectively FeSe$_{0.88}$S$_{0.12}$) and the black line (red and blue) corresponds to a field value of 0T (7T and 12T).

performed in order to get an estimation of these data points (dotted line in Fig.3.45). Fig. 3.45 shows a comparison of both the FeSe and FeSeS15 sample for the specific heat and the entropy. It is clearly visible that while the FeSe curve in entropy conserving, the FeSeS15 curve is not. Fig. 3.46 shows that the entropy of the FeSeS15 sample, when $H_{\perp ab}$, reaches a maximum around 7T. Such a feature is highly unusual and should be of concern.

3.3.5.1 Possible explanations

Interestingly the position of the vortices was observed with STM by Putilov et al. [[96]] and it has been noticed that the vortex lattice undergoes a structural transition from an hexagonal lattice to a quasi-squared lattice. That transition is also visible with a kink in the field dependent specific heat (see Fig. 1.26), splitting the curves into two different linear regimes, which is typical for multigap systems. As we explained before the FeSe$_{1-x}$S$_x$ system is multigap.It was shown by Putilov et al., considering their STM data, that in the case of FeSe, such a structural transition of the vortex lattice could
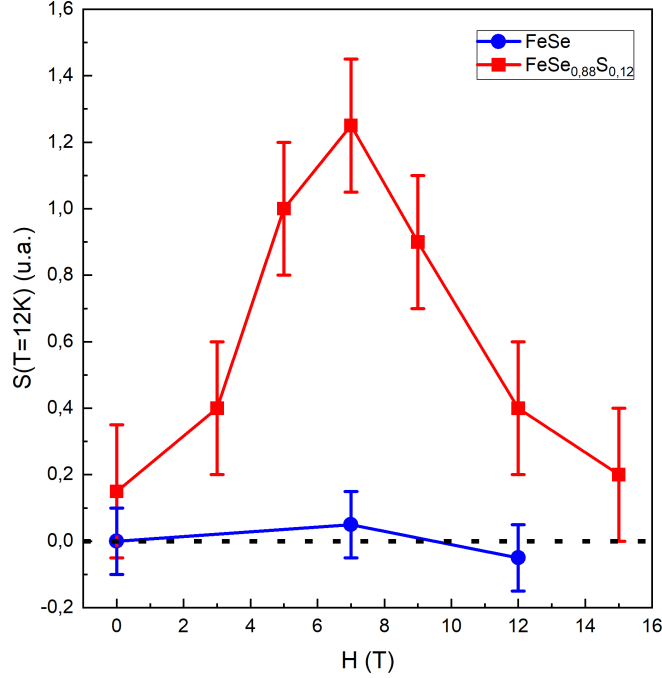
Figure 3.46: Comparison of the entropy in FeSe and FeSe$_{0.88}$S$_{0.12}$ as a function of the magnetic field when $H_{\perp ab}$.

be due to the multigap nature of FeSe and the weakest gap closing at low field. They showed that the structural transition can occur at a field H^* where $H_{c2}/H^* = 1.4$ (H_{c2} is here the upper critical field of the weakest gap). Interestingly we find the same ratio but rather with the melting anomaly than the upper critical field. However they observed the anomaly H^* at very low field compared to what we found in our data. For example the change in the slope of the field dependent specific heat was found to be around 1T at 1.5K, when we would find something closer to approximately 10T. Therefore more investigations are needed in order to see if these anomalies are linked or totally different.

If the new anomaly that we observed at H^* is related to the excess of entropy we have to rule out an interpretation in terms of superconducting mechanism and therefore a structural vortex lattice transition. On the other hand if we think about another transition, such as a magnetic one, we have to clarify the fact that the line due to the new anomaly scales very well with the one of the vortex lattice melting in the $H - T$ phase diagram. Both the non conservation of the entropy and the position of

the anomaly in the phase diagram are therefore challenging issues that might be related but we do not have explanations for that yet.

3.3.6 Conclusion on the vortex lattice melting in FeSe$_{0.88}$S$_{0.12}$

We obtained the $H - T$ phase diagram of the FeSe$_{0.88}$S$_{0.12}$ material up to 32T, showing very close properties with FeSe. Once again specific heat data show vortex lattice melting down to zero temperature when $H_{\perp ab}$, when in the other direction it was possible to observe melting up to 32T. The scaling analysis reveals that the upper critical field is very likely to merge with the vortex lattice melting line at the same field value when $H_{||ab}$. Once again paramagnetic effects had to be included to describe the dependence of the upper critical field in a better way. This time no fitting parameters were used since we showed that the phase diagram of FeSe$_{0.88}$S$_{0.12}$ scales with the one of FeSe with H/T_c^2 and T/T_c, particularly at low field. Because of that the analysis of the temperature dependence of the upper critical field relies on no fitting parameters and we found a value of $\alpha_{M,||} \approx 5.3$ which matches very well our data points.

The comparison of the data of FeSe$_{0.88}$S$_{0.12}$ and FeSe show a good scaling of the phase diagrams when normalizing the temperature with T_c and the upper critical field with T_c^2. This reveals that the samples are in the clean limit. The fitting parameters of the scaling approach of Li and Rosenstein are the same in both compounds. Such a behaviour could be explained by a theory given by Kogan, where he explains that the specific heat jump at T_c scales with T_c^3 due to strong pair breaking. Another anomaly was also found in the specific heat measurements. It scales very well with the vortex melting anomaly, and other measurements in FeSe made by Putilov reveal that it might be related to some change in the vortex lattice symmetry. However we do not have any direct observation of such a phenomenon and the observation of a non entropy conserving superconducting anomaly tends to contradict such a scenario. This is why further measurements are needed in order to have a better understranding of that behaviour.

4

Conclusion

English version   To conclude, we have determined the full $H - T$ phase diagram of FeSe and the one of $FeSe_{0.88}S_{0.12}$ until 32T for both field directions. Our specific heat data reveal the presence of an excess of specific heat related to a vortex lattice melting transition down to zero temperature when $H_{\perp ab}$ and down to T^* when $H_{||ab}$ in both compounds. We then took a closer look at the Gaussian fluctuations in the system with the help of a scaling analysis in order to have the temperature dependence of the upper critical field. A good agreement between the experimental and theoretical values of the parameters used for scaling was obtained. Only at high fields some deviations started to appear, probably due to paramagnetic effects.

We then studied the effects of orbital and Pauli depairing on the upper critical field. Our analysis of the temperature dependence of that field relies only on one fitting parameter, which is the Maki parameter found when $H_{\perp ab}$. All other quantities where found using our measurements. It was deduced that a possible effect of the Pauli depairing was already present when $H_{\perp ab}$, whereas it is absolutely impossible to neglect it when $H_{||ab}$, leading to a high value of the Maki parameter when $H_{||ab}$. We argue that the predominance of the paramagnetic effects at low temperature, causing the reduction of the upper critical field, causes the disappearance of the vortex lattice melting below T^* when $H_{||ab}$.

The melting line was also analyzed using a Lindemann criterion, which leads to a Lindemann constant in a very good agreement with empirical values. It is however still

complicated to know the real nature of the fluctuations causing the melting. In fact, in the FeSe compound, at low temperature, the field dependence of the specific heat shows a broad transition to the normal state that could be due to quantum fluctuations. This broad transition also casts doubt on the influence of paramagnetic effects on the upper critical field when $H_{\perp ab}$. While the thermal coefficient used to fit our data is quite robust, it is also possible that quantum fluctuations play also a significant role.

In pure Fese, when the field is along the FeSe planes a slight deviation from the standard curve of the upper critical field was found at low temperature, right after the vortex lattice melting transition joins the upper critical field line at T^*. I argue that it might be related to a FFLO phase when looking at the $H - T$ phase diagram and comparing it with the literature. However that phase would be on a very small interval of field in the $H - T$ phase diagram, that does not exceed our uncertainties. Further thermodynamical measurements are needed in order to observe a real first order transition that would tend to confirm the presence of a FFLO phase. We tried to look for such a transition by rotating the sample in field but none was found. Nevertheless our measurements suggest that we might observe two phases : one related to superconductivity and another one stable in field for all angles.

In FeSe$_{0.88}$S$_{0.12}$ another anomaly was also found that scales with the vortex melting line in the $H - T$ phase diagram. Looking at the literature I suppose that it might be related to a change in the vortex lattice symmetry, similar to what is observed in FeSe. However the entropy looks like it is not conserved, which would contradicts the previous idea. Once again further measurements are needed here. A direct observation of the symmetry of the vortex lattice over the complete phase diagram and measurements of the entropy on other samples would give more informations.

Version française   En conclusion, nous avons déterminé le diagramme de phase $H-T$ complet de FeSe et celui de FeSe$_{0.88}$S$_{0.12}$ jusqu'à 32T pour les deux directions de champ. Nos données de chaleur spécifique révèlent la présence d'un excès de chaleur spécifique lié à une transition de fusion du réseau vortex jusqu'à une température nulle lorsque le champ est orienté perpendiculairement aux couches de FeSe et jusqu'à T^* lorsque

le champ est orienté le long des couches de FeSe dans les deux composés. Nous avons ensuite effectué une analyse des fluctuations gaussiennes par loi d'échelle afin d'obtenir la dépendance en température du champ critique supérieur. Un bon accord entre les valeurs expérimentales et théoriques de paramètres utilisées pour la mise à l'échelle a été obtenu. Ce n'est qu'à des champs élevés que certaines déviations ont commencé à apparaître, probablement dus à des effets paramagnétiques.

Nous avons ensuite étudié les effets de brissure de paires de Copper de manière orbital et paramagnétique sur le champ critique supérieur. Notre analyse de la dépendance en température de ce champ ne repose que sur un seul paramètre d'ajustement, qui est le paramètre de Maki trouvé lorsque le champ est orienté perpendiculairement aux couches de FeSe. Toutes les autres quantités ont été trouvées en utilisant nos mesures. Nous avons déduit qu'un effet possible de la brisure de paires par effets paramagnétiques était déjà présent lorsque le champ est orienté perpendiculairement aux couches de FeSe, alors qu'il est absolument impossible de le négliger lorsque le champ est orienté le long des couches de FeSe, ce qui conduit à une valeur élevée du paramètre de Maki quand le champs est parallèle aux couches de FeSe. Nous soutenons que la prédominance des effets paramagnétiques à basse température, provoquant la réduction du champ critique supérieur, entraîne la disparition de la fusion du réseau de vortex en dessous de T^* lorsque le champ est parallèle aux couches de FeSe.

La ligne de fusion du réseau de vortex a également été analysée en utilisant un critère de Lindemann, qui conduit à une constante de Lindemann en très bon accord avec les valeurs empiriques. Il reste cependant compliqué de connaître la nature réelle des fluctuations à l'origine de la fusion. En effet, dans le composé FeSe, à basse température, la dépendance en champ de la chaleur spécifique montre une large transition vers l'état normal qui pourrait être due à des fluctuations quantiques. Cette large transition met également en doute l'influence des effets paramagnétiques sur le champ critique supérieur lorsque le champ est perpendiculaire aux couches de FeSe. Bien que le coefficient thermique utilisé pour ajuster nos données soit assez robuste, il est également possible que les fluctuations quantiques jouent également un rôle important.

4. CONCLUSION

Dans le FeSe pur, lorsque le champ est le long des plans de FeSe, une légère déviation de la courbe standard du champ critique supérieur a été trouvée à basse température, juste après que la transition de fusion du réseau de vortex rejoigne la ligne de champ critique supérieure à T^*. Nous pensons que cela pourrait être lié à une phase FFLO en regardant le diagramme de phase $H - T$ et en le comparant avec la littérature. Cependant, cette phase se situerait sur un très petit intervalle de champ dans le diagramme de phase $H - T$, qui ne dépasse pas nos incertitudes. D'autres mesures thermodynamiques sont nécessaires afin d'observer une réelle transition de premier ordre qui tendrait à confirmer la présence d'une phase FFLO. Nous avons essayé de rechercher une telle transition en faisant tourner l'échantillon en champ mais aucune n'a été trouvée. Néanmoins, nos mesures suggèrent que nous pourrions observer deux phases : une liée à la supraconductivité et une autre stable en champ pour tous les angles.

Dans le FeSe$_{0.88}$S$_{0.12}$, une autre anomalie a également été trouvée qui correspond à la ligne de fusion des vortex dans le diagramme de phase $H - T$. En consultant la littérature, nous supposons que cette anomalie pourrait être liée à un changement de la symétrie du réseau de vortex, similaire à ce qui est observé dans le FeSe. Cependant, l'entropie semble ne pas être conservée, ce qui contredit l'idée précédente. Une fois de plus, des mesures supplémentaires sont nécessaires ici. Une observation directe de la symétrie du réseau de vortex sur le diagramme de phase complet et des mesures de l'entropie sur d'autres échantillons donneraient plus d'informations.

References

[1] Joachim Wosnitza. **FFLO States in Layered Organic Superconductors**. *Annalen der Physik*, **530**(2):1700282, 2018. _eprint: https://onlinelibrary.wiley.com/doi/pdf/10.1002/andp.201700282. xviii, 44, 126

[2] M. D. Watson, T. K. Kim, A. A. Haghighirad, N. R. Davies, A. McCollam, A. Narayanan, S. F. Blake, Y. L. Chen, S. Ghannadzadeh, A. J. Schofield, M. Hoesch, C. Meingast, T. Wolf, and A. I. Coldea. **Emergence of the nematic electronic state in FeSe**. *Physical Review B*, **91**(15), April 2015. Number: 15. xxi, 40, 94, 96, 98

[3] H. KAMERLINGH ONNES. **The superconductivity of mercury**. *Comm. Phys. Lab. Univ. Leiden*, **122**:122–124, 1911. 1

[4] W. Meissner and R. Ochsenfeld. **Ein neuer Effekt bei Eintritt der Supraleitfähigkeit**. *Naturwissenschaften*, **21**(44):787–788, November 1933. Number: 44. 1

[5] V. L. Ginzburg. **On the theory of superconductivity**. *Il Nuovo Cimento (1955-1965)*, **2**(6):1234–1250, December 1955. Number: 6. 1

[6] J Bardeen, L N Cooper, and J R Schrieffer. **Theory of Superconductivity**. *THEORY OF SUPERCONDUCTIVITY*, page 30. 1, 56

[7] J G Bednorz. **Possible High Tc Superconductivity in the Ba - La- Cu- 0 System**. 1

[8] Michael Tinkham. *Introduction to Superconductivity*. Courier Corporation, January 2004. Google-Books-ID: VpUk3NfwDIkC. 2

[9] Shigeji Fujita, Kei Ito, and Salvador Godoy. **Superconductors–Introduction**. In Shigeji Fujita, Kei Ito, and Salvador Godoy, editors, *Quantum Theory of Conducting Matter: Superconductivity*, pages 1–13. Springer, New York, NY, 2009. 6

[10] Michel Héritier. **Mécanique statistique et transitions de phase.** 8

[11] A.A. Abrikosov. **The magnetic properties of superconducting alloys**. *Journal of Physics and Chemistry of Solids*, **2**(3):199–208, January 1957. Number: 3. 8, 65

[12] T. Klein, I. Joumard, S. Blanchard, J. Marcus, R. Cubitt, T. Giamarchi, and P. Le Doussal. **A Bragg glass phase in the vortex lattice of a type II superconductor**. *Nature*, **413**(6854):404–406, September 2001. Number: 6854. 9

[13] F. Bouquet, C. Marcenat, E. Steep, R. Calemczuk, W. K. Kwok, U. Welp, G. W. Crabtree, R. A. Fisher, N. E. Phillips, and A. Schilling. **An unusual phase transition to a second liquid vortex phase in the superconductor YBa2Cu3O7**. *Nature*, **411**(6836):448–451, May 2001. Number: 6836. 9, 11, 66, 67

[14] G. Blatter and V. B. Geshkenbein. **Vortex Matter**. In K. H. Bennemann and J. B. Ketterson, editors, *The Physics of Superconductors: Vol. I. Conventional and High-Tc Superconductors*, pages 725–936. Springer, Berlin, Heidelberg, 2003. 10

[15] E H Brandt. **The flux-line lattice in superconductors**. *Reports on Progress in Physics*, **58**(11):1465–1594, November 1995. Number: 11. 14

[16] A. Houghton, R. A. Pelcovits, and A. Sudbø. **Flux lattice melting in high Tc superconductors**. *Physical Review B*, **40**(10):6763–6770, October 1989. Number: 10. 15

[17] I. M. Babich, G. P. Mikitik, and Yu. V. Sharlai. **On the melting curve of a vortex lattice in high-temperature superconductors**. *Low Temperature Physics*, **20**:220–221, March 1994. 16

[18] Gianni Blatter, Boris Ivlev, Yuri Kagan, Martijn Theunissen, Yakov Volokitin, and Peter Kes. **Quantum liquid of vortices in superconductors at T=0**. *Physical Review B*, **50**(17):13013–13016, November 1994. Number: 17. 17, 18

[19] A. Houghton, R. A. Pelcovits, and A. Sudbø. **Flux lattice melting in high Tc superconductors**. *Physical Review B*, **40**(10):6763–6770, October 1989. Number: 10. 19

[20] G. P. Mikitik and E. H. Brandt. **Effect of pinning on the vortex-lattice melting line in type-II superconductors**. *Physical Review B*, **68**(5):054509, August 2003. Number: 5. 21, 119

[21] A. M. Clogston. **Upper Limit for the Critical Field in Hard Superconductors**. *Physical Review Letters*, **9**(6):266–267, September 1962. Number: 6. 22

[22] N. R. Werthamer, E. Helfand, and P. C. Hohenberg. **Temperature and Purity Dependence of the Superconducting Critical Field, H c 2 . III. Electron Spin and Spin-Orbit Effects**. *Physical Review*, **147**(1):295–302, July 1966. Number: 1. 23

[23] J.P. Brison, N. Keller, A. Vernière, P. Lejay, L. Schmidt, A. Buzdin, J. Flouquet, S.R. Julian, and G.G. Lonzarich. **Anisotropy of the upper critical field in URu2Si2 and FFLO state in antiferromagnetic superconductors**. *Physica C: Superconductivity*, **250**(1-2):128–138, August 1995. Number: 1-2. 23, 30, 127, 146

REFERENCES

[24] Hiroto Adachi and Ryusuke Ikeda. Effects of Pauli paramagnetism on the superconducting vortex phase diagram in strong fields. *Physical Review B*, **68**(18):184510, November 2003. Number: 18. 24, 25.

[25] M. Houzet and V. P. Mineev. Interplay of paramagnetic, orbital, and impurity effects on the phase transition of a normal metal to the superconducting state. *Physical Review B*, **74**(14):144522, October 2006. 25.

[26] Yu N Ovchinnikov. Density of states in inhomogeneous superconductors. 27.

[27] Peter Fulde and Richard A. Ferrell. Superconductivity in a Strong Spin-Exchange Field. *Physical Review*, **135**(3A):A550–A563, August 1964. Number: 3A. 27.

[28] Shigeru Kasahara, Tatsuya Watashige, Tetsuo Hanaguri, Yuhki Kohsaka, Takuya Yamashita, Yusuke Shimoyama, Yuta Mizukami, Ryota Endo, Hiroaki Ikeda, Kazushi Aoyama, Taichi Terashima, Shinya Uji, Thomas Wolf, Hilbert von Löhneysen, Takasada Shibauchi, and Yuji Matsuda. Field-induced superconducting phase of FeSe in the BCS-BEC cross-over. *Proceedings of the National Academy of Sciences*, **111**(46):16309–16313, November 2014. Number: 46. 27, 38, 42, 43, 137.

[29] Leonard W. Gruenberg and Leon Gunther. Fulde-Ferrell Effect in Type-II Superconductors. *Physical Review Letters*, **16**(22):996–998, May 1966. Number: 22. 28.

[30] A.I. Buzdin and J.P. Brison. New solutions for the superconducting order parameter in a high magnetic field. *Physics Letters A*, **218**(3-6):359–366, August 1996. Number: 3-6. 28.

[31] Yoichi Kamihara, Takumi Watanabe, Masahiro Hirano, and Hideo Hosono. Iron-Based Layered Superconductor La[O(1-x)FxFeAs (x = 0.050.12) with T c = 26 K. *Journal of the American Chemical Society*, **130**(11):3296–3297, March 2008. Number: 11. 30.

[32] A. A. Kordyuk. Iron-based superconductors: Magnetism, superconductivity, and electronic structure (Review Article). *Low Temperature Physics*, **38**(9):888–899, September 2012. Number: 9 Publisher: American Institute of Physics. 31.

[33] Kouji Segawa and Yoichi Ando. Magnetic and Transport Properties of FeAs Single Crystals. *Journal of the Physical Society of Japan*, **78**(10):104720–104720, 2009. 31.

[34] Fong-Chi Hsu, Jiu-Yong Luo, Kuo-Wei Yeh, Ta-Kun Chen, Tzu-Wen Huang, Phillip M. Wu, Yong-Chi Lee, Yi-Lin Huang, Yan-Yi Chu, Der-Chung Yan, and Maw-Kuen Wu. Superconductivity in the PbO-type structure -FeSe. *Proceedings of the National Academy of Sciences*, **105**(38):14262–14264, September 2008. Number: 38 Publisher: National Academy of Sciences Section: Physical Sciences. 31.

[35] T. Imai, K. Ahilan, F. L. Ning, T. M. McQueen, and R. J. Cava. Why Does Undoped FeSe Become a High Tc Superconductor under Pressure? *Physical Review Letters*, **102**(17):177005, April 2009. Number: 17 Publisher: American Physical Society. 31.

[36] B. C. Sales, A. S. Sefat, M. A. McGuire, R. Y. Jin, D. Mandrus, and Y. Mozharivskyj. Bulk superconductivity at 14 K in single crystals of Fe(1+y)Te(x)S(1-x)\$. *Physical Review B*, **79**(9):094521, March 2009. Number: 9 Publisher: American Physical Society. 31.

[37] K. Matsuura, Y. Mizukami, Y. Arai, Y. Sugimura, N. Maejima, A. Machida, T. Watanuki, T. Fukuda, T. Yajima, Z. Hiroi, K. Y. Yip, Y. C. Chan, Q. Niu, S. Hosoi, K. Ishida, K. Mukasa, S. Kasahara, J.-G. Cheng, S. K. Goh, Y. Matsuda, Y. Uwatoko, and T. Shibauchi. Maximizing T c by tuning nematicity and magnetism in FeSe(1x)S(x) superconductors. *Nature Communications*, **8**(1):1143, December 2017. 31.

[38] Joshua H. Tapp, Zhongjia Tang, Bing Lv, Kalyan Sasmal, Bernd Lorenz, Paul C. W. Chu, and Arnold M. Guloy. LiFeAs: An intrinsic FeAs-based superconductor with Tc = 18 K. *Physical Review B*, **78**(6):060505, August 2008. Number: 6. 31.

[39] M. A. Tanatar, N. Spyrison, Kyuil Cho, E. C. Blomberg, Guotai Tan, Pengcheng Dai, Chenglin Zhang, and R. Prozorov. Evolution of normal and superconducting properties of single crystals of Na(1-)FeAs upon interaction with environment. *Physical Review B*, **85**(1):014510, January 2012. Number: 1 Publisher: American Physical Society. 31.

[40] Marianne Rotter, Marcus Tegel, and Dirk Johrendt. Superconductivity at 38 K in the Iron Arsenide Ba(1-x)K(x)Fe2As2. *Physical Review Letters*, **101**(10):107006, September 2008. Number: 10 Publisher: American Physical Society. 31.

[41] Athena S. Sefat, Rongying Jin, Michael A. McGuire, Brian C. Sales, David J. Singh, and David Mandrus. Superconductivity at 22 K in Co-Doped BaFe2As2 Crystals. *Physical Review Letters*, **101**(11):117004, September 2008. Number: 11 Publisher: American Physical Society. 31.

[42] Ren Zhi-An, Lu Wei, Yang Jie, Yi Wei, Shen Xiao-Li, Zheng-Cai, Che Guang-Can, Dong Xiao-Li, Sun Li-Ling, Zhou Fang, and Zhao Zhong-Xian. Superconductivity at 55 K in Iron-Based F-Doped Layered Quaternary Compound Sm[O(1-x)F (x)]FeAs. *Chinese Physics Letters*, **25**(6):2215–2216, May 2008. Number: 6 Publisher: IOP Publishing. 32.

[43] J. Jaroszynski, F. Hunte, L. Balicas, Youn-jung Jo, I. Raičević, A. Gurevich, D. C. Larbalestier, F. F. Balakirev, L. Fang, P. Cheng, Y. Jia, and H. H. Wen. Upper critical fields and thermally-activated transport of NdFeAsO(0.7)F(0.3) single crystal. *Physical Review B*, **78**(17):174523, November 2008. Number: 17 Publisher: American Physical Society. 32.

[44] JOHNPIERRE PAGLIONE AND RICHARD L. GREENE. High-temperature superconductivity in iron-based materials. *Nature Physics*, **6**(9):645–658, September 2010. Number: 9. 32

[45] B. T. MATTHIAS, T. H. GEBALLE, AND V. B. COMPTON. Superconductivity. *Reviews of Modern Physics*, **35**(1):1–22, January 1963. Number: 1 Publisher: American Physical Society. 32

[46] JOHN M. TRANQUADA. Modulated superfluid density in an iron-pnictide superconductor. *Physics*, **3**, May 2010. Publisher: American Physical Society. 33

[47] ANDREY CHUBUKOV AND PETER J. HIRSCHFELD. Iron-based superconductors, seven years later. *Physics Today*, **68**(6):46–52, June 2015. Number: 6 Publisher: American Institute of Physics. 34, 36

[48] T. BAZHIROV. First-principles studies of electron-phonon induced superconductivity and beyond. *undefined*, 2013. 33

[49] A. V. CHUBUKOV, D. V. EFREMOV, AND I. EREMIN. Magnetism, superconductivity, and pairing symmetry in iron-based superconductors. *Physical Review B*, **78**(13), October 2008. Number: 13. 33

[50] P. J. HIRSCHFELD, M. M. KORSHUNOV, AND I. I. MAZIN. Gap symmetry and structure of Fe-based superconductors. *Reports on Progress in Physics*, **74**(12):124508, October 2011. Number: 12 Publisher: IOP Publishing. 34, 35

[51] S. AVCI, O. CHMAISSEM, D. Y. CHUNG, S. ROSENKRANZ, E. A. GOREMYCHKIN, J. P. CASTELLAN, I. S. TODOROV, J. A. SCHLUETER, H. CLAUS, A. DAOUD-ALADINE, D. D. KHALYAVIN, M. G. KANATZIDIS, AND R. OSBORN. Phase diagram of Ba(1-x)K(x)Fe2As2. *Physical Review B*, **85**(18):184507, May 2012. Number: 18 Publisher: American Physical Society. 36

[52] PAUL C. CANFIELD AND SERGEY L. BUD'KO. FeAs-based superconductivity: a case study of the effects of transition metal doping on BaFe2As2. *Annual Review of Condensed Matter Physics*, **1**(1):27–50, August 2010. Number: 1 arXiv: 1002.0858. 36

[53] M. G. KIM, R. M. FERNANDES, A. KREYSSIG, J. W. KIM, A. THALER, S. L. BUD'KO, P. C. CANFIELD, R. J. MCQUEENEY, J. SCHMALIAN, AND A. I. GOLDMAN. Character of the structural and magnetic phase transitions in the parent and electron-doped BaFe2As2 compounds. *Physical Review B*, **83**(13):134522, April 2011. Number: 13 Publisher: American Physical Society. 36, 38

[54] MING YI, DONGHUI LU, JIUN-HAW CHU, JAMES G. ANALYTIS, ADAM P. SORINI, ALEXANDER F. KEMPER, BRIAN MORITZ, SUNG-KWAN MO, ROB G. MOORE, MAKOTO HASHIMOTO, WEI-SHENG LEE, ZAHID HUSSAIN, THOMAS P. DEVEREAUX, IAN R. FISHER, AND ZHI-XUN SHEN. Symmetry-breaking orbital anisotropy observed for detwinned Ba[Fe(1-x)Co(x)]2As2 above the spin density wave transition. *Proceedings of the National Academy of Sciences of the United States of America*, **108**(17):6878–6883, April 2011. Number: 17. 36

[55] S. KASAHARA, H. J. SHI, K. HASHIMOTO, S. TONEGAWA, Y. MIZUKAMI, T. SHIBAUCHI, K. SUGIMOTO, T. FUKUDA, T. TERASHIMA, ANDRIY H. NEVIDOMSKYY, AND Y. MATSUDA. Electronic nematicity above the structural and superconducting transition in BaFe2(As(1-x)P(x))2. *Nature*, **486**(7403):382–385, June 2012. Number: 7403. 36

[56] R. M. FERNANDES, A. V. CHUBUKOV, AND J. SCHMALIAN. What drives nematic order in iron-based superconductors? *Nature Physics*, **10**(2):97–104, February 2014. Number: 2. 36

[57] F. L. NING, M. FU, D. A. TORCHETTI, T. IMAI, A. S. SEFAT, P. CHENG, B. SHEN, AND H.-H. WEN. Critical behavior of the spin density wave transition in underdoped Ba[Fe(1-x)Co(x)]2As2 (x<0.05): 75As NMR investigation. *Physical Review B*, **89**(21):214511, June 2014. Number: 21 Publisher: American Physical Society. 36

[58] QIANG ZHANG, RAFAEL M. FERNANDES, JAGAT LAMSAL, JIAQIANG YAN, SONGXUE CHI, GREGORY S. TUCKER, DANIEL K. PRATT, JEFFREY W. LYNN, R.W. MCCALLUM, PAUL C. CANFIELD, THOMAS A. LOGRASSO, ALAN I. GOLDMAN, DAVID VAKNIN, AND ROBERT J. MCQUEENEY. Neutron-Scattering Measurements of Spin Excitations in LaFeAsO and Ba[Fe(0.953)Co(0.047)]2As2: Evidence for a Sharp Enhancement of Spin Fluctuations by Nematic Order. *Physical Review Letters*, **114**(5):057001, February 2015. Number: 5 Publisher: American Physical Society. 36

[59] P. K. MAHESHWARI, L. M. JOSHI, BHASKER GAHTORI, A. K. SRIVASTAVA, ANURAG GUPTA, S. P. PATNAIK, AND V. P. S. AWANA. Flux free growth of superconducting FeSe single crystals. *Materials Research Express*, **3**(7):076002, July 2016. Number: 7 Publisher: IOP Publishing. 37

[60] TAKAHIRO URATA, YOICHI TANABE, KHUONG KIM HUYNH, HIDETOSHI OGURO, KAZUO WATANABE, AND KATSUMI TANIGAKI. Non-Fermi liquid behavior of electrical resistivity close to the nematic critical point in Fe(1-x)Co(x)Se and FeSe(1-y)S(y). *arXiv:1608.01044 [cond-mat]*, August 2016. arXiv: 1608.01044. 37

[61] YOSHIKAZU MIZUGUCHI, FUMIAKI TOMIOKA, SHUNSUKE TSUDA, TAKAHIDE YAMAGUCHI, AND YOSHIHIKO TAKANO. Substitution Effects on FeSe Superconductor. *Journal of the Physical Society of Japan*, **78**(7):074712, July 2009. Number: 7 Publisher: The Physical Society of Japan. 37

[62] M. D. WATSON, T. K. KIM, A. A. HAGHIGHIRAD, S. F. BLAKE, N. R. DAVIES, M. HOESCH, T. WOLF, AND A. I. COLDEA. Suppression of orbital ordering by chemical pressure in FeSe(1-x)S(x). *Physical Review B*, **92**(12):121108, September 2015. Number: 12 Publisher: American Physical Society. 38, 39, 139

[63] T. M. MCQUEEN, Q. HUANG, V. KSENOFONTOV, C. FELSER, Q. XU, H. ZANDBERGEN, Y. S. HOR, J. ALLRED, A. J. WILLIAMS, D. QU, J. CHECKELSKY, N. P. ONG, AND R. J. CAVA. Extreme sensitivity of superconductivity to stoichiometry in Fe(1+x)Se. *Physical Review B*, **79**(1):014522, January 2009. Number: 1. 37, 92

REFERENCES

[64] M. BENDELE, A. ICHSANOW, YU. PASHKEVICH, L. KELLER, TH. STRÄSSLE, A. GUSEV, E. POMJAKUSHINA, K. CONDER, R. KHASANOV, AND H. KELLER. Coexistence of superconductivity and magnetism in FeSe(1-x) under pressure. *Physical Review B*, **85**(6):064517, February 2012. Number: 6 Publisher: American Physical Society. 37

[65] S. MEDVEDEV, T. M. MCQUEEN, I. A. TROYAN, T. PALASYUK, M. I. EREMETS, R. J. CAVA, S. NAGHAVI, F. CASPER, V. KSENOFONTOV, G. WORTMANN, AND C. FELSER. Electronic and magnetic phase diagram of beta-Fe(1.01)Se with superconductivity at 36.7 K under pressure. *Nature Materials*, **8**(8):630–633, August 2009. Number: 8. 37

[66] ANNA E. BÖHMER AND ANDREAS KREISEL. Nematicity, magnetism and superconductivity in FeSe. November 2017. 37

[67] K. KOTHAPALLI, A. E. BÖHMER, W. T. JAYASEKARA, B. G. UELAND, P. DAS, A. SAPKOTA, V. TAUFOUR, Y. XIAO, E. ALP, S. L. BUD'KO, P. C. CANFIELD, A. KREYSSIG, AND A. I. GOLDMAN. Strong cooperative coupling of pressure-induced magnetic order and nematicity in FeSe. *Nature Communications*, **7**(1):12728, September 2016. 37, 38

[68] ELENA GATI, ANNA E. BÖHMER, SERGEY L. BUD'KO, AND PAUL C. CANFIELD. Bulk Superconductivity and Role of Fluctuations in the Iron-Based Superconductor FeSe at High Pressures. *Physical Review Letters*, **123**(16):167002, October 2019. 37

[69] JIANPING SUN, K MATSUURA, GU YE, Y MIZUKAMI, M SHIMOZAWA, KAZUYUKI MATSUBAYASHI, M YAMASHITA, T WATASHIGE, SHIGERU KASAHARA, Y MATSUDA, J.-Q YAN, B C. SALES, YOSHIYA UWATOKO, J.-G CHENG, AND T SHIBAUCHI. Dome-shaped magnetic order competing with high-temperature superconductivity at high pressures in FeSe. *Nature Communications*, **7**, December 2015. 38, 39

[70] XIAOYU WANG AND EREZ BERG. Scattering mechanisms and electrical transport near an Ising nematic quantum critical point. *arXiv:1902.04590 [cond-mat]*, February 2019. arXiv: 1902.04590. 38

[71] K. K. HUYNH, Y. TANABE, T. URATA, H. OGURO, S. HEGURI, K. WATANABE, AND K. TANIGAKI. Electric transport of a single-crystal iron chalcogenide FeSe superconductor: Evidence of symmetry-breakdown nematicity and additional ultrafast Dirac cone-like carriers. *Physical Review B*, **90**(14):144516, October 2014. Number: 14 Publisher: American Physical Society. 38

[72] M. L. AMIGÓ, V. ALE CRIVILLERO, D. G. FRANCO, AND G. NIEVA. Multiband character of FeSe: Angular dependence of the magnetoresistance and upper critical field. *Journal of Physics: Conference Series*, **568**(2):022005, December 2014. Number: 2 Publisher: IOP Publishing. 38

[73] SAHANA RÖSSLER, CEVRIYE KOZ, LIN JIAO, ULRICH K. RÖSSLER, FRANK STEGLICH, ULRICH SCHWARZ, AND STEFFEN WIRTH. Emergence of an incipient ordering mode in FeSe. *Physical Review B*, **92**(6):060505, August 2015. Number: 6 Publisher: American Physical Society. 38

[74] T. KLEIN, D. BRAITHWAITE, A. DEMUER, W. KNAFO, G. LAPERTOT, C. MARCENAT, P. RODIÈRE, I. SHEIKIN, P. STROBEL, A. SULPICE, AND P. TOULEMONDE. Thermodynamic phase diagram of FeSe(0.5)Te(0.5) single crystals in fields up to 28 tesla. *Physical Review B*, **82**(18):184506, November 2010. Number: 18 Publisher: American Physical Society. 38

[75] PIERRE MASSAT. *Spectroscopie Raman du supraconducteur FeSe*. These de doctorat, Sorbonne Paris Cité, April 2017. 38

[76] Y. SUZUKI, T. SHIMOJIMA, T. SONOBE, A. NAKAMURA, M. SAKANO, H. TSUJI, J. OMACHI, K. YOSHIOKA, M. KUWATA-GONOKAMI, T. WATASHIGE, R. KOBAYASHI, S. KASAHARA, T. SHIBAUCHI, Y. MATSUDA, Y. YAMAKAWA, H. KONTANI, AND K. ISHIZAKA. Momentum-dependent sign inversion of orbital order in superconducting FeSe. *Physical Review B*, **92**(20):205117, November 2015. Publisher: American Physical Society. 39

[77] LUKE C. RHODES, MATTHEW D. WATSON, AMIR A. HAGHIGHIRAD, D. V. EVTUSHINSKY, AND TIMUR K. KIM. Revealing the single electron pocket of FeSe in a single orthorhombic domain. *Physical Review B*, **101**(23):235128, June 2020. 39

[78] TAKASADA SHIBAUCHI, TETSUO HANAGURI, AND YUJI MATSUDA. Exotic Superconducting States in FeSe-based Materials. *arXiv:2005.07315 [cond-mat]*, May 2020. 39, 40, 41

[79] ALAIN AUDOUARD, FABIENNE DUC, LOÏC DRIGO, PIERRE TOULEMONDE, SANDRA KARLSSON, PIERRE STROBEL, AND ANDRÉ SULPICE. Quantum oscillations and upper critical magnetic field of the iron-based superconductor FeSe. *EPL (Europhysics Letters)*, **109**(2):27003, January 2015. Publisher: IOP Publishing. 40, 44

[80] TAICHI TERASHIMA, NAOKI KIKUGAWA, ANDHIKA KISWANDHI, EUN-SANG CHOI, JAMES S. BROOKS, SHIGERU KASAHARA, TATSUYA WATASHIGE, HIROAKI IKEDA, TAKASADA SHIBAUCHI, YUJI MATSUDA, THOMAS WOLF, ANNA E. BÖHMER, FRÉDÉRIC HARDY, CHRISTOPH MEINGAST, HILBERT V. LÖHNEYSEN, MICHI-TO SUZUKI, RYOTARO ARITA, AND SHINYA UJI. Anomalous Fermi surface in FeSe seen by Shubnikov–de Haas oscillation measurements. *Physical Review B*, **90**(14):144517, October 2014. 40, 96, 97

[81] A. I. COLDEA, S. F. BLAKE, S. KASAHARA, A. A. HAGHIGHIRAD, M. D. WATSON, W. KNAFO, E. S. CHOI, A. MCCOLLAM, P. REISS, T. YAMASHITA, M. BRUMA, S. SPELLER, Y. MATSUDA, T. WOLF, T. SHIBAUCHI, AND A. J. SCHOFIELD. Evolution of the Fermi surface of the nematic superconductors FeSe(1-x)S(x). *arXiv:1611.07424 [cond-mat]*, November 2016. 40

[82] AMALIA I. COLDEA AND MATTHEW D. WATSON. The key ingredients of the electronic structure of FeSe. *Annual Review of Condensed Matter Physics*, **9**(1):125–146, March 2018. Number: 1. 41, 139

[83] P. O. SPRAU, A. KOSTIN, A. KREISEL, A. E. BÖHMER, V. TAUFOUR, P. C. CANFIELD, S. MUKHERJEE, P. J. HIRSCHFELD, B. M. ANDERSEN, AND J. C. SÉAMUS DAVIS. Discovery of orbital-selective Cooper pairing in FeSe. *Science*, **357**(6346):75–80, July 2017. 40, 116

[84] Frédéric Hardy, Mingquan He, Liran Wang, Thomas Wolf, Peter Schweiss, Michael Merz, Maik Barth, Peter Adelmann, Robert Eder, Amir-Abbas Haghighirad, and Christoph Meingast. **Calorimetric evidence of nodal gaps in the nematic superconductor FeSe**. *Physical Review B*, **99**(3):035157, January 2019. Number: 3. 40, 58, 93, 100.

[85] H. Cercellier, P. Rodière, P. Toulemonde, C. Marcenat, and T. Klein. **Influence of the quasiparticle spectral weight in FeSe on spectroscopic, magnetic, and thermodynamic properties**. *Physical Review B*, **100**(10):104516, September 2019. Publisher: American Physical Society. 42, 102.

[86] Jong Mok Ok, Chang Il Kwon, Yoshimitsu Kohama, Jung Sang You, Sun Kyu Park, Ji-hye Kim, Y. J. Jo, E. S. Choi, Koichi Kindo, Woun Kang, Ki-Seok Kim, E. G. Moon, A. Gurevich, and Jun Sung Kim. **Observation of in-plane magnetic field induced phase transitions in FeSe**. *Physical Review B*, **101**(22):224509, June 2020. 42, 44, 47, 115, 129, 130, 131, 133, 134.

[87] Yuji Matsuda and Hiroshi Shimahara. **Fulde–Ferrell–Larkin–Ovchinnikov State in Heavy Fermion Superconductors**. *Journal of the Physical Society of Japan*, **76**(5):051005, May 2007. Number: 5 Publisher: The Physical Society of Japan. 44.

[88] Gertrud Zwicknagl and Jochen Wosnitza. **Breaking translational invariance by population imbalance: the fulde–ferrell–larkin–ovchinnikov states**. *International Journal of Modern Physics B*, **24**(20n21):3915–3949, August 2010. Number: 20n21 Publisher: World Scientific Publishing Co. 44.

[89] Shunsaku Kitagawa, Genki Nakamine, Kenji Ishida, H.S. Jeevan, C. Geibel, and F. Steglich. **Evidence for the Presence of the Fulde-Ferrell-Larkin-Ovchinnikov State in CeCu2Si2 Revealed Using 63Cu NMR**. *Physical Review Letters*, **121**(15):157004, October 2018. Number: 15 Publisher: American Physical Society. 44.

[90] Chang-woo Cho, Jonathan Haiwei Yang, Noah F.Q. Yuan, Junying Shen, Thomas Wolf, and Rolf Lortz. **Thermodynamic Evidence for the Fulde-Ferrell-Larkin-Ovchinnikov State in the KFe2As2 Superconductor**. *Physical Review Letters*, **119**(21):217002, November 2017. Publisher: American Physical Society. 44.

[91] R. X. Cao, Jun Dong, Q. L. Wang, Y. J. Yang, C. Zhao, X. H. Zeng, D. A. Chareev, A. N. Vasiliev, Bing Wu, and Guoqing Wu. **Measurements of the superconducting anisotropy in FeSe with a resonance frequency technique**. *AIP Advances*, **9**(4):045220, April 2019. Number: 4 Publisher: American Institute of Physics. 44, 48.

[92] S. Kasahara, Y. Sato, S. Licciardello, M. Čulo, S. Arsenijević, T. Ottenbros, T. Tominaga, J. Böker, I. Eremin, T. Shibauchi, J. Wosnitza, N.E. Hussey, and Y. Matsuda. **Evidence for an Fulde-Ferrell-Larkin-Ovchinnikov State with Segmented Vortices in the BCS-BEC-Crossover Superconductor FeSe**. *Physical Review Letters*, **124**(10):107001, March 2020. 45, 46, 129, 130.

[93] Y. De Wilde, M. Iavarone, U. Welp, V. Metlushko, A. E. Koshelev, Igor Aronson, G. W. Crabtree, and P. C. Canfield. **Scanning tunneling microscopy observation of a square abrikosov lattice in LuNi2B2C**. *Physical Review Letters*, **78**(22):4273–4276, January 1997. Number: 22 Publisher: American Physical Society. 44.

[94] W. H. Kleiner, L. M. Roth, and S. H. Autler. **Bulk Solution of Ginzburg-Landau Equations for Type II Superconductors: Upper Critical Field Region**. *Physical Review*, **133**(5A):A1226–A1227, March 1964. Number: 5A Publisher: American Physical Society. 44.

[95] Jun'ichi Shiraishi, Mahito Kohmoto, and Kazumi Maki. **Vortex lattice transition in d-wave superconductors**. *Physical Review B*, **59**(6):4497–4503, February 1999. Number: 6 Publisher: American Physical Society. 44.

[96] A. V. Putilov, C. Di Giorgio, V. L. Vadimov, D. J. Trainer, E. M. Lechner, J. L. Curtis, M. Abdel-Hafiez, O. S. Volkova, A. N. Vasiliev, D. A. Chareev, G. Karapetrov, A. E. Koshelev, A. Yu. Aladyshkin, A. S. Mel'nikov, and M. Iavarone. **Vortex-core properties and vortex-lattice transformation in FeSe**. *Physical Review B*, **99**(14):144514, April 2019. 44, 47, 156.

[97] D. Majer, E. Zeldov, and M. Konczykowski. **Separation of the Irreversibility and Melting Lines in Bi2Sr2CaCu2O8 Crystals**. *Physical Review Letters*, **75**(6):1166–1169, August 1995. 47.

[98] R. Lortz, F. Lin, N. Musolino, Y. Wang, A. Junod, B. Rosenstein, and N. Toyota. **Thermal fluctuations and vortex melting in the Nb3Sn superconductor from high resolution specific heat measurements**. *Physical Review B*, **74**(10):104502, September 2006. Number: 10 Publisher: American Physical Society. 47.

[99] A Schilling, R A Fisher, N E Phillips, U Weipt, D Dasguptat, W K Kwokt, and G W Crabtreet. **Calorimetric measurement of the latent heat of vortex- lattice melting in untwinned YBa2Cu3O(7-x)**. **382**:3, 1996. 47, 48, 67.

[100] A. P. Petrović, Y. Fasano, R. Lortz, C. Senatore, A. Demuer, A. B. Antunes, A. Paré, D. Salloum, P. Gougeon, M. Potel, and Ø. Fischer. **Real-Space Vortex Glass Imaging and the Vortex Phase Diagram of SnMo6S8**. *Physical Review Letters*, **103**(25):257001, December 2009. Number: 25 Publisher: American Physical Society. 47.

[101] H. K. Mak, P. Burger, L. Cevey, T. Wolf, C. Meingast, and R. Lortz. **Thermodynamic observation of a vortex melting transition in the Fe-based superconductor Ba(0.5)K(0.5)Fe2As2**. *Physical Review B*, **87**(21):214523, June 2013. Number: 21 Publisher: American Physical Society. 47.

[102] A. E. Koshelev, K. Willa, R. Willa, M. P. Smylie, J.-K. Bao, D. Y. Chung, M. G. Kanatzidis, W.-K. Kwok, and U. Welp. **Melting of vortex lattice in the magnetic superconductor RbEuFe4As4**. *Physical Review B*, **100**(9):094518, September 2019. Number: 9. 47, 68, 69, 70, 105, 110, 111, 121.

REFERENCES

[103] D. K. Finnemore, T. F. Stromberg, and C. A. Swenson. **Superconducting Properties of High-Purity Niobium**. *Physical Review*, **149**(1):231–243, September 1966. Number: 1. [48, 104]

[104] J. Ferreira Da Silva, E. A. Burgemeister, and Z. Dokoupil. **Low temperature specific heats of annealed high purity niobium in magnetic fields**. *Physics Letters A*, **25**(5):354–356, September 1967. Number: 5. [48]

[105] M. P. Smylie, K. Willa, J.-K. Bao, K. Ryan, Z. Islam, H. Claus, Y. Simsek, Z. Diao, A. Rydh, A. E. Koshelev, W.-K. Kwok, D. Y. Chung, M. G. Kanatzidis, and U. Welp. **Anisotropic superconductivity and magnetism in single-crystal RbEuFe4As4**. *Physical Review B*, **98**(10):104503, September 2018. Number: 10 Publisher: American Physical Society. [48]

[106] K. Willa, R. Willa, J.-K. Bao, A. E. Koshelev, D. Y. Chung, M. G. Kanatzidis, W.-K. Kwok, and U. Welp. **Strongly fluctuating moments in the high-temperature magnetic superconductor RbEuFe4As4**. *Physical Review B*, **99**(18):180502, May 2019. Number: 18 Publisher: American Physical Society. [48]

[107] U. Welp, J. A. Fendrich, W. K. Kwok, G. W. Crabtree, and B. W. Veal. **Thermodynamic Evidence for a Flux Line Lattice Melting Transition in YBa2Cu3O(7-x)**. *Physical Review Letters*, **76**(25):4809–4812, June 1996. Number: 25 Publisher: American Physical Society. [48]

[108] Neil W. Ashcroft, AshcroftNeil W, and N. David Mermin. *Solid State Physics*. Holt, Rinehart and Winston, 1976. Google-Books-ID: 1C9HAQAAIAAJ. [54, 55]

[109] Clément Girod. *Chaleur spécifique à basse température dans l'état normal des cuprates supraconducteurs*. phdthesis, Université Grenoble Alpes [2020-....] ; Université de Sherbrooke (Québec, Canada), October 2020. [57, 71, 75, 78, 80, 81, 82]

[110] Hai-Hu Wen. **Specific heat in superconductors**. *Chinese Physics B*, **29**(1):017401, January 2020. Number: 1. [58]

[111] H. Padamsee, J. E. Neighbor, and C. A. Shiffman. **Quasiparticle phenomenology for thermodynamics of strong-coupling superconductors**. *Journal of Low Temperature Physics*, **12**(3):387–411, August 1973. [58]

[112] John R Clem. **Effects of energy gap anisotropy in pure superconductors**. *Annals of Physics*, **40**(2):268–295, November 1966. [58]

[113] F Bouquet, Y Wang, R. A Fisher, D. G Hinks, J. D Jorgensen, A Junod, and N. E Phillips. **Phenomenological two-gap model for the specific heat of MgB2**. *Europhysics Letters (EPL)*, **56**(6):856–862, December 2001. [58, 59]

[114] A. V. Muratov, A. V. Sadakov, S. Yu. Gavrilkin, A. R. Prishchepa, G. S. Epifanova, D. A. Chareev, and V. M. Pudalov. **Specific heat of FeSe: Two gaps with different anisotropy in superconducting state**. *Physica B: Condensed Matter*, **536**:785–789, May 2018. [58, 60]

[115] J T Chen, Y Sun, T Yamada, S Pyon, and T Tamegai. **Two-gap features revealed by specific heat measurements in FeSe**. *Journal of Physics: Conference Series*, **871**:012016, July 2017. [58]

[116] G. E. Volovik. **Vortex motion in Fermi superfluids and the Callan-Harvey**. *JETP Lett*, **57**(4), 1993. [61]

[117] Yue Sun, Shunichiro Kittaka, Shota Nakamura, Toshiro Sakakibara, Koki Irie, Takuya Nomoto, Kazushige Machida, Jingting Chen, and Tsuyoshi Tamegai. **Gap structure of FeSe determined by field-angle-resolved specific heat measurements**. *Physical Review B*, **96**(22):220505, December 2017. Number: 22 arXiv: 1707.00547. [61]

[118] Scott C. Riggs, O. Vafek, J. B. Kemper, J. B. Betts, A. Migliori, F. F. Balakirev, W. N. Hardy, Ruixing Liang, D. A. Bonn, and G. S. Boebinger. **Heat capacity through the magnetic-field-induced resistive transition in an underdoped high-temperature superconductor**. *Nature Physics*, **7**(4):332–335, April 2011. Number: 4. [64, 65]

[119] Anatoly Larkin (late) and Andrei Varlamov. *Theory of Fluctuations in Superconductors*. Oxford University Press, June 2021. [65]

[120] Terukazu Nishizaki, Yasuaki Onodera, Norio Kobayashi, Hidehito Asaoka, and Humihiko Takei. **Magnetization jump and the vortex-lattice melting transition in YBa2Cu3Oy**. *Physical Review B*, **53**(1):82–85, January 1996. [67]

[121] R. Lortz, C. Meingast, U. Welp, W. K. Kwok, and G. W. Crabtree. **Crystal-Lattice Coupling to the Vortex-Melting Transition in YBa2Cu3O(7-x)**. *Physical Review Letters*, **90**(23):237002, June 2003. Number: 23 Publisher: American Physical Society. [67]

[122] Kathryn A. Moler, Alexander L. Fetter, and Aharon Kapitulnik. **Proposed thermodynamic method to determine the vortex mass in layered superconductors**. *Journal of Low Temperature Physics*, **100**(3-4):185–193, August 1995. Number: 3-4. [66]

[123] Matthew J. W. Dodgson, Vadim B. Geshkenbein, Henrik Nordborg, and Gianni Blatter. **Thermodynamics of the first-order vortex lattice melting transition in YBa2Cu3O(7-x)**. *Physical Review B*, **57**(22):14498–14506, June 1998. Number: 22. [67]

[124] Marlyse Roulin, Alain Junod, and Eric Walker. **Flux Line Lattice Melting Transition in YBa2Cu3O6.94 Observed in Specific Heat Experiments**. *Science*, **273**(5279):1210–1212, August 1996. Number: 5279. [67, 106, 107]

[125] D. J. Thouless. **Critical Fluctuations of a Type-II Superconductor in a Magnetic Field**. *Physical Review Letters*, **34**(15):946–949, April 1975. Number: 15. [68]

[126] Baruch Rosenstein and Dingping Li. **Ginzburg-Landau theory of type II superconductors in magnetic field**. *Reviews of Modern Physics*, **82**(1):109–168, January 2010. Number: 1. [68, 69, 110, 111, 112, 113, 146]

168

[127] S Riegel and G Weber. A dual-slope method for specific heat measurements. *Journal of Physics E: Scientific Instruments*, **19**(10):790–791, October 1986. Number: 10. 72, 73

[128] Bastien Michon. *Point critique quantique de la phase pseudogap dans les cuprates supraconducteurs*. Grenoble Alpes, October 2017. 82

[129] Dmitriy Chareev, Evgeniy Osadchii, Tatiana Kuzmicheva, Jiunn-Yuan Lin, Svetoslav Kuzmichev, Olga Volkova, and Alexander Vasiliev. Single crystal growth and characterization of tetragonal FeSe(1x) superconductors. *CrystEngComm*, **15**(10):1989–1993, February 2013. Publisher: The Royal Society of Chemistry. 92

[130] Yuki Sato, Shigeru Kasahara, Tomoya Taniguchi, Xiangzhuo Xing, Yuichi Kasahara, Yoshifumi Tokiwa, Youichi Yamakawa, Hiroshi Kontani, Takasada Shibauchi, and Yuji Matsuda. Abrupt change of the superconducting gap structure at the nematic critical point in FeSe(1x)S(x). *Proceedings of the National Academy of Sciences*, **115**(6):1227–1231, February 2018. Number: 6. 94, 100

[131] F. Hardy, L. Doussoulin, T. Klein, M. He, A. Demuer, R. Willa, K. Willa, A.-A. Haghighirad, T. Wolf, M. Merz, C. Meingast, and C. Marcenat. Vortex-lattice melting and paramagnetic depairing in the nematic superconductor FeSe. *Physical Review Research*, **2**(3):033319, August 2020. Publisher: American Physical Society. 102, 109, 114, 117, 118

[132] Philippe Mangin and Rémi Kahn. *Matériaux supraconducteurs*. EDP sciences, November 2017. 102

[133] Marlyse Roulin, Alain Junod, Andreas Erb, and Eric Walker. Calorimetric Transitions on the Melting Line of the Vortex System as a Function of Oxygen Deficiency in High-Purity YBa 2 Cu 3 O x. *Physical Review Letters*, **80**(8):1722–1725, February 1998. Number: 8. 106

[134] T. Watashige, Y. Tsutsumi, T. Hanaguri, Y. Kohsaka, S. Kasahara, A. Furusaki, M. Sigrist, C. Meingast, T. Wolf, H.v. Löhneysen, T. Shibauchi, and Y. Matsuda. Evidence for Time-Reversal Symmetry Breaking of the Superconducting State near Twin-Boundary Interfaces in FeSe Revealed by Scanning Tunneling Spectroscopy. *Physical Review X*, **5**(3):031022, August 2015. 106, 121

[135] Yue Sun, Sunseng Pyon, Tsuyoshi Tamegai, Ryo Kobayashi, Tatsuya Watashige, Shigeru Kasahara, Yuji Matsuda, and Takasada Shibauchi. Critical current density, vortex dynamics, and phase diagram of single-crystal FeSe. *Physical Review B*, **92**(14):144509, October 2015. Number: 14. 119

[136] M. Bristow, P. Reiss, A. A. Haghighirad, Z. Zajicek, S. J. Singh, T. Wolf, D. Graf, W. Knafo, A. McCollam, and A. I. Coldea. Anomalous high-magnetic field electronic state of the nematic superconductors FeSe(1-x)S(x). *Physical Review Research*, **2**(1):013309, March 2020. 124, 139, 141

[137] R. Lortz, Y. Wang, A. Demuer, P. H. M. Böttger, B. Bergk, G. Zwicknagl, Y. Nakazawa, and J. Wosnitza. Calorimetric Evidence for a Fulde-Ferrell-Larkin-Ovchinnikov Superconducting State in the Layered Organic Superconductor (BEDTTTF)2Cu(NCS)2. *Physical Review Letters*, **99**(18):187002, October 2007. 126

[138] W. Kwok, U. Welp, G. Crabtree, K. Vandervoort, R. Hulscher, and J. Liu. Direct observation of dissipative flux motion and pinning by twin boundaries in YBa2Cu3O(7-x) single crystals. *Physical Review Letters*, **64**(8):966–969, February 1990. 137

[139] S. Kasahara, T. Yamashita, A. Shi, R. Kobayashi, Y. Shimoyama, T. Watashige, K. Ishida, T. Terashima, T. Wolf, F. Hardy, C. Meingast, H. v. Löhneysen, A. Levchenko, T. Shibauchi, and Y. Matsuda. Giant superconducting fluctuations in the compensated semimetal FeSe at the BCS–BEC crossover. *Nature Communications*, **7**(1):12843, November 2016. 138, 139

[140] Feifei Yuan, Vadim Grinenko, Kazumasa Iida, Stefan Richter, Aurimas Pukenas, Werner Skrotzki, Masahito Sakoda, Michio Naito, Alberto Sala, Marina Putti, Aichi Yamashita, Yoshihiko Takano, Zhixiang Shi, Kornelius Nielsch, and Ruben Hühne. Universal scaling behavior of the upper critical field in strained FeSe $_{0.7}$ Te $_{0.3}$ thin films. *New Journal of Physics*, **20**(9):093012, September 2018. 148

[141] Vladimir P. Mineev and Vincent P. Michal. Temperature-Dependent Ginzburg–Landau Parameter. *Journal of the Physical Society of Japan*, **81**(9):093701, September 2012. Publisher: The Physical Society of Japan. 148

[142] Jie Xing, Sheng Li, Bin Zeng, Gang Mu, Bing Shen, J. Schneeloch, R. D. Zhong, T. S. Liu, G. D. Gu, and Hai-Hu Wen. Power-law-like correlation between condensation energy and superconducting transition temperatures in iron pnictide/chalcogenide superconductors: Beyond the BCS understanding. *Physical Review B*, **89**(14):140503, April 2014. Publisher: American Physical Society. 148

[143] V. G. Kogan. Strong pairbreaking in anisotropic superconductors. *Physical Review B*, **81**(18):184528, May 2010. 148

[144] M. Abdel-Hafiez, J. Ge, A. N. Vasiliev, D. A. Chareev, J. Van de Vondel, V. V. Moshchalkov, and A. V. Silhanek. Temperature dependence of lower critical field Hc1(T) shows nodeless superconductivity in FeSe. *Physical Review B*, **88**(17):174512, November 2013. 151